An Adaptive Immersed Mesh Method (AIMM) for Fluid-Structure Interaction (FSI)
Ramy Nemer

HAL Id: tel-03859469
https://pastel.hal.science/tel-03859469

Submitted on 18 Nov 2022

PSL ★
UNIVERSITÉ PARIS

THÈSE DE DOCTORAT
DE L'UNIVERSITÉ PSL

Préparée à MINES Paris

An Adaptive Immersed Mesh Method (AIMM) for Fluid–Structure Interaction (FSI)
Une Méthode Adaptative de Maillage Immergé (AIMM) pour l'Interaction Fluide–Structure (FSI)

Soutenue par
Ramy NEMER
Le 23 novembre 2021

École doctorale n°364
Sciences Fondamentales et Appliquées

Spécialité
Mathématiques Numériques, Calcul Intensif et Données

Composition du jury :

Thomas J.R. HUGHES Professeur, The University of Texas at Austin	*Président*
Arif MASUD Professeur, University of Illinois at Urbana-Champaign	*Rapporteur*
Ramon CODINA Professeur, Universitat Politècnica de Catalunya	*Rapporteur*
Stefanie ELGETI Professeur, Vienna University of Technology	*Examinateur*
Trond KVAMSDAL Professeur, NTNU: Norwegian University of Science and Technology	*Examinateur*
Aurélien LARCHER Chargé de Recherche, Mines Paris	*Examinateur*
Thierry COUPEZ Professeur, Mines Paris	*Co-directeur de thèse*
Elie HACHEM Professeur, Mines Paris	*Directeur de thèse*
Nicolas PEYRON AQUALUNG GROUP	*Invité*
Stéphanie GODIER Recherche et avenir	*Invité*

MINES ParisTech | PSL ★

To Eleonora

Acknowledgements

Words will not do right by the people that stood by me during this project, so I will keep this brief and straight to the point. If you feel like you have contributed in any way or form (academically, morally, ...) in the success of this PhD thesis, please accept my deepest thanks. I am grateful for your help. To a new chapter in the book of life.

Contents

Contents

Contents

Contents

List of Figures

List of Figures

List of Tables

List of Tables

Chapter 1

Introduction

Contents

L'interaction fluide-structure (FSI) est l'interaction multi-physique inévitable entre une structure solide déformable/mobile (lois de la mécanique des structures) immergée et/ou contenant un fluide de travail (lois de la dynamique des fluides). L'interaction peut être oscillatoire ou atteindre un état stationnaire stable. Le FSI est pris en compte dans un grand nombre d'applications dans le glossaire de l'ingénierie, qui incluent, mais sans s'y limiter, l'aérodynamique, l'hydrodynamique, l'acoustique et la biomécanique. Ne pas tenir compte de l'interaction des deux médiums peut conduire à des résultats catastrophiques. Le tristement célèbre cas du pont de Tacoma (1940) sert d'exemple d'une telle catastrophe à grande échelle. Le fluide, caractérisé par des champs de vitesse et de pression, exerce des forces aérodynamiques sur l'interface FSI du solide. Le solide est déplacé/déformé sous ces actions. Ce champ de déplacement affecte à son tour le champ d'écoulement du fluide, modifiant ainsi les forces aérodynamiques. Le couplage faible considère uniquement l'action du fluide sur le solide (ou l'inverse). Couplage fort, considère un couplage bidirectionnel entre les deux entités. Compte tenu de la nature intrinsèque complexe de tels phénomènes, peu ou pas de solution analytique peut décrire avec précision le comportement des milieux. On peut recourir à des études expérimentales, qui se sont avérées coûteuses en temps et en ressources. Comme alternative aux méthodes mentionnées ci-dessus, les simulations numériques qui modélisent avec précision de tels phénomènes présentent un intérêt croissant. Pour résoudre numériquement les équations aux dérivées partielles (EDP), nous utilisons des méthodes de discrétisation (élément fini, volume fini, différence finie...), qui à leur tour approximent les équations différentielles par un ensemble d'équations algébriques, qui sont résolues. Or, cette discrétisation s'applique à la fois à l'espace et au temps selon le problème (stationnaire ou transitoire). De plus, malgré les avancées dans les domaines de la dynamique des fluides computationnelle (CFD) et de la mécanique des solides computationnelle (CSM), le domaine informatique FSI est toujours à la traîne. Les méthodes FSI de différentes essences font l'objet d'investigations intensives. Certains des problèmes courants rencontrés sur le terrain sont la nécessité d'adapter le maillage, l'algorithme de couplage, les grandes déformations, le nombre de Reynolds élevé et les géométries complexes. Le chapitre présente les différentes formulations et approches de l'ISF. Il est important de noter qu'il ne s'agit pas d'une revue de littérature complète, mais plutôt d'une introduction aux différentes méthodes déjà existantes. Cette revue de la littérature sera complétée à chaque chapitre, où les spécificités de chaque sujet seront abordées dans l'introduction du chapitre. Comme déjà expliqué, différentes approches et formulations existent pour résoudre les problèmes FSI. Chacun avec son ensemble d'avantages et d'inconvénients. Cette thèse vise à tirer les avantages des différentes approches tout en ignorant autant que possible les inconvénients. L'utilisation de

l'expertise déjà développée dans les différents domaines de CimLib_CFD a permis d'atteindre l'objectif final. Une telle expertise réside dans la méthode du volume immergé (IVM) par exemple, qui est un outil efficace pour surmonter les problèmes de chevauchement de maillage. La méthode level set est utilisée pour immerger le maillage solide dans un maillage fluide-solide. Cela permet de suivre l'interface FSI pour deux domaines distincts. Pour mieux représenter l'interface FSI dans le maillage fluide-solide et obtenir une plus grande précision dans une région cruciale du calcul FSI, nous utilisons l'adaptation de maillage anisotrope. Cette technique va générer des éléments très étirés près de l'interface FSI. Un solveur CFD FE stabilisé pour la dynamique des fluides est également utilisé pour le calcul de l'écoulement de fluide. Toute cette expertise déjà existante sera couplée à un solveur lagrangien hyperélastique et à un schéma de couplage fort bidirectionnel (AIMM) pour réaliser notre simulateur FSI final. Pour pouvoir couvrir une large gamme d'applications FSI, un solveur Lagrangien séparé qui peut avoir des lois de comportement complexes est nécessaire. Dans ce travail, un solveur solide lagrangien est présenté. Le déplacement et la pression sont les principales variables du solveur. La méthode variationnelles multi-échelle (VMS) est utilisée pour stabiliser le solveur pour le même ordre d'interpolation de la variable, contournant ainsi la condition « inf-sup » et supprimant toute oscillation de pression parasite. Un solveur élastique linéaire a d'abord été développé, suivi d'un solveur hyperélastique. Cela nous permet de conserver les avantages de l'approche partitionnée, qui est principalement la flexibilité d'avoir un solveur lagrangien solide séparé. Ce solveur devant ensuite être couplé à un solveur fluide. Ainsi, les équations classiques de Navier–Stokes sont résolues. Un solveur interne déjà développé est utilisé avec la vitesse et la pression comme variables principales. La méthode VMS est également utilisée pour la stabilisation du solveur, ce qui aide à résoudre deux problèmes principaux : la condition « inf-sup » et les régimes dominés par la convection. Les équations de Navier–Stokes sont résolues sur un maillage fluide-solide. Le solide coexiste avec le fluide dans le maillage précité. Cela se fait en immergeant le maillage solide sur le maillage fluide-solide à chaque itération. Ainsi, suivi du mouvement solide dans le maillage fluide-solide. Un mécanisme de couplage bidirectionnel est utilisé, où la contrainte et la vitesse complètes sont interpolées entre les solveurs. Cette thèse a été soutenue par AquaLung. Leur but est de créer un simulateur pour leurs applications pour l'optimisation éventuelle de leur produit. Tous les développements et simulations numériques sont réalisés dans la librairie FR C++ CimLib_CFD. Le manuscrit suivant est organisé comme suit : Le deuxième chapitre présente l'expertise déjà développée du groupe de recherche qui va être utilisée pour créer le cadre FSI. Cela inclut la méthode des ensembles de niveau pour l'immersion, le mélange des propriétés pour l'écoulement multi phase, l'adaptation du maillage anisotrope et le solveur de fluide. Le troisième chapitre explique le solveur lagrangien de dynamique

solide. Commençant par le cas élastique linéaire et atteignant le cas hyperélastique. La méthode VMS pour la stabilisation du solveur est présentée. Enfin, plusieurs exemples 2D et 3D sont présentés pour prouver les capacités du solveur. Le quatrième chapitre constitue le cœur de la thèse. Il introduit le framework FSI hybride AIMM. Expliquer les différents composants utilisés pour réussir le couplage FSI. De nombreuses simulations numériques 2D et 3D sont réalisées pour mettre en valeur les capacités du framework. Le chapitre cinq présente l'application industrielle de notre partenaire industriel (AquaLung). Nous terminons le manuscrit par la conclusion et les perspectives au chapitre six.

1.1 An introduction to Fluid–Structure Interaction

Fluid–Structure Interaction (FSI) is the multi-physical inevitable interaction between a deformable/movable solid structure (laws of structural mechanics) immersed and/or containing a working fluid (laws of fluid dynamics) [1]. The interaction can be oscillatory or reach a stable steady state. FSI is considered in a vast number of applications in the engineering glossary, which include but are not restricted to, aerodynamics, hydrodynamics, acoustics, and biomechanics. Failure to account for the interaction of the two mediums may lead to catastrophic results. The infamous case of the Tacoma narrows bridge (1940) serves as an example of such a large-scale catastrophe [2]. Figure 1.1 showcases the failure of the bridge due to resonance vibration. Another example of such failures is the fluttering phenomena exhibited by aircraft, and wind turbine blades. Another small-scale, biological example is the accurate modeling of blood flows. Blood vessel's may alter in size significantly due to modifications in blood pressure, and blood velocity [3]. If vessels are considered as rigid bodies, an overestimation of the Wall Shear Stress (WSS) is computed. Therefore, an accurate depiction of the vessels properties leads to a better estimation of the behavior of such a biological system and inevitably leads to better treatments. One application of such a phenomenon is cerebral aneurysms. The neck of such an aneurysm risks failure when becoming thin enough, and undergoing high WSS values. Thus, an accurate and precise FSI simulation of a patient's case can help the practitioner decide on the possible remedies for a specific case[4–7].
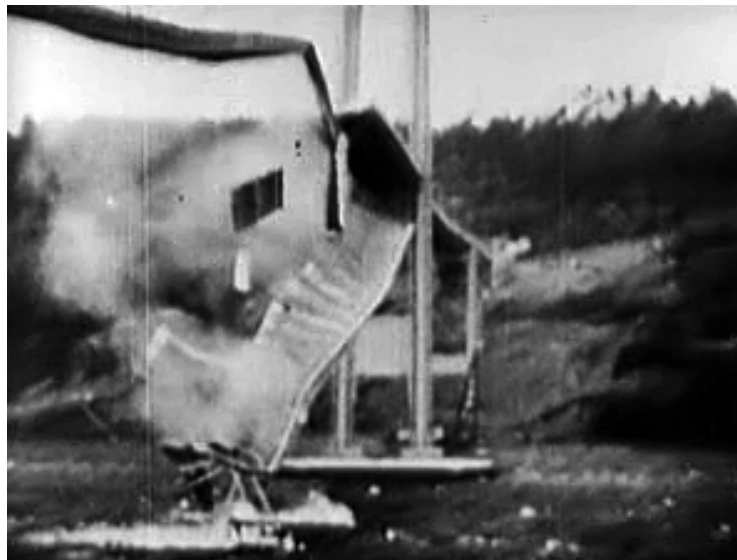
Figure 1.1: The catastrophic Tacoma narrows bridge incident in Detroit (1940). Retrieved from: https://commons.wikimedia.org/w/index.php?curid=1839248

The interaction happening between the entities is depicted in figure 1.2. The fluid, which is characterized by velocity, and pressure fields exercises aerodynamic forces on the FSI interface of the solid. The solid is moved/deformed under these actions. This displacement field in turn affects the flow field of the fluid, thus altering the aerodynamic forces. Weak coupling considers the action of the fluid on the solid (or the inverse) only. Strong coupling, considers a two-way coupling between the two entities.
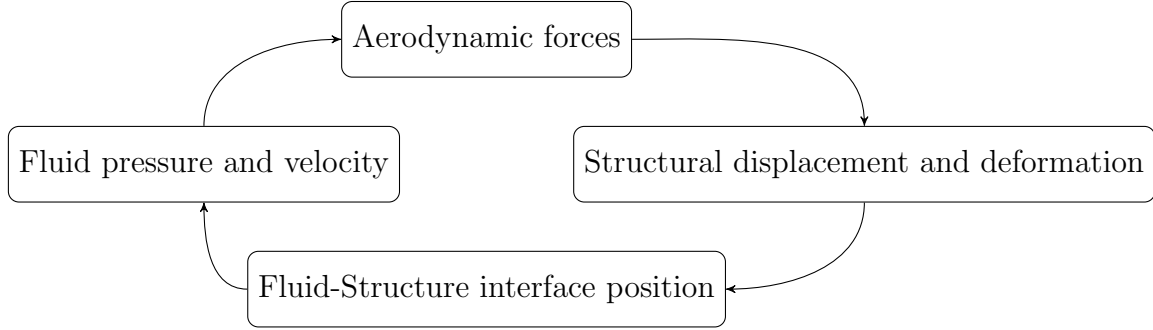
Figure 1.2: Schematic of the FSI interaction cycle.

Given the complex intrinsic nature of such phenomena, little to no analytical solution can accurately depict the behavior of the mediums. One can resort to experimental studies, which have proven to costly in terms of time and resources. As an alternative to the above-mentioned methods, numerical simulations that accurately model such phenomena are of increasing interest. According to Moore's law, this field is ever growing with the advances of integrated circuits and the evolution of computing power. Moore's law states that the number of transistors on an Integrated circuit (IC) is multiplied by two every two years [8]. His work was published in 1965 and was a projection of the following years. This law fulfilled its expectations in terms of the number of transistors on an integrated circuit and is a guideline for technological advancement in the semiconductor industry. This law full filled its expectations till around the 2000s, in terms of computational power, and still holds partially, due to the emergence of parallel computations. To solve Partial Differential Equations (PDEs) numerically, we use discretization methods (Finite Element, Finite Volume, Finite Difference . . .), which in turn approximate the differential equations by a set of algebraic equations, that are solved. A mesh can be generated using commercial software, like Gmsh [9]. Now, this discretization is applied to both space and time depending on the problem (steady-state or transient). Higher quality of discretization (second-order or higher) and finer mesh lead to better results and convergence of the solution. Furthermore, despite the advances in the fields of Computational Fluid Dynamics (CFD), and Computational Solid Mechanics (CSM), the computational FSI domain is still lagging. FSI meth-

ods of different essences are under intensive investigation. Some of the common problems encountered in the field are the need for mesh adaptation, the coupling algorithm, large deformation, high Reynolds number, and complex geometries.

1.2 Literature Review

This part of the chapter introduces the different formulations and approaches for FSI. It is important to note that this is not a full literature review, but more of an introduction to the different already existent methods. This literature review will be completed with each chapter, where specifics on each subject will be tackled in the introduction of the chapter.

1.2.1 Formulations

Different formulations are first presented while highlighting their advantages and disadvantages.

1.2.1.1 Lagrangian Formulation

The Lagrangian formulation treats the particle motion as a quantity moving in space on a reference frame attached to the particle. The initial reference frame is known. This technique is highly used in Computational Solid Mechanics (CSM) [10]. Using the finite element method, this formulation necessitates that each computational node is in touch with the initial particle throughout the motion of the solid. This property is of particular interest numerically speaking, as advective terms drop from the equation in this case. This is also of interest when considering the particles located at the wetted interface between the solid, and the fluid, as it renders interface tracking a lot easier. The main drawback of this formulation is that it cannot handle large deformations. Large deformation causes the mesh to distort This formulation is regarded as an interface-tracking formulation.

1.2.1.2 Eulerian Formulation

The Eulerian formulation tracks the change in a material quantity through a region. The reference system in this case is fixed. The Eulerian formulation necessitates a fixed mesh. It defines a constant volume, and the quantities can migrate from one element to another. Material particles can thus leave the defined volume, and subsequently, we lose any information on these particles. Tracking moving boundaries in an Eulerian framework is not straightforward, and requires additional methods [11]. In addition, if no type of mesh adaptation is applied, the material boundaries will not be overlapping on element edges, especially when the boundary is evolving

in time. Thus, rendering the boundary conditions on the interface tedious to apply. The Eulerian formulation can take into account large displacement and is very popular in the field of CFD. The interface between the fluid and the solid can move freely on the fixed Eulerian mesh. Elastic materials can also be modeled using an Eulerian framework. In [12] the interaction between an elastic membrane, and an incompressible fluid is presented. Authors in [13, 14] implemented a full Eulerian formulation for an incompressible fluid and a hyper-elastic solid. This formulation is seen as an interface-capturing formulation. The capturing of the interface was done using the Initial Point Set (IPS) method. A vector field Φ_{IPS} is used to transport the coordinate system. This interface-capturing tool was able to handle sharp corners.

1.2.1.3 Arbitrary Lagrangian-Eulerian (ALE) Formulation

The ALE formulation acquired a lot of attention among the different formulations [15–17]. It is based on the idea of having a grid moving at a different rate of the solid structure. Thus, having the structure move relative to the mesh, which is somewhat like the Eulerian formulation. Whilst having the elements controlled using the physical boundary conditions of the problem, which is also like the Lagrangian formulation. This supposedly combines a well-defined interface with the ability to easily impose physical boundary conditions, and the ability to handle large distortions. Note that in that case, the domain is deformable/movable, engendering modifications to the advective term of the equations. The method proved to work very well, under certain limitations for the solid rotations, and translations [11, 18, 19]. When these limits are exceeded, the mesh becomes distorted and the ALE formulation fails. Mesh adaptation techniques are usually resorted to, to help circumvent the problem [20]. However, this is easier said than done. Another solution, was developed in [21–23]. They make use of a fixed Eulerian mesh, by using the extended finite element method (XFEM), and Lagrange multipliers to couple it with the deformable ALE mesh. The mesh deformation is directly related to the interface position. This helps keep most of the mesh intact. In [24], the Finite Volume (FV) method is used for the fluid, and the Finite Element (FE) method is used for the solid. The ALE formulation is coupled with a multi-grid technique. When considering large enough deformations, the ALE formulation necessitates coupling with other techniques.

1.2.1.4 Eulerian-Lagrangian Formulation

As the name suggests, the Eulerian-Lagrangian formulation treats each component in its preferred setting. Thus, formulating the fluid in an Eulerian manner, and the solid in a Lagrangian manner [25]. The main difference between this formulation,

and the ALE formulation, lies within the fluid mesh. The mesh in the Eulerian-Lagrangian formulation does not move based on the interface position. Thus there are no limitations on the amplitude of deformation on the solid that may result in a distorted mesh. The interface may be represented using a signed distance function (level set). The coupling between the fluid and the solid can be achieved through Lagrange multipliers or the penalty method [26]. Authors in [27], utilized the Eulerian-Lagrangian formulation to handle multiple thin solid structures immersed in a fluid medium. The extended finite element method (XFEM) is used to enrich the space-time approximations of the variables to handle discontinuities that may arise due to phase change.

1.2.1.5   The Fictitious Domain Formulation

The Fictitious Domain Formulation [28] consists of extending the current problem domain, to a possibly bigger more simple domain called the fictitious domain. This method is known for having two main advantages:

1. The extended more simple domain is simpler than the initial one, thus a more regular mesh is chosen. This allows more direct ways of solving elliptical problems, for example, leading to lower resolution times.

2. The extended more trivial domain can be chosen to be time-independent, despite the possibility of the time dependency of the initial domain. This allows for the same fixed mesh to be used on the extended domain during the whole time, omitting any need for projection and remeshing.

The same boundary conditions on the initial domain should be respected by the extended domain. Authors in [28, 29], use the fictitious domain method to tackle FSI problems of rigid bodies with relatively important rotations/translations. The alluviation of solid rigid particles is modeled. The particles are immersed in the working fluid and are considered using Lagrange multipliers. Similar work can be found in [30], where thin structural bodies are considered and Lagrange multipliers are applied at the interface. If we consider the Lagrange multiplier on the whole solid, the method is not limited to thin bodies. Authors in [31], were able to model the pressure drop through a solid body, which is of interest in the biomechanics field. Authors in [32], coupled the fictitious domain method with a mesh adaptation method to model the shear stress, and the pressure drop of the solid interface.

1.2.2   The monolithic and partitioned approaches for FSI

There are two famous approaches for solving FSI, which are:

1. The partitioned approach

2. The monolithic approach

Authors in [33], classified different ways to tackle the problem from an engineering point of view in Table 1.1. We see the distinction between conforming and non-conforming mesh. In this work, the conforming mesh method treats the interface as part of the solution and the interface conditions as physical boundary conditions. Thus, when a solid move or deforms, re-meshing is required. However, non-conforming meshes treat the interface location and conditions as constraints embedded in the equations to be solved, thus leading to non-conforming meshes at the interface. Thus the equations can be solved separately with no re-meshing.

Methods	Monolithic		
	Partitioned	"Conforming mesh"	
		"Non-conforming mesh"	Immersed Boundary Method
			Immersed Domain Method

Table 1.1: Different Methods for FSI

1.2.2.1   The partitioned approach

The partitioned approach, as the name suggests, distinguishes between the two mediums at hand. Thus, two separate grids are used for each domain, enabling us to have separate solvers for the fluid and the solid. Multiple subsystems are solved separately. The interactions between the two subdomains are treated as Boundary Conditions (BC) at the FSI interface. The main challenge of such an approach is the communication between the different grids and subsystems. We distinguish between two main coupling methods for the partitioned approach [34–37]:

- Strongly coupled

- Weakly coupled

For strongly coupled systems, sub-iterations and relaxation are needed to guarantee convergence of the solution. They do however possess an inherent instability when dealing with incompressible flows. This is mainly related to the geometrical shape of the domain, and the fluid/solid density ratio [38]. One must also be careful when choosing the time step for a simulation. Reducing the time step does not always render a system more stable. For this case, for example, such a step may increase instabilities. This inherent instability is what is known as the artificial added mass effect [39]. Some parts of the fluid act as an additional weight on the structures Degrees Of Freedom (DOF) at the interface. Simply put, the fluid forces are dependent on the structural displacement field, and not the actual fluid force.

If not treated correctly, it may include inaccurate coupling forces. This instability is more prominent in biomechanical applications. Authors in [**?**], use a Laplacian matrix at the interface that helps in obtaining accurate results. This is done by separating the velocity from the pressure. The velocity is first calculated, and the pressure is then calculated from the previous result. This helps circumvent the artificial added mass effect problem. Different simulations of an incompressible fluid with an elastic solid are presented. For weakly coupled systems, the boundary conditions are treated explicitly with no sub-iterations. A single solution is required for each field at each time increment. This may lead to inaccurate coupling. Weakly coupled systems usually suffer from instability. The most widely used methods are the Immersed methods (Immersed Volume, Immersed Boundary ...), of which the most common is the Immersed Boundary Method (IBM), which was first developed for biomedical purposes [40, 41].

In most cases, the fluid flow requires a mesh finer mesh than that of the solid. This is why we have non-matching meshes at the interface. In FSI simulations, the domains are non-overlapping domains in general. The communication between the two mediums is done by Interpolation/Projection. Different methods of communication are found in the literature, such as the nearest neighbor interpolation, methods based on interpolation by spline, and projection methods. The most important criteria that should be satisfied by coupling strategies are: (i) global conservation of energy over the interface, (ii) global conservation of loads over the interface, (iii) accuracy, (iv) conservation of the order of the coupled solver, (v) efficiency. Efficiency is seen as the ratio of accuracy and computational cost. The simplest method by far is the nearest neighbor method, as it consists of obtaining the information from the closest point on the opposing mesh. This method is unsatisfactory for the slightest trace of complexity. The projection method is a lot more accurate. To obtain information from mesh A onto mesh B, we take a point from mesh A and do an orthogonal projection onto mesh B; the values of both points are the same. This method is widely used when Gauss Integration rules are used for the integral. This method in principle, respects (ii). However, some structural elements may not be considered in the integration, so they receive no pressure force. One can overcome this obstacle by using more Gauss points, but given the fact that the fluid has a far finer mesh than the solid, this is hardly an issue. The projection is done by minimal distance projection.

1.2.2.2 The monolithic approach

The monolithic approach solves a single system of equations on a single grid that considers both the solid, and the fluid, and inherently satisfies the interface coupling conditions. It allows for implicit solution schemes, integration of error-based estimators, and relatively large time steps. Only one of the two mediums, fluid or

solid, can be solved in its natural coordinate system and the other problem needs to be re-formulated in a transformed coordinate system. This is due to the fact that the solid is solved in a Lagrangian manner, while the fluid is solved in an Eulerian manner. Large deformations are better captured in an Eulerian framework. The main drawback of such an approach is the inability to use already existing solvers for independent mediums.

1.3 Objective of the thesis

As already explained, different approaches and formulations exist for solving FSI problems. Each with its set of advantages and drawbacks. This thesis aims to draw the advantages of the different approaches while hopefully disregarding as many of the drawbacks as possible. The use of the already developed expertise in the different domains of CimLib_CFD [42] helped reach the final goal. Such expertise lies in the Immersed Volume Method (IVM) for example [43, 44], which is an efficient tool to overcome problems of mesh overlapping. The level set method is used to immerse the solid mesh onto a fluid-solid mesh. This helps track the FSI interface for two separate domains. To better represent the FSI interface in the fluid-solid mesh, and obtain a higher accuracy at a crucial region of the FSI computation, we make use of the anisotropic mesh adaptation [45, 46]. This technique will generate highly stretched elements near the FSI interface. A CFD FE stabilized solver for fluid dynamics is also used for the computation of the fluid flow [47]. All this already existent expertise will be coupled with a hyperelastic Lagrangian solver and a two-way strong coupling scheme (AIMM) to achieve our final FSI simulator.

1.3.1 Numerical method and applications

To be able to cover a wide range of FSI applications, a separate Lagrangian solver that can have complex behavior laws is needed. In this work, a Lagrangian solid solver is presented. The displacement and pressure are the primary variables of the solver. The Variational Multi-Scale (VMS) method is used to stabilize the solver for the same order interpolation of the variable, thus circumventing the inf-sup condition and removing any spurious pressure oscillations. A linear elastic solver was first developed, and a hyperelastic solver followed. This enables us to retain the advantages of the partitioned approach, which is mainly the flexibility of having a separate solid Lagrangian solver. This solver then to be coupled with a fluid solver. Thus the classical Navier–Stokes equations are solved. An already developed in-house solver is used with velocity and pressure being the primary variables. The VMS method is also used for the stabilization of the solver, which helps with two main problems: the inf-sup condition and convection-dominated regimes. The

Navier–Stokes equations are solved on a fluid-solid mesh. The solid co-exists with fluid in the aforementioned mesh. This is done by immersing the solid mesh onto the fluid-solid mesh at each time iteration. Thus, tracking the solid movement in the fluid-solid mesh. A two-way coupling mechanism is employed, where full stress and velocity are interpolated between solvers.

1.4 Framework of the thesis

This thesis was supported by AquaLung. Their goal is to create a simulator for their applications for the eventual optimization of their product. This Ph.D. led to several new projects in the biomedical field. All the developments and numerical simulations are carried out in the house FR C++ library CimLib_CFD.

1.5 Layout of the thesis

The following manuscript is organized as follows: The second chapter introduces the already developed expertise of the research group that is going to be used to create the FSI framework. This includes the level set method for immersion, the mixing of properties for multi-phase flow, the anisotropic mesh adaptation, and the fluid solver. The third chapter explains the Lagrangian solid dynamics solver. Starting with the linear elastic case and reaching the hyperelastic case. The VMS method for the solver stabilization is presented. Finally, several 2D and 3D examples are shown to prove the capabilities of the solver. The fourth chapter consists of the heart of the thesis. It introduces the hybrid FSI framework AIMM. Explaining the different components used for the successful FSI coupling. Numerous 2D and 3D numerical simulations are conducted to showcase the capabilities of the framework. Chapter five introduces the industrial application of our industrial partner (AquaLung). We end the manuscript with the conclusion and perspectives in chapter six.

Bibliography

[1] H.-J. Bungartz, M. Schäfer, Fluid-structure interaction: modelling, simulation, optimisation, Vol. 53, Springer Science & Business Media, 2006. 5

[2] D. Olson, S. Wolf, J. Hook, The tacoma narrows bridge collapse, Physics Today 68 (2015) 64–65. doi:10.1063/PT.3.2991. 5

[3] J. A. Taren, Cerebral aneurysm, The American journal of nursing (1965) 88–91. 5

Bibliography

[4] D. M. Sforza, C. M. Putman, J. R. Cebral, Computational fluid dynamics in brain aneurysms, International journal for numerical methods in biomedical engineering 28 (6-7) (2012) 801–808. 5

[5] A. K. Khe, A. A. Cherevko, A. P. Chupakhin, M. S. Bobkova, A. L. Krivoshapkin, K. Y. Orlov, Haemodynamics of giant cerebral aneurysm: A comparison between the rigid-wall, one-way and two-way FSI models, Journal of Physics: Conference Series 722 (2016) 012042. doi:10.1088/1742-6596/722/1/012042.
URL https://doi.org/10.1088/1742-6596/722/1/012042

[6] R. Torii, M. Oshima, T. Kobayashi, K. Takagi, T. Tezduyar, Fluid-structure interaction modeling of blood flow and cerebral aneurysm: Significance of artery and aneurysm shapes, Computer Methods in Applied Mechanics and Engineering 198 (2009) 3613–3621. doi:10.1016/j.cma.2008.08.020.

[7] R. Razaghi, H. Biglari, A. Karimi, Risk of rupture of the cerebral aneurysm in relation to traumatic brain injury using a patient-specific fluid-structure interaction model, Computer Methods and Programs in Biomedicine 176 (2019) 9–16. doi:https://doi.org/10.1016/j.cmpb.2019.04.015.
URL   https://www.sciencedirect.com/science/article/pii/S0169260719303402 5

[8] G. E. Moore, Cramming more components onto integrated circuits, reprinted from electronics, volume 38, number 8, april 19, 1965, pp.114 ff., IEEE Solid-State Circuits Society Newsletter 11 (3) (2006) 33–35. doi:10.1109/N-SSC.2006.4785860. 6

[9] C. Geuzaine, J.-F. Remacle, Gmsh: A 3-d finite element mesh generator with built-in pre- and post-processing facilities, International Journal for Numerical Methods in Engineering 79 (11) (2009) 1309–1331. arXiv:https://onlinelibrary.wiley.com/doi/pdf/10.1002/nme.2579, doi:10.1002/nme.2579.
URL https://onlinelibrary.wiley.com/doi/abs/10.1002/nme.2579 6

[10] P.-O. Persson, J. Peraire, Curved mesh generation and mesh refinement using lagrangian solid mechanics, in: 47th AIAA Aerospace Sciences Meeting including The New Horizons Forum and Aerospace Exposition, 2009, p. 949. 7

[11] M. Souli, A. Ouahsine, L. Lewin, Ale formulation for fluid–structure interaction problems, Computer Methods in Applied Mechanics and Engineering 190 (5) (2000) 659–675. doi:https://doi.org/10.1016/S0045-7825(99)00432-6.
URL   https://www.sciencedirect.com/science/article/pii/S0045782599004326 7, 8

14

[12] G.-H. Cottet, E. Maitre, T. Milcent, Eulerian formulation and level set models for incompressible fluid-structure interaction, ESAIM: Mathematical Modelling and Numerical Analysis 42 (3) (2008) 471–492. 8

[13] T. Dunne, Adaptive Finite Element Approximation of Fluid-Structure Interaction Based on Eulerian and Arbitrary Lagrangian-Eulerian Variational Formulations , Theses, University of Heidelberg (2007).
URL https://archiv.ub.uni-heidelberg.de/volltextserver/7944/ 8

[14] T. Dunne, An eulerian approach to fluid–structure interaction and goal-oriented mesh adaptation, International Journal for Numerical Methods in Fluids 51 (9-10) (2006) 1017–1039. arXiv:https://onlinelibrary.wiley.com/doi/pdf/10.1002/fld.1205, doi:10.1002/fld.1205.
URL https://onlinelibrary.wiley.com/doi/abs/10.1002/fld.1205 8

[15] C. W. Hirt, A. A. Amsden, J. Cook, An arbitrary lagrangian-eulerian computing method for all flow speeds, Journal of computational physics 14 (3) (1974) 227–253. 8

[16] T. J. Hughes, W. K. Liu, T. K. Zimmermann, Lagrangian-eulerian finite element formulation for incompressible viscous flows, Computer methods in applied mechanics and engineering 29 (3) (1981) 329–349.

[17] J. Donea, S. Giuliani, J.-P. Halleux, An arbitrary lagrangian-eulerian finite element method for transient dynamic fluid-structure interactions, Computer methods in applied mechanics and engineering 33 (1-3) (1982) 689–723. 8

[18] D. J. Benson, An efficient, accurate, simple ale method for nonlinear finite element programs, Computer methods in applied mechanics and engineering 72 (3) (1989) 305–350. 8

[19] R. van Loon, P. D. Anderson, F. N. van de Vosse, S. J. Sherwin, Comparison of various fluid–structure interaction methods for deformable bodies, Computers & structures 85 (11-14) (2007) 833–843. 8

[20] P. Saksono, W. Dettmer, D. Perić, An adaptive remeshing strategy for flows with moving boundaries and fluid–structure interaction, International Journal for Numerical Methods in Engineering 71 (9) (2007) 1009–1050. 8

[21] A. Gerstenberger, W. A. Wall, An extended finite element method/lagrange multiplier based approach for fluid–structure interaction, Computer Methods in Applied Mechanics and Engineering 197 (19-20) (2008) 1699–1714. 8

15

Bibliography

[22] W. Wall, A. Gerstenberger, U. Mayer, Advances in fixed-grid fluid structure interaction, in: ECCOMAS Multidisciplinary Jubilee Symposium, Springer, 2009, pp. 235–249.

[23] W. A. Wall, A. Gerstenberger, P. Gamnitzer, C. Förster, E. Ramm, Large deformation fluid-structure interaction–advances in ale methods and new fixed grid approaches, in: Fluid-structure interaction, Springer, 2006, pp. 195–232. 8

[24] D. Sternel, M. Schäfer, M. Heck, S. Yigit, Efficiency and accuracy of fluid-structure interaction simulations using an implicit partitioned approach, Computational mechanics 43 (1) (2008) 103–113. 8

[25] R. Garg, C. Narayanan, S. Subramaniam, A numerically convergent lagrangian–eulerian simulation method for dispersed two-phase flows, International Journal of Multiphase Flow 35 (4) (2009) 376–388. 8

[26] A. Legay, J. Chessa, T. Belytschko, An eulerian–lagrangian method for fluid–structure interaction based on level sets, Computer Methods in Applied Mechanics and Engineering 195 (17-18) (2006) 2070–2087. 9

[27] A. Zilian, A. Legay, The enriched space–time finite element method (est) for simultaneous solution of fluid–structure interaction, International Journal for Numerical Methods in Engineering 75 (3) (2008) 305–334. 9

[28] R. Glowinski, T.-W. Pan, T. I. Hesla, D. D. Joseph, A distributed lagrange multiplier/fictitious domain method for particulate flows, International Journal of Multiphase Flow 25 (5) (1999) 755–794. 9

[29] R. Glowinski, T.-W. Pan, T. I. Hesla, D. D. Joseph, J. Periaux, A fictitious domain approach to the direct numerical simulation of incompressible viscous flow past moving rigid bodies: application to particulate flow, Journal of computational physics 169 (2) (2001) 363–426. 9

[30] J. De Hart, G. Peters, P. Schreurs, F. Baaijens, A three-dimensional computational analysis of fluid–structure interaction in the aortic valve, Journal of biomechanics 36 (1) (2003) 103–112. 9

[31] Z. Yu, A dlm/fd method for fluid/flexible-body interactions, Journal of computational physics 207 (1) (2005) 1–27. 9

[32] R. van Loon, P. D. Anderson, F. N. van de Vosse, A fluid–structure interaction method with solid-rigid contact for heart valve dynamics, Journal of computational physics 217 (2) (2006) 806–823. 9

[33] G. Hou, J. Wang, A. Layton, Numerical methods for fluid-structure interaction — a review, Communications in Computational Physics 12 (2) (2012) 337–377. `doi:10.4208/cicp.291210.290411s`. 10

[34] J.-F. Gerbeau, M. Vidrascu, A quasi-newton algorithm based on a reduced model for fluid-structure interaction problems in blood flows, ESAIM: Mathematical Modelling and Numerical Analysis 37 (4) (2003) 631–647. 10

[35] C. Michler, E. Van Brummelen, R. De Borst, An interface newton–krylov solver for fluid–structure interaction, International Journal for Numerical Methods in Fluids 47 (10-11) (2005) 1189–1195.

[36] M. A. Fernández, M. Moubachir, A newton method using exact jacobians for solving fluid–structure coupling, Computers & Structures 83 (2-3) (2005) 127–142.

[37] W. A. Wall, S. Genkinger, E. Ramm, A strong coupling partitioned approach for fluid–structure interaction with free surfaces, Computers & Fluids 36 (1) (2007) 169–183. 10

[38] P. Causin, J. Gerbeau, F. Nobile, Added-mass effect in the design of partitioned algorithms for fluid–structure problems, Computer Methods in Applied Mechanics and Engineering 194 (42) (2005) 4506–4527. `doi:https://doi.org/10.1016/j.cma.2004.12.005`.
URL `https://www.sciencedirect.com/science/article/pii/S0045782504005328` 10

[39] C. Förster, W. A. Wall, E. Ramm, Artificial added mass instabilities in sequential staggered coupling of nonlinear structures and incompressible viscous flows, Computer methods in applied mechanics and engineering 196 (7) (2007) 1278–1293. 10

[40] C. S. Peskin, Acta numerica 11 (2002) 479–517. 11

[41] C. S. Peskin, Numerical analysis of blood flow in the heart, Journal of Computational Physics 25 (3) (1977) 220 – 252. `doi:https://doi.org/10.1016/0021-9991(77)90100-0`.
URL `http://www.sciencedirect.com/science/article/pii/0021999177901000` 11

[42] T. Coupez, E. Hachem, Solution of high-reynolds incompressible flow with stabilized finite element and adaptive anisotropic meshing, Computer methods in applied mechanics and engineering 267 (2013) 65–85. 12

Bibliography

[43] E. Hachem, T. Kloczko, H. Digonnet, T. Coupez, Stabilized finite element solution to handle complex heat and fluid flows in industrial furnaces using the immersed volume method, International Journal for Numerical Methods in Fluids 68 (1) (2012) 99–121. 12

[44] E. Hachem, H. Digonnet, E. Massoni, T. Coupez, Immersed volume method for solving natural convection, conduction and radiation of a hat-shaped disk inside a 3d enclosure, International Journal of numerical methods for heat & fluid flow (2012). 12

[45] C. Gruau, T. Coupez, 3d tetrahedral, unstructured and anisotropic mesh generation with adaptation to natural and multidomain metric, Computer Methods in Applied Mechanics and Engineering 194 (48-49) (2005) 4951–4976. 12

[46] T. Coupez, Metric construction by length distribution tensor and edge based error for anisotropic adaptive meshing, Journal of computational physics 230 (7) (2011) 2391–2405. 12

[47] E. Hachem, B. Rivaux, T. Kloczko, H. Digonnet, T. Coupez, Stabilized finite element method for incompressible flows with high reynolds number, Journal of computational physics 229 (23) (2010) 8643–8665. 12

Chapter 2

The Immersed Volume Method and the resolution of the Navier–Stokes equations

Contents

Dans ce chapitre, les différents composants de la méthode du volume immergé (IVM) sont détaillés. Ainsi que la résolution des équations de Navier–Stokes est présentée. Ces outils déjà développés vont être utilisés dans le développement du cadre FSI. Les « Level Set Methods » (LSM) ont été développées pour la première fois en 1979. Le principal avantage d'une telle approche est la possibilité d'effectuer une analyse numérique avec des formes externes, sans avoir besoin de les paramétrer au préalable. De plus, la méthode des ensembles de niveaux peut suivre les formes avec une topologie changeante. Ces caractéristiques rendent le LSM attractif pour modéliser la dynamique transitoire des objets, comme le gonflage d'un airbag (FSI), ou une bulle montante (Multi-Phase flow). Compte tenu de la nature multi phase de certaines applications en FSI, il est intéressant d'étudier les lois de mélange. Certaines applications peuvent inclure plus d'un fluide avec la présence du solide. Chaque médium est caractérisé par une fonction level set, qui servira à mélanger les propriétés entre les différents médiums. La fonction de niveau peut passer par certains des éléments à l'interface, pour lesquels des mélanges des différentes propriétés du milieu sont appliqués. Le calcul exact et précis des vitesses, des pressions et des contraintes totales le long de l'interface FSI est de la plus haute importance pour le couplage correct entre le fluide et le solide. Ceci est principalement dû à la taille du maillage à l'interface, où les conditions aux limites sont finalement prescrites. On pourrait envisager un raffinement de maillage isotrope dans une certaine région d'intérêt. Cependant, cela ne peut être utilisé que dans les cas où le niveau de déplacement du solide est connu à l'avance, ce qui augmente considérablement le coût de calcul. Ainsi, une technique de remaillage anisotrope adaptatif est considérée. Différentes façons d'adapter le maillage existent. Dans ce qui suit, nous allons essayer de passer en revue les différentes techniques utilisées dans cette thèse. Un écoulement de fluide peut être incompressible ou compressible. Il est considéré comme incompressible lorsqu'aucun changement de densité n'est présenté. Les fluides tels que l'eau liquide sont considérés comme incompressibles. Alors que les fluides tels que les gaz sont considérés comme compressibles. De plus, ces fluides peuvent être considérés comme incompressibles pour un nombre de Mach $Ma \leq 0,3$. Le nombre de Reynolds aide à distinguer trois régimes d'écoulement importants, qui sont les régimes laminaires, transitoire et turbulent. La conservation de la quantité de mouvement et la conservation des équations de masse régissent l'écoulement du fluide. Cette approximation par éléments finis est sujette à l'échec pour deux raisons principales. L'une d'elles est la condition « inf-sup » (Babuska-Brezzi), qui nécessite une paire appropriée d'espaces fonctionnels pour la vitesse et la pression. Le second est la dominance du terme advectif non linéaire, qui peut conduire à des oscillations parasites qui polluent l'ensemble de la solution. Dans ce qui suit, nous utilisons les éléments finis P1-P1 pour leur précision et leur coût de calcul. Les

éléments P1-P1 sont connus pour avoir un comportement instable car ils ne satisfont pas la condition « inf-sup ». Dans ce qui suit, nous présenterons les schémas numériques utilisés pour contourner les obstacles mentionnés ci-dessus.

2.1 Introduction

In this chapter, the different components of the Immersed Volume Method (IVM) are detailed. As well as the resolution of the Navier–Stokes equations is presented. These already developed tools are going to be used in the development of the FSI framework.

2.2 The Level Set approach

The Level Set Methods (LSM)were first developed in 1979 [1]. The main advantage of such an approach is the ability to undergo a numerical analysis with external shapes, without the need to parameterize them beforehand [2]. Moreover, the level set method can track shapes with changing topology. These features render the LSM attractive in modeling the transient dynamics of objects, such as the inflation of an airbag (FSI) [3], or a rising bubble (Multi-Phase flow) [4].

It consists of a signed distance function α that helps localize the interface Γ of the immersed body Ω_s. Consider a point $\mathbf{x}$ in the computational domain Ω, then the value of the level set function α is the signed distance from the interface Γ to the point of interest $\mathbf{x}$. This inevitably leads to an iso-value of zero on the interface of the level set function. The level set function is given by

$$
\begin{cases}
\alpha(\mathbf{x}) = \pm d(\mathbf{x}, \Gamma), \mathbf{x} \in \Omega, \\
\Gamma = \{\mathbf{x}, \alpha(\mathbf{x}) = 0\}.
\end{cases}
\tag{2.1}
$$

In this work, the sign convention that is adopted consists of having $\alpha > 0$ inside Ω_s, and $\alpha < 0$ outside Ω_s. An example of the level set function of a disc immersed in a square domain is given in figure 4.5.

The solid domain can be a simple geometry, such as the disc example. Thus an analytical function is implemented to account for the level set. However, if this is not the case, and we have a complex geometry at hand, we immerse the solid mesh onto the domain. Figure 2.2, show a complex geometry immersed in a cubical domain. A "Standard Triangle Language" or "Standard Tessellation Language" (STL) file which describes the surface with a mesh using triangular elements, is used to create a mesh file. This mesh file is then immersed in the fluid domain. This will give us a field that is the minimum distance to the surface of the immersed mesh.
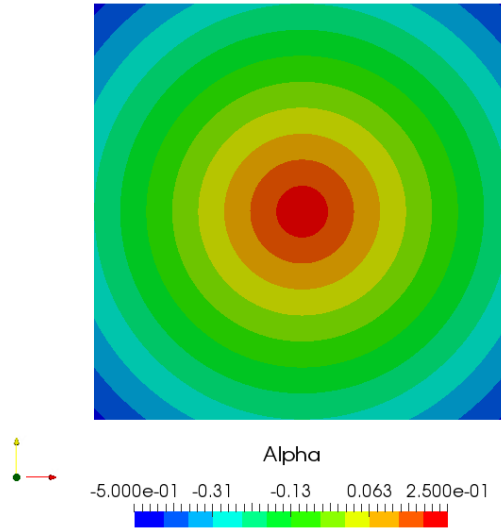
Figure 2.1: The Level Set function of a disc immersed in a square domain.
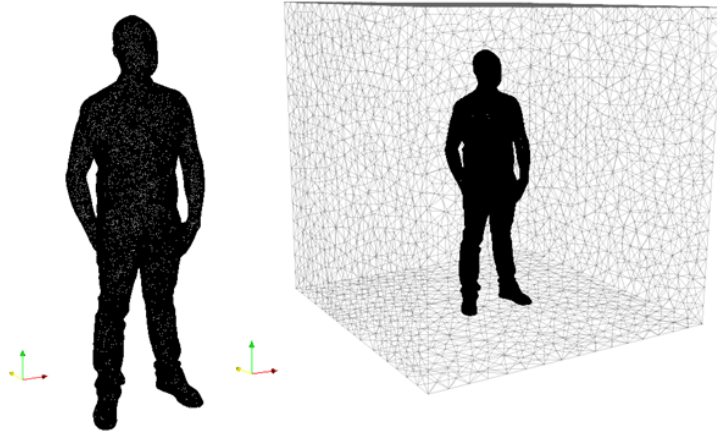
Figure 2.2: The immersion of a complex three-dimensional geometry in a cubical domain.

2.3   Mixing laws

Given the multi-phase nature of some applications in FSI, it is interesting to investigate mixing laws. Some applications may include more than one fluid along with the presence of the solid. Each medium is characterized by a level set function, which will be used to mix the properties between the different mediums. The level

function may go through some of the elements at the interface, for which mixtures of the different properties of the medium are applied. For this purpose, a Heaviside step function, or unit step function $H(\alpha)$ is defined as follows

$$H(\alpha) = \begin{cases} 1 \text{ if } \alpha(\mathbf{x}) > 0, \\ 0 \text{ if } \alpha(\mathbf{x}) < 0. \end{cases} \tag{2.2}$$

To avoid any sudden jumps in the properties [5], that may lead to numerical instabilities, a smoothed Heaviside function is proposed

$$H(\alpha) = \begin{cases} 1 & \text{if} & \alpha(\mathbf{x}) > \epsilon, \\ \frac{1}{2}(1 + \frac{\alpha}{\epsilon} + \frac{1}{\pi}\sin(\frac{\pi\alpha}{\epsilon})) & \text{if} & |\alpha(\mathbf{x})| \leq \epsilon, \\ 0 & \text{if} & \alpha(\mathbf{x}) < -\epsilon. \end{cases} \tag{2.3}$$

Where ϵ is related to the mesh size at a certain position, such that $\epsilon = O(h_i)$, called interface thickness. h_i is equal to the mesh size relative to the interface, in the normal direction. It can be written as

$$h_i = \max_{j,l \in K} \nabla\alpha \cdot \mathbf{x}^{jl}. \tag{2.4}$$

Where $\mathbf{x}^{jl} = \mathbf{x}^l - \mathbf{x}^j$, and K is the element. For first-order linear interpolation of the Heaviside function, it is straightforward since they are calculated by looking at the sign of $\alpha(\mathbf{x})$ at a certain node $\mathbf{x}$. For zero-order, piece wise constant interpolation, $H(\alpha)$ is given by

$$H(\alpha)_{|K} = \frac{\alpha_K^+}{|\alpha|_K}. \tag{2.5}$$

Where α_K^+ is the summation of all the positive α computed at the nodes of an element K, and $|\alpha|_K$ is the summation of the absolute values of α. The mixing of properties between two domain is thus formulated in function of $H(\alpha)$. For example, if we take the density mixture between two mediums we have

$$\rho = \rho_1 H(\alpha) + \rho_2(1 - H(\alpha)). \tag{2.6}$$

The first-order density variation of two mediums across the interface is shown in figure 2.3. For a zero-order variation, the mixing is done across an element. While for first-order variations, the mixing is done across a prescribed thickness ϵ, which is usually two times the mesh size.
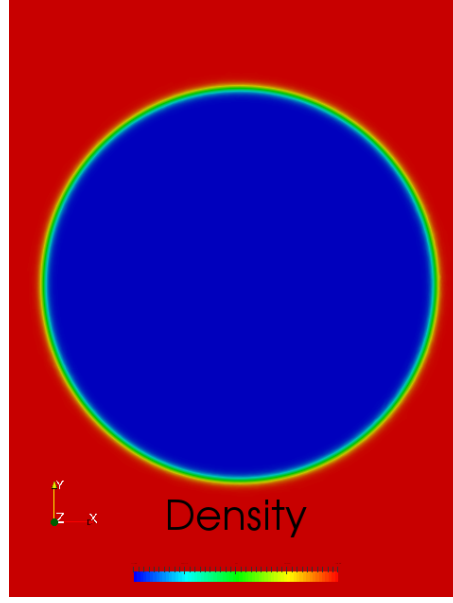
Figure 2.3: The first-order density variation of two mediums across the interface.

2.4   Anisotropic mesh

Accurate and precise computation of the velocities, pressures and full stress along the FSI interface is of utmost importance for the correct coupling between the fluid and the solid. This is mainly due to the mesh size at the interface, where the boundary conditions are eventually prescribed. One might consider an isotropic mesh refinement at a certain region of interest. However, this can only be used in cases where the level of displacement of the solid is known beforehand, and this increases the computational cost significantly. Thus, an adaptive anisotropic remeshing technique is considered. Different ways of adapting the mesh exist. In what follows, we will try to go through the different techniques used in this thesis.

2.4.1   Anisotropic local remeshing method

The idea behind the method is to couple the level set method with an anisotropic mesh adaptation. This enables us to have a locally refined zone around the interface. The refinement can act in one direction, which leads to anisotropic highly stretched elements. This helps us accurately and precisely define our interface while saving a great number of elements compared to isotropic mesh refinement.

To be able to generate such a mesh, we need to define a metric field and make use of a topological meshing tool. A metric is defined as a positive defined symmetric tensor that represents a local base modifying the distance calculations, as

$$\|\mathbf{x}\|_{\mathbb{M}} = \sqrt{\mathbf{x}^T \cdot \mathbb{M} \cdot \mathbf{x}}, \ \langle \mathbf{x}, \mathbf{y} \rangle_{\mathbb{M}} = \mathbf{x}^T \cdot \mathbb{M} \cdot \mathbf{y}. \tag{2.7}$$

If we assume for instance that the tensor $\mathbb{M}$ is equal to the identity tensor, we obtain the directions and the distances of classical Euclidean space. Given the fact that $\mathbb{M}$ is a positive definite symmetric tensor, then $\mathbb{M}$ is diagonalizable in an orthonormal basis of eigenvectors, where the eigenvalues are strictly positive. The metric is considered as a tensor where the eigenvectors dictate the direction, and the eigenvalues dictate the size of the mesh elements. When applying a metric in mesh construction, the element size in the direction of an eigenvector is equal to $\frac{1}{\sqrt{\lambda_i}}$, where λ_i is the ith eigenvalue of $\mathbb{M}$ associated with the eigenvector.

Let us explain the procedure in a concrete example. Assume only one interface Γ, the iso-value of zero of the level set corresponds to that interface. The normal vector to the interface, which is the chosen direction of mesh refinement, is given by

$$\mathbf{n} = \frac{\nabla \alpha}{||\nabla \alpha||} \tag{2.8}$$

To impose a certain mesh size, we impose a certain thickness e for which we consider the element either near the interface or far from it as follows

$$\begin{cases} |\alpha(\mathbf{x})| \leq \frac{e}{2} & \text{near the interface,} \\ |\alpha(\mathbf{x})| > \frac{e}{2} & far \text{far from the interface.} \end{cases} \tag{2.9}$$

A reference value, or default value for the mesh size is imposed far from the interface. This mesh size is reduced as we get closer to the interface in the orthogonal direction. If we consider an isotropic mesh of element size h_d outside a prescribed anisotropic boundary layer, the following evolution is a choice

$$h = \begin{cases} h_d & if \ |\alpha(\mathbf{x})| > \frac{e}{2}, \\ h_e = \frac{2h_d(m-1)}{me}|\alpha(\mathbf{x})| + \frac{h_d}{m} & if \ |\alpha(\mathbf{x})| \leq \frac{e}{2}. \end{cases} \tag{2.10}$$

At the interface, the mesh size of the element is equal to the default mesh size reduced by a factor m. This value increases until it reaches the default value h_d at half the thickness of the anisotropic boundary layer. The interface unit normal vector $\mathbf{n}$, and the mesh size defined above lead to the following metric construction

$$\mathbb{M} = C(\mathbf{n} \otimes \mathbf{n}) + \frac{1}{h_d}I. \tag{2.11}$$

Where

$$C = \begin{cases} 0 & if \ |\alpha(\mathbf{x})| \geq \frac{e}{2}, \\ \frac{1}{h_e^2} - \frac{1}{h_d^2} & if \ |\alpha(\mathbf{x})| < \frac{e}{2}. \end{cases} \cdot \tag{2.12}$$

Where I is the identity tensor. This allows us to have a mesh resolution specific to an area. We have an isotropic mesh far from the interface with a value equal to the prescribed default mesh size, and an anisotropic mesh near the surface that respects the above-mentioned equations.

Simply put, it relies on a local mesh topology optimization, with varying applications of meshing and remeshing through the principle of minimum volume. It considers the quality of the element, to improve the overall topology. The quality of the element is computed using a shape factor that takes into consideration the previously mentioned metric[6].

The suggested mesh generation algorithm performs well for applications in 2D and 3D, including complex shapes. It enables us to generate extremely stretched anisotropic elements at the interface. Thus, a mesh resolution in the direction of the normal vector to the interface is obtained, where important gradients are present. This allows us to accurately and precisely depict the FSI interface while decreasing the total number of degrees of freedom of the overall problem compared to an isotropic mesh. Since the mesh generation is focused on a specific region of the overall mesh, the computational power needed for mesh generation is relatively low.

2.4.2 Hessian strategy

This is an alternative for the metric computation, and to consider the anisotropic mesh region near the interface. A directional error estimator, which is based on the local interpolation error, and the recovery of the second derivative of the signed distance function is used. This approach is known as the Hessian strategy.

This approach aims to achieve a minimal directional error estimation. This allows us to have a refined mesh at the FSI interface. The elements are stretched and oriented in a way that allows for an accurate and precise depiction of the interface while keeping the number of elements relatively low and user-defined. The Hessian strategy is utilized to acquire better directional information of the error. The signed distance function is used to calculate the Hessian. This directional information, as per the previous method, is used to construct a mesh metric $\mathbb{M}$, which enforces the orientation and size of the element. This method can be applied with no error estimator.

2.4.3 Edge-based anisotropic mesh adaptation

This final approach, used in what follows, is mainly based on the a posteriori estimation of the length distribution tensor, and the related edge-based error analysis. It takes advantage of the level set function and the velocity field. This is done without a significant increase in the complexity of the calculations, nor the intersection of

different metrics. This allows us to consider not only the velocity magnitude but also the directional gradient of the velocity. We make use of a function that monitors a vector or a scalar to control the orientation, size, and shape of the mesh element. This gives us an estimate of the solution error, which is equidistributed over each mesh element. This helps us generate a mesh and a numerical solution for the problem. A numerical solution is first computed on the mesh, then an estimation of the interpolation error is computed. A minimization problem is then solved, which reduces the interpolation error in the L_1-norm. The development of the solution is monitored by an optimal metric which reduces the interpolation error. A new mesh is obtained, which is compatible with the metric. The edge of this approach is the fact that the metric and its associated edge-based error are computed easily.

2.4.3.1 Edge-based error estimation

Let $u \in C^2(\Omega)$ be a regular function, and u_h a P1 finite element approximation obtained through the Lagrange interpolation operator of that function. U_i is defined at each vertex i of the mesh as $U_i = u(x^i) = u_h(x^i)$, where x^i are the coordinates of the vertex i. Let us define a "patch" $\Gamma(i)$ linked to the vertex x_i of the mesh as the group of nodes that share a single edge with x_i. The edge connection between x_i to x_j is denoted by x_{ij}. Figure 4.6 showcases the concept.
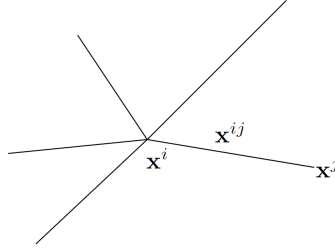
Figure 2.4: Patch associated with node x^i

Given the continuous nature of the gradient $\nabla u^h \cdot x^{ij}$ on the edge x_{ij} we can write

$$U^j = U^i + \nabla u^h \cdot x^{ij}, \tag{2.13}$$

Which in turn gives

$$\nabla u_h \cdot x^{ij} = U^j - U^i. \tag{2.14}$$

The following error estimator is obtained

$$\| \nabla u^h \cdot x^{ij} - \nabla u(x^i) \cdot x^{ij} \| \leq \max_{y \in |x^i, x^j|} | x^{ij} \cdot H_u(y) \cdot x^{ij} |, \qquad (2.15)$$

where H_u is the Hessian of u. The recovered gradient g^i of u_h at a node x^i is given by

$$\nabla g_h \cdot x^{ij} = g^j - g^i . \qquad (2.16)$$

The projection of the Hessian at the edge extremities, which is based on the gradient, is of interest

$$(\nabla g_h \cdot x^{ij}) \cdot x^{ij} = (g^j - g^i) \cdot x^{ij}, \qquad (2.17)$$
$$(H_u \cdot x^{ij}) \cdot x^{ij} = g^{ij} \cdot x^{ij}, \qquad (2.18)$$

where $g^{ij} = g^j - g^i$. An accurate second-order approximation of the second derivative of u along the edge x^{ij} is obtained by the quantity $| g^{ij} \cdot x^{ij} |$. Residuals on edges prevail over a posteriori error for first-order finite elements on anisotropic meshes[7], it is of interest to define an error indication function related to the edge x^{ij} by

$$e^{ij} = | g^{ij} \cdot x^{ij} | . \qquad (2.19)$$

The error is the exact interpolation error along the edge and enables us to compute a global L_1 error. The gradient however is unknown at the vertices, therefore a gradient recovery procedure is applied.

2.4.3.2   Gradient recovery procedure

The gradient recovery procedure is based on the succeeding optimization problem

$$G^i = arg \min_{G} \left(\sum_{j \in \Gamma(i)} | (G - \nabla u_h) \cdot x^{ij} |^2 \right), \qquad (2.20)$$

where G^i is the recovered gradient. $\otimes$ is the tensor product between two vectors. The length distribution tensor X^i at node i is given by

$$X^i = \frac{1}{\mid \Gamma(i) \mid} \left(\sum_{j \in \Gamma(i)} x^{ij} \otimes x^{ij} \right), \tag{2.21}$$

this gives us an average representation of the distribution of edges in the patch. The recovered gradient G^i is expressed in terms of the length distribution tensor as

$$G^i = (X^i)^{-1} \sum_{j \in \Gamma(i)} U^{ij} x^{ij}. \tag{2.22}$$

Which leads to an estimated error e_{ij} given by

$$e_{ij} = G^{ij}.x^{ij}. \tag{2.23}$$

2.4.3.3 Metric construction

To correlate the error indicator defined in (4.14) to the related metric, we introduce a stretching factor. The stretching factor s^{ij} is defined as the ratio between the length of the edges x^{ij} before and after the adaptation procedure. Thus we obtain the following expression for the metric

$$\widetilde{M^i} = (\widetilde{X^i})^{-1}, \tag{2.24}$$

where $\widetilde{X^i}$ is defined as

$$\widetilde{X^i} = \frac{1}{\mid \Gamma(i) \mid} \left(\sum_{j \in \Gamma(i)} s^{ij} \otimes s^{ij} \right). \tag{2.25}$$

To keep the number of nodes fixed, the stretching factor s^{ij} of the edge ij is chosen as

$$s^{ij} = \left(\frac{e_{ij}}{e(N)} \right), \tag{2.26}$$

where $e(N)$ the total error. An example of the mesh adaptation is shown in figure 2.5. This mesh adaptation was performed under multiple criteria. One of

which is the level set of the immersed solid. We can see the highly concentrated number of highly stretched elements on the interface, which will eventually help us better model the interface and have higher accuracy in this region of interest. Also, the mesh was adapted to the velocity. This will help concentrate the elements in regions of interest where the gradient of the scalar function is important.
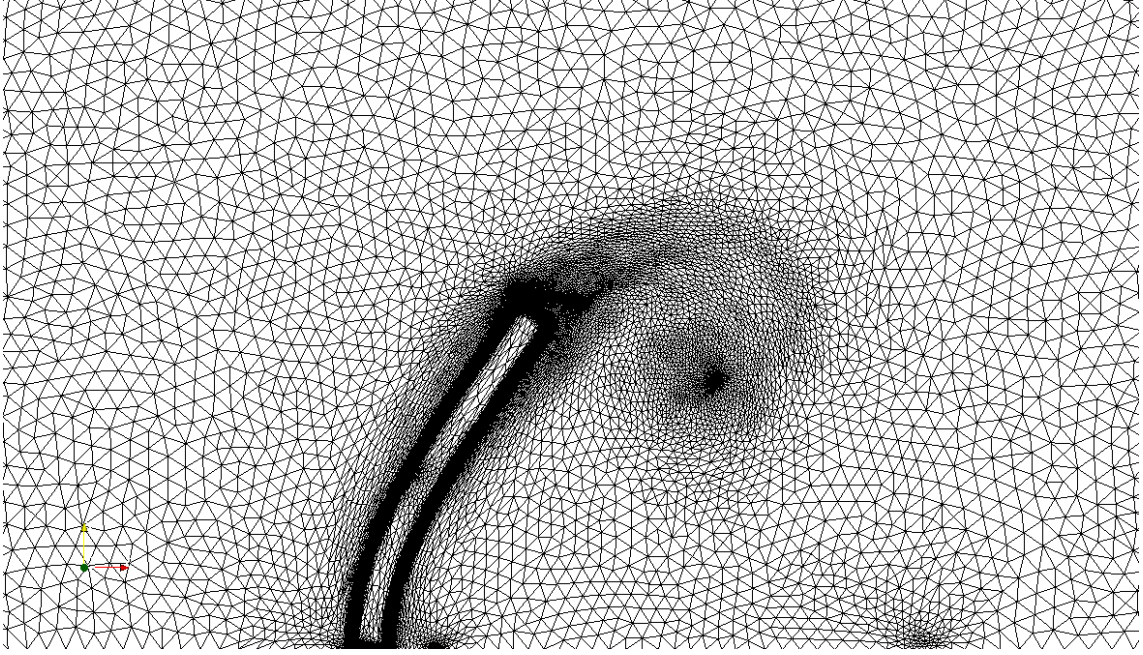
Figure 2.5: An example of the mesh adaptation on multiple criteria.

2.5   The resolution of the Navier–Stokes equations

A fluid flow can be either incompressible or compressible. It is considered incompressible when no density change is exhibited. Fluids such as liquid water are considered incompressible. While fluids such as gases are considered compressible. Also, these fluids can be considered incompressible for a Mach number $Ma \leq 0.3$ [8]. The Mach number is a non-dimensional number that quantifies the relation between a characteristic value v and the speed of sound c using

$$Ma = \frac{v}{c}. \tag{2.27}$$

It was named after renowned physicist and philosopher Ernst Mach (1836-1916). For example, the speed of sound in the air is about 340 m/s. Thus, air can be considered incompressible for values up to 100 m/s. In what follows, we consider

are fluid to be incompressible. Also, an important non-dimensional number for the characterization of a fluid flow is the Reynolds number

$$Re = \frac{LU}{\nu}, \tag{2.28}$$

where L is a characteristic length, U is a velocity and ν is the kinematic viscosity of the fluid. It is the ratio of inertial effects to viscous effects. Thus, it gives us an idea of which effects prevail in a given flow. The Reynolds number helps in distinguishing between three important flow regimes, which are the laminar, transitional, and turbulent regimes. Laminar regimes occur for low Reynolds number, which means that the viscous effects are more important than the inertial effects. It is characterized by a smooth, relatively constant fluid motion. Turbulent regimes occur at a relatively high Reynolds number, which means that the inertial effects are more important than viscous effects. It is characterized by the stochastic production of eddies, vortices, and different flow fluctuations. It is named after the renowned engineer and physicist Osborne Reynolds (1842-1912). The conservation of momentum and the conservation of mass equations govern the fluid flow. The transient incompressible Navier–Stokes equations to be solved on a domain $\Omega \subset \mathbb{R}^d$, where d is the spatial dimension, on a time period T are given by

$$\rho(\partial_t \mathbf{v} + (\mathbf{v} \cdot \nabla)\mathbf{v}) - \nabla \cdot \boldsymbol{\sigma} = \mathbf{f} \text{ in } \Omega, \tag{2.29}$$

$$\nabla \cdot \mathbf{v} = 0 \text{ in } \Omega. \tag{2.30}$$

Where $\boldsymbol{\sigma}$ is the stress tensor, ρ is the density, and $\mathbf{f}$ is a source term. The stress tensor for a Newtonian fluid is given by

$$\boldsymbol{\sigma} = 2\mu\varepsilon(\mathbf{v}) - p\mathbf{I}, \tag{2.31}$$

where μ is the dynamic viscosity, $\mathbf{I}$ is the identity tensor, and p is the pressure. The strain tensor $\varepsilon(\mathbf{v})$ is given by

$$\varepsilon(\mathbf{v}) = \frac{1}{2}[\nabla \mathbf{v} + \nabla^T \mathbf{v}]. \tag{2.32}$$

Which ultimately leads to

$$\rho(\partial_t \mathbf{v} + (\mathbf{v} \cdot \nabla)\mathbf{v}) - 2\mu\nabla \cdot \varepsilon(\mathbf{v}) + \nabla p = \mathbf{f} \text{ in } \Omega, \tag{2.33}$$

$$\nabla \cdot \mathbf{v} = 0 \text{ in } \Omega. \tag{2.34}$$

These equations define the transient incompressible Newtonian Navier–Stokes equations. They constitute a nonlinear system of mixed hyperbolic-parabolic PDEs in both $\mathbf{v}$ and p. These equations require initial and boundary conditions to be solved.

2.5.1 Initial and boundary conditions

The initial condition at time $t = 0$ should satisfy $\nabla \cdot \mathbf{v}_0 = 0$ for us to have a well-posed problem

$$\mathbf{v} = \mathbf{v}_0 \text{ in } \Omega_0. \tag{2.35}$$

No initial condition on the pressure is requested for an incompressible flow. There are two types of boundary conditions that can be applied to the problem at hand, which are the Dirichlet and Neumann boundary conditions. The Dirichlet boundary condition is applied on Γ_D, and the Neumann boundary condition is applied on Γ_N, where $\partial\Omega = \Gamma = \Gamma_D \cup \Gamma_N$ and $\Gamma_D \cap \Gamma_N = \varnothing$. They are given by the following expressions

$$\mathbf{v} = \mathbf{v}_D \text{ on } \Gamma_D, \tag{2.36}$$

$$\boldsymbol{\sigma} \cdot \mathbf{n} = h_N \text{ on } \Gamma_N. \tag{2.37}$$

Where $\mathbf{n}$ is the outward unit normal to Γ_N. It is important to mention that in the case where no Neumann boundary condition is applied in the domain, the resulting pressure is correct up to an arbitrary constant. Given the FSI context and the importance of the pressure field, pressure should be specified somewhere convenient in the domain for us to obtain a physically correct field of pressure.

2.5.2 Classic mixed formulation

We start by introducing the respective function spaces of our variables. The function spaces for the velocity, the weighting function space, and the pressure scalar function space are defined as respectively

$$\begin{cases} V = \left\{ \mathbf{v}, \, \mathbf{v} \in (H^1(\Omega))^d | \mathbf{v} = g \text{ on } \Gamma_D \right\} \\ W = \left\{ \mathbf{v}, \, \mathbf{v} \in (H^1(\Omega))^d | \mathbf{v} = 0 \text{ on } \Gamma_D \right\} \\ Q = \{ p, \, p \in L^2(\Omega) \} \end{cases} \tag{2.38}$$

The weak form of the PDE consist of finding $(\mathbf{v}, p) \in (V, Q)$ such that

$$\begin{cases} (\rho\partial_t\mathbf{v}, \mathbf{w}) + (\rho(\mathbf{v} \cdot \nabla)\mathbf{v}, \mathbf{w}) + (2\mu\varepsilon(\mathbf{v}) : \varepsilon(\mathbf{w})) - (p, \nabla \cdot \mathbf{w}) = (\mathbf{f}, \mathbf{w}) \\ (\nabla \cdot \mathbf{v}, q) = 0 \end{cases} \tag{2.39}$$

The Galerkin finite element approximation consists of decomposing the domain Ω into N_{el} number of elements K, in a way that they cover the whole domain. These elements are either disjoint or may share a complete edge. Using this partition, the previously mentioned function spaces are treated by finite-dimensional spaces spanned by continuous piecewise polynomials

$$\begin{cases} V_h = \left\{ \mathbf{v}_h \in (C^0(\Omega))^d | \mathbf{v}_{h|K} \in P^1(K)^d, \ \forall \ K \in \ \tau_h \right\} \\ V_{h,0} = \left\{ \mathbf{v}_h \in V_h, \mathbf{v}_{h|K} = 0 \right\} \\ Q_h = \left\{ q_h \in C^0(\Omega) | q_{h|K} \in P^1(K), \ \forall \ K \in \ \tau \right\} \end{cases} \quad (2.40)$$

The discrete Galerkin problem is finding $(\mathbf{v}_h, p_h) \in (V_h, Q_h), \forall (\mathbf{w}_h, q_h) \in (V_{h,0}, Q_h)$ in a way

$$\begin{cases} (\rho \partial_t \mathbf{v}_h, \mathbf{w}_h) + (\rho(\mathbf{v}_h \cdot \nabla)\mathbf{v}_h, \mathbf{w}_h) + (2\mu\varepsilon(\mathbf{v}_h) : \varepsilon(\mathbf{w}_h)) - (p_h, \nabla \cdot \mathbf{w}_h) = (\mathbf{f}, \mathbf{w}_h) \\ (\nabla \cdot \mathbf{v}_h, q_h) = 0 \end{cases}$$
$$(2.41)$$

This finite element approximation is prone to failure for two main reasons. One of which is the inf-sup (Babuska-Brezzi) condition, which requires an appropriate pair of the function spaces for velocity and pressure [9, 10]. The second one is the dominance of the nonlinear advective term, which may lead to spurious oscillations that pollute the entire solution. In what follows, we use P1-P1 finite elements for their accuracy and computational cost. P1-P1 elements are known for having an unstable behavior because they fail to satisfy the inf-sup condition. In what follows we will introduce the numerical schemes used to circumvent the above-mentioned obstacles.

2.5.3 Variational multi-scale method

Following the works in [11], we consider an overlapping sum decomposition of the variables into resolvable coarse-scale and unresolved fine-scale, such as

$$\mathbf{v} = \mathbf{v}_h + \mathbf{v}' \qquad \text{and} \qquad p = p_h + p'. \qquad (2.42)$$

The fine-scale part of the decomposition is modeled using residual-based terms that are derived consistently. The fine-scale solution is then substituted in the coarse-scale equation, which is known as static condensation. Additional terms will appear, which are tuned by a local time-dependent stabilizing parameter. They will enhance the overall stability and accuracy of the standard Galerkin formulation. The same decomposition is considered for the weighting functions as

$$\mathbf{w} = \mathbf{w}_h + \mathbf{w}' \qquad \text{and} \qquad q = q_h + q'. \qquad (2.43)$$

The functional spaces are enriched as well

$$V = V_h \oplus V', V_0 = V_{h,0} \oplus V_0', Q = Q_h \oplus Q' \quad \text{and} \quad Q_0 = Q_{h,0} \oplus Q_0'. \qquad (2.44)$$

The mixed finite element approximation consist now of finding $(\mathbf{v}, p) \in (V, Q)$

$$
\begin{cases}
(\rho\partial_t(\mathbf{v}_h + \mathbf{v}'), \mathbf{w}_h + \mathbf{w}') + (\rho((\mathbf{v}_h + \mathbf{v}') \cdot \nabla)(\mathbf{v}_h + \mathbf{v}'), \mathbf{w}_h + \mathbf{w}') \\
+(2\mu\varepsilon(\mathbf{v}_h + \mathbf{v}') : \varepsilon(\mathbf{w}_h + \mathbf{w}')) - (p_h + p', \nabla \cdot (\mathbf{w}_h + \mathbf{w}')) = (\mathbf{f}, \mathbf{w}_h + \mathbf{w}') \\
(\nabla \cdot (\mathbf{v}_h + \mathbf{v}'), q_h + q') = 0
\end{cases}
\quad (2.45)
$$

This system of equations can be split into two different subproblems corresponding either to the coarse or fine-scale problem as

-The coarse-scale problem

$$
\begin{cases}
(\rho\partial_t(\mathbf{v}_h + \mathbf{v}'), \mathbf{w}_h) + (\rho((\mathbf{v}_h + \mathbf{v}') \cdot \nabla)(\mathbf{v}_h + \mathbf{v}'), \mathbf{w}_h) \\
+(2\mu\varepsilon(\mathbf{v}_h) : \varepsilon(\mathbf{w}_h)) - (p_h + p', \nabla \cdot (\mathbf{w}_h)) = (\mathbf{f}, \mathbf{w}_h) \\
(\nabla \cdot (\mathbf{v}_h + \mathbf{v}'), q_h) = 0
\end{cases}
\quad (2.46)
$$

-The fine-scale problem

$$
\begin{cases}
(\rho\partial_t(\mathbf{v}_h + \mathbf{v}'), \mathbf{w}') + (\rho((\mathbf{v}_h + \mathbf{v}') \cdot \nabla)(\mathbf{v}_h + \mathbf{v}'), \mathbf{w}') \\
+(2\mu\varepsilon(\mathbf{v}') : \varepsilon(\mathbf{w}')) - (p_h + p', \nabla \cdot (\mathbf{w}')) = (\mathbf{f}, \mathbf{w}') \\
(\nabla \cdot (\mathbf{v}_h + \mathbf{v}'), q') = 0
\end{cases}
\quad (2.47)
$$

To reach the final stabilized formulation, we first solve the fine-scale problem, which is defined on the sum of elements interior and written in function of the time-dependent large-scale variables. The obtained fine-scale solution is then substituted into the coarse-scale problem, thus modeling the effects of the fine-scales without explicitly appearing. A couple of remarks should be stated in order to move forward with some of the assumptions we are taking

- For P1 functions, the second derivatives and all terms involving integrals over the element interior boundary vanish.

- The fine-scale space is assumed to be orthogonal to the finite element spaces, thus the crossed viscous terms vanish.

Re-arranging the terms of the fine-scale problem

$$
\begin{cases}
(\rho\partial_t(\mathbf{v}'), \mathbf{w}') + (\rho((\mathbf{v}_h + \mathbf{v}') \cdot \nabla)(\mathbf{v}'), \mathbf{w}') + (2\mu\varepsilon(\mathbf{v}') : \varepsilon(\mathbf{w}')) + (\nabla p', \mathbf{w}') \\
= (\mathbf{f} - \rho\partial_t(\mathbf{v}_h) - (\rho(\mathbf{v}_h + \mathbf{v}') \cdot \nabla)(\mathbf{v}_h) - \nabla p, \mathbf{w}') \\
= (R_m, \mathbf{w}') \\
(\nabla \cdot (\mathbf{v}'), q') = -(\nabla \cdot (\mathbf{v}_h), q') = (R_c, q')
\end{cases}
\quad (2.48)
$$

From these equations, we can observe that the fine-scale problem is time-dependent and highly nonlinear. It is to the best of our knowledge, that the first attempt into incorporating and using time-dependent sub-scales for the Navier–Stokes equations is credited to the works in [12]. It was also shown in [13, 14], that by tracking

the subscales in time and including their nonlinear contribution in the advection velocity, the global conservation of momentum is guaranteed. Following the work in [15], on the use of the Newton-Raphson linearization method for the treatment of the nonlinear advection term, and the works in [13], we extend the method to the multi-scale finite element formulation. The Newton-Raphson method is known for its rapid convergence when the initial condition is sufficiently good. However, we need to solve the Newton equation at each iteration. Considering the advective term in the coarse-scale problem, it can be approximated as follows

$$
\begin{aligned}
(\mathbf{v}_h \cdot \nabla \mathbf{v}_h, \mathbf{w})^i &= (\mathbf{v}_h^{i-1} + (\mathbf{v}_h^i - \mathbf{v}_h^{i-1}) \cdot \nabla(\mathbf{v}_h^{i-1} + (\mathbf{v}_h^i - \mathbf{v}_h^{i-1})), \mathbf{w}) = (\mathbf{v}_h^{i-1} \cdot \nabla \mathbf{v}_h^i, \mathbf{w}) + \\
&\quad (\mathbf{v}_h^i \cdot \nabla \mathbf{v}_h^{i-1}, \mathbf{w}) - (\mathbf{v}_h^{i-1} \cdot \nabla \mathbf{v}_h^{i-1}, \mathbf{w}) + ((\mathbf{v}_h^i - \mathbf{v}_h^{i-1}) \cdot \nabla((\mathbf{v}_h^i - \mathbf{v}_h^{i-1})), \mathbf{w}) \\
&\approx (\mathbf{v}_h^{i-1} \cdot \nabla \mathbf{v}_h^i, \mathbf{w}) + (\mathbf{v}_h^i \cdot \nabla \mathbf{v}_h^{i-1}, \mathbf{w}) - (\mathbf{v}_h^{i-1} \cdot \nabla \mathbf{v}_h^{i-1}, \mathbf{w}),
\end{aligned}
\tag{2.49}
$$

Where $\mathbf{v}^{i-1}$ is the previous Newton-Raphson's iteration. In what follows, the subscales will not be tracked in time, we are considering 'quasi-static subscales'. Our choice is justified by the work in [16]. We also assume the advective velocity to be approximated using only the large scale components by $(\mathbf{v}_h + \mathbf{v}') \cdot \nabla(\mathbf{v}_h + \mathbf{v}') \approx \mathbf{v}_h \cdot \nabla \mathbf{v}_h + \mathbf{v}_h \cdot \nabla \mathbf{v}'$. Thus, leading to

$$
\begin{cases}
(\rho((\mathbf{v}_h^{i-1}) \cdot \nabla)(\mathbf{v}'), \mathbf{w}') + (2\mu\varepsilon(\mathbf{v}') : \varepsilon(\mathbf{w}')) + (\nabla p', \mathbf{w}') = (R_m, \mathbf{w}') \\
(\nabla \cdot (\mathbf{v}'), q') = (R_c, q')
\end{cases}
\tag{2.50}
$$

It is important to consider the small-scale pressure term, to complete the continuity condition for the small-scale problem [17, 18]. It will provide additional stability for the fluid flow, for high Reynolds number. It is important to note that solving the small-scale equations for the velocity and pressure is somewhat tedious. A separation technique for the small-scale variables was proposed in [9]. The small-scale continuity equation was replaced by the Pressure Poisson Equation (PPE). Now that the small-scale PPE replaced the continuity equation, it was proposed in [19] to approximate the solution of the equation by an additional stabilization term. This approximation is given by

$$
p' \approx -\tau_C \nabla \cdot \mathbf{v}_h.
\tag{2.51}
$$

This equation can be integrated directly into the large-scale equations. Here τ_C is defined by the work in [13, 20]

$$
\tau_C = [\nu^2 + (\frac{c_2}{c_1} \frac{|\mathbf{v}|_K}{h})^2]^{\frac{1}{2}},
\tag{2.52}
$$

where c_1 and c_2 are tuning parameters, h is the characteristic element length and ν is the kinematic viscosity. Applying the integration by parts to the coarse-scale problem and substituting the fine-scale variables with their respective models we get

$$
\begin{aligned}
(\rho\frac{\partial \mathbf{v}_h}{\partial t}, \mathbf{w}_h) + (\rho(\mathbf{v}_h \cdot \nabla)\mathbf{v}_h, \mathbf{w}_h) + (2\mu\varepsilon(\mathbf{v}_h) : \varepsilon(\mathbf{w}_h)) \\
-(p_{f_h}, \nabla \cdot \mathbf{w}_h) + (\nabla \cdot \mathbf{v}_h, q_h) - (\boldsymbol{f}, \mathbf{w}_h) \\
+ \sum_{K \in T_h} (\tau_K((\rho\frac{\partial \mathbf{v}_h}{\partial t} + \rho(\mathbf{v}_h^{i-1} \cdot \nabla)\mathbf{v}_h) + \nabla p_h - \boldsymbol{f}), \rho_f \mathbf{v}_h \nabla \mathbf{w}_h)_K \\
+ \sum_{K \in T_h} (\tau_K((\rho\frac{\partial \mathbf{v}_h}{\partial t} + \rho(\mathbf{v}_h \cdot \nabla)\mathbf{v}_h) + \nabla p_h - \boldsymbol{f}), \nabla q_h)_K \\
+ \sum_{K \in T_h} (\tau_C \nabla \cdot \mathbf{v}_h, \nabla \cdot \mathbf{w}_h)_K = 0 \; \forall \, \mathbf{w}_h \in W_{h,0}, \; \forall \, q_h \in Q_{h,0}.
\end{aligned}
\tag{2.53}
$$

Here τ_K is defined by the work in [18]

$$
\tau_K = ((\frac{2\rho}{\Delta t})^2 + (\frac{4\mu}{h_k^2})^2 + (\frac{\rho|\boldsymbol{v}_h|_K}{h_K})^2)^{-\frac{1}{2}}.
\tag{2.54}
$$

In this equation that considers both the momentum and continuity equations, we have the standard Galerkin terms with three additional stabilizations terms. The first and second terms represent the influence of the fine-scale velocity on the finite element components, while the third one is the influence of the fine-scale pressure on the coarse-scale problem. The additional terms are integrals that are evaluated element-wise. They represent the effects of the subscales. Thus, stabilization terms are introduced consistently. They are used to overcome the instability of the classical Galerkin formulation, circumventing the inf-sup conditions, and highly advective flow regimes. For more details on the derivation procedure, and more information on the subject, the interested reader is pointed to the following references [21, 22].

Bibliography

[1] A. Dervieux, F. Thomasset, A finite element method for the simulation of a rayleigh-taylor instability, in: Approximation methods for Navier-Stokes problems, Springer, 1980, pp. 145–158. 22

[2] S. Osher, J. A. Sethian, Fronts propagating with curvature-dependent speed: Algorithms based on hamilton-jacobi formulations, Journal of computational physics 79 (1) (1988) 12–49. 22

[3] F. Cirak, R. Radovitzky, A lagrangian–eulerian shell–fluid coupling algorithm based on level sets, Computers & Structures 83 (6-7) (2005) 491–498. 22

[4] M. Khalloufi, Y. Mesri, R. Valette, E. Massoni, E. Hachem, High fidelity anisotropic adaptive variational multiscale method for multiphase flows with surface tension, Computer Methods in Applied Mechanics and Engineering 307 (2016) 44–67. 22

[5] S. Van der Pijl, A. Segal, C. Vuik, P. Wesseling, A mass-conserving level-set method for modelling of multi-phase flows, International journal for numerical methods in fluids 47 (4) (2005) 339–361. 24

[6] C. Gruau, Génération de métriques pour adaptation anisotrope de maillages, applications à la mise en forme des matériaux, Ph.D. thesis, Paris, ENMP (2004). 27

[7] G. Kunert, R. Verfürth, Edge residuals dominate a posteriori error estimates for linear finite element methods on anisotropic triangular and tetrahedral meshes, Numer. Math. 86 (2) (2000) 283–303. 29

[8] J. H. Ferziger, M. Perić, R. L. Street, Computational methods for fluid dynamics, Vol. 3, Springer, 2002. 31

[9] L. P. Franca, A. Neslituurk, M. Stynes, On the stability of residual-free bubbles for convection-diffusion problems and their approximation by a two-level finite element method, Computer Methods in Applied Mechanics and Engineering 166 (1-2) (1998) 35–49. 34, 36

[10] A. I. Neslituurk, Approximating the incompressible Navier-Stokes equations using a two-level finite element method, University of Colorado at Denver, 1999. 34

[11] T. J. Hughes, G. R. Feijóo, L. Mazzei, J.-B. Quincy, The variational multiscale method—a paradigm for computational mechanics, Computer methods in applied mechanics and engineering 166 (1-2) (1998) 3–24. 34

[12] R. Codina, J. Blasco, Stabilized finite element method for the transient navier–stokes equations based on a pressure gradient projection, Computer Methods in Applied Mechanics and Engineering 182 (3-4) (2000) 277–300. 35

[13] R. Codina, Stabilized finite element approximation of transient incompressible flows using orthogonal subscales, Computer methods in applied mechanics and engineering 191 (39-40) (2002) 4295–4321. 35, 36

Bibliography

[14] R. Codina, J. Principe, O. Guasch, S. Badia, Time dependent subscales in the stabilized finite element approximation of incompressible flow problems, Computer Methods in Applied Mechanics and Engineering 196 (21-24) (2007) 2413–2430. 35

[15] S. O. Unverdi, G. Tryggvason, A front-tracking method for viscous, incompressible, multi-fluid flows, Journal of computational physics 100 (1) (1992) 25–37. 36

[16] T. Dubois, F. Jauberteau, R. Temam, Dynamic multilevel methods and the numerical simulation of turbulence, Cambridge University Press, 1999. 36

[17] W. A. Wall, M. Bischoff, E. Ramm, A deformation dependent stabilization technique, exemplified by eas elements at large strains, Computer Methods in Applied Mechanics and Engineering 188 (4) (2000) 859–871. 36

[18] T. E. Tezduyar, Y. Osawa, Finite element stabilization parameters computed from element matrices and vectors, Computer Methods in Applied Mechanics and Engineering 190 (3-4) (2000) 411–430. 36, 37

[19] L. P. Franca, S. P. Oliveira, Pressure bubbles stabilization features in the stokes problem, Computer Methods in Applied Mechanics and Engineering 192 (16-18) (2003) 1929–1937. 36

[20] R. Codina, J. Principe, Dynamic subscales in the finite element approximation of thermally coupled incompressible flows, International journal for numerical methods in fluids 54 (6-8) (2007) 707–730. 36

[21] E. Hachem, Stabilized finite element method for heat transfer and turbulent flows inside industrial furnaces, Ph.D. thesis, Ecole Nationale Supérieure des Mines de Paris (2009). 37

[22] E. Hachem, B. Rivaux, T. Kloczko, H. Digonnet, T. Coupez, Stabilized finite element method for incompressible flows with high reynolds number, Journal of computational physics 229 (23) (2010) 8643–8665. 37

Bibliography

Chapter 3

Stabilized finite element method for incompressible solid dynamics using an updated Lagrangian formulation

Contents

3 Stabilized finite element method for incompressible solid dynamics using an updated Lagrangian formulation

Ce chapitre propose une nouvelle façon de résoudre la dynamique solide transitoire linéaire et non linéaire pour un matériau compressible, presque incompressible et incompressible dans le cadre lagrangien mis à jour pour les éléments finis non structurés tétraédriques. Il consiste en une formulation mixte en déplacement et en pression, où l'équation de quantité de mouvement du continuum est complétée par une équation de pression qui gère l'incompressibilité de manière inhérente. Elle est obtenue par la répartition déviatorique et volumique de la contrainte, ce qui permet de résoudre le problème dans la limite incompressible. Une linéarisation de la partie déviatorique de la contrainte est également implémentée. La méthode variationnelles multi-échelle (VMS) est développée sur la base de la décomposition orthogonale des variables, qui amortit les champs de pression parasites pour les éléments tétraédriques linéaires par morceaux. Divers exemples numériques sont présentés pour évaluer la robustesse, la précision et les capacités de notre schéma dans des problèmes dominés par la flexion et pour des géométries complexes.

This chapter proposes a novel way to solve transient linear, and non-linear solid dynamics for compressible, nearly incompressible, and incompressible material in the updated Lagrangian framework for tetrahedral unstructured finite elements. It consists of a mixed formulation in both displacement and pressure, where the momentum equation of the continuum is complemented with a pressure equation that handles incompressibility inherently. It is obtained through the deviatoric and volumetric split of the stress, which enables us to solve the problem in the incompressible limit. A linearization of the deviatoric part of the stress is implemented as well. The Variational Multi-Scale method (VMS) is developed based on the orthogonal decomposition of the variables, which damps out spurious pressure fields for piece-wise linear tetrahedral elements. Various numerical examples are presented to assess the robustness, accuracy, and capabilities of our scheme in bending-dominated problems, and for complex geometries.

3.1   Introduction

The need for a solid solver that can handle complex geometry is at its highest peaks. Whether it be in everyday life applications, such as the behavior of electrical wires [1], or the complex electro-elasticity behavior of components [2], to the understanding the elastic shock in solids [3]. Unconventional shapes, which result from complex algorithms, such as shape optimization, need to be tested. In addition, bio-medical, and biomechanical applications usually include complex geometries based on human organs. This can also be of high interest in the field of AI, which is generating atypical geometries through coupling with the aforementioned fields. Furthermore, a high range of materials can be considered incompressible or nearly incompressible. Ranging from certain polymers that do not undergo high volume changes, to biological tissues.

A finite element formulation in which the displacement field is the unknown, and all other physical quantities are obtained using post-processing methodology is typically used in solid dynamics [4] [5]. This method performs poorly near the incompressibility limit. Locking, spurious pressure fields, and poor performance in bending-related applications are some of the shortcomings of the preceding formulation [6].

This subject has seen its fair share of developments, aiming to dampen or eliminate the above-stated limitations. Selective and reduced integration's methods, such as the B-bar [6] [7] [8], the F-bar [9] [10] [11] [12], or the mean dilatation finite element methods [13] are used for their ease of implementation. By reducing the order

of incompressibility at quadrature points, these methods circumvent the numerical instabilities of the inf-sup or Ladyzhenskaya-Babuska-Brezzi(LBB) conditions [14]. These strategies have proven to be accurate for structured quadrilateral, and hexahedral meshes. It is important to mention that automated grid generation of hexahedral elements for complex geometries, is work-intensive. It requires at least two times the order of magnitude of the actual computing time [15]. This is however surpassed when using unstructured tetrahedral elements.

When considering the case of static, incompressible elasticity, we obtain an elliptic equation, like that of the Stokes problem in fluid mechanics, while the transient case or elastodynamics leads to a hyperbolic equation. Given the similarities in the equations, it is natural to extend the mixed/coupled velocity/pressure formulation of the Stokes problem [16], to the mixed displacement/pressure problem of the static elastic case [17]. This extension acts as a bridge for the different, already implemented methods in fluid mechanics, to solid mechanics.

In [18], an incompressible steady-state linear elastic material was modeled using the mixed formulation in displacement/pressure using the Orthogonal Sub Scale method [19]. This work showed the capabilities of the mixed formulation (displacement/pressure) using the Orthogonal Sub Scale (OSS) method in the incompressible limit. Also in [20] [21], an incompressible non-linear material was also modeled using the Orthogonal Sub Scale method. These works show the capabilities of a mixed formulation using strain/displacement or stress/displacement formulation. There is a compromise however between computational cost and accuracy. In [22], a three-field (displacement/pressure/strain) formulation was tested and showed to be effective and accurate in the nearly incompressible limit.

Most of the former formulations were developed for the steady-state solution, and as mentioned before, transient elastodynamics converts the parabolic problem to an elliptic problem. This is due to the second-order derivative of displacement of the momentum equation. This problem was addressed in different works, trying to circumvent this issue.

Some of these works include [23][24] [25][26], where a finite-strain non-linear solid dynamics model is based on a new first-order (mixed) form of the equations in the Lagrangian framework. The proposed methodology consists of adding an additional variable, which is the deformation tensor $\mathbf{F}$, and Lagrange multipliers for the conservation of angular momentum if needed. The results obtained are second-order accurate in stress. Moreover, in the incompressible limit, and bending-dominated problems, an additional variable was introduced, which is the Jacobian determinant of the deformation gradient J [27][28]. In recent works [29][30][31], a nodal co-factor tensor $\mathbf{H} = cof : \mathbf{F}$ is added. This method, like others in the family of methods based on nodal interpolations of $\mathbf{F}$, is inherently unstable. Thus, a stabilization based on the Streamline Upwind/Petrov-Galerkin (SUPG) method, and

added penalties on the deformation gradient $\mathbf{F}$ is utilized. Tests show the capabilities of this methodology to solve problems in the incompressible limit, it is however costly in terms of the number of unknowns per node.

In [15][32], a mixed problem in velocity and pressure, where the displacement field is calculated based on the discretization of the velocity is presented. Authors claim that the Variational Multi-Scale (VMS) method was insufficient for the stabilization of the problem in the transient regime. They resorted to a pressure rate equation to alleviate the problem, which they called the Dynamic Variational Multi-Scale (D-VMS). The tests also prove to be accurate and robust. In [33], a mixed formulation in displacement and pressure, resolved in the total Lagrangian framework was presented with different variations of the VMS methods. The method proved to be accurate and robust as well.

In [34], a mixed problem in displacement and pressure in finite elements for nearly incompressible material is presented. The Variational Multi-Scale (VMS) is used for the displacement field, and two types of error estimators are exploited. The formulation was investigated across different numerical convergence tests.

This chapter proposes a novel method for solving non-linear elasticity in solid dynamics. Based on unstructured tetrahedral meshes, the method can depict complex geometries with ease and acceptable computational cost. A split of the strain energy into its deviatoric and volumetric part [35], gives rise to the proposed mixed formulation. The momentum equation is complemented with a constitutive equation in pressure. A fully implicit, mixed coupled in displacement and pressure (piece-wise linear) formulation in an updated Lagrangian context is proposed. The set of equations obtained is prone to spurious pressure fields. A stabilization method based on the Variational Multi-Scale (VMS) method is thus implemented to elevate the problem. The framework is coupled with the moving mesh method, the mesh thus follows the body in the updated Lagrangian framework. This method can handle complex geometries with a reasonable computational time.

The rest of the chapter consists of: Section 2 contains the problem definition; Section 3 presents the stabilized linear elastic formulation both in its steady-state and transient form; Section 4 contains the stabilized hyperelastic formulation and introduces the adopted Moving Mesh Method (MMM)[36] [37]; Section 5 provides the numerical validation of the framework. Finally, perspective and conclusions are given in section 6.

3.2 Lagrangian Solid Dynamics

The variation rate of density and displacement for a solid material is governed by the equations of Lagrangian solid dynamics. Ω_0, and Ω represent the initial and current domain, which are two open sets in $\mathbb{R}^d$ with Lipshitz boundaries, where d

denotes the spatial dimension. The boundary is given by Γ, which is split into two separate sets given by $\Gamma = \overline{\partial\Omega_{\mathbf{u}} \cup \partial\Omega_{\mathbf{t}}}$ and $\partial\Omega_{\mathbf{u}} \cap \partial\Omega_{\mathbf{t}} = \emptyset$. Where $\partial\Omega_{\mathbf{u}}$ denotes the Dirichlet boundary that specifies the displacement, and $\partial\Omega_{\mathbf{t}}$ denotes the Neumann boundary that specifies the traction force. The motion of the deformable body is given by:

$$\boldsymbol{\phi} := \Omega_0 \rightarrow \Omega = \boldsymbol{\phi}(\Omega_0), \tag{3.1}$$

$$\boldsymbol{\phi} := \Gamma_0 \rightarrow \Gamma = \boldsymbol{\phi}(\Gamma_0), \tag{3.2}$$

$$\mathbf{X} \rightarrow \mathbf{x} = \boldsymbol{\phi}(\mathbf{X}, t) \,\forall \mathbf{X} \in \Omega_0. \tag{3.3}$$

It serves as a mapping of the material coordinate $\mathbf{X}$, in the total Lagrangian framework of an infinitesimal material particle of the solid, to $\mathbf{x}$, the coordinate of the same particle in the updated Lagrangian framework. $\boldsymbol{\phi}$ is assumed to be smooth, and invertible. The deformation gradient and the Jacobian determinant are given by: $\mathbf{F} = \nabla_{\mathbf{X}}\boldsymbol{\phi}$ and $J = det\mathbf{F}$.

The displacement of the solid is given by: $\mathbf{u} = \mathbf{x} - \mathbf{X}$. The governing equations are given by:

$$\rho\ddot{\boldsymbol{u}} - \nabla \cdot \boldsymbol{\sigma} = \boldsymbol{f} \text{ in } \Omega, \tag{3.4}$$

$$\rho J = \rho_0 \text{ on } \partial\Omega_u. \tag{3.5}$$

Where ρ and ρ_0 are the current and initial body density respectively, $\boldsymbol{f}$ is a forcing term, $\boldsymbol{\sigma}$ is the symmetric Cauchy stress tensor, and the derivatives are taken with the respect to the updated reference frame. Moreover, $\ddot{\boldsymbol{u}}$ represents the material second derivative of displacement, which is the acceleration. This set of equations, along with a constitutive model for the solid that defines $\boldsymbol{\sigma}$, and the corresponding initial and boundary condition, describes the development of the system.

One way to model a solid is using a mixed formulation, containing both displacement and pressure fields. This is obtained with a decomposition of the stress into a volumetric and deviatoric component. This decomposition is essential when dealing with incompressible or nearly incompressible material. It is significant to mention that this is done for isotropic material. Thus, the stress is given by:

$$\boldsymbol{\sigma} = p\mathbf{I} + dev[\boldsymbol{\sigma}]. \tag{3.6}$$

Where $\mathbf{I}$ is the identity matrix

The problem is completed with the addition of the initial and boundary conditions of the problem. Assuming zero displacement initial conditions, given by $\boldsymbol{u}(\mathbb{X}, 0) = \boldsymbol{u}_0 = 0$. This gives: $\boldsymbol{\phi}(\mathbf{X}, 0) = \mathbf{X}$, $\mathbf{F}|_{t=0} = \mathbf{I}$, and $J|_{t=0} = 1$. The material is also assumed to be stress-free. The boundary conditions are given by:

$$\boldsymbol{u}|_{\Gamma_{\boldsymbol{u}}} = \boldsymbol{u}(\boldsymbol{x}, t), \tag{3.7}$$

$$\boldsymbol{\sigma}\mathbf{n}|_{\Gamma_{\mathbf{t}}} = \mathbf{t}(\boldsymbol{x}, t). \tag{3.8}$$

Where $\mathbf{n}$ is the outward-pointing normal on the boundary Γ.

3.3 Linear Elastic Formulation

For very small displacement, the elastic behavior of the solid can be modeled using Hook's law. By considering a linear relationship between stress and strain, the solid is modeled using a spring. A steady-state formulation is first introduced for comparison purposes, and a transient formulation is then developed.

3.3.1 Steady-state Formulation

To put the different implementations that are going to be presented in this chapter into perspective, the steady-state linear elastic solver is first developed, followed by the transient formulation. The latter is a direct extension of the Stokes problem, where the displacement $\boldsymbol{u}$ is the primary variable instead of the velocity. This extension will better explain the stabilization techniques that are being exploited. For linear elasticity, $\mathbf{x} \approx \mathbf{X}$, $\Omega_0 \approx \Omega$, $\nabla_{\mathbb{X}} \approx \nabla_{\mathbf{x}}$, and $\rho_0 = \rho$. A linear elastic problem can be formulated based on the decomposition of the stress, using the hydro-static pressure p and the displacement field $\boldsymbol{u}$. It is worthwhile to note that the pressure convention in solid mechanics is opposite to that of fluid mechanics.

The stress tensor is thus given by:

$$\boldsymbol{\sigma} = p\mathbf{I} + 2\mu\, dev[\nabla^s \boldsymbol{u}], \tag{3.9}$$

$$p = K\epsilon_v, \tag{3.10}$$

$$\epsilon_v = \nabla \cdot \boldsymbol{u}. \tag{3.11}$$

Where ϵ_v is the volumetric strain. In equations (3.9)(3.10)(3.11), we distinguish between the deviatoric and volumetric part of the deformation. ∇^s is the symmetrical gradient operator:

$$\nabla^s = \frac{1}{2}(\nabla + \nabla^T). \tag{3.12}$$

μ is the Lamé constant, also known as the shear modulus of the material, and it is specified by:

$$\mu = \frac{E}{2(1 + \nu)}. \tag{3.13}$$

K is the bulk modulus or modulus of volumetric compressibility, and it is defined by:

$$K = \frac{1}{3}\frac{E}{(1 - 2\nu)}. \tag{3.14}$$

Using the stress tensor formulation, along with a body force $\boldsymbol{f}$ and the necessary Dirichlet and Neumann boundary conditions, the steady-state problem can be formulated as follows:

$$-\nabla p - 2\mu\nabla \cdot dev[\nabla^s\boldsymbol{u}] = \boldsymbol{f} \text{ in } \Omega \tag{3.15}$$

$$\nabla \cdot \boldsymbol{u} - \frac{1}{K}p = 0 \text{ in } \Omega, \tag{3.16}$$

$$\boldsymbol{u} = 0 \text{ on } \partial\Omega_u, \tag{3.17}$$

$$\boldsymbol{\sigma}\boldsymbol{n} = \boldsymbol{t} \text{ on } \partial\Omega_t, \tag{3.18}$$

$$\rho J = \rho_0 \text{ in } \Omega. \tag{3.19}$$

This formulation considers both incompressible and compressible material, with the difference being in equation (16) and a constant density ρ_0. For an incompressible material, $K \to \infty$ and equation (16) becomes simply:

$$\nabla \cdot \boldsymbol{u} = 0 \text{ in } \Omega. \tag{3.20}$$

Whereas if we assume an isochoric phenomenon, implying $\epsilon_v = 0$, we will get the same result. The variational formulation of this problem is given by:

$$a(\boldsymbol{u}, \boldsymbol{w}) + (p, \nabla \cdot \boldsymbol{w}) = L(\boldsymbol{w}) \,\forall \boldsymbol{w} \, \in W_0, \tag{3.21}$$

$$(\nabla \cdot \boldsymbol{u}, q) - (\frac{1}{K}p, q) = 0 \,\forall q \, \in Q. \tag{3.22}$$

Where $a(\boldsymbol{u}, \boldsymbol{w})$ and $L(\boldsymbol{w})$ are given by:

$$a(\boldsymbol{u}, \boldsymbol{w}) = \int_\Omega 2\mu \, dev[\nabla^s\boldsymbol{u}] : \nabla^s\boldsymbol{w} \, d\Omega, \tag{3.23}$$

$$L(\boldsymbol{w}) = \int_\Omega \boldsymbol{f} \cdot \boldsymbol{w}d\Omega + \int_{\partial\Omega_t} \boldsymbol{w} \cdot \bar{\boldsymbol{t}}d\Gamma. \tag{3.24}$$

The discrete form of the problem is given by:

$$a(\boldsymbol{u}_h, \boldsymbol{w}_h) + (p_h, \nabla \cdot \boldsymbol{w}_h) = L(\boldsymbol{w}_h) \, \forall \boldsymbol{w}_h \in W_{h,0}, \tag{3.25}$$

$$(\nabla \cdot \boldsymbol{u}_h, q_h) - (\frac{1}{K} p_h, q_h) = 0 \, \forall q_h \in Q_h. \tag{3.26}$$

Where the subscript h refers to the discrete value of the variable.

The Babuska–Brezzi or inf-sup stability [14] condition constrains the interpolation relation between the fields, thus forcing different interpolations for $\boldsymbol{u}$ and p. Equal order interpolation has poor numerical performance as it does not respect the condition. Several types of stabilization are available in this case. We used P1/P1 elements, with a Variational Multi-Scale Method (VMS), which enables us to have the same order of interpolation. In [16], equal order elements were used for the Stokes problem. It contained proof of convergence, and stability. This work led to the extension of the formulation to the Navier–Stokes equations [38]. In [39] [17], the linear elastic problem was tackled. VMS provides natural stabilization by an orthogonal decomposition of the solution (displacement, pressure) spaces. Orthogonal decomposition of the function spaces is first done by:

$$W_0 = W_{h,0} + W'_0, \tag{3.27}$$

$$W = W_h + W', \tag{3.28}$$

$$Q = Q_h + Q'. \tag{3.29}$$

Following [19], the resolvable coarse and unresolved fine-scale components of the displacement and pressure are given by:

$$\boldsymbol{u} = \boldsymbol{u}_h + \boldsymbol{u}', \tag{3.30}$$

$$p = p_h + p'. \tag{3.31}$$

We also apply the same decomposition for the weighting functions:

$$\boldsymbol{w} = \boldsymbol{w}_h + \boldsymbol{w}', \tag{3.32}$$

$$q = q_h + q'. \tag{3.33}$$

Equations (25), and (26) are divided into two sets: coarse, and fine-scale. Most of the time the unresolved fine scales are modeled in function of the residual-based terms. Using static condensation, the fine-scale equations are solved in an approximate matter (residual-based) and re-injected into the coarse-scale equations. This will provide us with additional terms, calibrated by a local stabilizing parameter. These terms are responsible for the enhanced stability, reduced pressure oscillations, and increased accuracy of the standard Galerkin formulation.

The fine-scale problem, defined on the sum of elements interiors [40], and formulated in function of the transient coarse-scale variables, is solved. The fine-scale approximation is given by:

$$\boldsymbol{u}' = \sum_{T_h} (\tau_{\boldsymbol{u}} P'_{\boldsymbol{u}}(R_{\boldsymbol{u}})), \tag{3.34}$$

$$p' = \sum_{T_c} (\tau_c P'_c(R_c)). \tag{3.35}$$

Where $R_{\boldsymbol{u}}$, and R_c are the finite elements residuals, $P'_{\boldsymbol{u}}$, and P'_c are the projection operators, and $\tau_{\boldsymbol{u}}$, and τ_c are the stabilization parameters. Note that in this current work, both $P'_{\boldsymbol{u}}$, and P'_c are taken as the Identity matrix.

The fine-scale approximations are subsequently substituted in the coarse problem. The new variational formulation for the coarse-scale equations is given by:

$$a((\boldsymbol{u}_h + \boldsymbol{u}'), \boldsymbol{w}_h) + (p_h + p', \nabla \cdot \boldsymbol{w}_h) = L(\boldsymbol{w}_h) \, \forall \, \boldsymbol{w}_h \, \in \, W_{h,0}, \tag{3.36}$$

$$(\nabla \cdot (\boldsymbol{u}_h + \boldsymbol{u}'), q_h) - (\frac{1}{K}(p_h + p'), q_h) = 0 \, \forall \, q_h \, \in \, Q_h, \tag{3.37}$$

and that of the fine-scale equations are given by:

$$a((\boldsymbol{u}_h + \boldsymbol{u}'), \boldsymbol{w}') + (p', \nabla \cdot \boldsymbol{w}') = L(\boldsymbol{w}') \, \forall \, \boldsymbol{w}' \, \in \, W'_0, \tag{3.38}$$

$$(\nabla \cdot (\boldsymbol{u}_h + \boldsymbol{u}'), q') - (\frac{1}{K}(p_h), q') = 0 \, \forall \, q' \, \in \, Q'. \tag{3.39}$$

Assuming quasi-static sub-scales, and calculating the fine-scale equation based on the initial residual, and re-entering the physics in the coarse-scale equation, we get the final set of the coarse-scale equations with the pressure stabilization term for the case of linear elasticity, given by:

$$a((\boldsymbol{u}_h, \boldsymbol{w}_h) + (p_h, \nabla \cdot \boldsymbol{w}_h) = L(\boldsymbol{w}_h) \, \forall \, \boldsymbol{w}_h \in W_{h,0}, \tag{3.40}$$

$$(\nabla.\boldsymbol{u}_h, q_h) - (\frac{1}{K}p_h, q_h) - \sum_{K \in T_h} (\tau_K R(\boldsymbol{u}_h), \nabla q_h) = 0 \, \forall \, q_h \in Q_h, \tag{3.41}$$

$$R(\boldsymbol{u}_h) = \boldsymbol{f} + \nabla p_h + 2\mu \nabla \cdot \, dev[\nabla^s \boldsymbol{u}_h]. \tag{3.42}$$

Where $R(\boldsymbol{u}_h)$ is the finite element residual, and τ_K is a coefficient based on the study of the response of the stabilization parameters coming from a Fourier analysis of the problem for the sub-scales [20].

Comparing the standard Galerkin and the stabilized formulation, we distinguish additional integrals that are evaluated element-wise. These terms represent the sub-grid scales, which help damp out spurious pressure oscillations, and overcome instabilities in our case. When using linear elements, which is the case, all second order derivatives vanishes. These terms were removed from the equations.

3.3.2   Transient Formulation

This creates the primary difference between the Stokes equations and the transient linear elastic equations. In the Stokes equations, the primary variable is velocity. A first-order derivative is required to obtain the inertia term. However, for the transient linear elastic equations, $\boldsymbol{u}$ is the displacement. Thus, a second-order derivative in time for the displacement is needed to account for the transient regime. This gives the set of equations the structure of the d'Alembert operator. While the transient Stokes problem equations are parabolic in nature, the added transient term renders the PDE hyperbolic[15][32]. When dealing with materials in the incompressible limit, the PDE becomes degenerate hyperbolic. The pressure acts as a Lagrangian multiplier required to force the divergence-free constraint of the displacement. The transient elastic solid solver governing equations are given by:

$$\rho\ddot{\boldsymbol{u}} - \nabla p - 2\mu\nabla \cdot \, dev[\nabla^s \boldsymbol{u}] = \boldsymbol{f} \text{ in } \Omega, \tag{3.43}$$

$$\nabla \cdot \boldsymbol{u} - \frac{1}{K}p = 0 \text{ in } \Omega, \tag{3.44}$$

$$\boldsymbol{u} = 0 \text{ on } \partial\Omega_u, \tag{3.45}$$

$$\boldsymbol{\sigma}\boldsymbol{n} = \boldsymbol{t} \text{ on } \partial\Omega_t. \tag{3.46}$$

The Courant-Friedrichs-Lewy (CFL) condition imposes limits on the time step. For explicit time integrators, very small time steps are needed to obtain accurate results. Consider a time interval, where $t \in [0, T]$, and a discretization of this interval into N time steps of equal intervals(Δt). A Backward differentiation formula (BDF) is adopted in this work. A first, and second-order accurate BDF's are considered. These equations are given by:

$$\mathbf{a}^{n+1} \approx \frac{1}{\Delta t^2}(\boldsymbol{u}^{n+1} - 2\boldsymbol{u}^n + \boldsymbol{u}^{n-1}) + O(\Delta t), \tag{3.47}$$

$$\mathbf{a}^{n+1} \approx \frac{1}{\Delta t^2}(2\boldsymbol{u}^{n+1} - 5\boldsymbol{u}^n + 4\boldsymbol{u}^{n-1} - \boldsymbol{u}^{n-2}) + O(\Delta t^2). \tag{3.48}$$

Where a is the acceleration. The backward differentiation formulas are known for their high-frequency dissipation that will help damp out spurious high-frequency oscillations.

The discrete/stabilized variational form of the above equations, following the same steps as in section 3.1 [16][39], is given by:

$$(\rho\ddot{\boldsymbol{u}}, \boldsymbol{w}_h) + a(\boldsymbol{u}_h, \boldsymbol{w}_h) + (p_h, \nabla.\boldsymbol{w}_h) = L(\boldsymbol{w}_h) \; \forall \; \boldsymbol{w}_h \in W_{h,0}, \tag{3.49}$$

$$(\nabla \cdot \boldsymbol{u}_h, q_h) - (\frac{1}{K}p_h, q_h) - \sum_{K \in T_h} (\tau_K R(\boldsymbol{u}_h), \nabla q_h) = 0 \; \forall \; q_h \in Q_h, \tag{3.50}$$

$$R(\boldsymbol{u}_h) = \boldsymbol{f} - \rho\ddot{\boldsymbol{u}} + \nabla p_h + 2\mu\nabla.\,dev[\nabla^s\boldsymbol{u}_h]. \tag{3.51}$$

Where $R(\boldsymbol{u}_h)$ is the new finite element residual. The same additional elements that damp out pressure oscillations are found in these equations as well.

3.4 Transient Non-Linear Elastic Lagrangian Formulation

3.4.1 Hyperelasticity model and pressure equation

Elastic materials in general are better modeled with a non-linear depiction of their real-life behavior. As mentioned earlier, the material at hand is isotropic. Consider a nonlinear material with a Helmholtz free energy or strain energy $\Psi(\mathbf{C})$ function, where $\mathbf{C}$ is the right Cauchy-Green strain tensor $\mathbf{C} = \mathbf{F}^T\mathbf{F}$. $\mathbf{F}$ is the deformation gradient given by $\mathbf{F}_{ij} = x_{i,j} = \frac{\partial x_i}{\partial X_j}$. The second Piola-Kirchhoff stress tensor $\mathbf{S} = J\mathbf{F}^{-1}\boldsymbol{\sigma}\mathbf{F}^{-T}$ where J is the Jacobian determinant of $\mathbf{F}$, is derived by taking derivatives of the Helmholtz free energy functional $\boldsymbol{\Psi}(\mathbf{C})$ with respect to $\mathbf{C}$:

$$\mathbf{S} = 2\partial_{\mathbf{C}}\Psi(\mathbf{C}). \tag{3.52}$$

To be able to model both incompressible and compressible material, we will apply the same decomposition as before. Decomposing $\Psi(\mathbf{C})$ into its volumetric and deviatoric part respectively as follows:

$$\Psi(\mathbf{C}) = U(J) + W(\bar{\mathbf{C}}). \tag{3.53}$$

Where $\bar{\mathbf{C}} = J^{-\frac{2}{3}}\mathbf{C}$ is the deviatoric/volume-preserving part of $\mathbf{C}$, and $J = \sqrt{det\mathbf{C}}$.

The Helmholtz free energy of isotropic hyperelastic models is written as a function of the strain invariant. Consider a Neo-Hookean elastic material, and a Simo-Taylor volumetric model [48] with:

$$U(J) = \frac{1}{4}\kappa(J^2 - 1) - \frac{1}{2}\kappa lnJ, \tag{3.54}$$

$$W(\bar{\mathbf{C}}) = \frac{1}{2}\mu(tr\bar{\mathbf{C}} - 3) = \frac{1}{2}\mu(\bar{I}_1 - 3). \tag{3.55}$$

where κ and μ are material properties, and $I_1 = tr\bar{\mathbf{C}}$. For small displacements, the model reduces to a linear elastic model where κ and μ are the bulk and shear modulus of the material. The stress can also be split to its deviatoric and volumetric part:

$$p = 2J^{-1}\mathbf{F}\frac{\partial U(J)}{\partial\mathbf{C}}\mathbf{F}^T = U'(J) = \frac{1}{2}\kappa(J + J^{-1}), \tag{3.56}$$

$$\mathbf{dev}[\boldsymbol{\sigma}] = 2J^{-1}\mathbf{F}\frac{\partial W(\bar{\mathbf{C}})}{\partial \mathbf{C}}\mathbf{F}^T = \mu J^{-\frac{5}{3}}\mathbf{dev}[\mathbf{FF}^T]. \tag{3.57}$$

Recall, $\mathbf{F} = \nabla_{\mathbf{X}}\boldsymbol{u} + I$. Thus:

$$\mathbf{FF^T} = \nabla_{\mathbf{X}}\boldsymbol{u} + \nabla_{\mathbf{X}}^T\boldsymbol{u} + \nabla_{\mathbf{X}}\boldsymbol{u}\nabla_{\mathbf{X}}^T\boldsymbol{u} + I. \tag{3.58}$$

We are solving all of the previous equations in the updated Lagrangian framework, while the above equation is given in the total Lagrangian framework. Considering the following mathematical equation:

$$\nabla_{\mathbf{X}}\boldsymbol{u} = (I - \nabla\boldsymbol{u})^{-1} - I. \tag{3.59}$$

And assuming a very small variation in the displacement noted $\delta\boldsymbol{u}$. Recalling that for very small displacement, $(I - \nabla\boldsymbol{u})^{-1} = I + \nabla\boldsymbol{u}$, we get:

$$\begin{aligned}\mathbf{FF^T} =& (I - \nabla\boldsymbol{u})^{-1} - I + ((I - \nabla\boldsymbol{u})^{-1} - I)^T + ((I - \nabla\boldsymbol{u})^{-1} - I)((I - \nabla\boldsymbol{u})^{-1} - I)^T \\ &+ I + 2\epsilon(\delta\boldsymbol{u}) + \nabla\delta\boldsymbol{u}(\nabla\delta\boldsymbol{u})^T + \nabla\delta\boldsymbol{u}(\nabla\boldsymbol{u})^T + (\nabla\boldsymbol{u})(\nabla\delta\boldsymbol{u})^T.\end{aligned} \tag{3.60}$$

Recall that we are using isotropic hyperelastic material models, thus the strain energy density is written in function of the strain invariants such as $I_1 = tr\bar{\mathbf{C}}$ for the Neo-Hookean model. The other invariants are

$$I_2 = \frac{1}{2}[(tr\bar{\mathbf{C}})^2 - tr(\bar{\mathbf{C}})^2], \tag{3.61}$$

$$I_3 = \det\bar{\mathbf{C}} = \det(J^{-\frac{2}{3}}\mathbf{C}) = 1. \tag{3.62}$$

Thus, it can be deduced that $W(\bar{\mathbf{C}})$ is written in function of the first and second invariants. The Neo-Hookean model presented as an example previously involves the first invariant and is the easiest mathematical model for the nonlinear deformation behavior of polymers. However, this model fails to reproduce experimental data of several isotropic elastic materials. Another model worth mentioning is the Mooney-Rivlin model, which is dependent on the second invariant. This model is given by

$$W(\bar{\mathbf{C}}) = \alpha_1(I_1 - 3) + \alpha_2(I_2 - 3), \tag{3.63}$$

where α_1 and α_2 are material parameters that satisfy $\mu = 2(\alpha_1 + \alpha_2) > 0$. Note that for $\alpha_2 = 0$, we obtain the previous Neo-Hookean model. The interested reader is invited to read [?] for further information on these models. Other volumetric models of the strain energy function exist, such as the Quadratic model [?] given by

$$U(J) = \frac{\kappa}{2}(J-1)^2; \ U'(J) = \kappa(J-1). \tag{3.64}$$

This model is widely used in practice, even though it does not satisfy the fundamental condition of requiring an infinite amount of strain energy to compress the solid into a single point with a vanishing volume state. Another model that circumvents this problem is given by [48]

$$U(J) = \frac{\kappa}{4}(lnJ)^2; \ U'(J) = \frac{\kappa}{2J}lnJ. \tag{3.65}$$

The system of equations to be solved now is given by:

$$\rho\ddot{\boldsymbol{u}} - \nabla_x p - \nabla_x \cdot \ dev[\boldsymbol{\sigma}] = \boldsymbol{f} \text{ in } \Omega, \tag{3.66}$$

$$\nabla_x \cdot \boldsymbol{u} - \frac{1}{K}p = g \text{ in } \Omega, \tag{3.67}$$

$$\boldsymbol{u} = 0 \text{ on } \partial\Omega_u, \tag{3.68}$$

$$\boldsymbol{\sigma}\boldsymbol{n} = \boldsymbol{t} \text{ on } \partial\Omega_t, \tag{3.69}$$

$$\rho J = \rho_0. \tag{3.70}$$

$\ddot{\boldsymbol{u}}$ represents the material derivative of displacement, which is the acceleration, given by:

$$a = \dot{\boldsymbol{v}} = \ddot{\boldsymbol{u}} = \frac{\partial\boldsymbol{v}}{\partial t} + \nabla_x(\boldsymbol{v}).(\boldsymbol{v} - \boldsymbol{v}_{\text{domain}}) = \frac{\partial^2\boldsymbol{u}}{\partial t^2} + \nabla_x(\frac{\boldsymbol{u} - \boldsymbol{u}^-}{\Delta t}).(\boldsymbol{v} - \boldsymbol{v}_{domain}) \tag{3.71}$$

Substituting in (61), the formulation becomes:

$$\rho\left(\frac{\partial^2\boldsymbol{u}}{\partial t^2} + (\nabla_x(\frac{\boldsymbol{u} - \boldsymbol{u}^-}{\Delta t}).(\boldsymbol{v} - \boldsymbol{v}_{domain})\right) - \nabla_x p - \nabla_x. \ dev[\boldsymbol{\sigma}] = \boldsymbol{f} \text{ in } \Omega. \tag{3.72}$$

3.4.2 Moving Mesh Method (MMM)

For $\boldsymbol{v}_{\text{domain}}$, we adopt the R-method as an adaptive strategy [41]. The r-method or moving mesh method (MMM), consists of relocating mesh nodes so that nodes get condensed in regions with high gradients. This is done, through a mapping from the non-deformed domain in a parameter space Ω_c, to the deformed domain in the physical space Ω. The connections of points in Ω, representing discrete points in Ω_c, ensure the coverage of the physical domain with a computational mesh. The key components are threefold:

1. Mesh equations

2. Monitor Function

3. Interpolation

Choosing the appropriate mesh equations for a given application and resolving them efficiently is essential for the method. This method includes some challenges for inelastic problems due to internal variable mapping, which is relevant to the biological applications [42]. In our case, the mesh is guided by the solid dynamics equation. Guiding the mesh redistribution is done via the monitor function. It is dependent on the solutions arc-length in 1D, curvature, and a posteriori errors if needed. It also requires smoothing in practice. Interpolation of dependent variables from the old, to the new mesh, is only needed if the mesh equations are not time-dependent and are solved independently from the partial differential equation.

In interpolation-free MMM, such as the moving finite element method of Miller [36] [37], both the differential equation and the mesh equations are resolved simultaneously. The essential components of such methods include:

1. Equidistribution principle

2. Mesh equations

3. The method of lines (MOL) approach

First introduced by de Boor in [43], the equidistribution principle was used to solve Boundary Value Problems (BVP) for Ordinary Differential Equations (ODE). It consists of choosing mesh nodes so that a certain measure describing the solution error is adjusted over every sub-interval. The method of lines approach is usually considered in most moving mesh codes, which may result in a stiff equation. Thus requiring a very small time step to converge. A moving mesh finite element approach is used in our case, where the mesh equations are based on the solid dynamics equation, and the equidistribution principle is applied on the residual of the partial differential equation written in finite element form. This method is particularly interesting for its various advantages:

- Interpolation-free method.

- Detect, track and resolve moving boundaries.
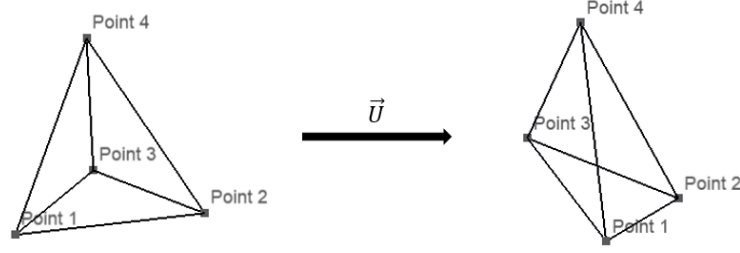
- The method of lines (MOL) approach

Figure 3.1: Moving mesh illustration with varying volume in 3D

It is however necessary to use an implicit time scheme to overcome the stiffness of the system. An illustration of an element subjected to a displacement vector is shown in figure 3.1. The displacement vector can induce a volume change if needed.

Since this method is adopted, thus we move the mesh with the velocity of the solid. $\boldsymbol{v} = \boldsymbol{v}_{domain} \rightarrow \boldsymbol{v} - \boldsymbol{v}_{domain} = 0$. The variational formulations thus become:

$$(\rho\frac{\partial^2 \boldsymbol{u}}{\partial t^2}, \boldsymbol{w}_h) + a'((\boldsymbol{u}_h, \boldsymbol{w}_h) + (p_h, \nabla.\boldsymbol{w}_h) = L(\boldsymbol{w}_h) \ \forall \ \boldsymbol{w}_h \in W_{h,0}, \tag{3.73}$$

$$(\nabla.\boldsymbol{u}_h, q_h) - (\frac{1}{K}p_h, q_h) = (g, q_h) \ \forall \ q_h \in Q_h, \tag{3.74}$$

where a' is given by:

$$a'((\boldsymbol{u}_h, \boldsymbol{w}_h) = \int_\Omega \mu \ dev[\boldsymbol{\sigma}] : \nabla^s \boldsymbol{w} \ d\Omega. \tag{3.75}$$

3.4.3   Variational Multi-Scale Method

In this section, we derive a consistent Variational Multi-scale Method (VMS) for hyperelastic materials. Applying the same orthogonal decomposition of the function spaces as in (27)(28)(29), and subsequently decomposing the variables into their coarse resolvable, and fine unresolved scales as in (30)(31). This decomposition is also applied for the weighting function following (32)(33). Thus, the time-dependent mixed-finite element approximation of the dynamic hyperelastic response reads:

Coarse-scale

$$(\rho\frac{\partial^2(\boldsymbol{u} + \boldsymbol{u}')}{\partial t^2}, \boldsymbol{w}_h) + a'((\boldsymbol{u}_h + \boldsymbol{u}'), \boldsymbol{w}_h) + (p_h + p', \nabla.\boldsymbol{w}_h) = L(\boldsymbol{w}_h)\forall\boldsymbol{w}_h \in W_{h,0}, \tag{3.76}$$

$$(\nabla.(\boldsymbol{u}_h + \boldsymbol{u}'), q_h) - (\frac{1}{K}(p_h + p'), q_h) = (g, q_h) \ \forall \ q_h \in Q_h, \tag{3.77}$$

56

Fine-scale

$$(\rho\frac{\partial^2(\boldsymbol{u}+\boldsymbol{u}')}{\partial t^2}, \boldsymbol{w}') + a'((\boldsymbol{u}_h+\boldsymbol{u}'), \boldsymbol{w}') + (p_h+p', \nabla.\boldsymbol{w}') = L(\boldsymbol{w}') \,\forall\, \boldsymbol{w}' \in W', \quad (3.78)$$

$$(\nabla.(\boldsymbol{u}_h+\boldsymbol{u}'), q') - (\frac{1}{K}(p_h+p'), q') = (g, q') \,\forall\, q' \in Q'. \quad (3.79)$$

The fine-scale problem is first solved, which is written in function of the time-dependent coarse-scale problem and defined on the sum of elements interior. The fine scales are then re-injected into the coarse-scale equations, thus modeling them implicitly. An important remark to mention is that sub-scales are not tracked in time. An elaboration of this choice is found in [44]. On the other hand, sub-scales are still quasi time-dependent, since the large scale residual is time-dependent. For more information on time-tracked sub-scales, please refer to [45]. Afterward, the coarse-scale equations are given by:

$$(\rho\frac{\partial^2(\boldsymbol{u})}{\partial t^2}, \boldsymbol{w}_h) + a'((\boldsymbol{u}_h), \boldsymbol{w}_h) + (p_h, \nabla.\boldsymbol{w}_h) + \sum_{K\in T_h}(p', \nabla.\boldsymbol{w}_h) = L(\boldsymbol{w}_h) \,\forall\, \boldsymbol{w}_h \in W_{h,0},$$
$$(3.80)$$

$$(\nabla.(\boldsymbol{u}_h), q_h) - (\frac{1}{K}(p_h), q_h) - \sum_{K\in T_h}(\frac{1}{K}(p'), q_h) - \sum_{K\in T_h}(u', \nabla q_h) = (g, q_h) \,\forall\, q_h \in Q_h.$$
$$(3.81)$$

The finite element residuals are given by:

$$R(\boldsymbol{u}_h) = \boldsymbol{f} - \rho\ddot{\boldsymbol{u}}_h + \nabla_x p_h + \nabla_x \cdot dev[\boldsymbol{\sigma}], \quad (3.82)$$

$$R(p_h) = g - \nabla_x \cdot \boldsymbol{u}_h + \frac{1}{K}p_h. \quad (3.83)$$

Modeling the fine scales as in (34)(35), we finally get:

$$(\rho\frac{\partial^2(\boldsymbol{u})}{\partial t^2}, \boldsymbol{w}_h) + a'((\boldsymbol{u}_h), \boldsymbol{w}_h) + (p_h, \nabla.\boldsymbol{w}_h) + \sum_{K\in T_h}(\tau_c(g - \nabla_x \cdot \boldsymbol{u}_h + \frac{1}{K}p_h), \nabla.\boldsymbol{w}_h$$
$$= L(\boldsymbol{w}_h) \,\forall\, \boldsymbol{w}_h \in W_{h,0},$$
$$(3.84)$$

$$(\nabla.(\boldsymbol{u}_h), q_h) - (\frac{1}{K}(p_h), q_h) + \sum_{K\in T_h}(\frac{\tau_c}{K}(\nabla_x \cdot \boldsymbol{u}_h - \frac{1}{K}p_h - g), q_h)$$
$$+ \sum_{K\in T_h}(\tau_{\boldsymbol{u}}(\rho\ddot{\boldsymbol{u}}_h - \nabla_x p_h - \nabla_x \cdot dev[\boldsymbol{\sigma}] - \boldsymbol{f}), \nabla q_h) = (g, q_h) \,\forall\, q_h \in Q_h.$$
$$(3.85)$$

Compared to the standard Galerkin formulation, or even to the previous stabilized formulation for linear elasticity, this formulation contains new additional integrals

that are evaluated elementwise. These additional terms model the effect of the sub-scales in both compressible and incompressible regimes. These terms are developed consistently and help elevate problems of spurious pressure oscillations. The general definition of the stabilization parameters [46][47], computed within each element gives:

$$\tau_{\boldsymbol{u}} = ((\frac{\rho}{(c_0 \Delta t)^2})^2 + (\frac{2\mu}{c_1 h_k^2})^2)^{-\frac{1}{2}}, \tag{3.86}$$

$$\tau_c = ((2c_2\mu)^2)^{-\frac{1}{2}}. \tag{3.87}$$

Where h_k is the characteristic length of the element, and c_0, c_1, and c_2 are constants to be determined.

3.5 Numerical Validation

The finite element formulation was implemented and solved using the in-house C++ CimLib_CFD [49] parallel finite element library. All the numerical simulations were carried out using the same library. The algebraic problems obtained from the finite element formulation are assembled, and solved using the generalized minimal residual method (GMRES) with the incomplete LU preconditioner from the Portable Extensive Toolkit for Scientific Computation (PETSc) library [50].

3.5.1 Linear Elastic

2D rotating plate The rotating plate test [24], revisited in [15], is used to assess the order of convergence in displacement and pressure of our framework. The square plate has a dimension of 2x2 m. All boundaries are constrained to move only tangentially. The analytical solution of the displacement for the problem is given by:

$$\boldsymbol{u}^*(\boldsymbol{x},t) = U_0 sin(\omega t) \begin{cases} -sin(\frac{\pi}{2}x)cos(\frac{\pi}{2}y) \\ cos(\frac{\pi}{2}x)sin(\frac{\pi}{2}y) \end{cases} \tag{3.88}$$

Where $U_0 = 0.01$ m, and $\omega = \frac{\pi}{2}\sqrt{\frac{2\mu}{\rho_0}}$. This analytical displacement field leads to $\nabla \cdot \boldsymbol{u} = 0$; thus the analytical pressure is $p^* = 0$. The material properties are given by $E = 17$ MPa, and $\rho_0 = 1100$ Kg/m³. The initial conditions of the problem are $\boldsymbol{u}(\boldsymbol{x},0) = \boldsymbol{u}^*(\boldsymbol{x},0)$, $\boldsymbol{v}(\boldsymbol{x},0) = \boldsymbol{v}^*(\boldsymbol{x},0)$, and $p(\boldsymbol{x},0) = 0$. Zero normal displacement homogeneous Dirichlet boundary conditions are imposed on all four boundaries of the problem. Typical unstructured and structured meshes of the square are shown in figures 3.2a, and 3.2b. An example showcasing the displacement field of the problem is shown in figure 3.2c. Classical P1/P1 Galerkin finite elements exhibit pressure oscillations in the incompressible limit, which rapidly pollutes the

numerical solution. Thus, a convergence study in both displacement and pressure of
the proposed method is conducted. Two sequences of unstructured and structured
meshes are considered. Unstructured meshes vary from 40 elements to 100 000
elements. Structured meshes range from 2x8x8 to 2x512x512 elements. The fully
incompressible case of $\nu = 0.5$ is considered. The convergence curves are plotted in
figures 3.3, 3.4, 3.5, and 3.6. We compute the L2-error norm for both displacement
and pressure. They are versus the mesh size on a logarithmic scale. We observe
from the convergence plots, a second-order convergence rate for both $\boldsymbol{u}$, and p.

(a) Structured Mesh

(b) Unstructured mesh

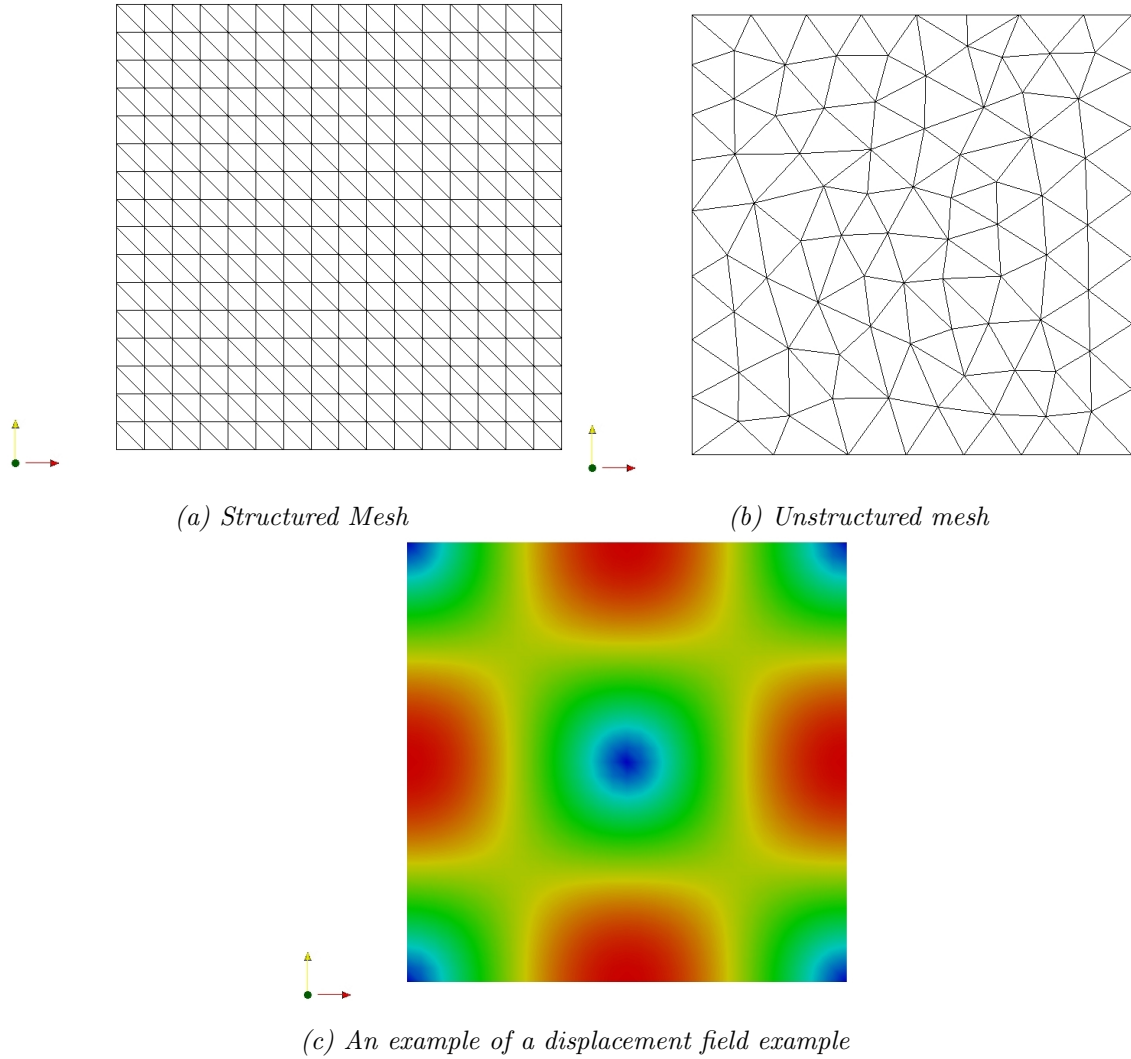*(c) An example of a displacement field example*

*Figure 3.2: 2D structured 3.2a and unstructured 3.2b meshes for the two-dimensional ro-
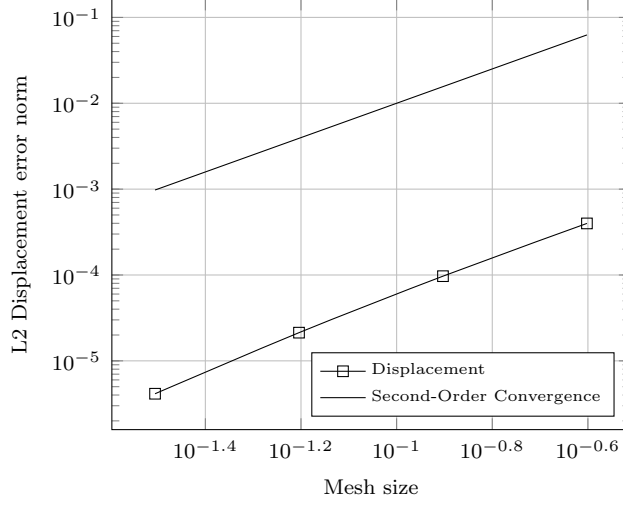tating plate, and an example of the displacement field 3.2c.*

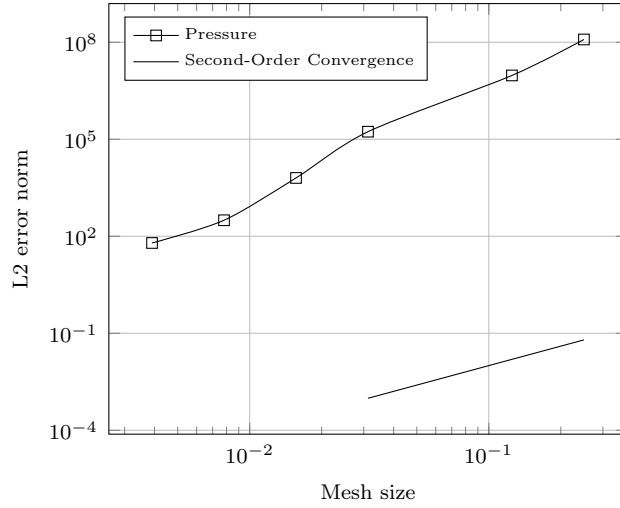*Figure 3.3: L2 displacement error convergence study for the rotating plate test on a structured mesh.*

Figure 3.4: L2 pressure error convergence study for the rotating plate test on a structured mesh.

Static Cook's membrane test A typical problem where the P1/P1 elements for both displacement and pressure produce a polluted pressure field is the Cook's membrane problem [51]. The problem setup and a structured, and unstructured 2D mesh are shown in figures 3.7a,3.7b and 3.7c. The structured mesh is generated by splitting each element of the quadrilateral grid.

The material is assumed to have a linear elastic behavior with $\rho = 1$, $E = 250$, and $\nu = 0.5$. Zero displacement Dirichlet boundary conditions are imposed on the
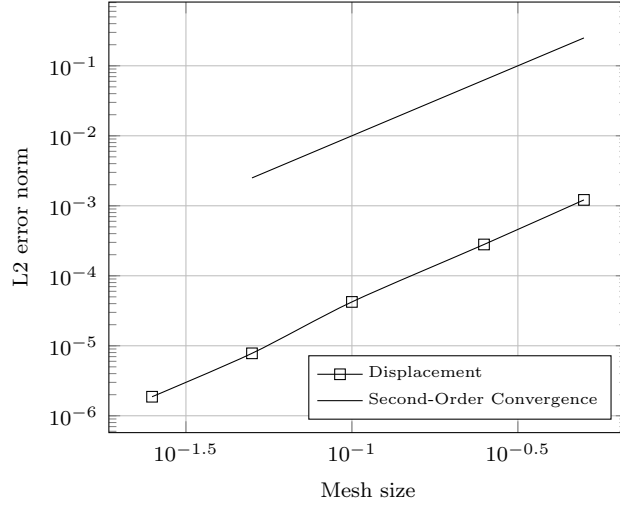
Figure 3.5: L2 displacement error convergence study for the rotating plate test on an unstructured mesh.
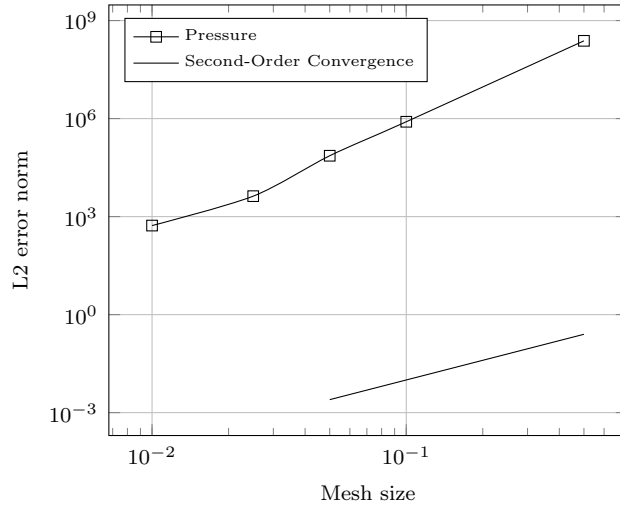

Figure 3.6: L2 pressure error convergence study for the rotating plate test on an unstructured mesh.

left side of the membrane, and a uniform vertical traction force equal to 6.25 is imposed on the right side of the membrane. The two lateral sides are traction-free. Standard Galerkin P1/P1 elements for both the displacement and pressure lead to oscillations in pressure when no stabilization is included. However, when the VMS stabilization is applied the pressure field has no oscillatory pulses in the pressure. Also note, that the tip displacement converges rapidly on relatively coarse meshes. Different pressure contours are found in figure 3.9. It is important to note that we

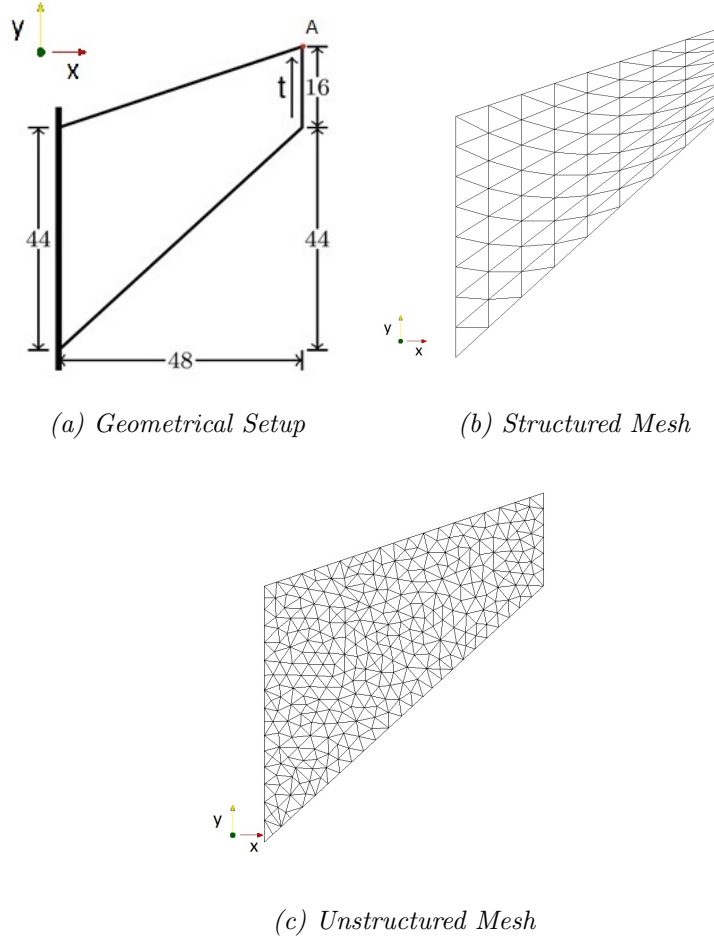(a) Geometrical Setup   (b) Structured Mesh

(c) Unstructured Mesh

Figure 3.7: Geometrical setup and 2D structured and unstructured meshes for Cook's membrane test.

get similar results when using unstructured tetrahedral meshes. A mesh convergence study was applied on refined structured meshes, and the results obtained conform with the literature and can be found in figure 5.8.

Transient Cook's membrane test An extension of the aforementioned cook's membrane test to a transient regime is presented here. This is a bending-dominated problem. Although this is a linear elastic case, we used the Neo-Hookean model, which converges to the linear elastic response for very small strains. The simulations are run until t=7 s. All the previous properties, along with the initial, and boundary conditions are preserved. The geometry of the membrane was scaled with a factor of 0.1. The solution obtained oscillates around the steady-state solution computed earlier. To be able to study the different time integration schemes, we show in fig-
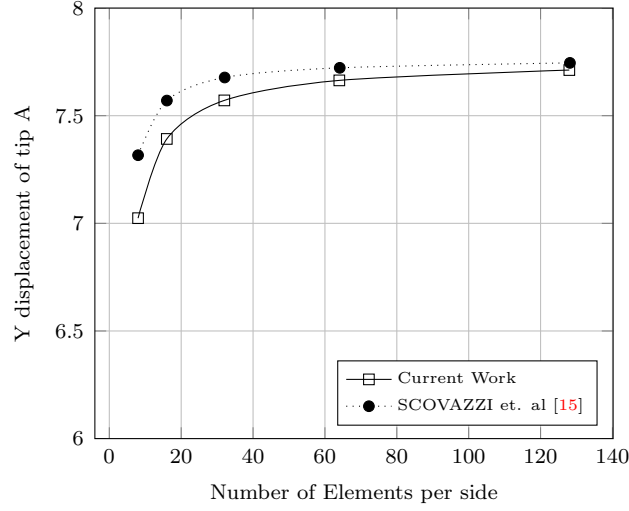
Figure 3.8: Mesh convergence study for the steady-state Cook's membrane test and comparison with that from Scovazzi et. al [15]

ure3.10, and 3.11 the evolution of tip A with respect to time. A fixed unstructured mesh of approximately 6000 elements is used, and a time step of $\Delta t = 0.025s$. Pressure contours at different positions in time can also be found in figure 3.12. One can conclude, from the figures that the BDF1 time scheme is first-order accurate and highly dissipating, while the BDF2 time scheme is less dissipating and second-order accurate. This is shown by the higher amplitude achieved by the BDF2 scheme, and the slower dissipation of energy through time.

Upsetting problem   This example shows the capabilities of the formulation in the nearly incompressible case, even in the case of coarse tetrahedral meshes in 3D. It consists of a 14x14x10 specimen that is deformed up to 7 % of its height. The specimen is clamped at the bottom and top to a rigid plate, where the top one gradually moves downwards while compressing it. A linear elastic constitutive model is used. The young's modulus and poisson ratio are given as $E = 2.0e + 5MPa$, and $\nu = 0.4999$. Figures 3.13a, 3.13b,3.13c,3.13d and 3.13e shows the behavior of our formulation. For a relatively coarse unstructured 3D mesh, we obtained satisfactory results. The problem is conducted in the linear elastic case, so for relatively small strain, so that the model holds. The Von Mises stresses are also computed for the completeness of the study. The results correlate with the literature [18] and no pressure locking is observed.
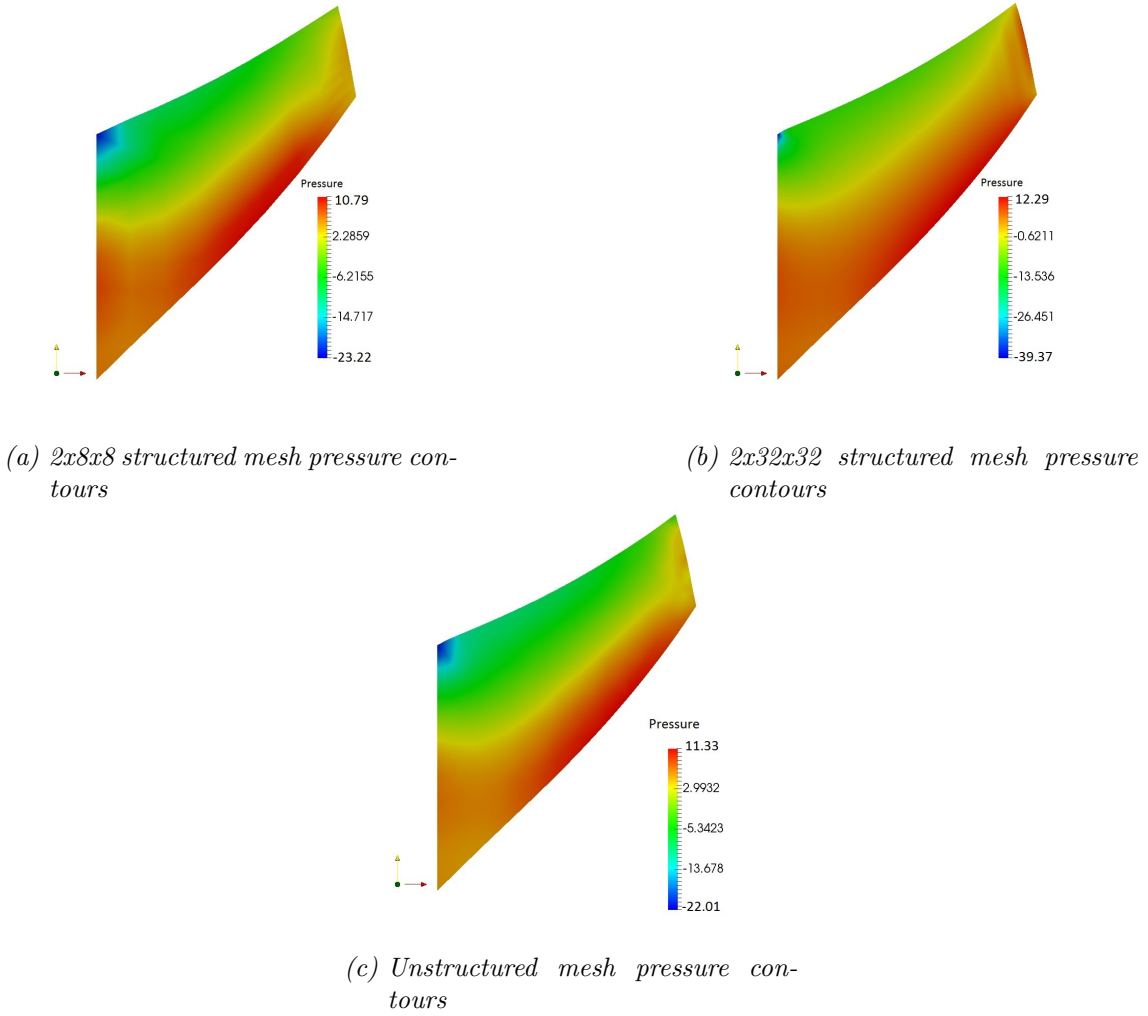
(a) 2x8x8 structured mesh pressure con-
    tours

(b) 2x32x32 structured mesh pressure
    contours

(c) Unstructured mesh pressure con-
    tours

Figure 3.9: Pressure Contours of the steady-state Cook's membrane problem for different
         meshes.

3.5.2 HyperElastic

A Computational Solid Mechanics test This test is a part of a well-documented benchmark on Fluid–Structure Interaction, which deals with the solid part alone [52]. The structure is assumed to be elastic and compressible. The constitutive law of the material is given by the St. Venant–Kirchhoff material. The elastic beam is taken alone and subjected to a gravitational force $\gg = (0, g)$. The beam has a length $l = 0.35$, and a thickness $t = 0.02$. A typical unstructured mesh is shown in figure 3.14. Three variations of the test are presented, two of which converge towards a steady-state solution and a non-diffusive transient case. The different parameters are given in table 3.1. The steady-state results are summarized
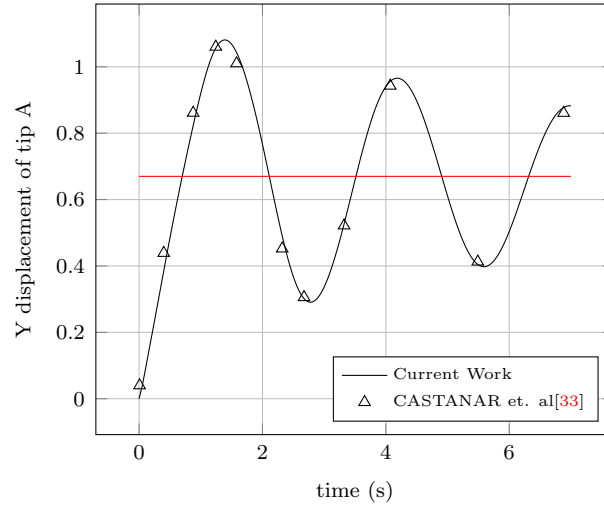
Figure 3.10: *Y displacement of tip A versus time for first-order time discretization and comparison with that from Castanar et. al [33].*
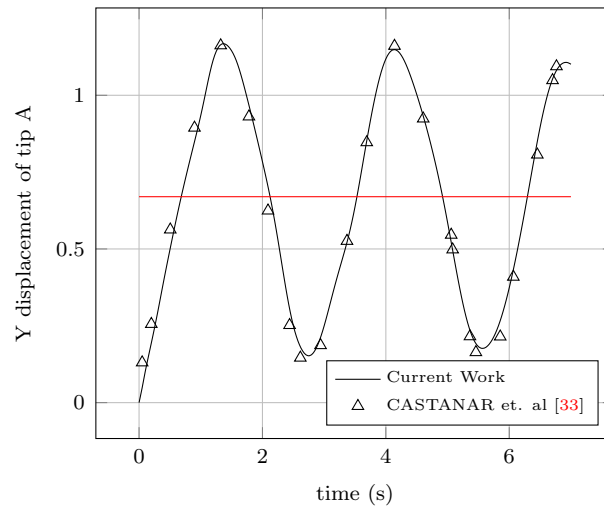

Figure 3.11: *Y displacement of tip A versus time for second-order time discretization and comparison with that from Castanar et. al [33].*

in table 3.2. Both components of the displacement are present. The error interval is within an acceptable range. The pressure contours of the steady-state cases can be found in figure 3.15 in their final position. The variation of the y component and the x component of the displacement with respect to time are found in figures 3.16, and 3.17 respectively. The results obtained for this relatively thin beam, which has a membrane-like behavior given its aspect ratio, are coherent with the literature. This shows the ability of the solver to handle high aspect ratio geometries, with

(a) t=1s

(b) t=3s

(c) t=5s

(d) t=7s
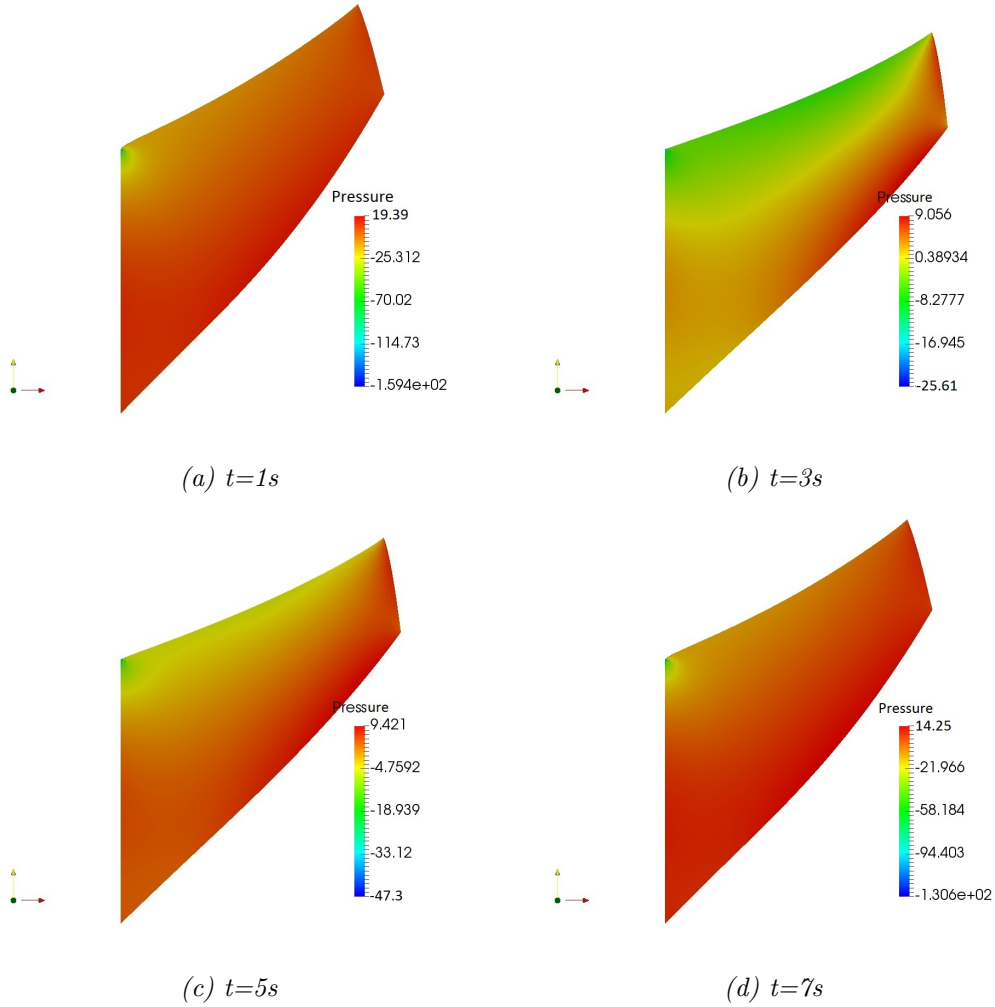
Figure 3.12: Pressure contours of the transient Cook's membrane problem at different positions in time.

relatively coarse meshes.

Bending Beam test (3D)   This test consists of a bending problem of a square cylinder in 3D. The dimensions of the square cylinder are 1x1x6 m. The beam is also rotated with respect to the z-axis with an angle of 5.2 degrees to avoid symmetry. At $t = 0$, the beam is stress-free, and the displacement is equal to 0.

An initial velocity is applied on the beam, given by:

$$\boldsymbol{v}(\boldsymbol{x}, 0) = \boldsymbol{v}(x, y, z, 0) = (\frac{5z}{3}, 0, 0)^T \, m/s \; y \in [0, 6] m. \tag{3.89}$$

66

(a) Mesh

(b) Displacement

(c) Pressure contours

(d) Von Mises Stress

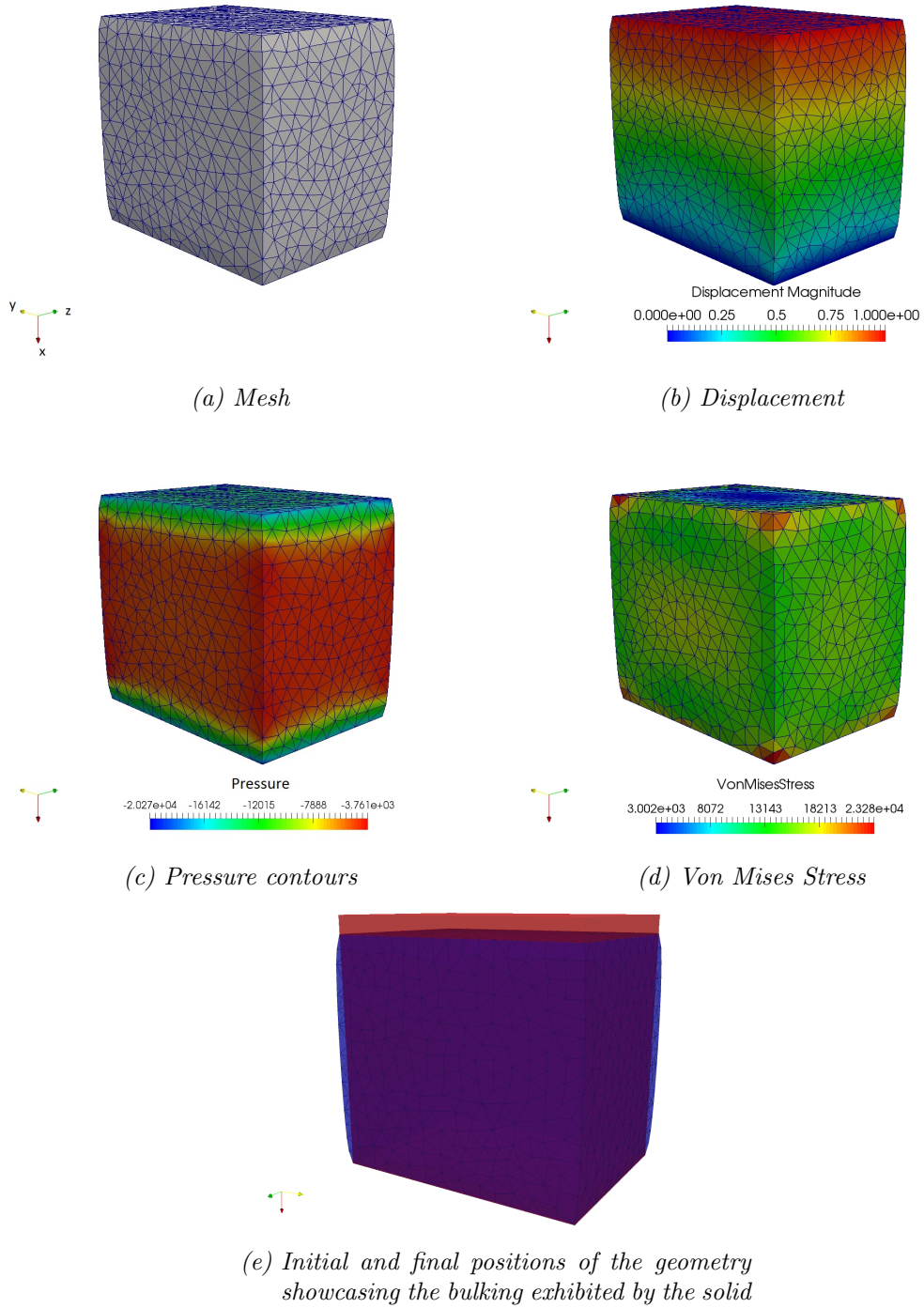*(e) Initial and final positions of the geometry showcasing the bulking exhibited by the solid*

Figure 3.13: 3.13a *the unstructured 3D mesh,* 3.13b *displacement field,* 3.13c *pressure contours,* 3.13d *Von Mises Stress, and* 3.13e *the initial and final positions of the geometry.*
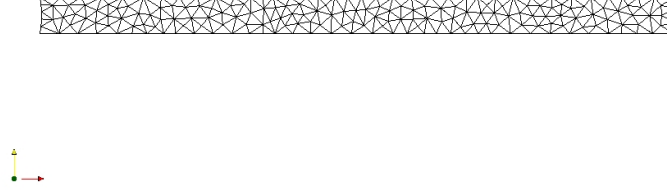
Figure 3.14: Unstructured 2D mesh

CSM Cases			
Solid Properties	Case 1	Case 2	Case 3
ρ	1000	1000	1000
ν	0.4	0.4	0.4
μ	500000	2000000	500000
E	1400000	5600000	1400000
g	2	2	2

Table 3.1: Solid properties for different variations of the CSM test.

CSM Cases				
Field	Case 1		Case 2	
	Dx	Dy	Dx	Dy
Benchmark	$-7.187\text{x}10^{-3}$	$-66.1\text{x}10^{-3}$	$-0.4690\text{x}10^{-3}$	$-16.97\text{x}10^{-3}$
Simulation	$-7.277\text{x}10^{-3}$	$-67.14\text{x}10^{-3}$	$-0.4408\text{x}10^{-3}$	$-17\text{x}10^{-3}$

Table 3.2: Steady-State simulation results for CSM 1 & 2 and comparison with that from Turek et. al [52].

The origin of our coordinates system is located at $(0.5, 0.5, 0)$. The material is Neo-Hookean with the following properties: $\rho_0 = 1100$ kg/m ^{3}, $E = 17$ MPa, and $\nu = 0.5$.

Zero displacement Dirichlet boundary condition is imposed on the bottom of the cylinder, which is assumed to be clamped. Zero traction boundary condition is applied on all other surfaces.

The simulation was run until T= 2s. The simulation is computed for three different refined meshes, to perform a mesh convergence study, and to achieve con-
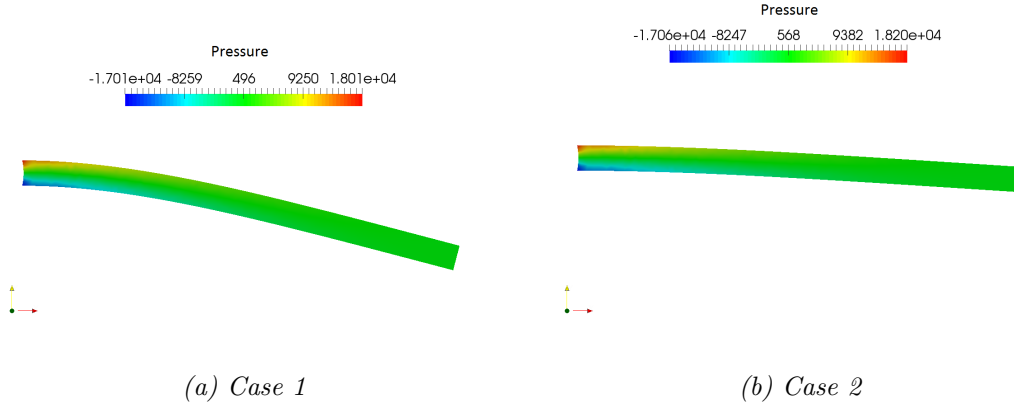
(a) Case 1

(b) Case 2

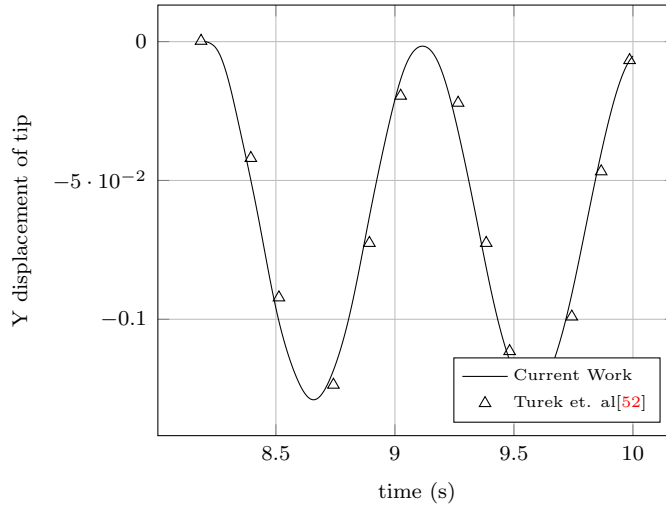Figure 3.15: Steady-state pressure contours for CSM 1 & 2.

Figure 3.16: Case 3: Y displacement versus time for the transient case and comparison with that from Turek et. al [52].

vergence for very fine meshes. Such formulations are more prone to divergence for refined meshes. Three levels of refinement are considered, with the number of elements equaling 1790, 11660, and 81018 respectively. The meshes are shown in figures 4.41a, 4.41b, and 4.41c respectively. The pressure contours for the three meshes are shown in figure 3.19. The pressure contours of the beam at different steps in time are shown in figure 3.20. This figure shows how the MMM method moves the mesh with the domain at each time step, to be able to be consistent with the formulation. The x component of the displacement is shown in figure 3.21, for the three levels of refinement of the meshes, along with the reference solution. As can be seen from the figure, convergence is rapidly obtained even for the coarse mesh. This shows

69
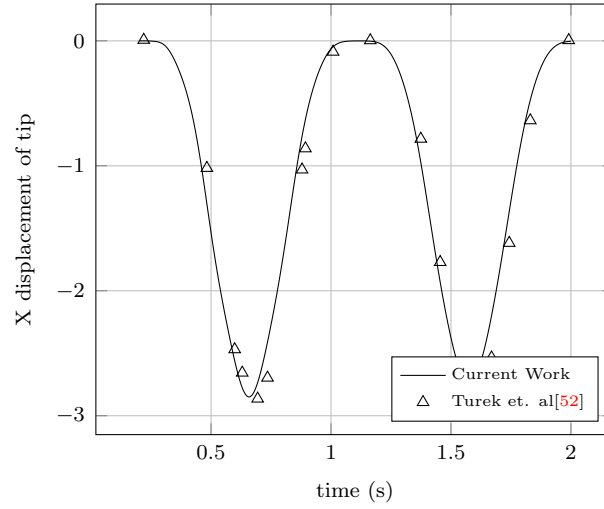
Figure 3.17: Case 3: X displacement versus time for the transient case and comparison with that from Turek et. al [52].

the capabilities of the formulations of relatively coarse unstructured meshes. Figure 3.22, is added for the completeness of the study. It shows the Z displacement of the same tip A with respect to time.
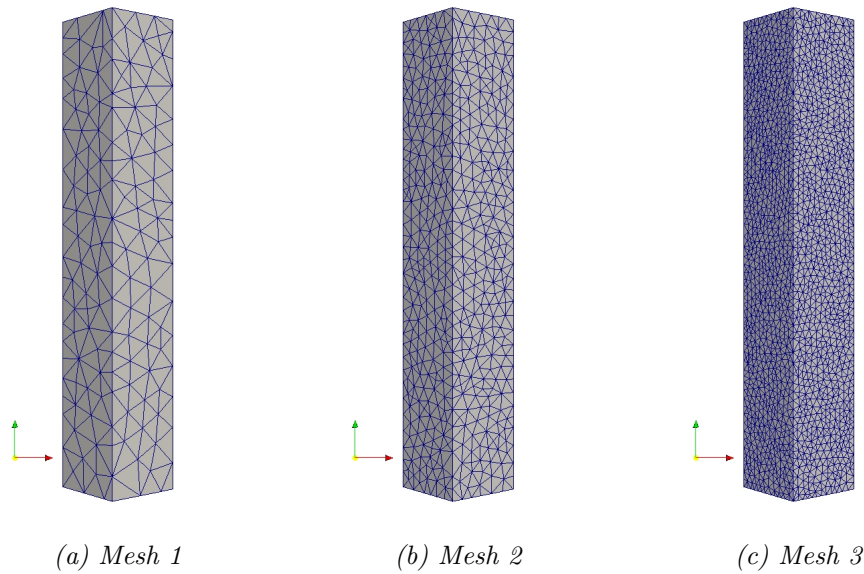

(a) Mesh 1   (b) Mesh 2   (c) Mesh 3

Figure 3.18: Three different levels of refinement of unstructured meshes

(a) Pressure contours for Mesh 1

(b) Pressure contours for Mesh 2
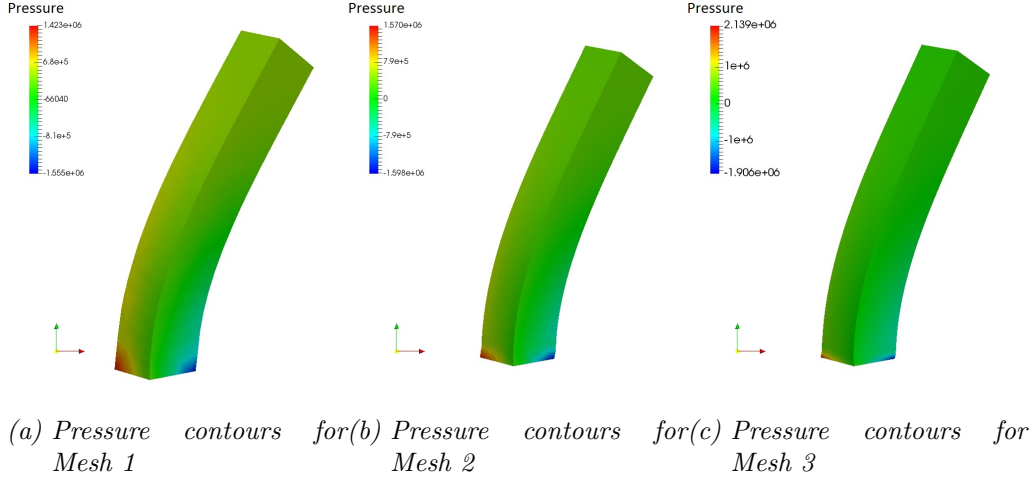
(c) Pressure contours for Mesh 3

Figure 3.19: 3D Bending Beam mesh convergence study

Complex Geometry As a final numerical test, the ability of the framework to handle complex geometries is evaluated. A helical gear is shown in figure 3.23, along with its computational mesh, consisting of 9865 tetrahedral 3D elements. The material is assumed to have a non-linear transient elastic behavior and is considered fully incompressible with $\rho = 1$, $E = 250$, and $\nu = 0.5$. The Neo-Hookean model is used. A vertical downward forcing term of magnitude 5 is imposed on the top plane of the geometry. Homogeneous Dirichlet boundary conditions are imposed on the bottom plane of the geometry. Zero traction Neumann boundary conditions are applied on the rest of the boundaries. Pressure contours at times equal to 10,20,30,40, and 50 s are shown in figures 3.24a, 3.24b, 3.24c, 3.24d and 3.24e. High-pressure gradients can be observed around the hole of the geometry. The solution converged properly, and no spurious pressure oscillation was observed.

(a) t=0.5s

(b) t=1s

(c) t=1.5s

(d) t=2s
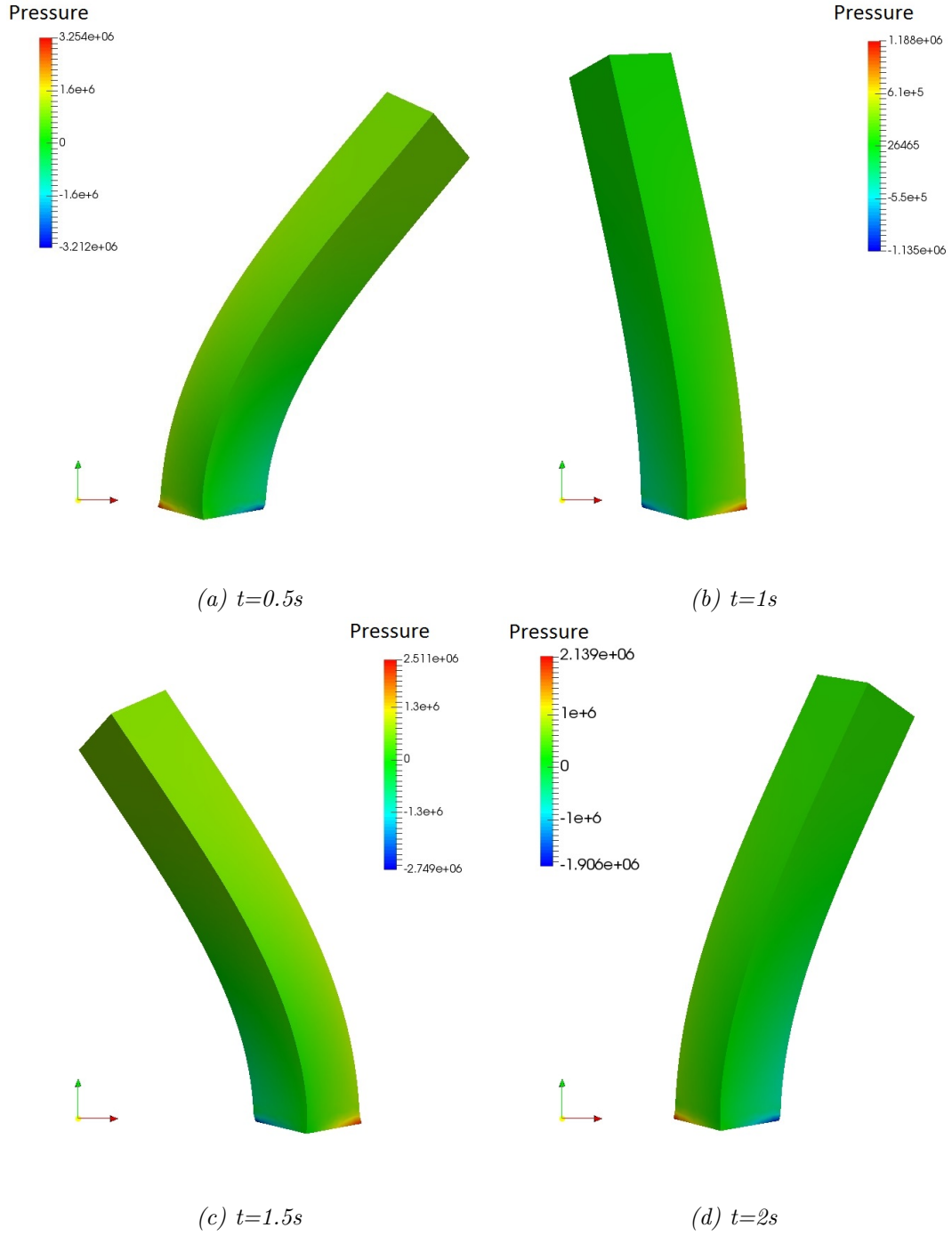
Figure 3.20: Pressure contours of the beam at different times.
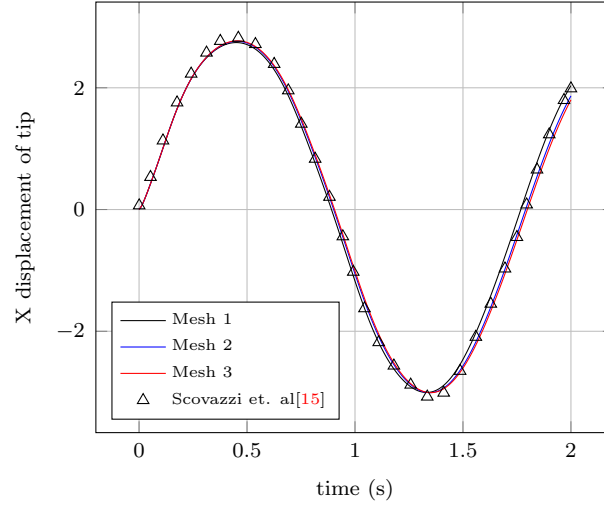
Figure 3.21: X displacement of tip versus time and comparison with that from Scovazzi et. al [15].
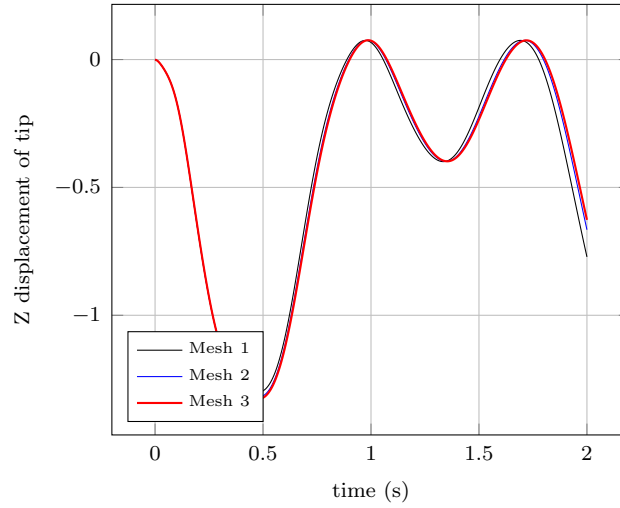
Figure 3.22: Z displacement of tip versus time

3.6 Perspectives and conclusion

In this work, we have presented a framework based on unstructured tetrahedral meshes that can handle complex geometries, which models the nonlinear behavior of solid elastodynamics. By combining the proposed new mixed formulation in the updated Lagrangian framework, and the R-method for moving meshes, the framework was able to handle nearly, and fully incompressible material in bending-dominated problems. This was achieved through the deviatoric/volumetric split of the stress

73
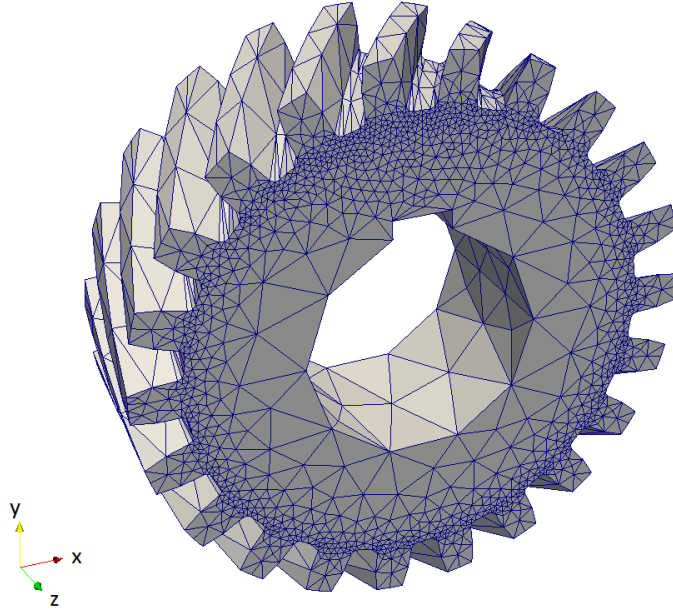
Figure 3.23: Geometrical Setup and computational mesh [53]

tensor. A piece-wise linear mixed formulation in displacement and pressure was obtained in the updated Lagrangian formulation. We achieved piece-wise linear interpolation for both displacement and pressure through the Variational Multi-Scale approach, based on the orthogonal decomposition of the function spaces (extended from fluid mechanics). The stabilization proved effective in both steady-state and transient regimes. We are in the process of applying this newly developed solver for Fluid–Structure Interaction (FSI) applications.
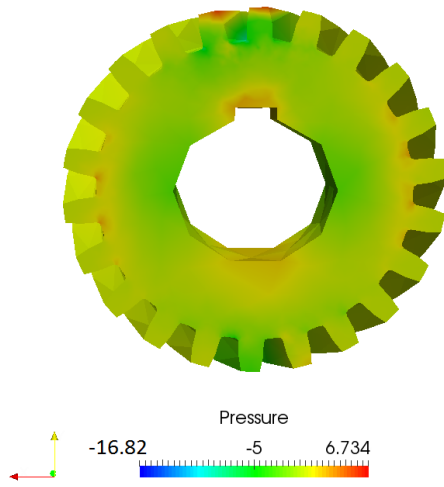
(a) t=10s
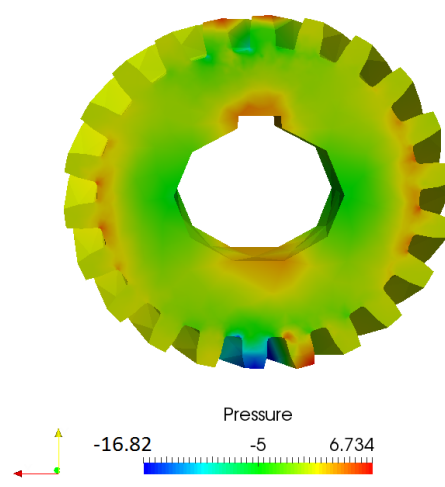
(b) t=20s
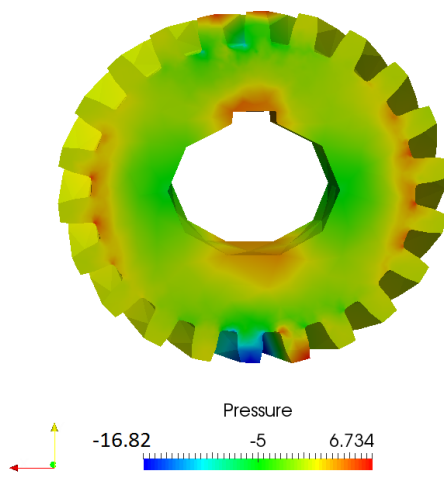
(c) t=30s
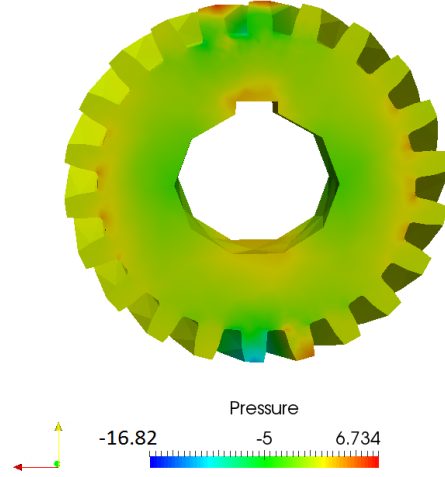
(d) t=40s

(e) t=50s

Figure 3.24: Pressure Contours at different time steps.

Bibliography

[1] E. Taghipour, S. S. Vemula, Z. Wang, Y. Zhou, H. Qarib, K. Gargesh, L. M. Headings, M. J. Dapino, S. Soghrati, Characterization and computational modeling of electrical wires and wire bundles subject to bending loads, International Journal of Mechanical Sciences 140 (2018) 211 – 227. 43

[2] R. Poya, A. J. Gil, R. Ortigosa, R. Sevilla, J. Bonet, W. A. Wall, A curvilinear high order finite element framework for electromechanics: From linearised electro-elasticity to massively deformable dielectric elastomers, Computer Methods in Applied Mechanics and Engineering 329 (2018) 75 – 117. 43

[3] H. al Boustany, C. Ghnatios, Modeling elastic shock in isotropic solids: Solving the uniaxial shock problem, in: 2019 Fourth International Conference on Advances in Computational Tools for Engineering Applications (ACTEA), 2019, pp. 1–6. `doi:10.1109/ACTEA.2019.8851076`. 43

[4] T. Belytschko, W. Liu, B. Moran, Nonlinear Finite Elements for Continua and Structures, John Wiley & Sons, Ltd, 2000. 43

[5] S. M. Shontz, S. A. Vavasis, A robust solution procedure for hyperelastic solids with large boundary deformation, Eng. with Comput. 28 (2) (2012) 135–147. 43

[6] T. Hughes, The Finite Element Method: Linear Static and Dynamic Finite Element Analysis, Dover Civil and Mechanical Engineering, Dover Publications, 2012. 43

[7] T. J. R. Hughes, Equivalence of Finite Elements for Nearly Incompressible Elasticity, Journal of Applied Mechanics 44 (1) (1977) 181–183. 43

[8] T. J. R. Hughes, Generalization of selective integration procedures to anisotropic and nonlinear media, International Journal for Numerical Methods in Engineering 15 (9) (1980) 1413–1418. 43

[9] E. A. S. Neto, F. M. A. Pires, D. R. J. Owen, F-bar-based linear triangles and tetrahedra for finite strain analysis of nearly incompressible solids. part i: formulation and benchmarking, International Journal for Numerical Methods in Engineering 62 (3) (2005) 353–383. 43

[10] E. A. de Souza Neto, D. Perić, G. C. Huang, D. R. J. Owen, Remarks on the stability of enhanced strain elements in finite elasticity and elastoplasticity,

Communications in Numerical Methods in Engineering 11 (11) (1995) 951–961.
43

[11] E. de Souza Neto, D. Perić, M. Dutko, D. Owen, Design of simple low order finite elements for large strain analysis of nearly incompressible solids, International Journal of Solids and Structures 33 (20) (1996) 3277 – 3296. 43

[12] A. Masud, T. J. Truster, A framework for residual-based stabilization of incompressible finite elasticity: Stabilized formulations and f̄ methods for linear triangles and tetrahedra, Computer Methods in Applied Mechanics and Engineering 267 (2013) 359 – 399. 43

[13] J. C. Nagtegaal, D. M. Parks, J. Rice, On numerically accurate finite element solutions in the fully plastic range, Computer methods in applied mechanics and engineering 4 (2) (1974) 153–177. 43

[14] I. Babuška, Error-bounds for finite element method, Numerische Mathematik 16 (4) (1971) 322–333. 44, 49

[15] G. Scovazzi, B. Carnes, X. Zeng, S. Rossi, A simple, stable, and accurate tetrahedral finite element for transient, nearly and fully incompressible solid dynamics: A dynamic variational multiscale approach, International Journal for Numerical Methods in Engineering 106 (09 2015). v, vi, 44, 45, 51, 58, 63, 73

[16] T. J. Hughes, L. P. Franca, M. Balestra, A new finite element formulation for computational fluid dynamics: V. circumventing the babuška-brezzi condition: a stable petrov-galerkin formulation of the stokes problem accommodating equal-order interpolations, Computer Methods in Applied Mechanics and Engineering 59 (1) (1986) 85 – 99. 44, 49, 51

[17] L. P. Franca, T. J. Hughes, A. F. Loula, I. Miranda, A new family of stable elements for nearly incompressible elasticity based on a mixed petrov-galerkin finite element formulation, Numer. Math. 53 (1–2) (1988) 123–141. 44, 49

[18] M. Chiumenti, Q. Valverde, C. A. De Saracibar, M. Cervera, A stabilized formulation for incompressible elasticity using linear displacement and pressure interpolations, Computer methods in applied mechanics and engineering 191 (46) (2002) 5253–5264. 44, 63

[19] T. J. Hughes, G. R. Feijóo, L. Mazzei, J.-B. Quincy, The variational multiscale method—a paradigm for computational mechanics, Computer methods in applied mechanics and engineering 166 (1-2) (1998) 3–24. 44, 49

[20] M. Cervera, M. Chiumenti, R. Codina, Mixed stabilized finite element methods in nonlinear solid mechanics: Part i: Formulation, Computer Methods in Applied Mechanics and Engineering 199 (37-40) (2010) 2559–2570. 44, 50

[21] M. Cervera, M. Chiumenti, R. Codina, Mixed stabilized finite element methods in nonlinear solid mechanics: Part ii: Strain localization, Computer Methods in Applied Mechanics and Engineering 199 (37-40) (2010) 2571–2589. 44

[22] M. Chiumenti, M. Cervera, R. Codina, A mixed three-field fe formulation for stress accurate analysis including the incompressible limit, Computer Methods in Applied Mechanics and Engineering (09 2014). 44

[23] J. Bonet, A. J. Burton, A simple average nodal pressure tetrahedral element for incompressible and nearly incompressible dynamic explicit applications, Communications in Numerical Methods in Engineering 14 (5) (1998) 437–449. 44

[24] J. B. Chun Hean Lee, Antonio J. Gil, Development of a cell centred upwind finite volume algorithm for a new conservation law formulation in structural dynamics, Computers & Structures 118 (2013) 13 – 38, special Issue: UK Association for Computational Mechanics in Engineering. 44, 58

[25] M. Aguirre, A. J. Gil, J. Bonet, A. Arranz Carreño, A vertex centred Finite Volume Jameson-Schmidt-Turkel (JST) algorithm for a mixed conservation formulation in solid dynamics, Journal of Computational Physics 259 (2014) 672–699. 44

[26] C. H. Lee, A. J. Gil, J. Haider, O. Ibrahim, J. Bonet, A first order hyperbolic framework for large strain computational solid dynamics: An upwind finite volume method, International Journal for Numerical Methods in Engineering (2017). 44

[27] A. J. Gil, C. H. Lee, J. Bonet, M. Aguirre, A stabilised petrov–galerkin formulation for linear tetrahedral elements in compressible, nearly incompressible and truly incompressible fast dynamics, Computer Methods in Applied Mechanics and Engineering 276 (2014) 659–690. 44

[28] M. Aguirre, A. J. Gil, J. Bonet, C. H. Lee, An upwind vertex centred finite volume solver for lagrangian solid dynamics, Journal of Computational Physics 300 (2015) 387 – 422. 44

[29] J. Bonet, A. J. Gil, C. H. Lee, M. Aguirre, R. Ortigosa, A first order hyperbolic framework for large strain computational solid dynamics. part i: Total lagrangian isothermal elasticity, Computer Methods in Applied Mechanics and Engineering 283 (2015) 689–732. 44

[30] A. J. Gil, C. H. Lee, J. Bonet, R. Ortigosa, A first order hyperbolic framework for large strain computational solid dynamics. part ii: Total lagrangian compressible, nearly incompressible and truly incompressible elasticity, Computer Methods in Applied Mechanics and Engineering 300 (2016) 146–181. 44

[31] O. I. Hassan, A. Ghavamian, C. H. Lee, A. J. Gil, J. Bonet, F. Auricchio, An upwind vertex centred finite volume algorithm for nearly and truly incompressible explicit fast solid dynamic applications: Total and updated lagrangian formulations, Journal of Computational Physics: X 3 (2019) 100025. 44

[32] S. Rossi, N. Abboud, G. Scovazzi, Implicit finite incompressible elastodynamics with linear finite elements: A stabilized method in rate form, Computer Methods in Applied Mechanics and Engineering 311 (11 2016). 45, 51

[33] I. Castañar, J. Baiges, R. Codina, A stabilized mixed finite element approximation for incompressible finite strain solid dynamics using a total lagrangian formulation, Computer Methods in Applied Mechanics and Engineering 368 (2020) 113164. v, vi, 45, 65

[34] A. Masud, T. J. Truster, L. A. Bergman, A variational multiscale a posteriori error estimation method for mixed form of nearly incompressible elasticity, Computer Methods in Applied Mechanics and Engineering 200 (47) (2011) 3453 – 3481. 45

[35] C. Sansour, On the physical assumptions underlying the volumetric-isochoric split and the case of anisotropy, European Journal of Mechanics - A/Solids 27 (1) (2008) 28 – 39. 45

[36] K. Miller, Moving finite elements. ii, SIAM Journal on Numerical Analysis 18 (6) (1981) 1033–1057. 45, 55

[37] K. Miller, R. N. Miller, Moving finite elements. i, SIAM Journal on Numerical Analysis 18 (6) (1981) 1019–1032. 45, 55

[38] E. Hachem, B. Rivaux, T. Kloczko, H. Digonnet, T. Coupez, Stabilized finite element method for incompressible flows with high reynolds number, Journal of Computational Physics 229 (23) (2010) 8643 – 8665. 49

[39] T. J. Hughes, L. P. Franca, A new finite element formulation for computational fluid dynamics: Vii. the stokes problem with various well-posed boundary conditions: Symmetric formulations that converge for all velocity/pressure spaces, Computer Methods in Applied Mechanics and Engineering 65 (1) (1987) 85 – 96. 49, 51

Bibliography

[40] F. Brezzi, L. Franca, T. Hughes, A. Russo, b = ∫ g, Computer Methods in Applied Mechanics and Engineering 145 (3) (1997) 329 – 339. 50

[41] T. Tang, Moving mesh methods for computational fluid dynamics, Contemporary mathematics 383 (8) (2005) 141–173. 54

[42] S. Federico, T. C. Gasser, Nonlinear elasticity of biological tissues with statistical fibre orientation, Journal of the Royal Society Interface 7 (47) (2010) 955–966. 55

[43] C. de Boor, Good approximation by splines with variable knots. ii, in: G. A. Watson (Ed.), Conference on the Numerical Solution of Differential Equations, Springer Berlin Heidelberg, Berlin, Heidelberg, 1974, pp. 12–20. 55

[44] T. Dubois, Y. Matras, F. Jauberteau, R. Temam, Dynamic multilevel methods and the numerical simulation of turbulence, Cambridge University Press, 1999. 57

[45] R. Codina, J. Principe, Dynamic subscales in the finite element approximation of thermally coupled incompressible flows, International Journal for Numerical Methods in Fluids 54 (6-8) (2007) 707–730. arXiv:https://onlinelibrary.wiley.com/doi/pdf/10.1002/fld.1481, doi:https://doi.org/10.1002/fld.1481.
URL https://onlinelibrary.wiley.com/doi/abs/10.1002/fld.1481 57

[46] E. Hachem, M. Khalloufi, J. Bruchon, R. Valette, Y. Mesri, Unified adaptive variational multiscale method for two phase compressible–incompressible flows, Computer Methods in Applied Mechanics and Engineering 308 (2016) 238–255. doi:https://doi.org/10.1016/j.cma.2016.05.022.
URL https://www.sciencedirect.com/science/article/pii/S0045782516304236 58

[47] R. Codina, Stabilized finite element approximation of transient incompressible flows using orthogonal subscales, Computer Methods in Applied Mechanics and Engineering 191 (39) (2002) 4295–4321. doi:https://doi.org/10.1016/S0045-7825(02)00337-7.
URL https://www.sciencedirect.com/science/article/pii/S0045782502003377 58

[48] J. Simo, R. L. Taylor, K. Pister, Variational and projection methods for the volume constraint in finite deformation elasto-plasticity, Computer methods in applied mechanics and engineering 51 (1-3) (1985) 177–208. 52, 54

Bibliography

[49] T. Coupez, E. Hachem, Solution of high-reynolds incompressible flow with stabilized finite element and adaptive anisotropic meshing, Computer Methods in Applied Mechanics and Engineering 267 (2013) 65–85. doi:https://doi.org/10.1016/j.cma.2013.08.004.
URL https://www.sciencedirect.com/science/article/pii/S0045782513002077 58

[50] S. Balay, W. D. Gropp, L. C. McInnes, B. F. Smith, Efficient management of parallelism in object oriented numerical software libraries, in: E. Arge, A. M. Bruaset, H. P. Langtangen (Eds.), Modern Software Tools in Scientific Computing, Birkhäuser Press, 1997, pp. 163–202. 58

[51] R. D. Cook, Improved two-dimensional finite element, Journal of the Structural Division 100 (Proc. Paper 10808) (1974). 60

[52] S. Turek, J. Hron, Proposal for numerical benchmarking of fluid-structure interaction between an elastic object and laminar incompressible flow, in: H.-J. Bungartz, M. Schäfer (Eds.), Fluid-Structure Interaction, Springer Berlin Heidelberg, Berlin, Heidelberg, 2006, pp. 371–385. vi, xi, 64, 68, 69, 70

[53] Helical gear, https://grabcad.com/library/helical-gear-183, accessed: 14-11-2020. vi, 74

Chapter 4

Adaptive Immersed Mesh Method (AIMM) for Fluid–Structure Interaction

Contents

La nécessité de simuler des structures flexibles et relativement minces suscite un intérêt croissant avec des applications allant des capteurs cylindriques minces aux structures de type membrane. Ces structures interagissent généralement avec leur environnement pour accumuler des données ou dans un but précis. L'inévitable interaction entre le fluide environnant et le solide est résolue à l'aide d'un nouveau schéma de couplage Interaction Fluide–Structure (IFS). Ce chapitre propose une nouvelle façon de modéliser l'interaction entre fluide et solide. Il s'agit d'une méthode hybride qui combine à la fois les approches traditionnelles monolithiques et partitionnées pour l'Interaction Fluide-Structure (IFS). Le maillage solide est immergé dans un maillage fluide-solide à chaque itération, tout en ayant son propre solveur hyperélastique lagrangien indépendant. Le maillage eulérien contient à la fois du fluide et du solide, et s'adapte à des phénomènes physiques supplémentaires. L'adaptation de maillage anisotrope et les méthodes Level-Set sont utilisées pour le couplage d'interface entre le solide et le fluide afin de mieux capturer l'interaction entre eux. Tous les composants ci-dessus forment la méthode de maillage immergé adaptatif (AIMM). La méthode VMS (Variationnelles Multi-Echelle) est utilisée pour les deux solveurs afin d'amortir les oscillations parasites pouvant survenir pour les éléments tétraédriques linéaires par morceaux. Le cadre est construit en 3D avec le calcul parallèle à l'esprit. Divers problèmes numériques 2D sont étudiés pour évaluer la précision, la robustesse et les capacités de notre méthode. Différents cas de test tridimensionnels sont présentés et sont également comparés à des résultats expérimentaux.

The need to simulate flexible, relatively thin structures is of growing interest with applications ranging from thin cylindrical sensors to membrane-like structures. These structures usually interact with their surroundings to accumulate data, or for a specific purpose. The inevitable interaction between the surrounding fluid and the solid is solved using a novel Fluid–Structure Interaction (FSI) coupling scheme. This chapter proposes a novel way to model the interaction between fluid and solid. It consists of a hybrid method that combines both the traditional monolithic and partitioned approaches for Fluid–Structure Interaction (FSI). The solid mesh is immersed in a fluid-solid mesh at each time iteration, whilst having its own independent Lagrangian hyperelastic solver. The Eulerian mesh contains both fluid and solid, and accommodates additional physical phenomena. Anisotropic mesh adaptation and the Level-Set methods are used for the interface coupling between the solid and fluid to better capture the interaction between them. All of the above components form the Adaptive Immersed Mesh Method (AIMM). The Variational Multi-Scale (VMS) method is used for both solvers to damp out any spurious oscillations that may arise for piece-wise linear tetrahedral elements. The framework is constructed in 3D with parallel computing in mind. Various 2D numerical problems are investigated to evaluate the accuracy, robustness, and capabilities of our method. Different three-dimensional test cases are presented and are compared to experimental results as well.

4.1   Introduction

Fluid–Structure Interaction has been getting a lot of attention lately, due to the increase in computational power, advancements in the field, and the need to solve real-life problems using numerical simulations. It consists of an interaction between entities; the fluid and the solid. FSI applications can be found in various engineering applications [1], such as: technology [2], automotive [3], aerodynamics [4], and biomechanics [5]. FSI problems are rather complex, and experimental studies of such phenomena proved to be often time-consuming [6][7]. Whilst surrounded by the fluid, the structures exhibit distortion crucial to its performance. This is due to the interaction between both bodies.

Different formulations are used in FSI, such as Eulerian, Lagrangian, Arbitrary Lagrangian-Eulerian, and Eulerian-Lagrangian[8]. As well as the Fictitious Domain method [9].

Eulerian formulations, also known as the monolithic approach for FSI, examine the evolution of a quantity of material through a specified region in space. Both

86

the fluid and the solid are considered as one, on a single grid, where the reference system is fixed. Thus, a single set of constitutive equations describing both fluid and solid is solved. Interface tracking is generally used with this approach, by using, for example, the level set method. The embedded boundary method [10], can handle large structural deformations and meshing of the domain. It does, however, exhibit shortcomings when coupling fluid-structure stresses. This is circumvented by treating both the fluid pressure and velocity conditions together [11]. Among other fixed mesh methods, is the immersed boundary method [12], and the fictitious domain method [9], which handle the coupling by imposing constraints across the structure using an augmented Lagrange multiplier. Irregularities may arise in the transient regime, due to the uncoupled physics in the different sub-domains. This method's main limitation consists of having a single physical model for the solid and not being able to include other behavior laws.

Lagrangian formulations examine the particle's dynamics as a quantity moving in space with respect to a known reference frame. The reference frame follows the particle. Thus, the advective term does not appear in the equations. Also, the nodes at the interface will always be at the interface, and hence the tracking process is simplified. However, for large deformations, the mesh quality is reduced and may lead to polluted solutions. This problem can be circumvented using mesh adaptation. This formulation is mainly adopted in Computational Solid Mechanics (CSM) [13].

The Arbitrary Lagrangian-Eulerian (ALE) formulations were first developed to handle FSI and free surface problems [14][15][16]. For large element distortion, the ALE formulation often requires remeshing to avoid element stretching. One can also use the fixed mesh ALE formulation [17][18][19]. At each time step, the results from the deformed fluid mesh are coupled to a fixed Eulerian mesh. The coupling is done using the extended finite element method (XFEM), and Lagrange multipliers.

The Eulerian-Lagrangian formulation is as its name implies. The fluid is treated in an Eulerian fashion, which is the natural choice for fluid flow. The solid is treated in a Lagrangian fashion, where the structure's behavior is tracked in time. On the contrary, in fluid mechanics, the interest lies in the effect of the flow over a certain region in space. The main difference with ALE is that the fluid mesh is not affected by the movement of the FSI interface. The FSI interface is tracked by using the level set method. The coupling is achieved through Lagrangian multipliers, and penalty methods [20]. This method was used for immersed structures in Fluid [21][22]. The XFEM was used to consider the discontinuities that arise from the structure present in the fluid.

Plate vibration, flapping, stability, flutter, and natural frequency are investigated when subject to axial flow [23–27]. It was deduced that the flapping amplitude is directly related to the elastic modulus and density ratio. Also, the frequency is

dependent on the density ratio, and the ratio of length to thickness of the beam. An increase in the Reynolds number results in a transition from symmetric to asymmetric flapping. Resonance of the plate is strongly influenced by the forcing amplitude, while rigidity, and flow velocity play a less important role [28].

A laminar boundary layer flow over a vertically mounted flat plate is also an application for FSI. The dynamic behavior of the plate is represented by the Reynolds number, the ratio between structure density and fluid density. In [29], a 2D numerical study showcases the dynamics of a plate for Reynolds number varying between 100 and 800, using the Immersed Boundary Method (IBM) [12]. For Reynolds number below 800, the plate reaches a steady-state solution, while for Reynolds number equal to 800, the plate starts vibrating. When it comes to rigidity, the plate first exhibits periodic vibrations, then transitions to chaotic movements, and back to periodic vibrations with increasing rigidity. Different responses were observed for the flapping flag problem [30].

In [31], an immersed boundary flow solver, and a nonlinear finite element solver have been coupled to tackle FSI in presence of large deformations. Different numerical simulations are studied, some of which are three-dimensional. In particular, the results of a flexible plate problem, such as the free end deflections and drag calculations, are presented for different Reynolds numbers in the interval 1000-1600. Both the effect of gravity, and buoyancy are considered in the aforementioned test case. They start by comparing their results with that of an experimental study [32], before introducing new benchmark cases. They extended their model to study the behavior of aquatic plants. They claim overall stability for all their cases.

The solid dynamics response can induce variations in the fluid flow. Therefore its effects on multi-phase flow are preferred to be tackled for industrial applications. In [33], the tip displacement of a rubber beam in a multi-phase flow of oil and air is tackled. A two-way coupling FSI method is used. They compare their results with that of [34], and they also explain the differences encountered in the 2D and 3D simulations.

In [35], the deflection line of single or tandem beams configurations is studied. Both experimental, and Direct Numerical Simulation (DNS) are conducted for Reynolds varying from 1 to 60. For the numerical simulations part, the bending is calculated based on the beam bending theory via the calculated fluid forces from the simulations. Experimental and numerical results are in good agreement. In [36], a two-way coupled FSI method has been utilized to simulate several rows of flexible flaps. The behavior of the tip of the flaps, alongside vortex development in between the flaps are studied. The numerical results are compared with experimental results, conducted in glycerin and water reaching Reynolds number of 120. Silicon rubber flaps are used in the experimental setup. Good agreement is found between the experimental and numerical results.

The Arbitrary Lagrangian-Eulerian (ALE) method [37], and the Eulerian method [38, 39] have been used to study the time-dependent, directional strain of flexible structures. The work done in [37] showcases some interesting problems in 2D, while the works in [38, 39] present interesting test cases of free surface flows, and elastic structures. The Immersed Structural Potential Method (ISPM), which is based on the IBM method was presented in [40]. It was used to tackle problems of hemo-dynamics. The proposed method consists of calculating the FSI force on a fluid mesh, and the behavior of cardiovascular tissues, modeled using a fiber-reinforced viscoelastic constitutive model. A novel time integration method was also used for the calculation of the deformation gradient tensor. Different numerical examples were presented. The Fluid-Solid Interface Tracking/Interface Capturing (FSITICT) method is used on FSI problems along with ALE, and Eulerian interface tracking to study moving boundaries [41]. The objective of this method was to be able to study cardiac cycles.

This chapter proposes a novel coupling method for solving Fluid-Structure Interaction, referred to as the Adaptive Immersed Mesh Method (AIMM). This is a hybrid method, that combines the advantages of having two separate solvers for both the fluid and solid while having the solid co-exist in an Eulerian fluid-solid mesh. The solid is immersed in the fluid-solid mesh through the level set method; this helps track the FSI interface in time. Full stress and velocity boundary conditions are enforced at the FSI interface. The FSI interface on the Lagrangian grid is naturally tracked. A mesh adaptation technique is then applied, that creates anisotropic stretched elements to better capture the boundary layer, and to have a higher precision at the fluid-solid interface. Both solvers are stabilized using the Variational Multi-Scale (VMS) method for P1/P1 finite elements. The fluid is solved naturally on an Eulerian grid, where the advective term is taken into account, while the solid is modeled as an elastic structure having its independent Lagrangian grid.

The chapter is structured as follows: Section 2 contains the coupling method AIMM; Section 3 contains the stabilized solid solver formulation; Section 4 presents the stabilized fluid solver, along with the mesh adaptation technique; Section 5 provides numerical examples and new benchmarks. Finally, perspective and conclusions are given in section 6.

4.2 Coupling

Two famous approaches for handling FSI exist in the literature, which are the monolithic and partitioned approaches. Figure 4.1 explains the types of coupling visually. The monolithic approach consists of solving on a single mesh the same system of equations that describe both the fluid and the solid. The coupling mechanism in a monolithic approach is considered strong. While the partitioned approach con-

sists of solving on separate fluid and solid meshes the respective system of equations that describe the fluid and solid separately. In the partitioned approach, two types of coupling exist. Either the coupling is considered as a two-way strong coupling or a one-way weak coupling.
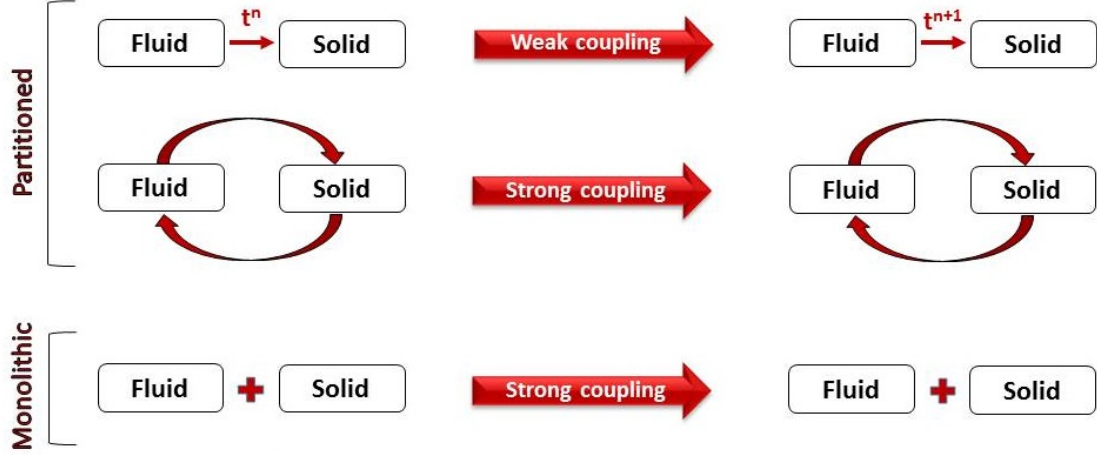

Figure 4.1: Different approaches for FSI.

The Adaptive Immersed Mesh Method (AIMM) consists of a hybrid method, that combines the advantages of each approach while disregarding the disadvantages to the best of our capabilities. Thus, we retain the flexibility of having two separate solvers for the fluid and the solid, while insuring robust, stable, and strong coupling as in the monolithic approach. It consists of immersing the solid mesh at each time step in a fluid-solid mesh where both the fluid and solid co-exist. Then, the signed distance function (level set), is computed for the given solid mesh. This helps us track the FSI interface for the fluid-solid mesh. The FSI interface is naturally tracked in the solid mesh by using the Moving Mesh Method (MMM). Full stress and velocity are communicated at the interface between the two solvers through interpolations of the field between the different meshes. A mesh refinement technique is considered, which refines the mesh in an anisotropic fashion at the FSI interface, by calculating the gradient of the level set. This enables us to have a higher precision for the coupling method. Figure 4.2 explains the hybrid AIMM method.

Figure 4.2: Different approaches for FSI.

The steps that are followed by the algorithm are shown in figure 4.3. They are as follows:

1. The solid mesh is immersed onto the fluid-solid mesh using the level set method detailed in sub-section 4.2.1.

2. Anisotropic mesh adaptation is applied at the interface detailed in sub-section 4.2.3.

3. The Navier–Stokes equations are solved with the velocity boundary condition on the FSI interface on the fluid-solid mesh detailed in section 4.4.

4. The fluid stress is computed and then interpolated onto the solid mesh.

5. The solid dynamics are solved on the solid mesh with Neumann traction boundary conditions applied at the FSI interface detailed in section 4.3.

6. The velocity of the solid is computed and interpolated on the fluid-solid mesh.

These steps are repeated until we reach the final time t of the simulation. Figure 4.4, explains the whole process visually.
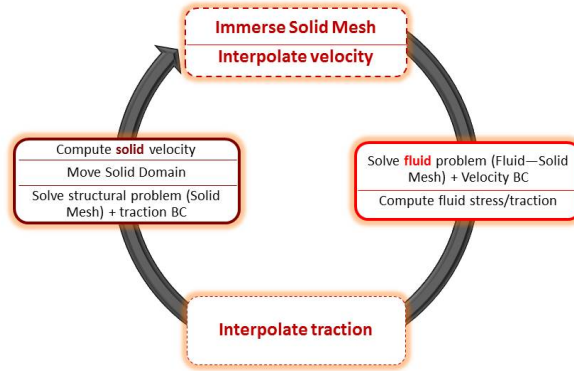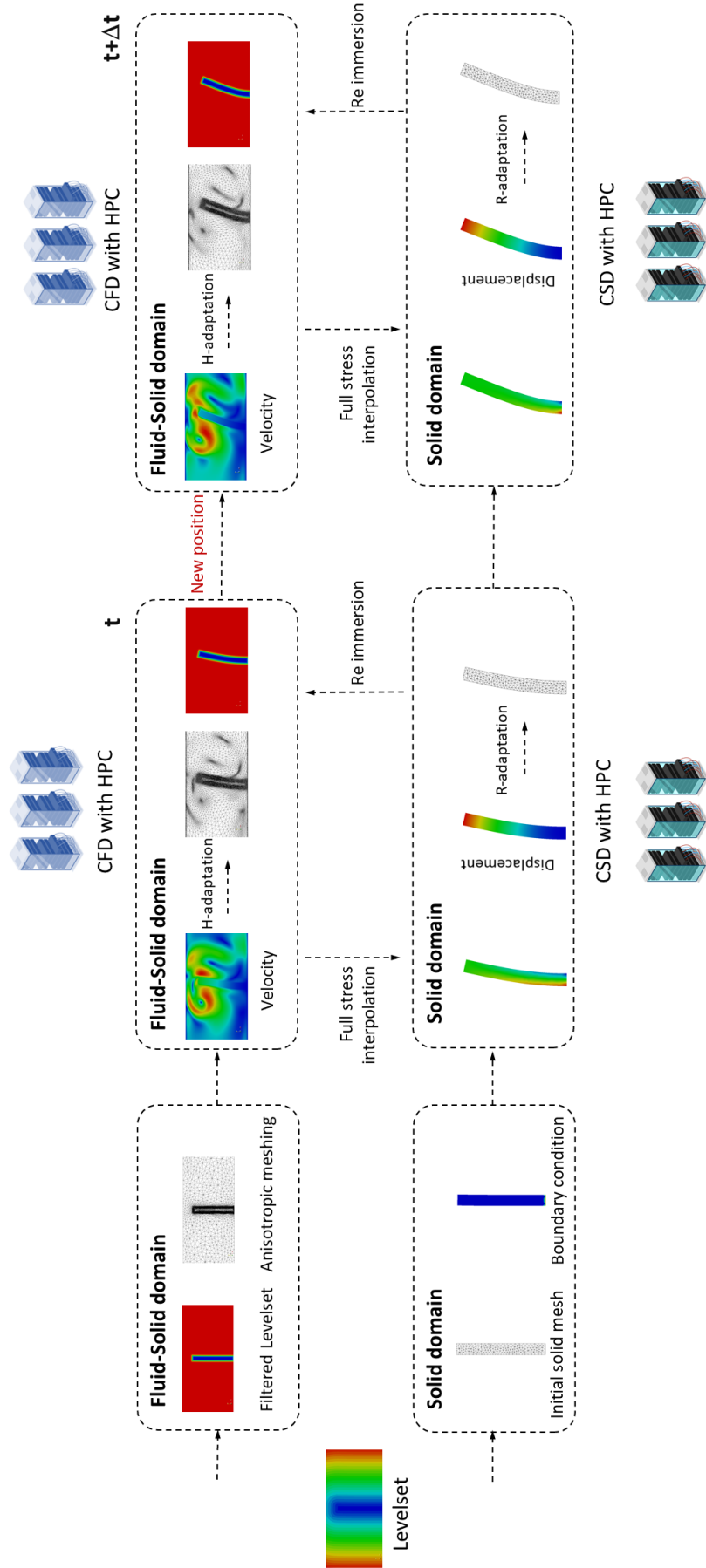

Figure 4.3: Two-way coupling loop.

Figure 4.4: AIMM coupling loop.

4.2.1 Level set approach

We make use of the signed distance function of the FSI interface Γ_{FSI} to delimit the contact surface between the fluid, and the solid. The level set function α_{FSI}, is the signed distance from Γ_{FSI} to any point $\mathbf{x}$ of the fluid-solid mesh. Consequently, the interface Γ_{FSI} is defined by the iso-zero of the level set function

$$\begin{cases} \alpha_{FSI}(\boldsymbol{x}) = \pm d(\boldsymbol{x}, \Gamma_{FSI}), \ \boldsymbol{x} \in \Omega \\ \Gamma_{FSI} = \{\boldsymbol{x}, \alpha_{FSI}(\boldsymbol{x}) = 0\} \end{cases} \tag{4.1}$$

The reader is invited to read [42] for more details on the algorithm used. One can also use smoother function, other than $d(\boldsymbol{x}, \Gamma_{FSI})$ away from Γ_{FSI} [43].
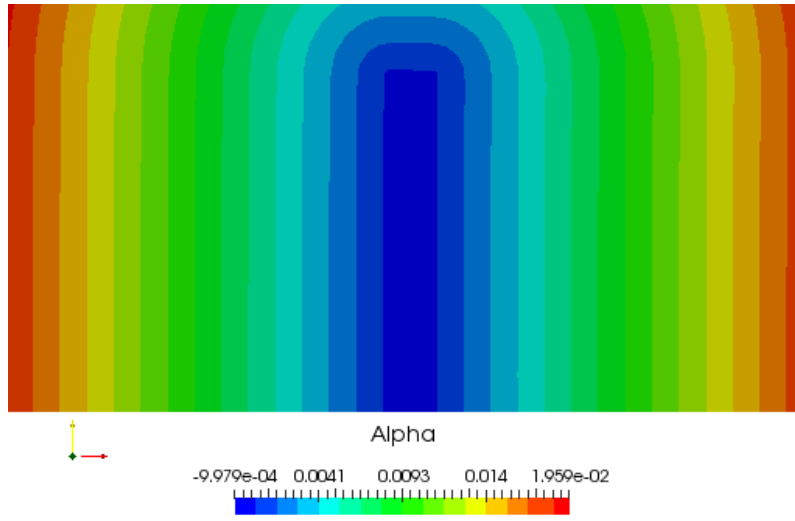

Figure 4.5: The signed distance function α example of an immersed circle.

4.2.2 Physical continuity

On Γ_{FSI}, we have to ensure a two-way coupling scheme between the fluid and the solid. This is done partly by imposing on the interface velocity and stress continuity

$$\boldsymbol{v}_s = \boldsymbol{v}_f \text{ on } \Gamma_{FSI}, \tag{4.2}$$

$$\boldsymbol{\sigma}_s \boldsymbol{n} = \boldsymbol{\sigma}_f \boldsymbol{n} \text{ on } \Gamma_{FSI}. \tag{4.3}$$

4.2.3 Edge-based mesh adaptation

Anisotropic mesh adaptation of unstructured mesh, take part in the AIMM for FSI. It aids in achieving high accuracy, while significantly reducing the computation time

of the problem[44, 45]. In the works of [46, 47], it was shown that anisotropic mesh adaptation overmatch adaptive octree. Anisotropic meshes enable us to capture smaller features than octree. It also allows us to reduce the number of integration points by an order of magnitude [47]. The main idea lies in the concentration of elements in a specific region of interest. This region usually exhibits high variations in either variable or their gradient. In our case, an accurate depiction of the interface between the fluid and the solid is needed, where we might exhibit sudden variations in variables. Thus, reducing the error, while maintaining a certain number of degrees of freedom. A monitor function consisting of either a vector or a scalar is employed to control the shape, size, and orientation of the mesh elements. This function gives an estimate of a measure of the solution error. This error is then equidistributed over each mesh element. This mesh adaptation algorithm is built to generate a mesh and a numerical solution. At each time step, a numerical solution is computed on the mesh. We then evaluate an estimation of the interpolation error. Finally, a minimization problem that reduces the interpolation error in the L_1-norm is set up independently of the current problem [48]. To monitor the development of the solution, an optimal metric is derived that minimizes the interpolation error. A new mesh is thus generated that is compatible with the metric field. The advantage of this approach consists of computing a metric and its associated edge-based error in a simple manner.

4.2.3.1 Edge-based error estimation

Let u_h be a first-order finite element approximation, acquired through the Lagrange interpolation operator of a regular function $u \in C^2(\Omega)$. At each vertex i of the mesh, we have $U_i = u(x^i) = u_h(x^i)$ (where x^i are the coordinates of the vertex i). Let $\Gamma(i)$ be the "patch" associated to a vertex x_i of the mesh defined as the set of nodes which share one edge with x_i, and let us denote by x_{ij} the edge connecting x_i to x_j as in Figure 4.6.
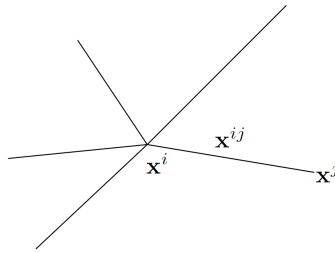

Figure 4.6: Patch associated with node x^i

The continuity of the gradient $\nabla u^h \cdot x^{ij}$ on the edge x_{ij} enables us to write

$$U^j = U^i + \nabla u^h \cdot x^{ij}, \tag{4.4}$$

This leads to

$$\nabla u_h \cdot x^{ij} = U^j - U^i. \tag{4.5}$$

Following the works from [48], we can write the following error estimator

$$\| \nabla u^h \cdot x^{ij} - \nabla u(x^i) \cdot x^{ij} \| \leq \max_{y \in |x^i, x^j|} | x^{ij} \cdot H_u(y) \cdot x^{ij} |, \tag{4.6}$$

with H_u being the Hessian of u. At the node x^i, we seek the recovered gradient g^i of u_h

$$\nabla g_h \cdot x^{ij} = g^j - g^i. \tag{4.7}$$

We are interested in the projection of the Hessian based on the gradient at the edge extremities, thus

$$(\nabla g_h \cdot x^{ij}) \cdot x^{ij} = (g^j - g^i) \cdot x^{ij}, \tag{4.8}$$

$$(H_u \cdot x^{ij}) \cdot x^{ij} = g^{ij} \cdot x^{ij}, \tag{4.9}$$

with $g^{ij} = g^j - g^i$. It can be shown in [48] that the quantity $| g^{ij} \cdot x^{ij} |$ gives a second order accurate approximation of the second derivative of u along the edge x^{ij}. Motivated by the fact that, for first-order finite elements on anisotropic meshes, edge residuals dominate a posteriori errors[49], it is, therefore, suitable to define an error indicator function associated to the edge x^{ij} as

$$e^{ij} = | g^{ij} \cdot x^{ij} | . \tag{4.10}$$

And this error is the exact interpolation error along the edge and allows us to evaluate the global L_1 error. However, the gradient is not known at the vertices, thus a recovery procedure must be considered.

4.2.3.2 Gradient recovery procedure

The gradient recovery procedure relies on the following optimization problem

$$G^i = arg \min_G \left(\sum_{j \in \Gamma(i)} | (G - \nabla u_h) \cdot x^{ij} |^2 \right) , \tag{4.11}$$

where G^i is the recovered gradient. Denoting by $\otimes$ the tensor product between two vectors, let us introduce X^i the length distribution tensor at node i

$$X^i = \frac{1}{| \Gamma(i) |} \left(\sum_{j \in \Gamma(i)} x^{ij} \otimes x^{ij} \right) , \tag{4.12}$$

this gives us an average representation of the distribution of edges in the patch. Let us express the recovered gradient G^i in terms of the length distribution tensor

$$G^i = (X^i)^{-1} \sum_{j \in \Gamma(i)} U^{ij} x^{ij} . \tag{4.13}$$

Therefore, the estimated error e_{ij} is thus written as

$$e_{ij} = G^{ij} . x^{ij} . \tag{4.14}$$

4.2.3.3 Metric construction

A stretching factor s^{ij} defined as the ratio between the length of the edges x^{ij} before and after the adaptation procedure is introduced to correlate the error indicator defined in (4.14) to the associated metric [48]. We end up with the following expression for the metric

$$\widetilde{M^i} = (\widetilde{X}^i)^{-1}, \tag{4.15}$$

where $\widetilde{X}^i$ is defined as

$$\widetilde{X}^i = \frac{1}{| \Gamma(i) |} \left(\sum_{j \in \Gamma(i)} s^{ij} \otimes s^{ij} \right) . \tag{4.16}$$

The stretching factor s^{ij} of the edge ij is chosen so that the total number of nodes in the mesh is kept fixed and is defined as

$$s^{ij} = \left(\frac{e_{ij}}{e(N)} \right), \tag{4.17}$$

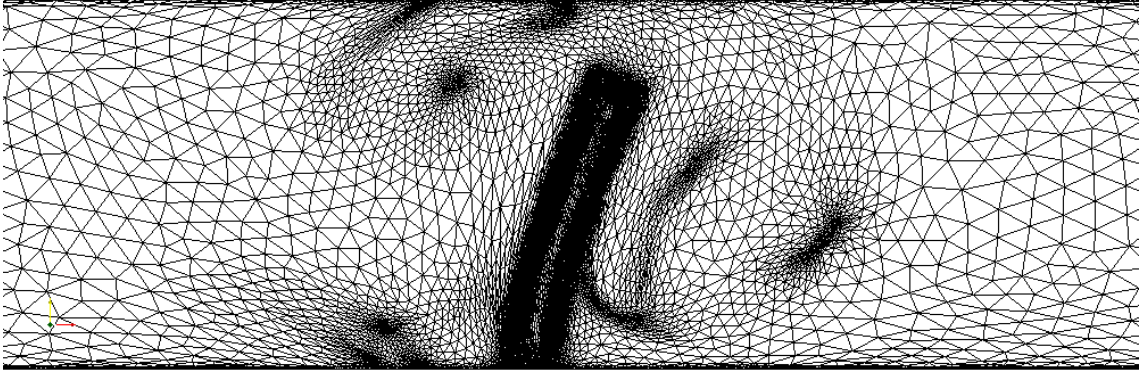where $e(N)$ the total error. An example of the mesh adaptation is shown in figure 4.7.

Figure 4.7: An example of the mesh adaptation on multiple criteria.

4.3   Solid solver

4.3.1   Solid Dynamics

The equations of Lagrangian Solid Dynamics, model the displacement and variation rate of the density of a structure. Ω_s and Ω_{s_0} are the current and initial domains. They are two open sets in $\mathbb{R}^d$ with Lipshitz boundaries. d denotes the spatial dimension. Γ_s is the domain boundary, that is defined using the following equations: $\Gamma_s = \overline{\partial\Omega_{su} \cup \partial\Omega_{st}}$ and $\partial\Omega_{su} \cap \partial\Omega_{st} = \emptyset$. Where $\partial\Omega_{su}$ is the Dirichlet boundary that define the displacement, and $\partial\Omega_{st}$ is the Neumann boundary that designates the traction.

The dynamics of a solid structure are given by the following invertible, and smooth mapping:

$$\boldsymbol{\phi} := \Omega_{s_0} \rightarrow \Omega_s = \boldsymbol{\phi}(\Omega_{s_0}), \tag{4.18}$$

$$\boldsymbol{\phi} := \Gamma_{s_0} \rightarrow \Gamma_s = \boldsymbol{\phi}(\Gamma_{s_0}), \tag{4.19}$$

$$\mathbf{X} \to \mathbf{x} = \boldsymbol{\phi}(\mathbf{X}, t) \ \forall \mathbf{X} \in \Omega_{s_0}. \tag{4.20}$$

Here we distinguish between the two coordinates $\mathbf{X}$, and $\mathbf{x}$. The material coordinates in the total Lagrangian framework, and the coordinate in the updated Lagrangian framework respectively. The relationship to the displacement of the a solid particle by $\mathbf{u} = \mathbf{x} - \mathbf{X}$. The Jacobian determinant and the deformation gradient are defined as: $\mathbf{F} = \nabla_{\mathbf{X}} \boldsymbol{\phi}$ and $J = \det\mathbf{F}$.

The governing equations are given by:

$$\rho_s \ddot{\boldsymbol{u}} - \nabla_{\mathbf{x}} \cdot \boldsymbol{\sigma} = \boldsymbol{f} \text{ in } \Omega_s, \tag{4.21}$$

$$\rho_s J = \rho_{s_0} \text{ on } \partial\Omega_{s_u}. \tag{4.22}$$

Where ρ_s is the density, $\boldsymbol{f}$ is the source term, and $\boldsymbol{\sigma}$ is the symmetric Cauchy stress tensor. Moreover, $\ddot{\boldsymbol{u}}$ represents the material second derivative of displacement. We consider isotropic, compressible, and incompressible material. Thus, we split the stress into its deviatoric and volumetric parts.

$$\boldsymbol{\sigma} = p_s \mathbf{I} + dev[\boldsymbol{\sigma}]. \tag{4.23}$$

4.3.2 HyperElastic model

Consider a material with a Helmholtz free energy $\Psi(\mathbf{C})$ function, where $\mathbf{C}$ is the right Cauchy-Green strain tensor given by $\mathbf{C} = \mathbf{F}^T\mathbf{F}$. The second Piola–Kirchhoff stress tensor given by $\mathbf{S} = J\mathbf{F}^{-1}\boldsymbol{\sigma}\mathbf{F}^{-T}$ is also obtained by deriving the Helmholtz free energy functional $\boldsymbol{\Psi}(\mathbf{C})$ with respect to $\mathbf{C}$:

$$\mathbf{S} = 2\partial_{\mathbf{C}}\Psi(\mathbf{C}). \tag{4.24}$$

Decomposing $\Psi(\mathbf{C})$ into its volumetric and deviatoric part respectively as previously done for the stress leads to:

$$\Psi(\mathbf{C}) = U(J) + W(\bar{\mathbf{C}}). \tag{4.25}$$

Where $J = \sqrt{det\mathbf{C}}$, and $\bar{\mathbf{C}} = J^{-\frac{2}{3}}\mathbf{C}$ is the volumetric/deviatoric part of $\mathbf{C}$.
Consider a Neo-Hookean, and a Simo–Taylor volumetric model:

$$U(J) = \frac{1}{4}\kappa(J^2 - 1) - \frac{1}{2}\kappa \ln J, \tag{4.26}$$

$$W(\bar{\mathbf{C}}) = \frac{1}{2}\mu_s(\mathrm{tr}\bar{\mathbf{C}} - 3) = \frac{1}{2}\mu_s(\bar{\mathbf{I}}_1 - 3). \tag{4.27}$$

where κ and μ_s are material properties, and $\mathbf{I}_1 = \mathrm{tr}\bar{\mathbf{C}}$. The stress can also be split to its deviatoric and volumetric part:

$$p_s = 2J^{-1}\mathbf{F}\frac{\partial U(J)}{\partial \mathbf{C}}\mathbf{F}^T = U'(J) = \frac{1}{2}\kappa(J + J^{-1}), \tag{4.28}$$

$$\mathbf{dev}[\boldsymbol{\sigma}] = 2J^{-1}\mathbf{F}\frac{\partial W(\bar{\mathbf{C}})}{\partial \mathbf{C}}\mathbf{F}^T = \mu_s J^{-\frac{5}{3}}\mathbf{dev}[\mathbf{FF}^T]. \tag{4.29}$$

We can also write:

$$\mathbf{FF^T} = \nabla_{\mathbf{X}}\boldsymbol{u} + \nabla_{\mathbf{X}}^T\boldsymbol{u} + \nabla_{\mathbf{X}}\boldsymbol{u}\nabla_{\mathbf{X}}^T\boldsymbol{u} + \mathbf{I}. \tag{4.30}$$

A linearization of the above equation is considered, by starting with:

$$\nabla_{\mathbf{X}}\boldsymbol{u} = (\mathbf{I} - \nabla_{\mathbf{x}}\boldsymbol{u})^{-1} - \mathbf{I}. \tag{4.31}$$

Assuming a small variation in displacement denoted by $\delta\boldsymbol{u}$, and recalling that for very small displacement, $(\mathbf{I} - \nabla\boldsymbol{u})^{-1} = \mathbf{I} + \nabla\boldsymbol{u}$, we end up with the following, as explained in [50]

$$
\begin{aligned}
\mathbf{FF^T} =& (\mathbf{I} - \nabla_{\mathbf{x}}\boldsymbol{u})^{-1} - \mathbf{I} + ((\mathbf{I} - \nabla_{\mathbf{x}}\boldsymbol{u})^{-1} - \mathbf{I})^T \\
& + ((\mathbf{I} - \nabla_{\mathbf{x}}\boldsymbol{u})^{-1} - \mathbf{I})((\mathbf{I} - \nabla_{\mathbf{x}}\boldsymbol{u})^{-1} - \mathbf{I})^T \\
& + \mathbf{I} + 2\epsilon(\delta\boldsymbol{u}) + \nabla_{\mathbf{x}}\delta\boldsymbol{u}(\nabla_{\mathbf{x}}\delta\boldsymbol{u})^T + \nabla_{\mathbf{x}}\delta\boldsymbol{u}(\nabla_{\mathbf{x}}\boldsymbol{u})^T + (\nabla_{\mathbf{x}}\boldsymbol{u})(\nabla_{\mathbf{x}}\delta\boldsymbol{u})^T.
\end{aligned}
\tag{4.32}
$$

The final system of equations to be solved now is given by:

$$\rho_s\ddot{\boldsymbol{u}} - \nabla_{\mathbf{x}}p_s - \nabla_{\mathbf{x}} \cdot \ dev[\boldsymbol{\sigma}] = \boldsymbol{f} \text{ in } \Omega_s, \tag{4.33}$$

$$\nabla_{\mathbf{x}} \cdot \boldsymbol{u} - \frac{1}{\kappa}p_s = g \text{ in } \Omega_s, \tag{4.34}$$

$$\boldsymbol{u} = \mathbf{l} \text{ on } \partial\Omega_{s_u}, \tag{4.35}$$

$$\boldsymbol{\sigma}\boldsymbol{n} = \boldsymbol{t} \text{ on } \partial\Omega_{s_t}, \tag{4.36}$$

$$\rho_s J = \rho_{s_0}. \tag{4.37}$$

The weak discrete form of the above equation in Galerkin finite elements is given by:

$$(\rho_s\frac{\partial^2\boldsymbol{u}_h}{\partial t^2}, \boldsymbol{w}_h) + a'(\boldsymbol{u}_h, \boldsymbol{w}_h) + (p_{s_h}, \nabla_{\mathbf{x}}.\boldsymbol{w}_h) = L(\boldsymbol{w}_h) \ \forall \ \boldsymbol{w}_h \in W_{h,0}, \tag{4.38}$$

$$(\nabla_{\mathbf{x}} \cdot \boldsymbol{u}_h, q_h) - (\frac{1}{\kappa} p_{s_h}, q_h) = (g, q_h) \,\forall\, q_h \in Q_h, \tag{4.39}$$

where a' is given by:

$$a'(\boldsymbol{u}_h, \boldsymbol{w}_h) = \int_{\Omega_s} \mu_s \, dev[\boldsymbol{\sigma}] : \nabla_{\mathbf{x}}^s \boldsymbol{w}. \tag{4.40}$$

4.3.3   Variational Multi Scale stabilization

The inf-sup stability or Babuska–Brezzi[51] condition coerces the interpolation relationship between the variables. This leads to different interpolation order for $\boldsymbol{u}$ and p_s. Same order interpolation exhibits weak numerical performance since it does not respect the in-sup condition. Different types of stabilization exist, that help alleviate this problem. P1/P1 elements are used in our case for the displacement and pressure variables, with a Variational Multi-Scale Method (VMS) stabilization. This allows us to have the same order of interpolation for both variables. In [52], equal order elements for velocity and pressure were utilized to solve the Stokes equations. The author also proved the convergence and stability of this method. This work inspired the extension of the VMS method to solve the Navier–Stokes equations [53]. The linear elastic equations were also tackled in [54, 55] using VMS. It provides a natural stabilization using an orthogonal decomposition of the solution spaces. The function spaces are first decomposed into their coarse and fine-scale components, which yields:

$$W_0 = W_{h,0} + W_0', \tag{4.41}$$

$$W = W_h + W', \tag{4.42}$$

$$Q = Q_h + Q'. \tag{4.43}$$

Following [56], the displacement and pressure are decomposed:

$$\boldsymbol{u} = \boldsymbol{u}_h + \boldsymbol{u}', \tag{4.44}$$

$$p_s = p_{s_h} + p_s'. \tag{4.45}$$

The same decomposition is also applied for the test functions:

$$\boldsymbol{w} = \boldsymbol{w}_h + \boldsymbol{w}', \tag{4.46}$$

$$q = q_h + q'. \tag{4.47}$$

The transient mixed finite element approximation of equations (38)(39)(40):
Coarse-scale

$$(\rho_s \frac{\partial^2(\boldsymbol{u} + \boldsymbol{u}')}{\partial t^2}, \boldsymbol{w}_h) + a'((\boldsymbol{u}_h + \boldsymbol{u}'), \boldsymbol{w}_h) + (p_{s_h} + p_s', \nabla_{\mathbf{x}} \cdot \boldsymbol{w}_h) = L(\boldsymbol{w}_h) \forall \boldsymbol{w}_h \in W_{h,0} \subset [H_0^1]^d, \tag{4.48}$$

$$(\nabla_{\mathbf{x}} \cdot (\boldsymbol{u}_h + \boldsymbol{u}'), q_h) - (\frac{1}{\kappa}(p_{s_h} + p'_s), q_h) = (g, q_h) \ \forall \ q_h \in Q_h \subset L^2_{\int=0}, \tag{4.49}$$

Fine-scale

$$(\rho_s \frac{\partial^2(\boldsymbol{u} + \boldsymbol{u}')}{\partial t^2}, \boldsymbol{w}') + a'((\boldsymbol{u}_h + \boldsymbol{u}'), \boldsymbol{w}') + (p_{s_h} + p'_s, \nabla_{\mathbf{x}}.\boldsymbol{w}') = L(\boldsymbol{w}') \forall \boldsymbol{w}' \in W', \tag{4.50}$$

$$(\nabla_{\mathbf{x}} \cdot (\boldsymbol{u}_h + \boldsymbol{u}'), q') - (\frac{1}{\kappa}(p_{s_h} + p'_s), q') = (g, q') \ \forall \ q' \in Q'. \tag{4.51}$$

The fine-scale problem is first solved, which is written in function of the time-dependent coarse-scale problem. The fine scales are then re-injected into the coarse-scale equations, thus modeling them implicitly. Sub-scales are not tracked in time. An elaboration of this choice is found in [57]. On the other hand, sub-scales are still quasi time-dependent since the large-scale residual is time-dependent. For more information on time-tracked sub-scales, please refer to [58].

The fine-scale approximations are given by:

$$\boldsymbol{u}' = (\tau_{\boldsymbol{u}} P'_{\boldsymbol{u}}(R_{\boldsymbol{u}})), \tag{4.52}$$

$$p'_s = (\tau_c P'_c(R_c)). \tag{4.53}$$

Where $R_{\boldsymbol{u}}$ and R_c are the finite element residuals, $P'_{\boldsymbol{u}}$ and P'_c are the projection operators, and $\tau_{\boldsymbol{u}}$ and τ_c are tuning parameters. Note that in this current work, both $P'_{\boldsymbol{u}}$, and P'_c are taken as the identity matrix $\mathbf{I}$.

Afterward, the coarse-scale equations are given by:

$$(\rho_s \frac{\partial^2 \boldsymbol{u}}{\partial t^2}, \boldsymbol{w}_h) + a'(\boldsymbol{u}_h, \boldsymbol{w}_h) + (p_{s_h}, \nabla_{\mathbf{x}} \cdot \boldsymbol{w}_h) + (p'_s, \nabla_{\mathbf{x}} \cdot \boldsymbol{w}_h) = L(\boldsymbol{w}_h) \forall \boldsymbol{w}_h \in W_{h,0}, \tag{4.54}$$

$$(\nabla_{\mathbf{x}} \cdot \boldsymbol{u}_h, q_h) - (\frac{1}{\kappa}p_{s_h}, q_h) - (\frac{1}{\kappa}p'_s, q_h) - (u', \nabla_{\mathbf{x}}q_h) = (g, q_h) \ \forall \ q_h \in Q_h. \tag{4.55}$$

The finite element residuals are given by

$$R_{\boldsymbol{u}} = \boldsymbol{f} - \rho_s \ddot{\boldsymbol{u}}_h + \nabla_{\mathbf{x}}p_{s_h} + \nabla_{\mathbf{x}} \cdot dev[\boldsymbol{\sigma}], \tag{4.56}$$

$$R_c = g - \nabla_{\mathbf{x}} \cdot \boldsymbol{u}_h + \frac{1}{\kappa}p_{s_h}. \tag{4.57}$$

Modeling the fine scales as in (52)(53), we finally get

$$(\rho_s \frac{\partial^2(\boldsymbol{u})}{\partial t^2}, \boldsymbol{w}_h) + a'(\boldsymbol{u}_h), \boldsymbol{w}_h) + (p_{s_h}, \nabla \cdot \boldsymbol{w}_h) +$$
$$\sum_{K \in T_h} (\tau_c(g - \nabla_{\mathbf{x}} \cdot \boldsymbol{u}_h + \frac{1}{\kappa}p_{s_h}), \nabla.\boldsymbol{w}_h) = L(\boldsymbol{w}_h) \ \forall \ \boldsymbol{w}_h \in W_{h,0}, \tag{4.58}$$

$$(\nabla.(\boldsymbol{u}_h), q_h) - (\frac{1}{\kappa}(p_{s_h}), q_h) + \sum_{K \in T_h} (\frac{\tau_c}{\kappa}(\nabla_{\mathbf{x}} \cdot \boldsymbol{u}_h - \frac{1}{\kappa}p_{s_h} - g), q_h)$$

$$+ \sum_{K \in T_h} (\tau_{\boldsymbol{u}}(\rho_s \ddot{\boldsymbol{u}}_h - \nabla_{\mathbf{x}}p_{s_h} - \nabla_{\mathbf{x}} \cdot dev[\boldsymbol{\sigma}] - \boldsymbol{f}), \nabla q_h) = (g, q_h) \; \forall \; q_h \in Q_h. \tag{4.59}$$

Compared to the standard Galerkin formulation, this formulation contains new additional terms. These additional terms model the effect of the sub-scales. These terms are developed consistently and help circumvent problems of spurious pressure oscillations. The general definition of the stabilization parameters [59][60], computed within each element gives:

$$\tau_{\boldsymbol{u}} = ((\frac{\rho_s}{(c_0 \Delta t)^2})^2 + (\frac{2\mu_s}{c_1 h_K^2})^2)^{-\frac{1}{2}}, \tag{4.60}$$

$$\tau_c = ((2c_2\mu_s)^2)^{-\frac{1}{2}}. \tag{4.61}$$

Where h_k is the characteristic length of the element, and c_0, c_1, and c_2 are constants to be determined.

4.4 Fluid solver

4.4.1 Newtonian incompressible equations

Let $\Omega_f \subset \mathbb{R}^d$ be the spatial domain at time $t \in [0, T]$, where d is the spatial dimension. Γ_f is the boundary of Ω_f. The mixed formulation in velocity and pressure for the transient incompressible Navier–Stokes equations is given by:

$$(\rho_f \frac{\partial \boldsymbol{v}}{\partial t} + (\boldsymbol{v} \cdot \nabla)\boldsymbol{v}) - \nabla \cdot \boldsymbol{\sigma} = \boldsymbol{f} \text{ in } \Omega_f, \tag{4.62}$$

$$\nabla \cdot \boldsymbol{v} = 0 \text{ in } \Omega_f. \tag{4.63}$$

where ρ_f and $\boldsymbol{v}$ are the fluid density and velocity. $\boldsymbol{f}$ is the source term, and $\boldsymbol{\sigma}$ is defined as

$$\boldsymbol{\sigma} = 2\mu_f \epsilon(\boldsymbol{v}) - p_f \mathbf{I}, \tag{4.64}$$

$$\epsilon(\boldsymbol{v}) = \frac{1}{2}(\nabla \boldsymbol{v} + \nabla^T \boldsymbol{v}). \tag{4.65}$$

The boundary conditions of the problem are as follows

$$\boldsymbol{v} = \mathbf{m} \text{ on } \partial\Omega_{f_u}, \tag{4.66}$$

$$\boldsymbol{\sigma}\boldsymbol{n} = \boldsymbol{t} \text{ on } \partial\Omega_{f_t}. \tag{4.67}$$

Where l is a known imposed value. Ω_{f_u} and Ω_{f_t}, are the domain boundaries where we apply the Dirichlet and Neumann boundary conditions respectively. The weak discrete form of the above equations in Galerkin finite elements is as follows

$$(\rho_f \frac{\partial \boldsymbol{v}_h}{\partial t}, \boldsymbol{w}_h) + (\rho_f(\boldsymbol{v}_h \cdot \nabla)\boldsymbol{v}_h, \boldsymbol{w}_h) + (2\mu\epsilon(\boldsymbol{v}_h) : \epsilon(\boldsymbol{w}_h)) - (p_{f_h}, \nabla \cdot \boldsymbol{w}_h) = \\ (\boldsymbol{f}, \boldsymbol{w}_h) \,\forall\, \boldsymbol{w}_h \in W_{h,0} \subset [H_0^1]^d, \tag{4.68}$$

$$(\nabla \cdot \boldsymbol{v}_h, q_h) = 0 \,\forall\, q_h \in Q_h \subset L^2_{f=0}. \tag{4.69}$$

4.4.2 Variational Multi Scale (VMS) stabilization

Applying the same principles of VMS already applied for the fluid solver we end up with the following [52, 53]

$$(\rho_f \frac{\partial \boldsymbol{v}_h}{\partial t}, \boldsymbol{w}_h) + (\rho_f(\boldsymbol{v}_h \cdot \nabla)\boldsymbol{v}_h, \boldsymbol{w}_h) + (2\mu\epsilon(\boldsymbol{v}_h) : \epsilon(\boldsymbol{w}_h)) - (p_{f_h}, \nabla \cdot \boldsymbol{w}_h) + (\nabla \cdot \boldsymbol{v}_h, q_h)$$

$$- (\boldsymbol{f}, \boldsymbol{w}_h) + \sum_{K \in T_h} (\tau_{\boldsymbol{u},K}((\rho_f \frac{\partial \boldsymbol{v}_h}{\partial t} + (\boldsymbol{v}_h \cdot \nabla)\boldsymbol{v}_h) + \nabla p_{f_h} - \boldsymbol{f}), \rho_f \boldsymbol{v}_h \nabla \boldsymbol{w}_h)_K$$

$$+ \sum_{K \in T_h} (\tau_{\boldsymbol{u},K}((\rho_f \frac{\partial \boldsymbol{v}_h}{\partial t} + (\boldsymbol{v}_h \cdot \nabla)\boldsymbol{v}_h) + \nabla p_{f_h} - \boldsymbol{f}), \nabla q_h)_K$$

$$+ \sum_{K \in T_h} (\tau_{c,K} \nabla \cdot \boldsymbol{v}_h, \nabla \cdot \boldsymbol{w}_h)_K = 0 \,\forall\, \boldsymbol{w}_h \in W_{h,0}, \,\forall\, q_h \in Q_h. \tag{4.70}$$

Compared to the standard Galerkin formulation, this formulation contains new additional integrals that are evaluated element-wise. These additional terms represent the effects of the sub-scales. These terms are developed consistently. These additional terms help circumvent the instabilities that arise due to the advective-dominated regimes. An additional term that models the small-scale pressure is also added that helps alleviate stabilization problems for high Reynolds number. An implicit linearization of the advective term is handled using a Newton-Raphson linearization method. The reader is invited to read [53] for more information on the final formulation.

4.5 Numerical Validation

4.5.1 Bending beam 1

This test consists of a 2D semi-stationary beam bending problem tackled in [61][62]. A clamped plate is positioned parallel to the direction of the flow. The flow will induce bending in the plate. After some time, the plate reaches a stationary position where it will no longer oscillate. The fluid and solid properties are given in Table 4.1 below.

Fluid		Solid	
ρ_f	2.0	ρ_s	1.0 or 10.0
μ_f	0.2	μ_s	5000
		λ_s	2000
Model	Newtonian	Model	Neo-Hookean

Table 4.1: Fluid and solid properties for the bending beam 1 problem.

The problem geometrical setup and meshes is shown in Figure 4.8, where $L = 80$, $H = 20$, $l = 10$, and $h = 1$. An inlet velocity of 1 in the x direction is imposed at the inlet. The outlet is free, and the top and bottom of the domain are free to move tangentially. The solid velocity is imposed at the FSI interface. As already implied, a zero displacement boundary condition is imposed at the bottom of the plate. Fluid stress or traction force is imposed on the FSI interface.

4.5.2 Bending beam 2

Another variation of the problem is tackled in [63][64], where the aspect ratio of the beam is half that of the first iteration. The geometrical setup of the case is shown in Figure 4.11. The height of the fluid tunnel is $H = 1$ cm and the length $L = 4$ cm. The beam residing in the tunnel has a thickness $a = 0.04cm$ and a length of $b = 0.8$ cm. No-slip boundary condition is imposed on the bottom part of the tunnel. At the top part, the flow is constrained to move only tangentially (symmetry). The inlet velocity is given by $v_1(t) = 1.5(-y^2 + 2y)$ cm/s, and $v_2(t) = 0$. Zero gauge pressure is imposed at the outlet. The bottom part of the beam has a zero Dirichlet boundary condition. The fluid and solid properties are summarized in Table 4.2 for two variations of the case.

Initially, both the fluid and the solid are at rest. In both variations of the case, the system will reach a steady-state solution where the solid will no longer oscillate. Since the Young's modulus in the first case is relatively low, we can expect

(a) Fluid-Solid Mesh

(b) Anisotropic mesh at the interface

(c) Solid Mesh
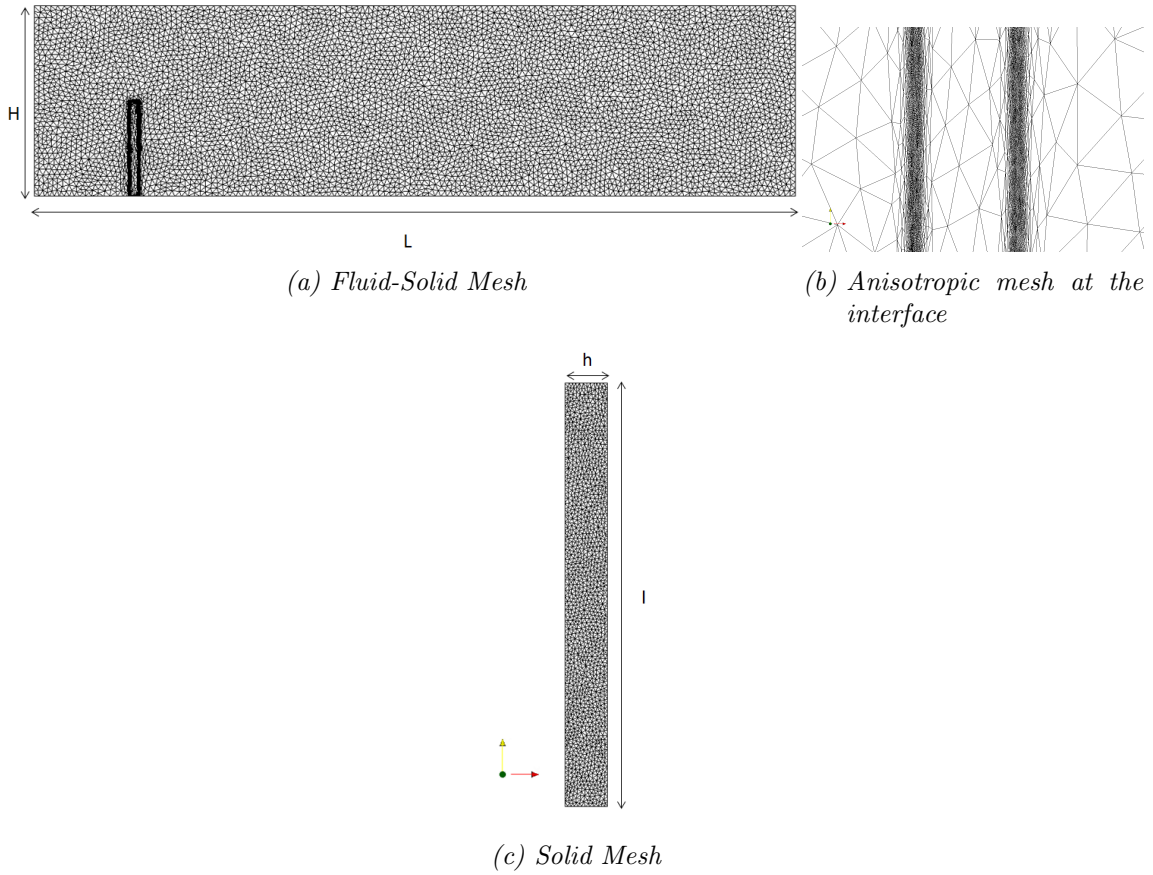
Figure 4.8: Problem set up and mesh

Fluid		Solid	
ρ_f	1.0 g/cm^3	ρ_s	7.8 g/cm^3
μ_f	0.1 g/(cm.s)	μ_s	10^5 or $2\text{x}10^{12}$ g/(cm.s^2)
		ν_s	0.3
Model	Newtonian	Model	St. Venant–Kirchhoff

Table 4.2: Fluid and solid properties for the bending beam 2 problem.

large deformations to be exhibited in the first variation. Both the displacement and velocity versus time are shown in figures 4.12 4.13. Figures 4.144.154.16, show velocity and pressure contours of the fluid on the fluid-solid mesh. Velocity and pressure are also visualized close to the beam in the neighboring Figure.

One can see pressure oscillations in the vicinity of the beam, and this is due to the high gradient in the velocity that appears because of the sharp corners. This
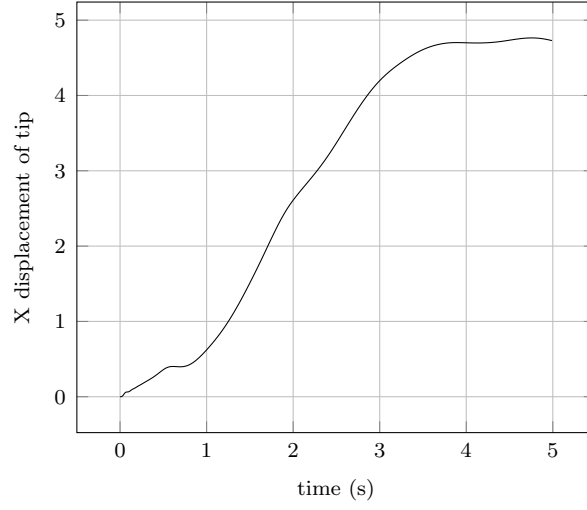
Figure 4.9: X displacement of tip versus time for Bending Beam 1 and a density of 10
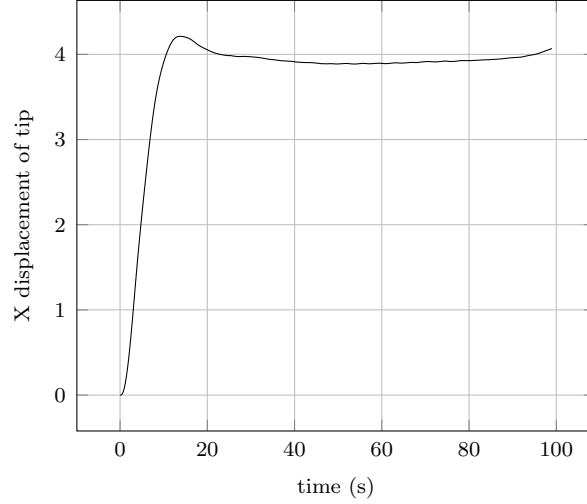
Figure 4.10: X displacement of tip versus time for Bending Beam 1 and a density of 1

pressure is dissipated far from the beam. No oscillation is observed in the velocity field itself. In the second case, a metal-like material is considered. The Young's modulus is much higher than the first case. Thus, the time step is much lower than that for the first case. We chose a time step that is lower by a factor of 1000. Due to the high stiffness of the beam, very small deformation is exhibited by the beam. The vibration of the beam is induced by the fluid traction forces. The vibration dissipates rather fast, due to the viscous effect of the fluid. Even though no damping is considered in the solid, the velocity decays until reaching 0. The velocity of the tip of the beam in the x-direction is shown in Figure 4.17 for a time
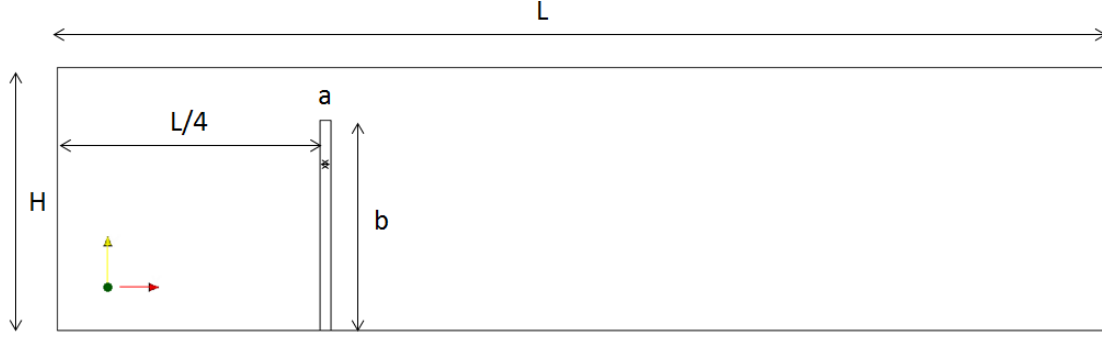
Figure 4.11: Problem set up for bending beam 2
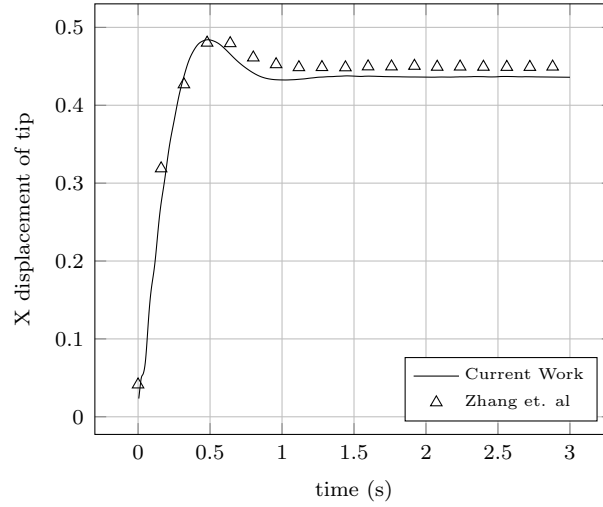
Figure 4.12: Bending beam 2 X displacement of tip versus time and comparison with that from Zhang et. al.

step $\Delta t = 0.000001s$.

4.5.3   2D flow induced vibration of an elastic plate

A two-dimensional problem is first presented to showcase the capabilities of the framework in 2D before presenting the three-dimensional problems. In this case, which was first conducted by [65], a plate is placed at the center of the channel as shown in figure 4.18. The length and height of the channel are $0.2m$, and $0.02m$ respectively. The thickness and height of the elastic plate are $0.002m$, and $0.016m$ respectively. The fluid and solid properties are tabulated in Table 4.3. No-slip Dirichlet boundary conditions are applied at the top and bottom of the 2D channel. A zero-gauge pressure outlet is imposed. At the inlet, we impose a sinusoidal velocity
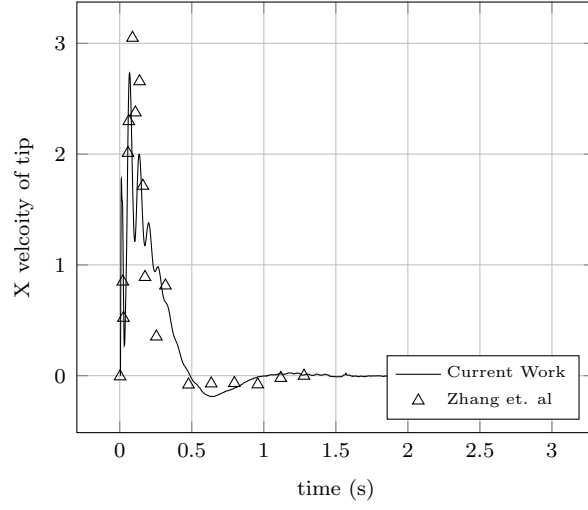
Figure 4.13: Bending beam 2 X velocity of tip versus time and comparison with that from Zhang et. al.
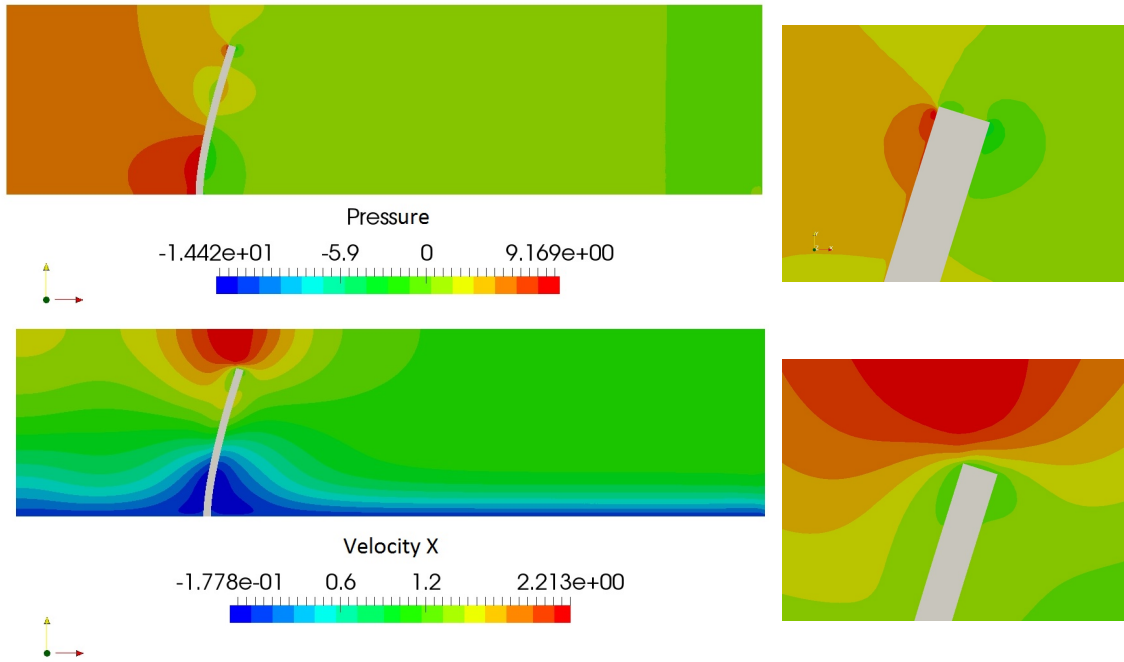
Figure 4.14: Velocity and pressure contours at t=0.1 s for bending beam 2

function given by $U_{in} = 0.015sin(2\pi t)$, with an equivalent period of $1s$. The peak velocity magnitude is equal to $0.015m/s$, which is equivalent to a Reynolds number of 300.

108
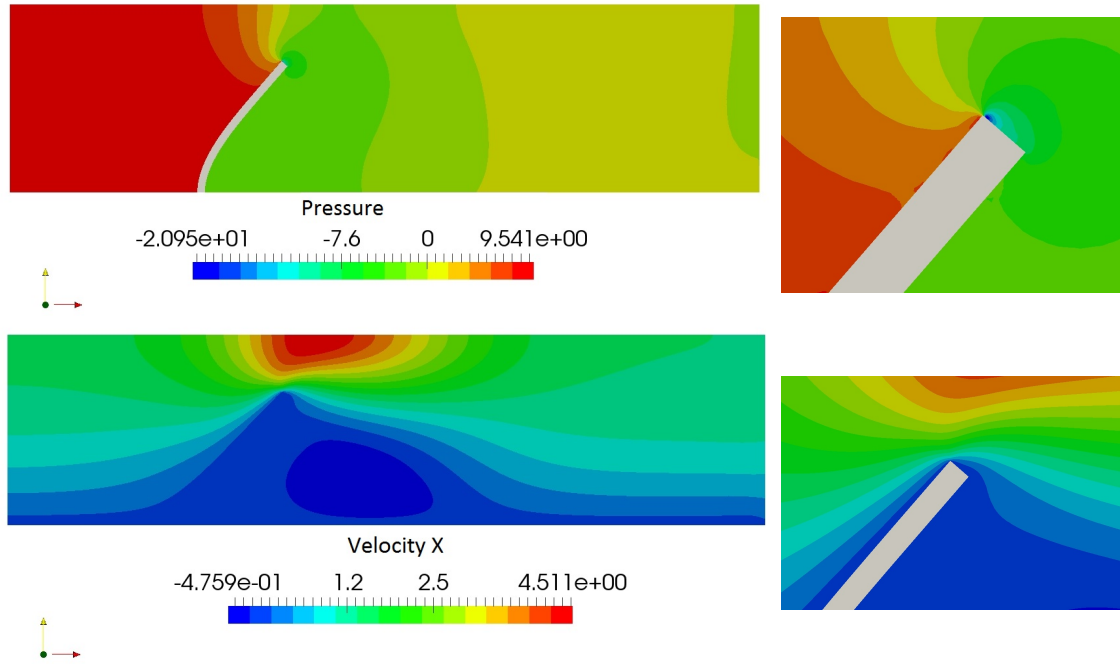
Figure 4.15: Velocity and pressure contours at t=0.8 s for bending beam 2
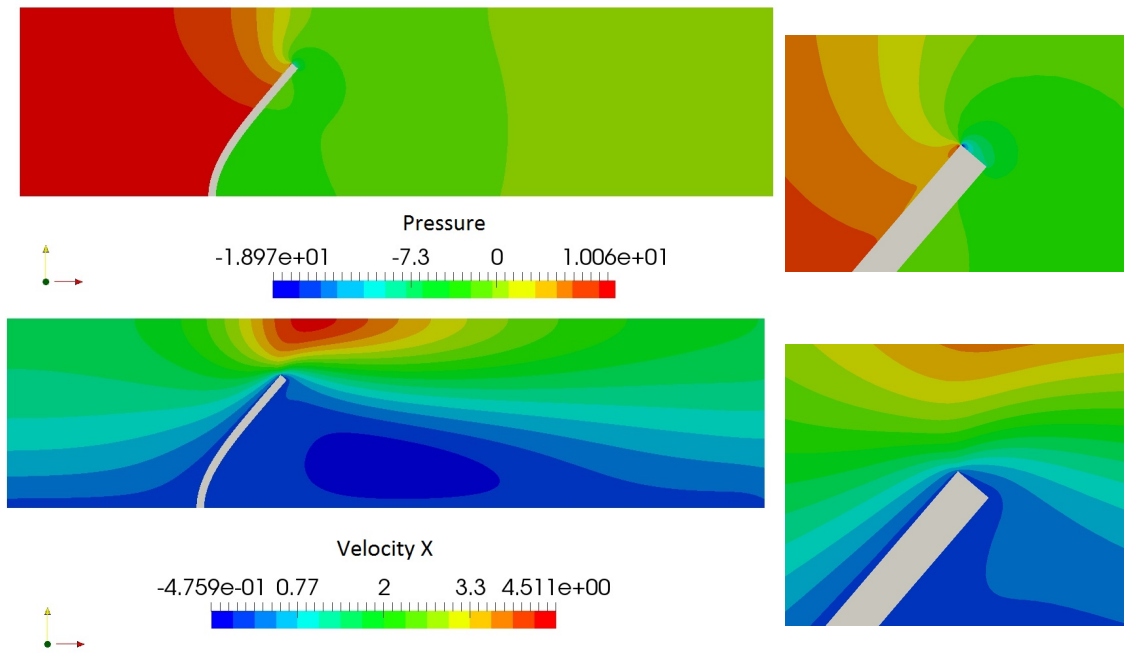
Figure 4.16: Velocity and pressure contours at t=3 s for bending beam 2
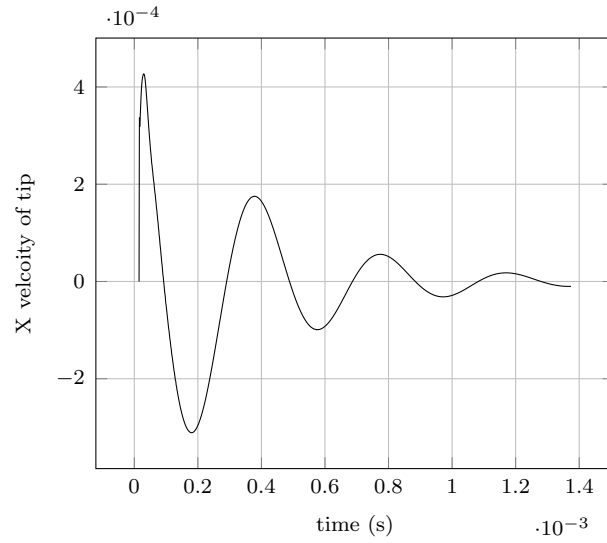
Figure 4.17: Bending beam 2 X velocity of tip versus time for the second variation.
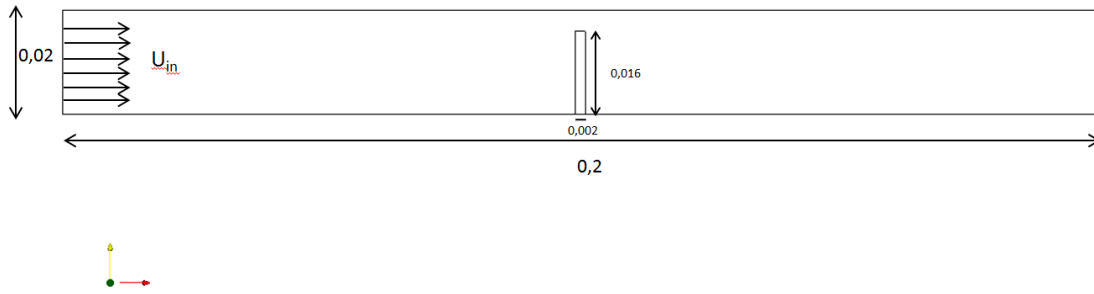
Figure 4.18: Problem set up for the2D flow-induced vibration of an elastic plate.

Fluid properties		Solid properties	
ρ_f	1000 Kg/m^3	ρ_s	1000 Kg/m^3
μ_f	0.001 Kg/ms	μ_s	1677.85 Pa
		E	5000 Pa
		ν	0.49
Model	Newtonian	Model	Neo-Hookean

Table 4.3: Fluid and solid properties for the 2D flow induced vibration of an elastic plate.

As stated earlier, we use an anisotropic mesh adaptation for the fluid-solid mesh. It can be seen from Figure 4.19a, that the elements are localized at the interface. A magnified picture at the interface is shown in Figure 4.19b that shows the anisotropic properties of the elements. The number of elements is capped at 30000. The solid

mesh is shown in Figure 4.19c, where the number of elements is equivalent to 324 elements. The time step for the simulation is set at $0.005s$.

Given the sinusoidal nature of the flow, the elastic plate will swing back and forth from its original position. We ran the simulation for $15T$. We are interested in the deflection of the plate at $T/4$ of the beginning of the period where the inlet velocity is at its maximum. The velocity magnitude field for both the fluid and the solid on the fluid-solid mesh for different positions in time are shown in Figure 4.20. The mesh adaptation highlighting the interface, and the vortices of the flow is shown in Figure 4.21. Pressure contours inside the solid are shown in Figure 4.22b, for two different positions in time, that showcases the tension and compression that the plate exhibits when undergoing significant bending. The x and y displacements of the top right node are plotted versus time in Figures 4.23 and 4.24 respectively.

(a) Fluid-Solid Mesh

(b) Anisotropic mesh at the interface
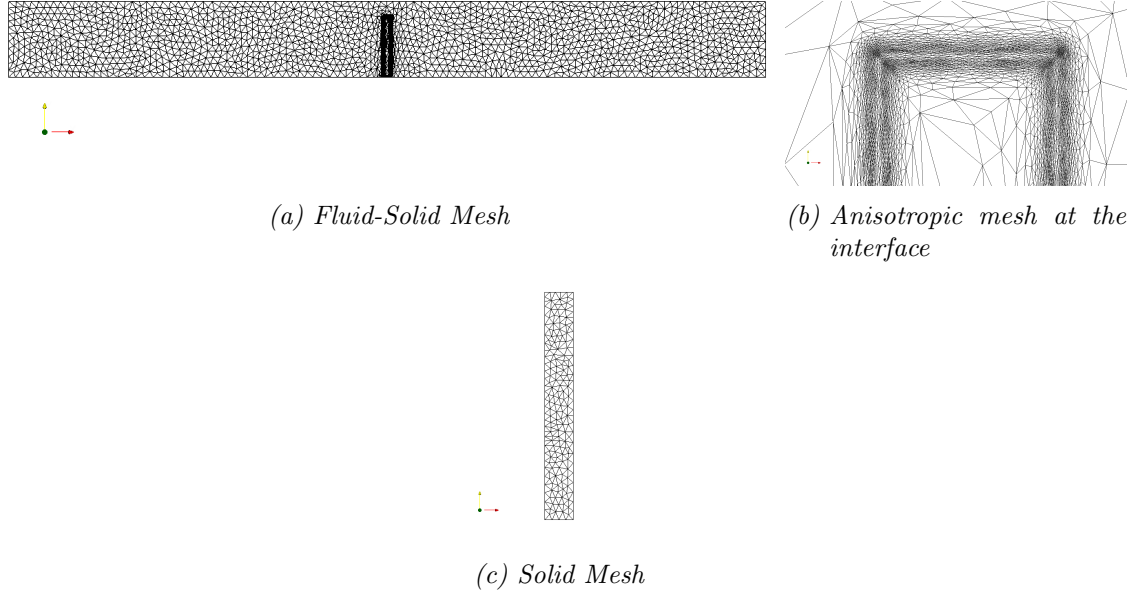
(c) Solid Mesh

Figure 4.19: Fluid-solid and solid meshes for the 2D flow induced vibration of an elastic plate.

Velocity Magnitude

0.000e+00 0.02   0.04   0.06 7.954e-02

(a) t=10

Velocity Magnitude

0.000e+00 0.017   0.035   0.052 6.919e-02

(b) t=10.25

Velocity Magnitude

0.000e+00 0.025   0.05   0.075 1.002e-01

(c) t=10.5

Velocity Magnitude

0.000e+00 0.017   0.034   0.052 6.889e-02

(d) t=10.75

Velocity Magnitude

0.000e+00 0.02   0.04   0.06 7.934e-02

(e) t=11
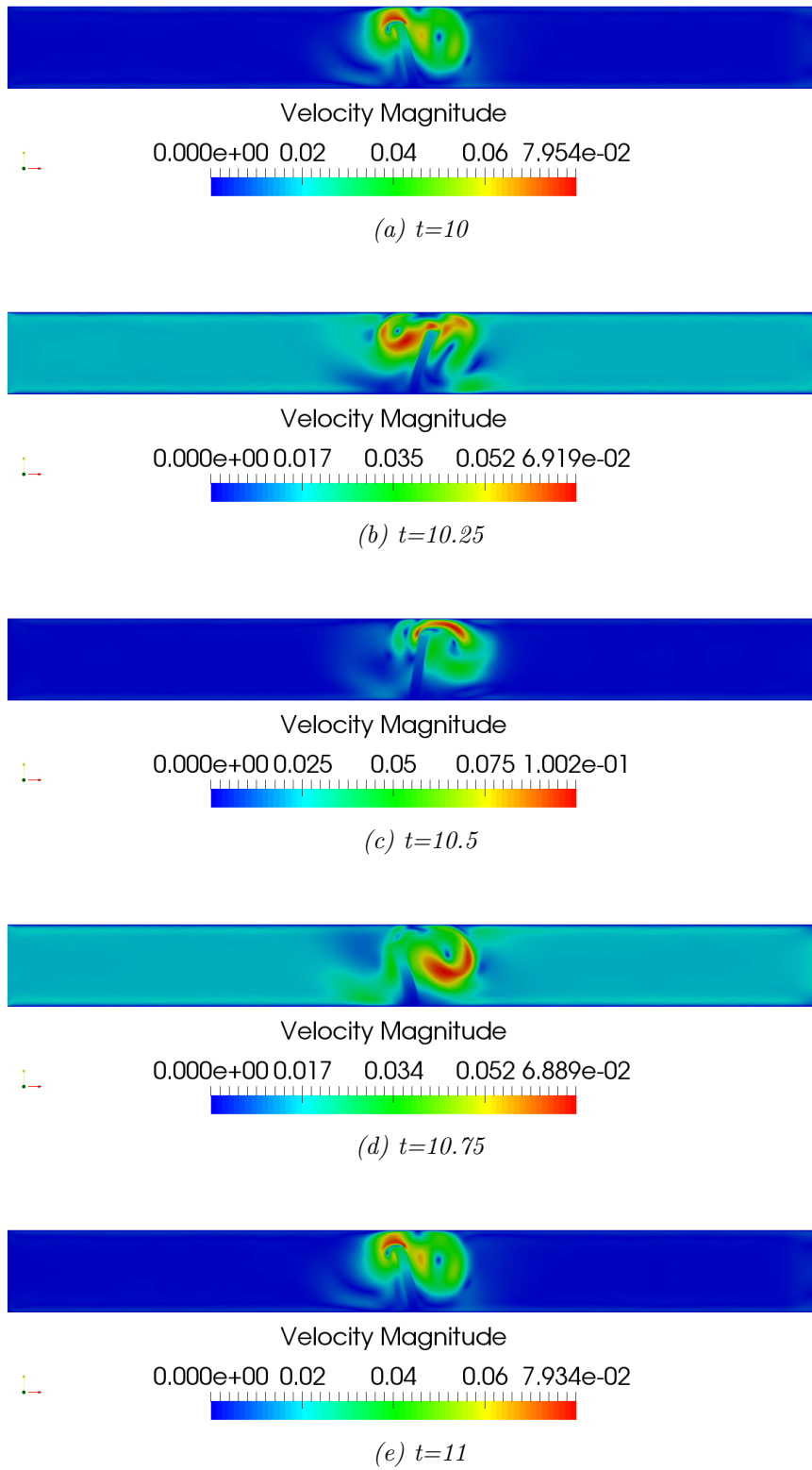
Figure 4.20: Velocity magnitude field of the fluid and solid on the fluid-solid mesh at different positions in time for 2D flow induced vibration of an elastic plate.

(a) (b)
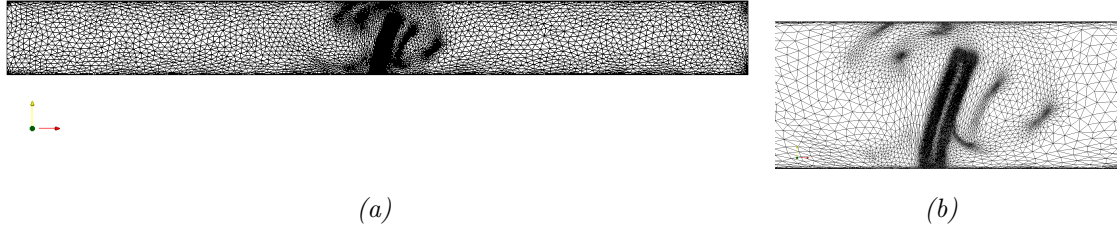
Figure 4.21: Full 4.21a and magnified 4.21b Fluid-Solid Mesh with mesh adaptation on different criteria at time t.

(a) t=10.75 (b) t=11.25
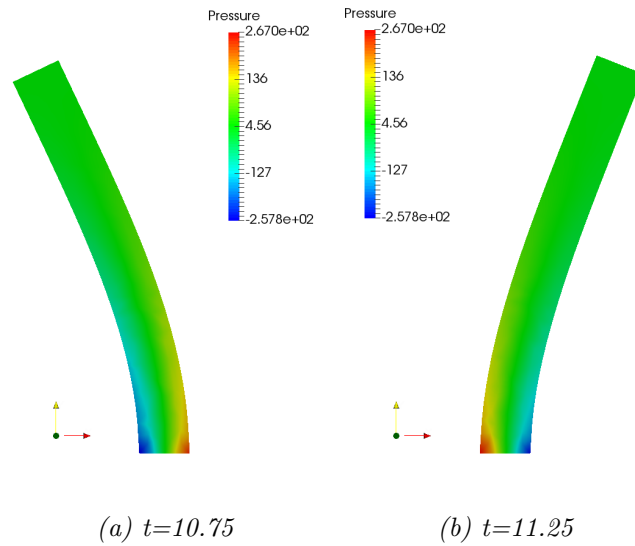
Figure 4.22: Solid pressure contours at different times for 2D flow induced vibration of an elastic plate.

4.5.4 Turek's FSI benchmark

4.5.4.1 FSI2 & FSI3

The fluid-solid domain is identical to that of the well-known benchmarks in CFD, and FSI [66][67] and is shown in Figure 4.25. In that figure, we can see the geometrical

113
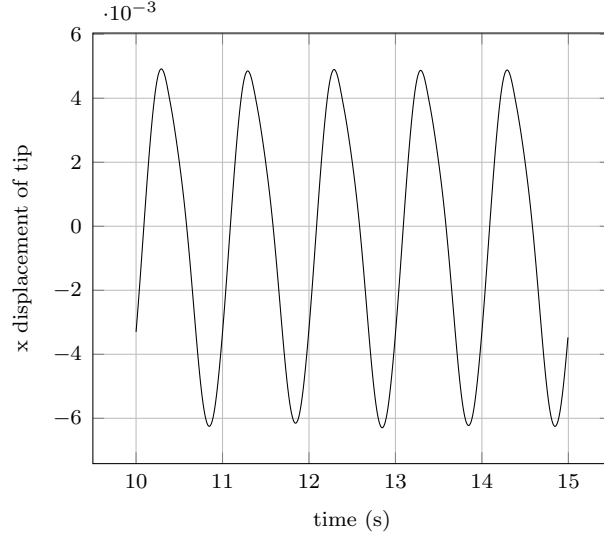
Figure 4.23: x displacement of top right node versus time for 2D flow induced vibration of an elastic plate.
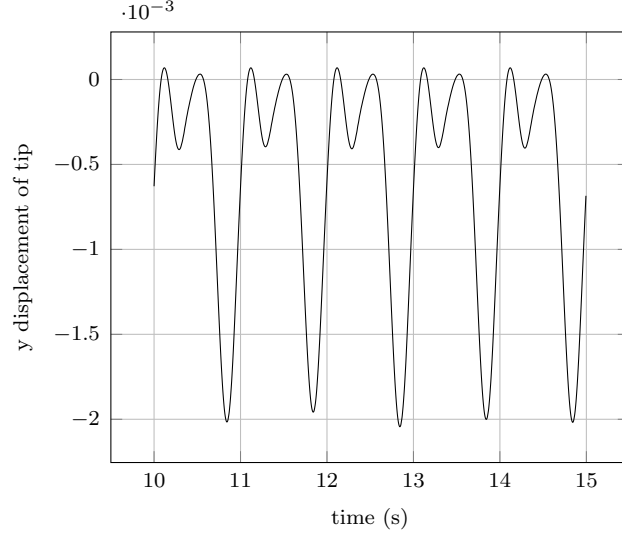
Figure 4.24: y displacement of top right node versus time for 2D flow induced vibration of an elastic plate.

set-up and the type of mesh used for the computations. Figure 4.25a shows the fluid-solid, and solid mesh, and 4.25b shows a close-up of the anisotropic stretched elements at the interface. The bottom left of the domain is at $(0, 0)$. The height is $H = 0.41$, and the length is $L = 2.5$. The center point of the cylinder is positioned at $(0.2, 0.2)$, with a diameter $d = 0.1$. The bottom right of the solid is positioned at $(0.6, 0.19)$, and the left part is fully fixated on the cylinder. The control point for which the values are collected is positioned at $(0.6, 0.2)$. The solid has a length

114

of $l = 0.35$, and a height of $h = 0.02$. A non-symmetry is intentionally prevalent in the y-direction, to avoid the dependency of the beginning of the oscillations on the calculations. A parabolic inlet velocity is imposed on the left side of the fluid-solid domain with the following function

$$\boldsymbol{v}_f = 1.5\overline{U}\frac{y(H-y)}{(\frac{H}{2})^2} = 1.5\overline{U}\frac{4}{0.1681}y(0.41-y). \tag{4.71}$$

This will ensure a mean velocity of $\overline{U}$ at the inlet, and a maximum velocity of $1.5\overline{U}$.

(a)   (b)
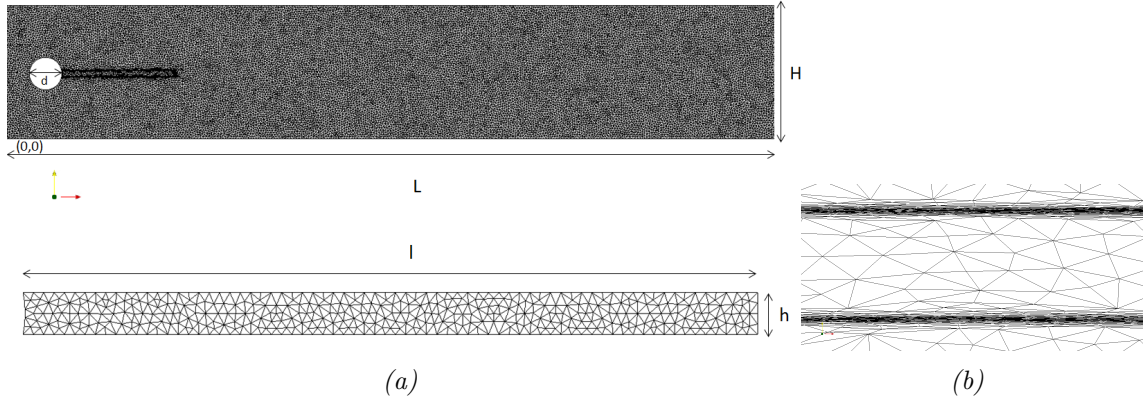
Figure 4.25: Problem set up and mesh

A zero-gauge pressure is imposed at the outlet. The no-slip boundary condition is imposed on the top and bottom of the domain. A smooth increase in velocity is prescribed by the following function

$$\boldsymbol{v}_f(t) = \boldsymbol{v}_f(1 - e^{-(2.5(t))^2}) \tag{4.72}$$

Different variations of the problem are tackled in this chapter and compared with the benchmark.

An example of the mesh and time step convergence study conducted in the numerical benchmarks in this chapter is shown here. First, a mesh convergence study and a time convergence study were conducted to assess the optimal fluid-solid mesh, solid mesh, and time step for the test cases. The different fluid meshes used are shown in figure 4.26, where we have meshes of 20 000, 30 000, and 40 000 elements respectively. The different solid meshes used are shown in figure 4.27, where we have meshes of 354 and 747 elements. Three different time steps are also used, with values equal to 0.004, 0.003, and 0.002 seconds. FSI2 is run until 35 seconds.

parameter	FSI2	FSI3
ρ_s [Kg/m^3]	10000	1000
ν_s	0.4	0.4
μ_s [Kg/(m.s^2)]	500000	2000000
ρ_f [Kg/m^3]	1000	1000
μ_f [Kg/(m.s)]	1	1
$\overline{U}$ [m/s]	1	2
$Re = \frac{\rho_f \overline{U} d}{\mu_f}$	100	200
$Ae = \frac{E}{\rho_f \overline{U}^2}$	1.4 x 10^3	1.4 x 10^3

Table 4.4: Fluid and solid parameters for the Turek's FSI benchmarks variations.

The solid mesh was found to correlate the most with the X displacement of the beam, and not so much with the Y displacement of the beam, which converges to the benchmark values for rather coarse meshes. Figure 4.28 show the dependency of the X displacement of the beam on the number of elements of the solid mesh.

The time dependency changes the values of the displacement, and the drag and lift of the problem. This shown in figures 4.29, and 4.30 for the components of the displacement, and in figures 4.31, and 4.32 for the drag and lift respectively.

The fluid-solid mesh also plays an important role in the accuracy and the precision of the drag and lift a shown in figures 4.34, and 4.33. It is important to note however that the elements are distributed in a way that the displacement of the solid converges rapidly to the final solution for rather coarse meshes, because of the way the elements are distributed close to the interface.

It can be seen from the graphs that the frequency of the oscillations and the amplitude correlate with that of the benchmark.

FSI3 is run until 20 seconds with a time step of $\Delta t = 0.0005$. The Y, and X displacements for FSI3 are plotted versus time in figures 4.36,4.37. It can be seen from the graph that the frequency of the oscillations and the amplitude correlate with that of the benchmark.

4.5.4.2 Double Turek benchmark proposal

In this part of the chapter, we propose a new benchmark for FSI validation. The test consists of two beams instead of one. This will create a dependency on the traction forces exhibited by the solids. Two main variations of the beam are presented. Either we consider two beams in series or parallel. For the two beams in series, we duplicate both the cylinder and the beam while translating the initial beam by 1 in the positive x-direction. The fluid tunnel remains the same. We now have two control points that we gather information from the initial point and a point
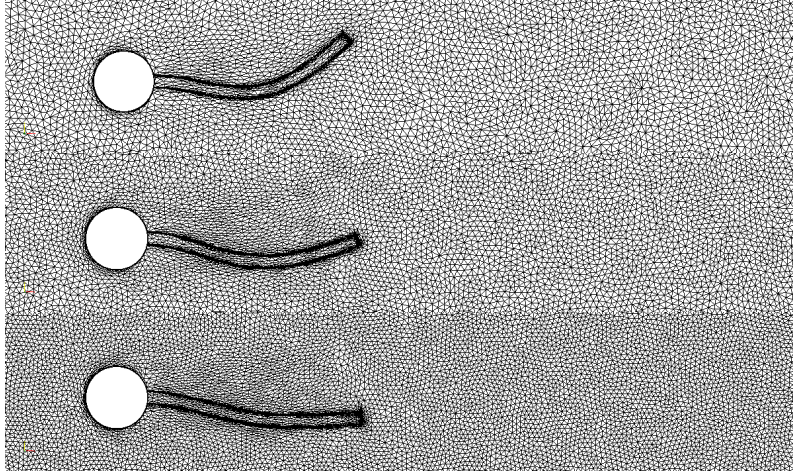
Figure 4.26: *Fluid mesh convergence study consisting of three different meshes of 20 000, 30 000, and 40 000 elements respectively.*
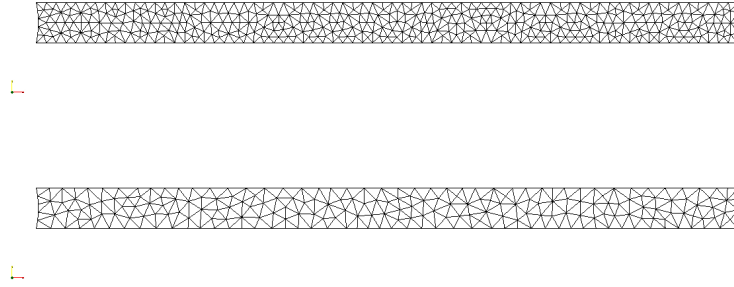
Figure 4.27: *Solid mesh convergence study consisting of two different meshes of 354, and 747 elements.*

translated by 1 in the x-direction as well. The calculation is ran until we reach a periodic movement of the beams, and then we stop the flow on the left-hand side of the tunnel while leaving it free. We continue the calculations until the beams reach zero displacement fields.

Another variation is considering two beams in parallel. We consider two variations of this problem as well. For both variations, the cylinder and the beam are duplicated and translated with a distance of 0.2 if the y-direction. For the first one, the non-symmetrical case, the top plate will now be at 0.61 in the positive y-direction, while for the second one, the symmetrical case, the top plate will be at 0.6 in the positive y-direction.
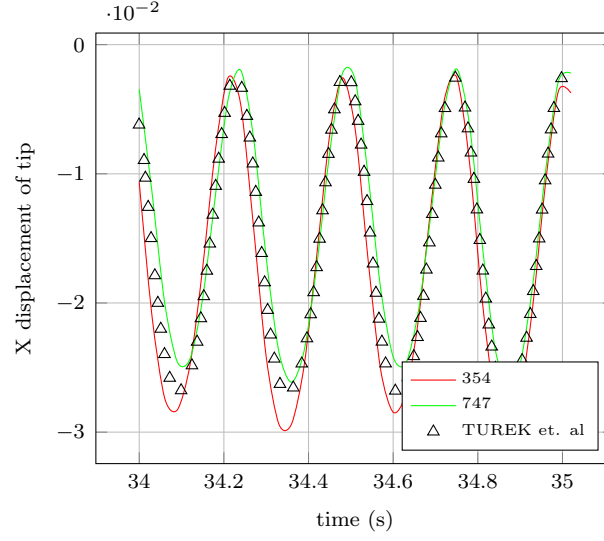
Figure 4.28: *FSI 2 X displacement of tip versus time and comparison with that from Turek et. al for different solid meshes.*
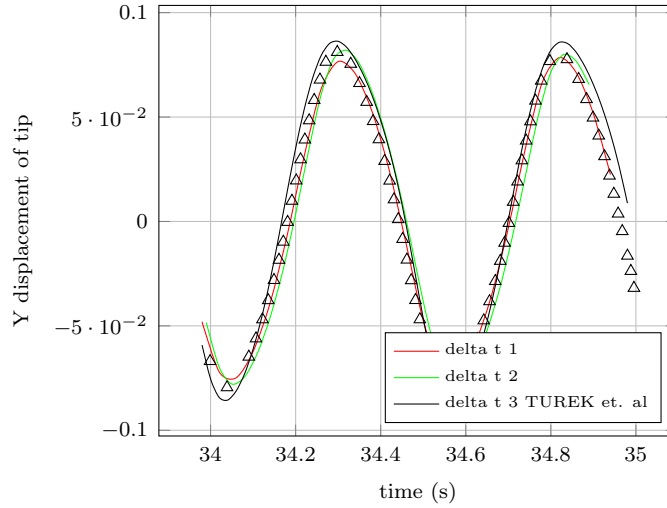
Figure 4.29: *FSI 2 Y displacement of tip versus time and comparison with that from Turek et. al for different time steps.*

4.5.5 Pillar in a Laminar cross flow

Sensory structures are more in more shaped as a cantilever beam in different applications, such as sensors for flux, force, ... measurements. The interaction of such sensors with the surrounding fluid is shown to be of utmost importance in applications like aerodynamics sensors [68]. The application of such a validated framework can be extended to cover natural sensors in animals and biomedical applications.

118
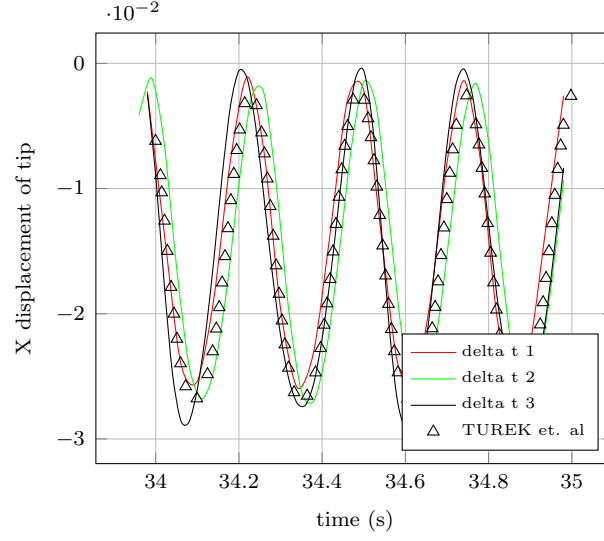
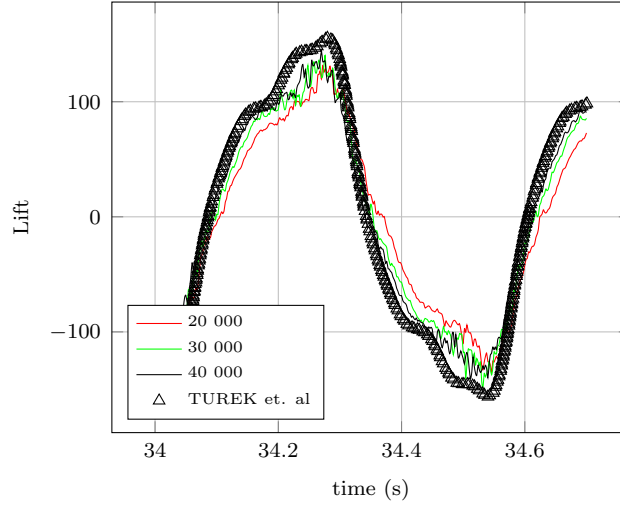Figure 4.30: FSI 2 X displacement of tip versus time and comparison with that from Turek et. al for different time steps.
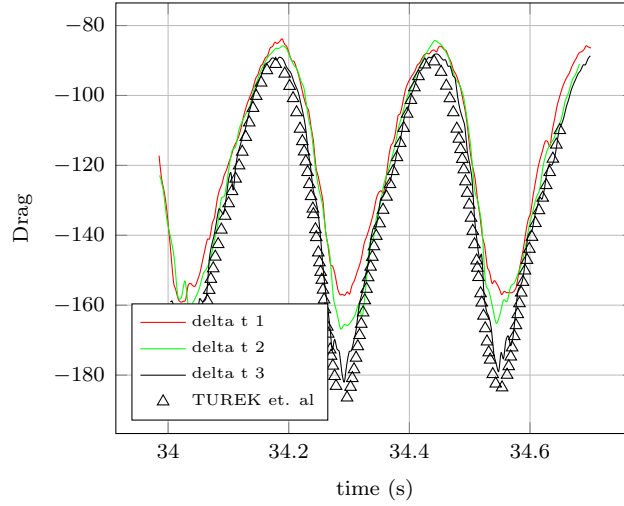
Figure 4.31: FSI 2 drag over the cylinder and membrane versus time for different time steps and comparison with that from Turek et. al.

The sensor examined in this numerical validation is that of a Wall Shear Stress (WSS) sensor. It is modeled as a flexible cylinder made of silicone of micro-scale. Given the small diameter of the cylinder-like structure, typically the Reynolds number is of the order of 10. An experimental setup that is going to be used afterward to compare our results is explained in [35]. A transparent basin with dimensions of (3, 2.5, 0.4) is filled with the working fluid. On top of the fluid container exists a support that can move with a velocity of up to $1m/s$. The cylinder, along with a

119
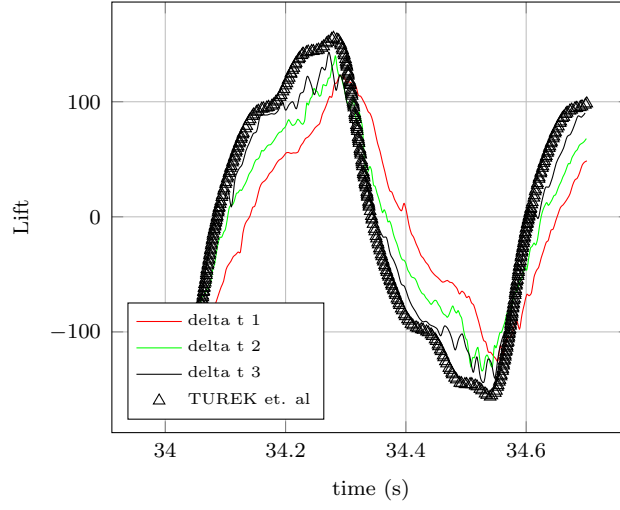
Figure 4.32: FSI 2 lift over the cylinder and membrane versus time for different time steps and comparison with that from Turek et. al.
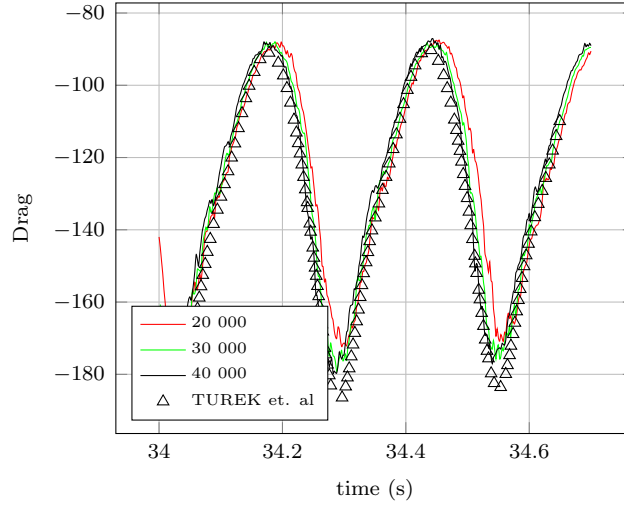
Figure 4.33: FSI 2 drag over the cylinder and membrane versus time for different number of elements and comparison with that from Turek et. al.

plate, are mounted on the mechanism to be able to depict a flow around a cylinder. A high-speed camera was used to extract the necessary information from the experiment. The bending line of the beam is of interest in this particular setup. The fluid chosen for the experiment is glycerin. The material chosen for the solid structure cylinder is silicone, with a diameter $d = 20mm$, and height of $h = 200mm$, which leads to an aspect ratio $l/d = 10$. Glycerin and silicone have approximately the same density, thus a simplification of the problem by not considering buoyancy

Figure 4.34: FSI 2 lift over the cylinder and membrane versus time for different number of elements and comparison with that from Turek et. al.

forces is justified. The material properties of both fluid and solid are summarized in Table 4.5.

Fluid (Glycerin)		Solid(Silicone)	
ρ_f	1220 Kg/m^3	ρ_s	1030 Kg/m^3
μ_f	1 Kg/ms	μ_s	0.473 MPa
		E	1.23 MPa
		ν	0.3
Model	Newtonian	Model	Neo-Hookean

Table 4.5: Fluid and solid properties for the pillar in a Laminar cross flow problem.

We conduct a fully coupled two-way FSI simulation in 3D of the experimental setup shown in figure 4.48, to validate the framework. Yo duplicate the experimental setup into a numerical simulation, we create our virtual fluid basin, which is our 3D fluid-solid mesh. A separate solid mesh is created that represents our polymer structure, which is immersed in the fluid-solid mesh. Instead of moving the solid at a certain velocity like in the experiment, we impose a velocity at the inlet equal to that of the velocity of the plate where the polymer cylinder is clamped. We impose a zero gauge pressure outlet. Perfect slip condition is imposed on the virtual domain walls. Zero slip condition is imposed on both the cylinder and the plate. We conducted the simulation for Reynolds number equal to 12. The geometrical setup is shown if Figure 4.49. The fluid-solid mesh is shown in Figure 4.50a. A close-up of the mesh is shown in Figure 4.50b, which shows the anisotropic nature of the
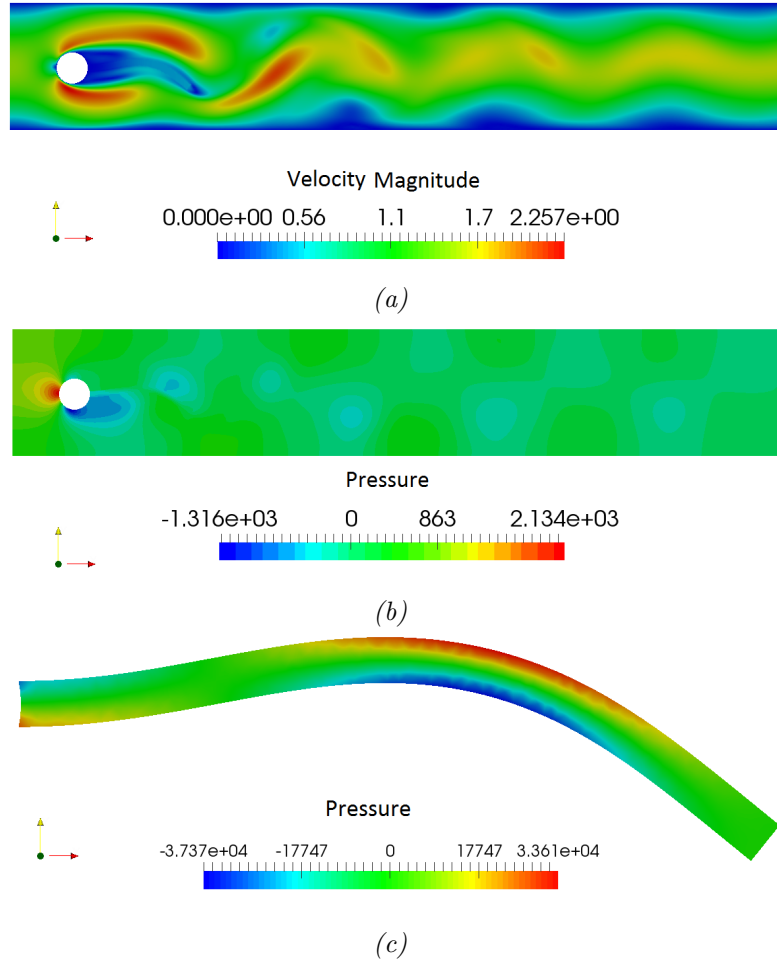
Figure 4.35: Velocity and pressure contour for the fluid-solid and solid domains for FSI2.

elements near the interface. The solid structure mesh is shown in Figure 4.50c. The solid mesh consists of 35 000 elements, while the fluid-solid mesh is capped at 150 000 elements. The time step of the simulation is 0.001 s, and the simulation is run for 2 seconds.

The normalized bending line is plotted and compared to the experimental results in Figure 4.51. A good correlation is found between the FSI simulation and the experimental results. Figure 4.53 shows the velocity streamlines around the cylinder where we can see the displacement field for different times t. The x and y components of the displacement are plotted versus time in Figure 4.52 respectively, to give more insights on the dynamics of the structure.
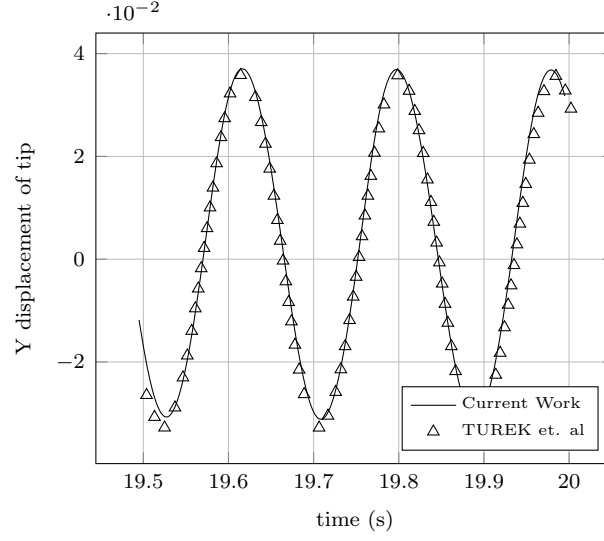
Figure 4.36: *FSI 3 Y displacement of tip versus time and comparison with that from Turek et. al.*
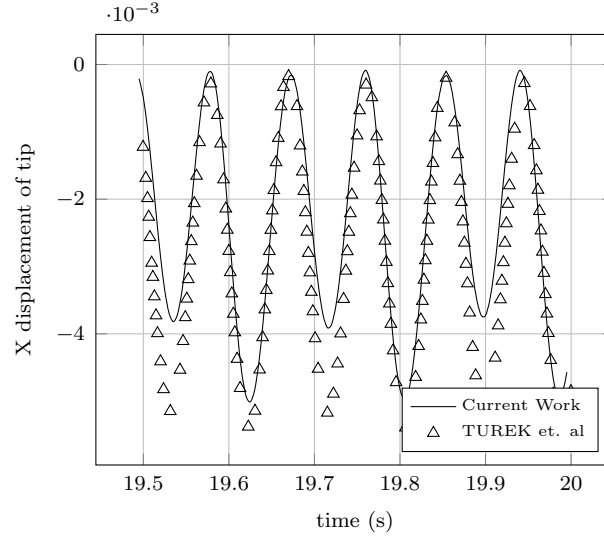
Figure 4.37: *FSI 3 X displacement of tip versus time and comparison with that from Turek et. al.*

4.5.6 Bending of elastic flaps in a cross flow

A variation of the above case was conducted in [69], where flap-like structures are emerged in the fluid instead of the cylinder. The fluid and solid properties of the problem are the same as the previous problem. The solid flap structure geometry consists of a rectangular cylinder with a length of $l = 100mm$, a width of $w = 20mm$, and a varying thickness of $b = 5, 10mm$. Figure 4.54, shows the solid geometry for

123

(a)

(b)

(c)
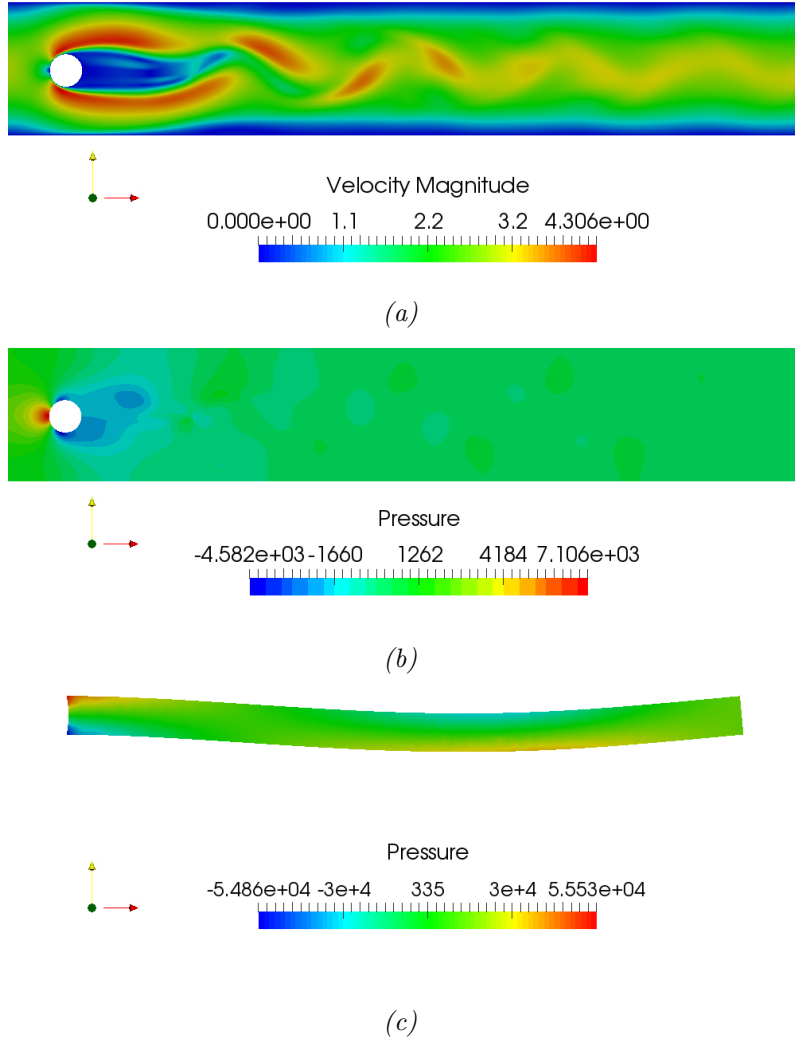
Figure 4.38: Velocity and pressure contour for the fluid-solid and solid domains for FSI3.

a thickness of $5mm$, while Figure 4.55, shows that of thickness of $10mm$. Different orientations were considered for the case of the thick beam. Angles varies between 0, 45, and 90 degrees as shown in Figure 4.56. The maximum displacement magnitude, as well as the steady-state displacement magnitude, are tabulated in Table 4.6 and compared to the benchmark maximum transient deformation. The streamlines highlighted by the velocity magnitude, around the structural flap highlighted by the displacement magnitude are shown for the different beam orientations of the 10mm thick flap for different time steps in Figures 4.58, 4.59 and 4.60.
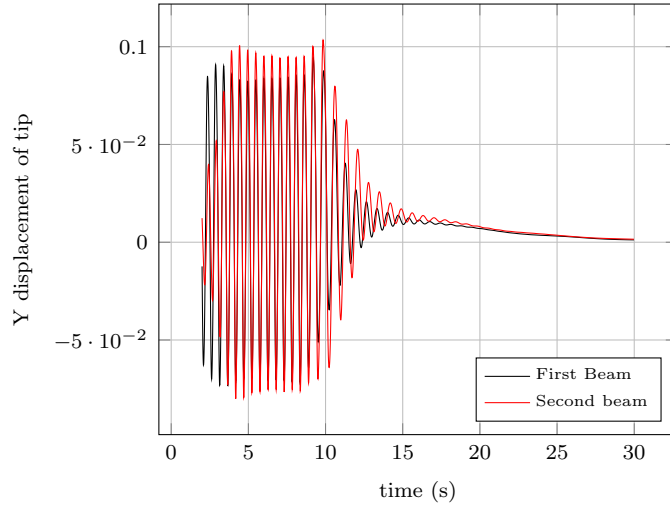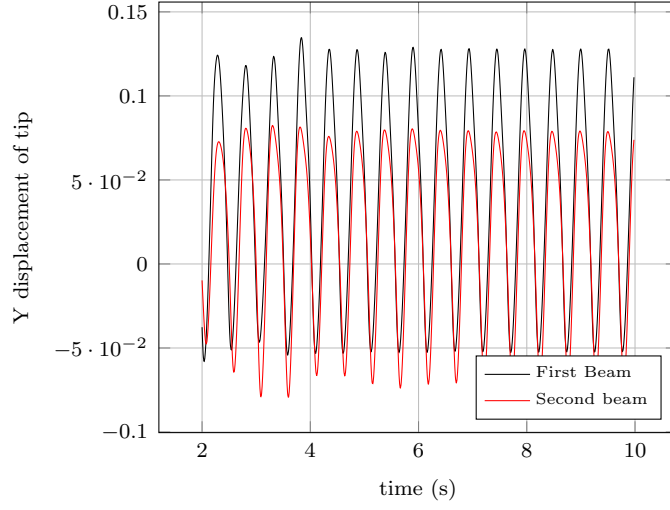
Figure 4.39: FSI two beams in series Y displacement of tips versus time.
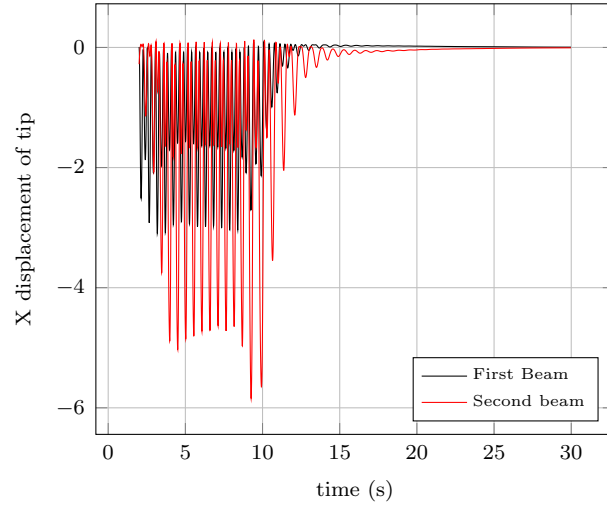
Figure 4.40: FSI two beams in series X displacement of tips versus time.
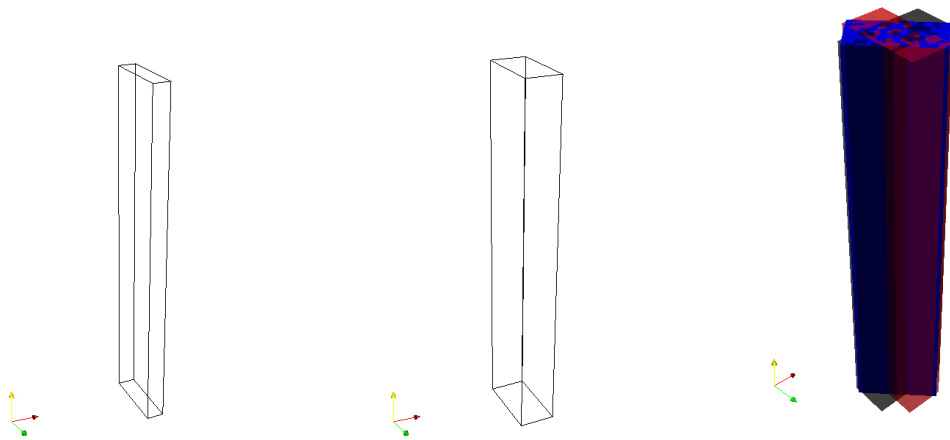
Figure 4.54: b= 5 mm

Figure 4.55: b= 10 mm

Figure 4.56: b= 10 mm, for angles 0, 45, and 90 °

Figure 4.57: Different flap geometries and orientations.

(a)

(b)

(c)
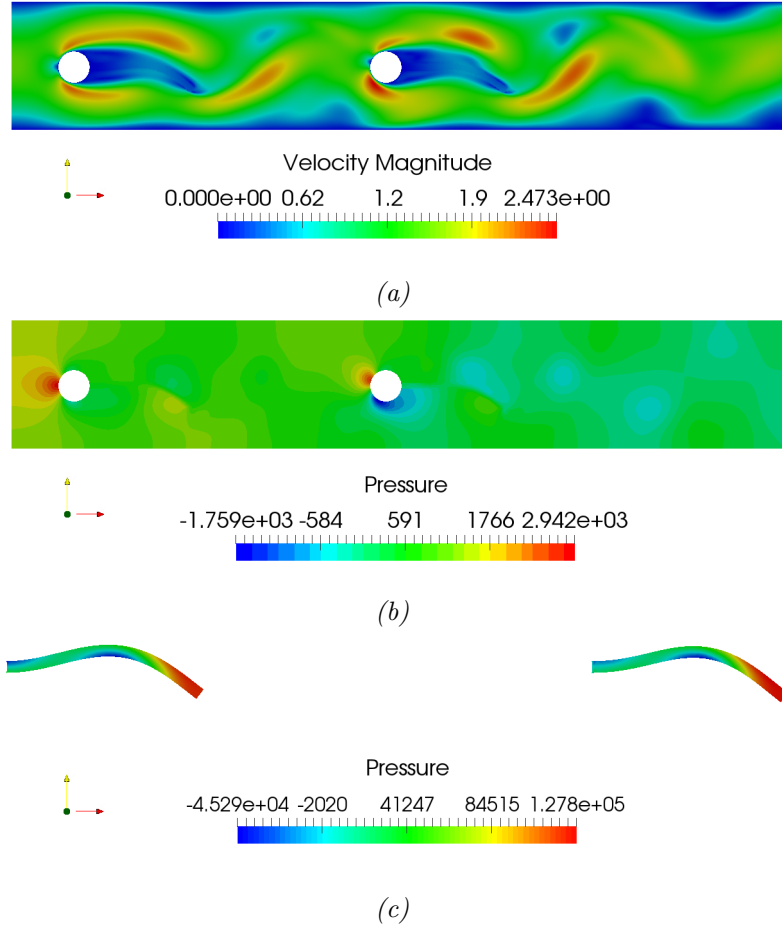
Figure 4.41: Velocity and pressure contour for the fluid-solid and solid domains for the FSI with two beams in series.

Angle(°)	Maximum Displacement Magnitude (m)	Steady-state Displacement Magnitude (m)	Benchmark Maximum Transient Deformation (m)
0	0.06623	0.05082	0.0526
45	0.05581	0.04564	0.0463
90	0.01788	0.01104	0.0196

Table 4.6: Fluid and solid properties for the pillar in a Laminar cross flow problem.

Figure 4.42: FSI two beams in series Y displacement of tips versus time.
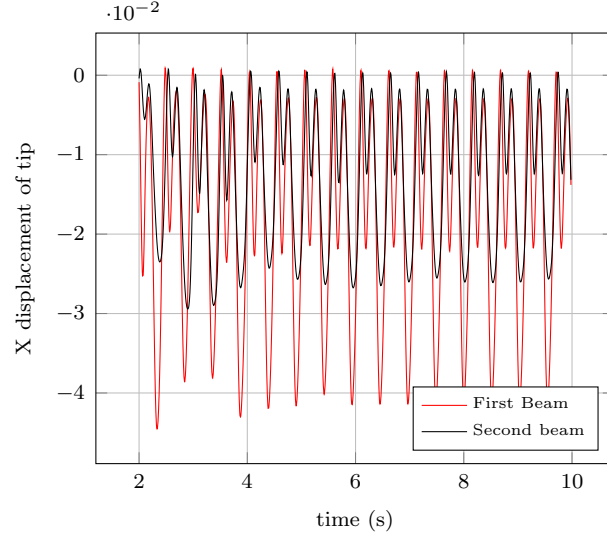
Figure 4.43: FSI two beams in series X displacement of tips versus time.

4.6 Perspectives and conclusion

This article presents the hybrid Fluid–Structure Interaction (FSI) framework that combines the advantages of other well-known methods in the literature. The Adaptive Immersed Mesh Method (AIMM) combines the advantages of a Monolithic (Eulerian) approach for FSI, by having the fluid and the solid co-exist on a single fluid-solid grid, and the Partitioned (Lagrangian) approach for FSI, by having a separate solid solver resolved on a solid grid. This enables us to enrich the solid model.
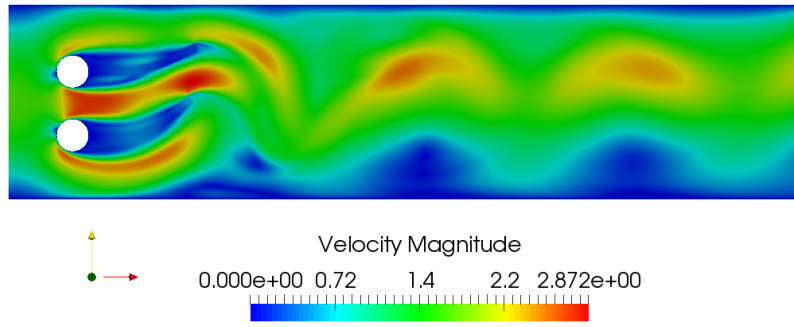
(a)
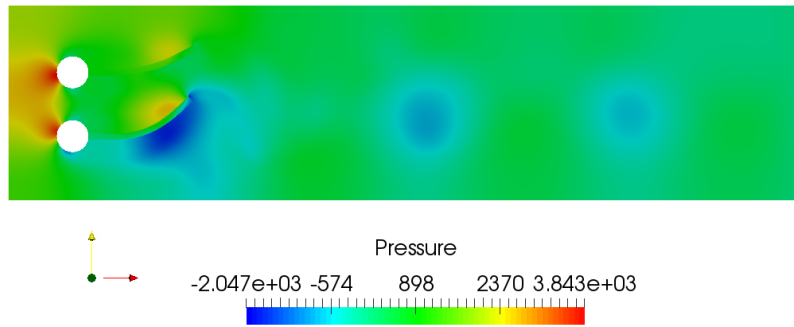
(b)
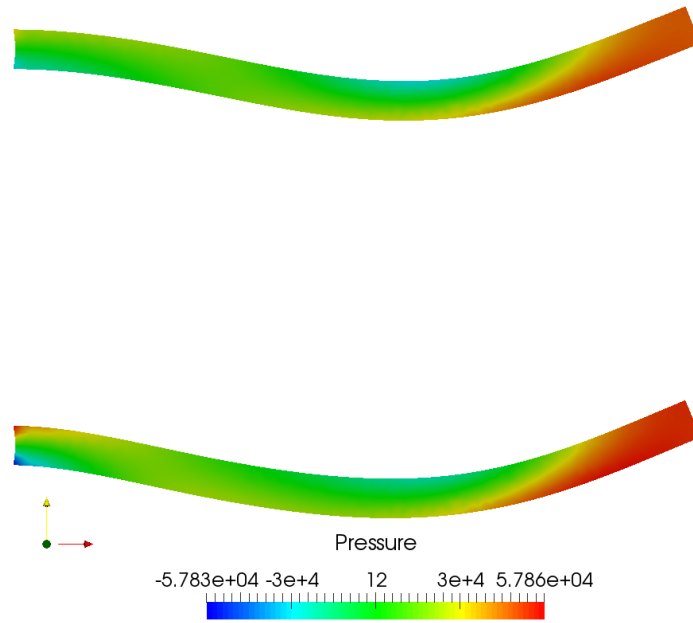
(c)

Figure 4.44: Velocity and pressure contour for the fluid-solid and solid domains for the FSI with two beams in parallel (non-symmetrical).
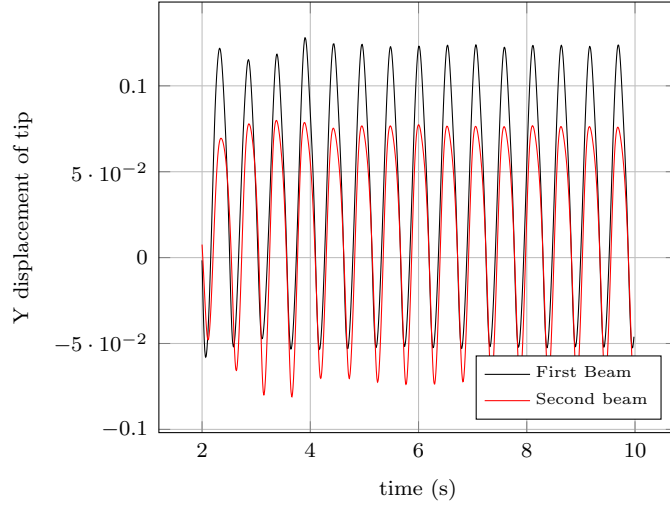
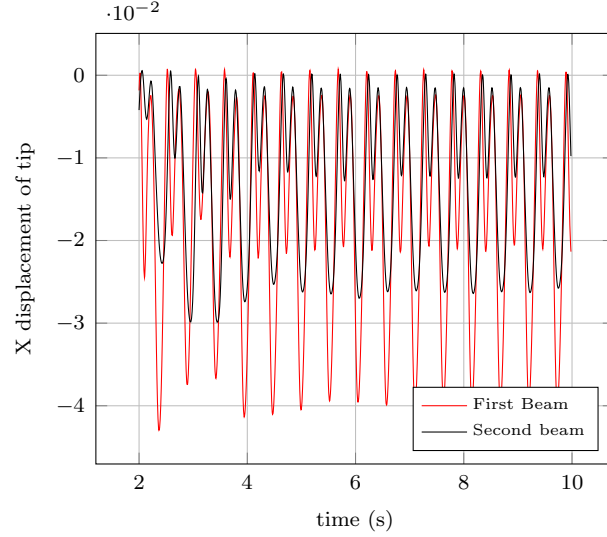*Figure 4.45: FSI two beams in series Y displacement of tips versus time.*


*Figure 4.46: FSI two beams in series X displacement of tips versus time.*

The solid mesh is immersed upon the fluid-solid mesh at each point in time using the level set method. This enables us to track the fluid-solid interface on the fluid-solid mesh. This is done naturally on the solid mesh. Velocity and full stress are communicated at the fluid-solid interface of each grid. Anisotropic mesh adaptation is applied under different criteria, one of which creates stretched elements at the interface based on the gradient of the level set. The helps us obtain more accurate, and precise results. The Variational Multi-Scale (VMS) Method is applied to both solvers to be able to use first-order unstructured finite elements while respecting the inf-sup condition. Different two-dimensional benchmarks are presented
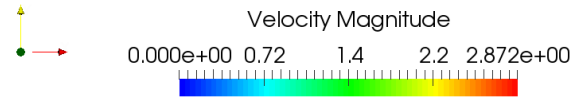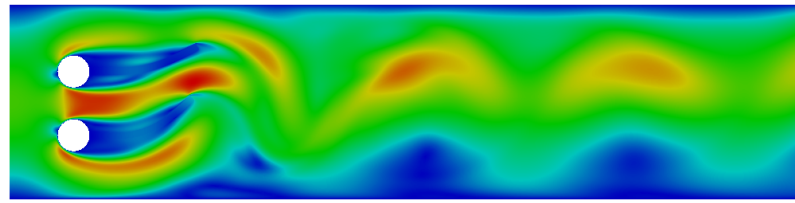
(a)
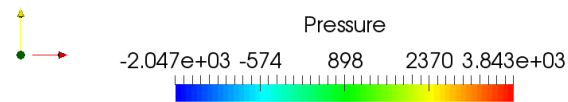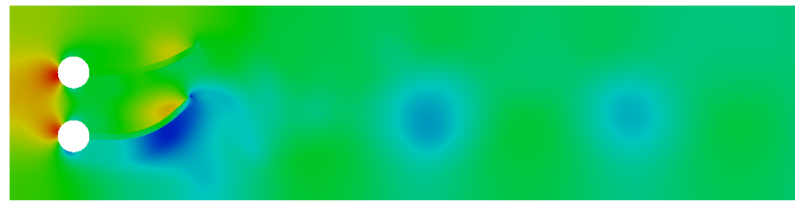
(b)
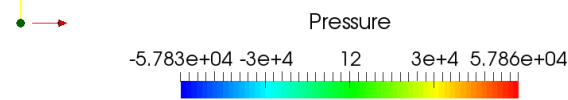
(c)

Figure 4.47: Velocity and pressure contour for the fluid-solid and solid domains for the FSI with two beams in parallel (symmetrical).
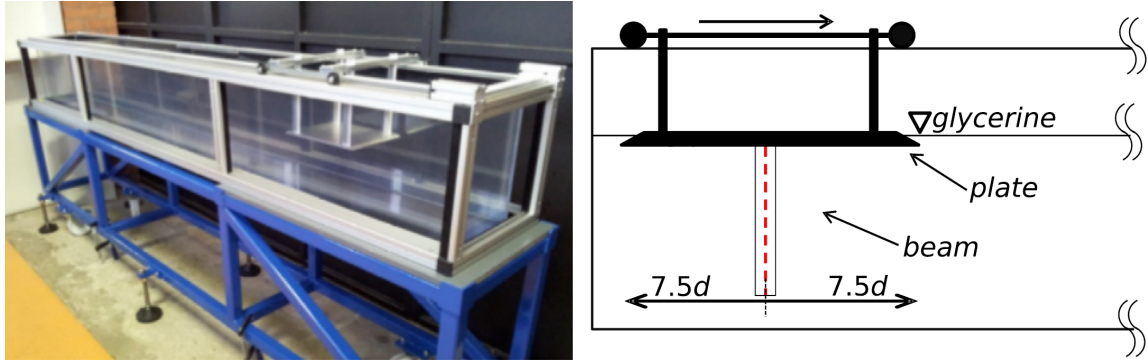
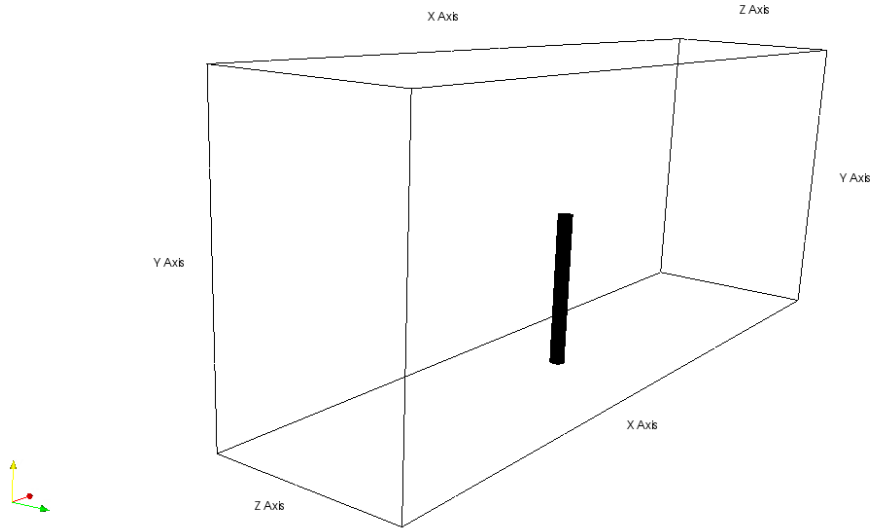Figure 4.48: Experimental setup and schematic from Axtmann et. al[35]

Figure 4.49: Problem set up for bending beam 2

and the results obtained are in coherence with that of the literature. Also, new FSI benchmarks for multiple solids are presented to serve as future references for the community. Different, three-dimensional, FSI simulations are presented to showcase the ability of the solver in simulating flexible, and relatively thin structures immersed in a fluid. We are in the process of extending the framework to more complex applications that involve for example biomechanical applications.
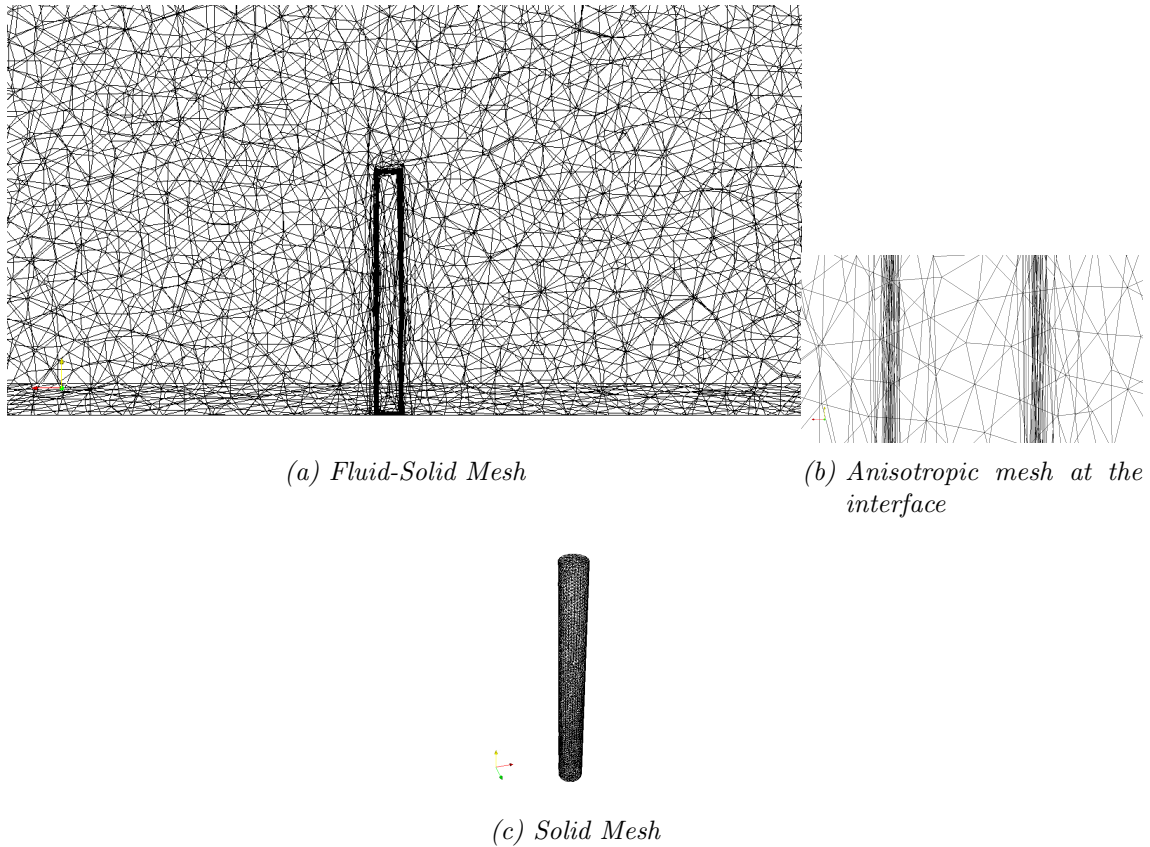
131

(a) Fluid-Solid Mesh

(b) Anisotropic mesh at the interface

(c) Solid Mesh

Figure 4.50: Fluid-solid and solid meshes for the pillar in a Laminar cross flow.

Bibliography

[1] F. Hamdan, P. Dowling, Fluid-structure interaction: application to structures in an acoustic fluid medium, part 1: an introduction to numerical treatment, Engineering Computations (1995). 86

[2] D. Hartwanger, A. Horvat, 3d modelling of a wind turbine using cfd, in: NAFEMS Conference, United Kingdom, 2008. 86

[3] H. Hou, Coupled fluid-structure analysis for exhaust system nvh, Tech. rep., SAE Technical Paper (2014). 86

[4] D. Trimarchi, S. Turnock, D. Chapelle, D. Taunton, Fluid-structure interactions of anisotropic thin composite materials for application to sail aerodynamics of a yacht in waves (1970). 86

[5] J. H. Leung, A. R. Wright, N. Cheshire, J. Crane, S. A. Thom, A. D.
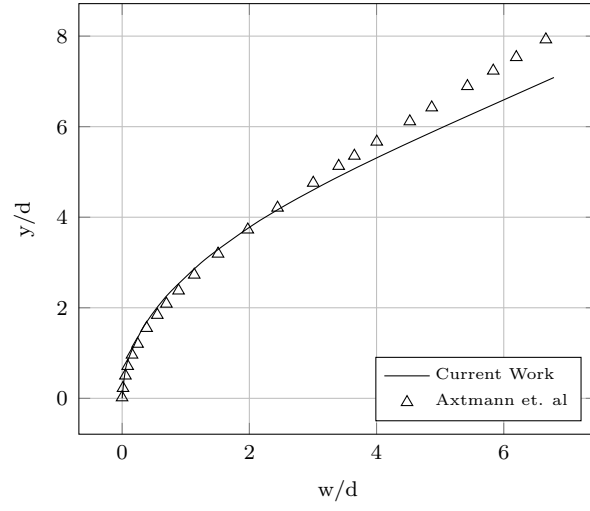
Figure 4.51: Bending line of the beam at the final time t compared with the work of that of Axtmann et. al[35].
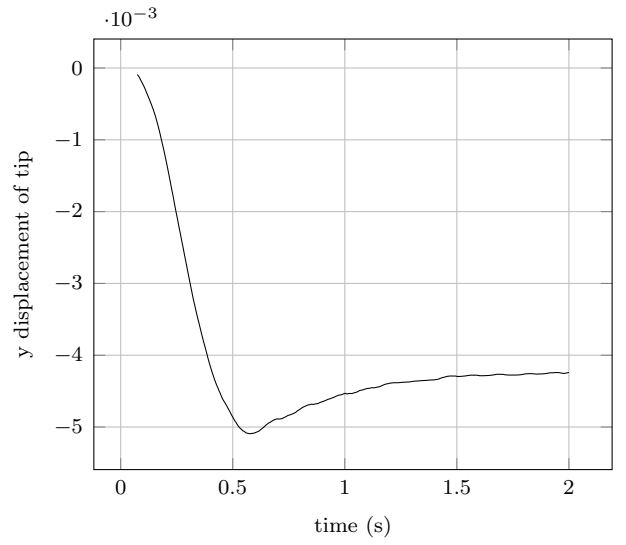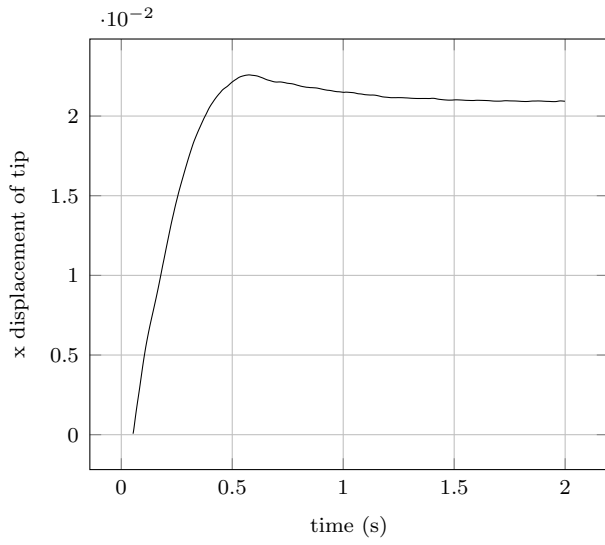
Figure 4.52: x and y displacement of top center versus time for pillar in a Laminar cross flow

Figure 4.53: Velocity and displacement magnitudes of the fluid and solid respectively at different positions in time.

Figure 4.58: Velocity and displacement magnitudes of the fluid and solid respectively at different positions in time for the 10mm flap.

Figure 4.59: Velocity and displacement magnitudes of the fluid and solid respectively at different positions in time for the 45 degrees variation of the 10mm flap.

Figure 4.60: Velocity and displacement magnitudes of the fluid and solid respectively at different positions in time for the 90 degrees variation of the 10mm flap.
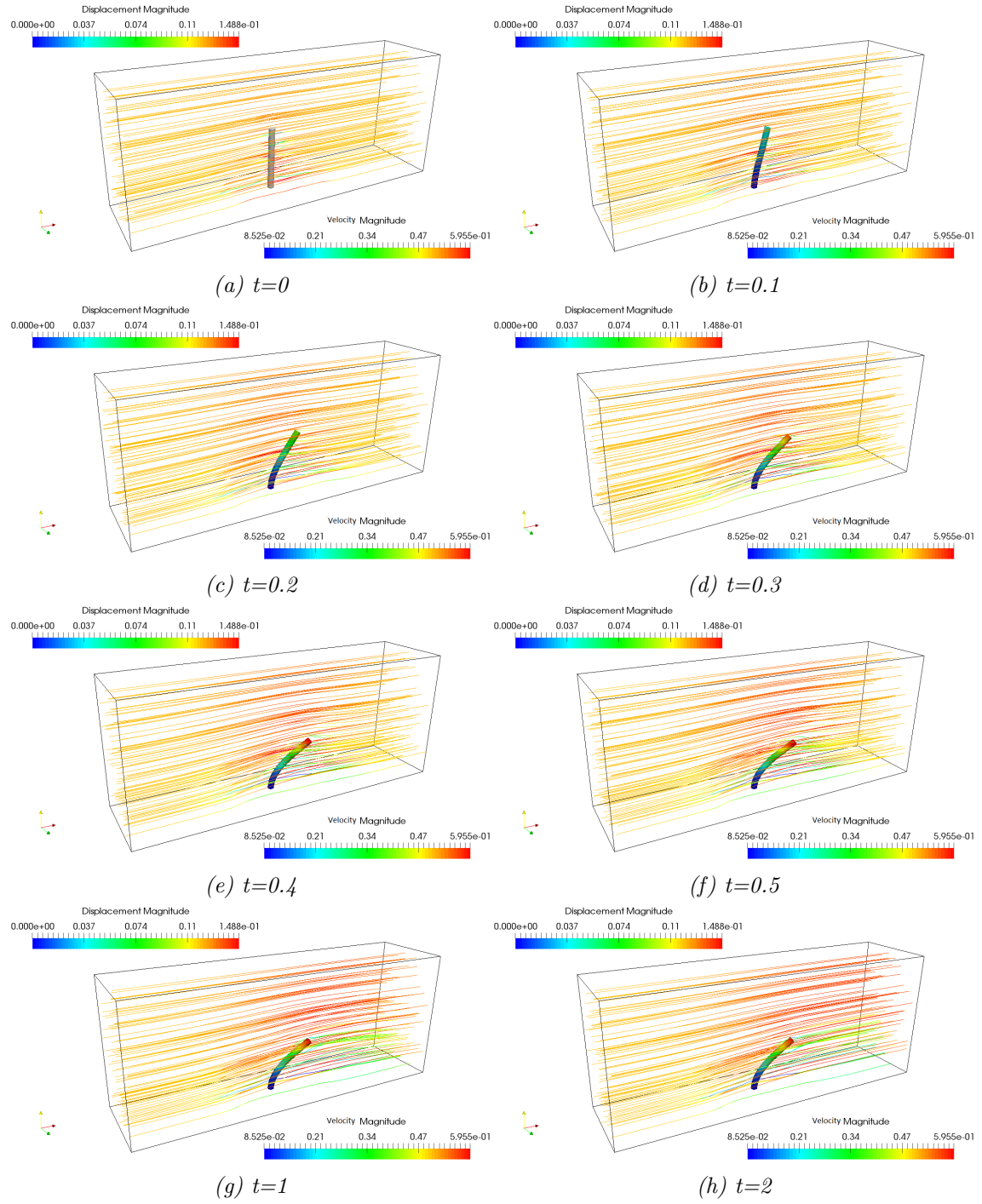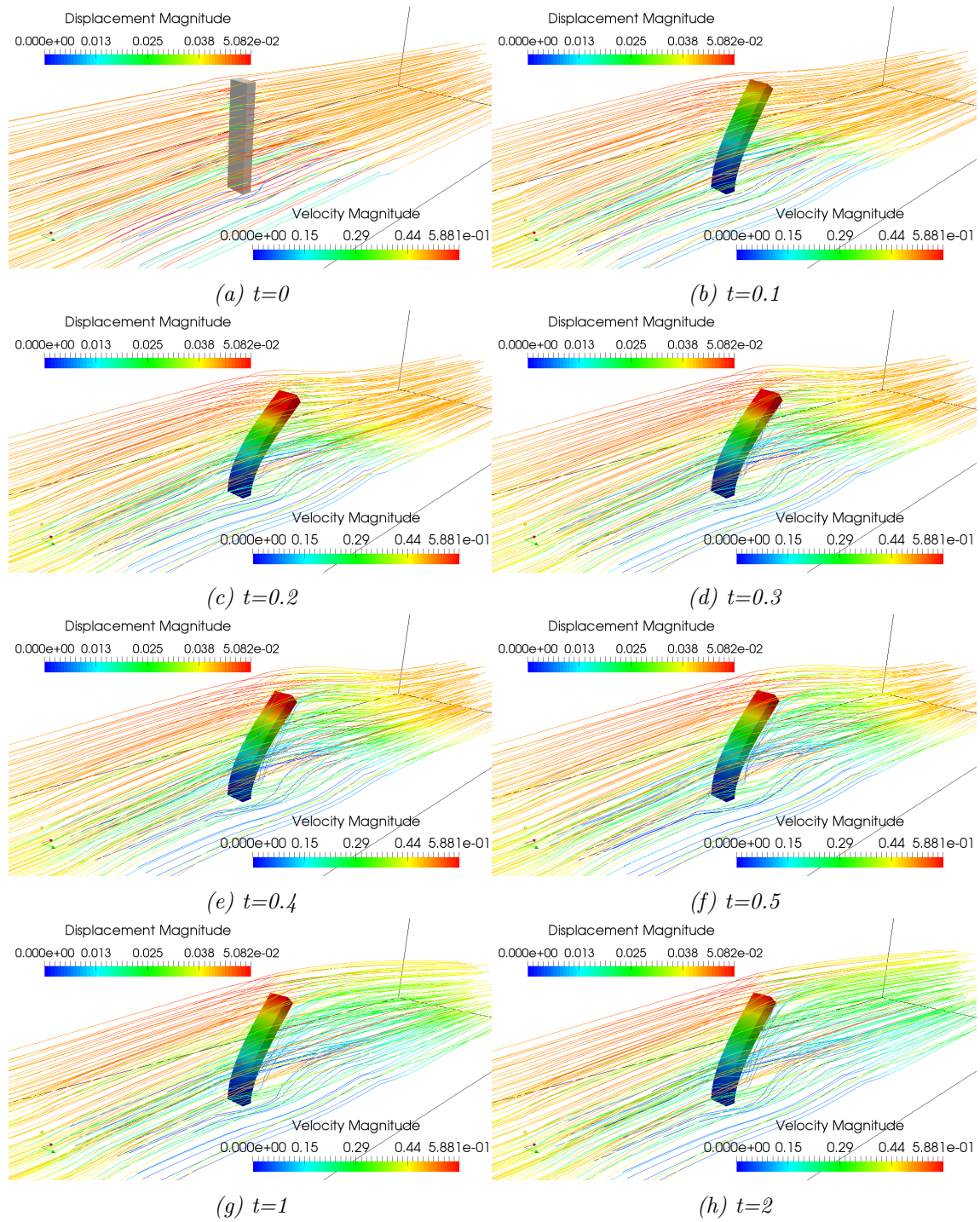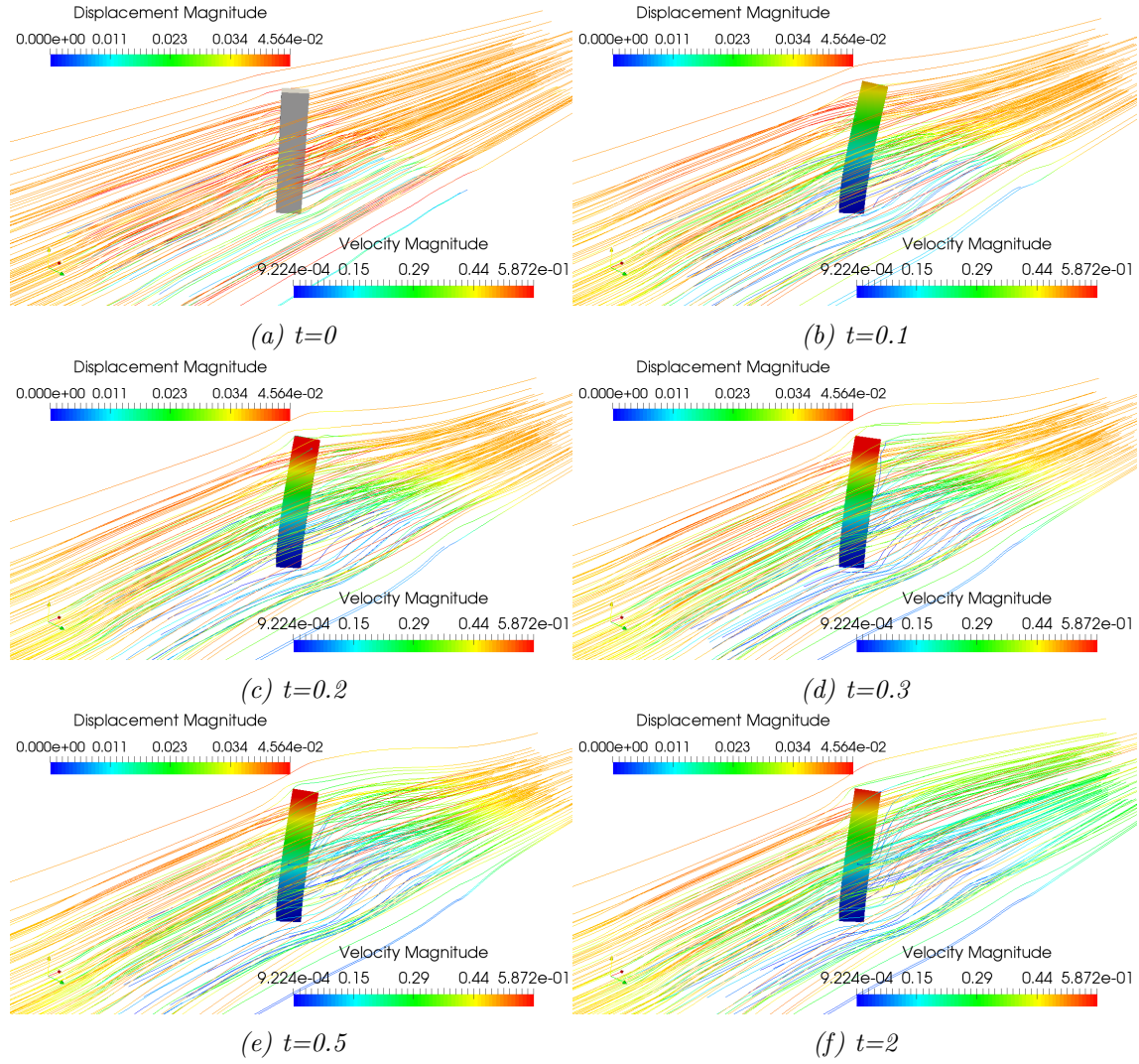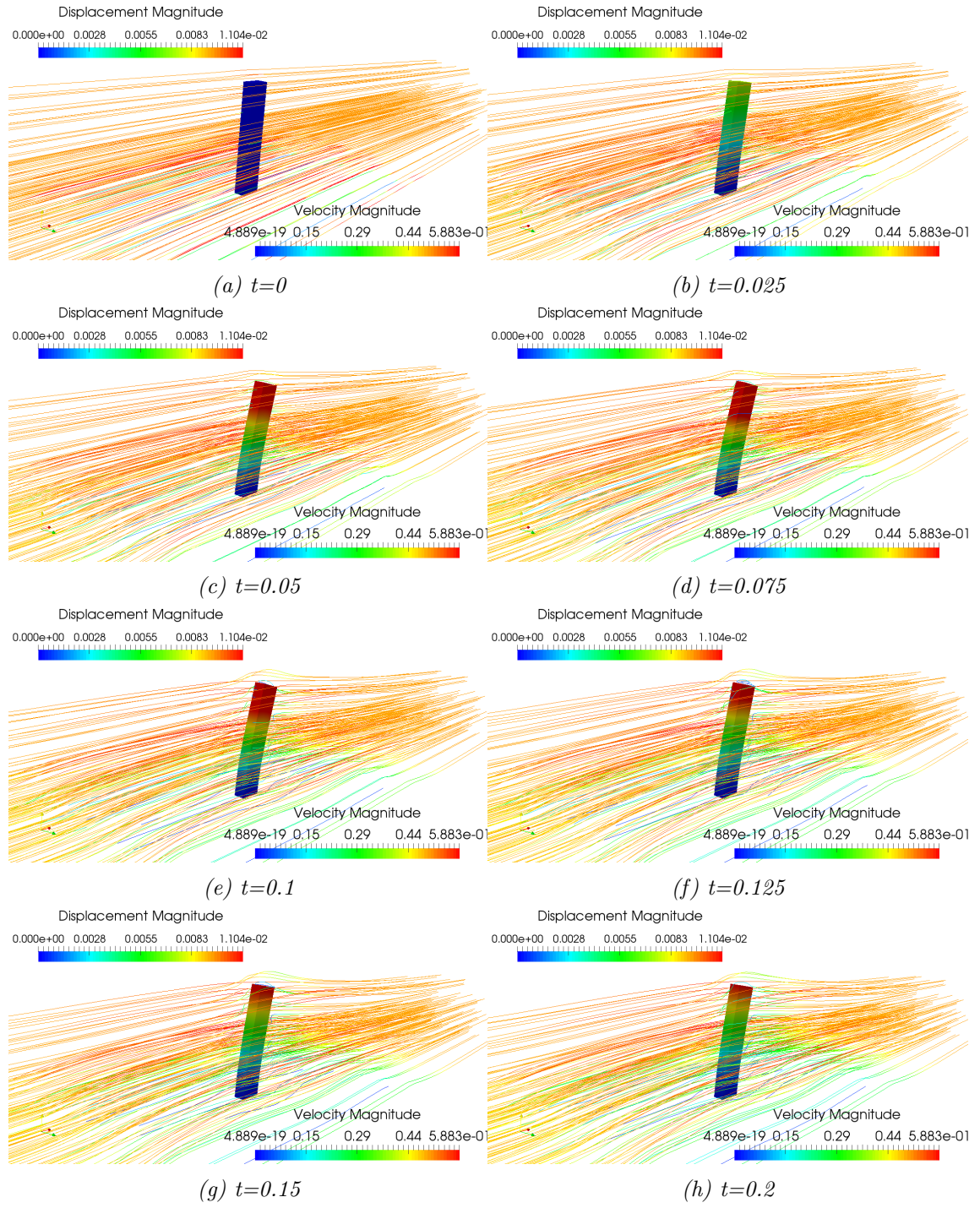
Hughes, Y. Xu, Fluid structure interaction of patient specific abdominal aortic aneurysms: a comparison with solid stress models, Biomedical engineering online 5 (1) (2006) 1–15. 86

[6] S. Deparis, M. A. Fernández, L. Formaggia, Acceleration of a fixed point algorithm for fluid-structure interaction using transpiration conditions, ESAIM: Mathematical Modelling and Numerical Analysis 37 (4) (2003) 601–616. 86

[7] F. Chouly, A. Van Hirtum, P.-Y. Lagrée, J.-R. Paoli, X. Pelorson, Y. Payan, Simulation of the retroglossal fluid-structure interaction during obstructive sleep apnea, in: International Symposium on Biomedical Simulation, Springer, 2006, pp. 48–57. 86

[8] R. Garg, C. Narayanan, S. Subramaniam, A numerically convergent lagrangian–eulerian simulation method for dispersed two-phase flows, International Journal of Multiphase Flow 35 (4) (2009) 376–388. 86

[9] R. Glowinski, T. Pan, T. Hesla, D. Joseph, A distributed lagrange multiplier/fictitious domain method for particulate flows, International Journal of Multiphase Flow 25 (5) (1999) 755–794. doi:10.1016/S0301-9322(98)00048-2. 86, 87

[10] H.-O. Kreiss, N. A. Petersson, A second order accurate embedded boundary method for the wave equation with dirichlet data, SIAM Journal on Scientific Computing 27 (4) (2006) 1141–1167. arXiv:https://doi.org/10.1137/040604728, doi:10.1137/040604728.
URL https://doi.org/10.1137/040604728 87

[11] K. Wang, A. Rallu, J.-F. Gerbeau, C. Farhat, Algorithms for Interface Treatment and Load Computation in Embedded Boundary Methods for Fluid and Fluid-Structure Interaction Problems, International Journal for Numerical Methods in Fluids 67 (9) (2011) 1175–1206. doi:10.1002/fld.2556.
URL https://hal.inria.fr/hal-00651118 87

[12] C. S. Peskin, The immersed boundary method, Acta Numerica 11 (2002) 479–517. doi:10.1017/S0962492902000077. 87, 88

[13] P.-O. Persson, J. Peraire, Curved mesh generation and mesh refinement using lagrangian solid mechanics, in: 47th AIAA Aerospace Sciences Meeting including The New Horizons Forum and Aerospace Exposition, 2009, p. 949. 87

[14] J. Donéa, P. Fasoli-Stella, S. Giuliani, Lagrangian and eulerian finite element techniques for transient fluid-structure interaction problems (1977). 87

[15] A. Huerta, W. K. Liu, Viscous flow with large free surface motion, Computer Methods in Applied Mechanics and Engineering 69 (3) (1988) 277–324. doi:https://doi.org/10.1016/0045-7825(88)90044-8.
URL https://www.sciencedirect.com/science/article/pii/0045782588900448 87

[16] T. J. Hughes, W. K. Liu, T. K. Zimmermann, Lagrangian-eulerian finite element formulation for incompressible viscous flows, Computer methods in applied mechanics and engineering 29 (3) (1981) 329–349. 87

[17] A. Gerstenberger, W. A. Wall, An extended finite element method/lagrange multiplier based approach for fluid–structure interaction, Computer Methods in Applied Mechanics and Engineering 197 (19) (2008) 1699–1714, computational Methods in Fluid–Structure Interaction. doi:https://doi.org/10.1016/j.cma.2007.07.002.
URL https://www.sciencedirect.com/science/article/pii/S0045782507002915 87

[18] W. Wall, A. Gerstenberger, U. Mayer, Advances in fixed-grid fluid structure interaction, in: ECCOMAS Multidisciplinary Jubilee Symposium, Springer, 2009, pp. 235–249. 87

[19] W. A. Wall, A. Gerstenberger, P. Gamnitzer, C. Förster, E. Ramm, Large deformation fluid-structure interaction–advances in ale methods and new fixed grid approaches, in: Fluid-structure interaction, Springer, 2006, pp. 195–232. 87

[20] A. Legay, J. Chessa, T. Belytschko, An eulerian–lagrangian method for fluid–structure interaction based on level sets, Computer Methods in Applied Mechanics and Engineering 195 (17-18) (2006) 2070–2087. 87

[21] A. Legay, J. Chessa, T. Belytschko, An eulerian-lagrangian method for fluid-structure interaction based on level sets, Computer Methods in Applied Mechanics and Engineering 195 (2006) 2070–2087. doi:10.1016/j.cma.2005.02.025. 87

[22] A. Zilian, A. Legay, The enriched space–time finite element method (est) for simultaneous solution of fluid–structure interaction, International Journal for Numerical Methods in Engineering 75 (3) (2008) 305–334. 87

[23] Z. Yu, Y. Wang, X. Shao, Numerical simulations of the flapping of a three-dimensional flexible plate in uniform flow, Journal of Sound and Vibration 331 (20) (2012) 4448–4463. doi:https://doi.org/10.1016/j.jsv.2012.05.

009.
URL https://www.sciencedirect.com/science/article/pii/
S0022460X12003616 87

[24] On the instability and the post-critical behaviour of two-dimensional can-
tilevered flexible plates in axial flow, Journal of Sound and Vibration 305 (1)
(2007) 97–115. doi:https://doi.org/10.1016/j.jsv.2007.03.042.
URL https://www.sciencedirect.com/science/article/pii/
S0022460X07002295

[25] L. Tang, M. P. Paı̈doussis, The influence of the wake on the stability of
cantilevered flexible plates in axial flow, Journal of Sound and Vibration
310 (3) (2008) 512–526, eUROMECH Colloquium 484 on Wave Mechanics
and Stability of Long Flexible Structures Subject to Moving Loads and Flows.
doi:https://doi.org/10.1016/j.jsv.2007.09.025.
URL https://www.sciencedirect.com/science/article/pii/
S0022460X07007754

[26] Y. Kerboua, A. Lakis, M. Thomas, L. Marcouiller, Vibration analysis of
rectangular plates coupled with fluid, Applied Mathematical Modelling 32 (12)
(2008) 2570–2586. doi:https://doi.org/10.1016/j.apm.2007.09.004.
URL https://www.sciencedirect.com/science/article/pii/
S0307904X07002260

[27] C. ELOY, R. LAGRANGE, C. SOUILLIEZ, L. SCHOUVEILER, Aeroelastic
instability of cantilevered flexible plates in uniform flow, Journal of Fluid Me-
chanics 611 (2008) 97–106. doi:10.1017/S002211200800284X. 87

[28] F. Paraz, C. Eloy, L. Schouveiler, Experimental study of the response of a flex-
ible plate to a harmonic forcing in a flow, Comptes Rendus Mécanique 342 (9)
(2014) 532–538. doi:https://doi.org/10.1016/j.crme.2014.06.004.
URL https://www.sciencedirect.com/science/article/pii/
S1631072114001247 88

[29] L. Wang, C. Lei, F.-B. Tian, Fluid-structure interaction of a flexible plate
vertically fixed in a laminar boundary layer over a rigid wall, 2018. 88

[30] B. S. H. CONNELL, D. K. P. YUE, Flapping dynamics of a flag in a uni-
form stream, Journal of Fluid Mechanics 581 (2007) 33–67. doi:10.1017/
S0022112007005307. 88

[31] F.-B. Tian, H. Dai, H. Luo, J. F. Doyle, B. Rousseau, Fluid–structure
interaction involving large deformations: 3d simulations and applications to

biological systems, Journal of Computational Physics 258 (2014) 451–469.
doi:https://doi.org/10.1016/j.jcp.2013.10.047.
URL https://www.sciencedirect.com/science/article/pii/
S0021999113007237 88

[32] M. Luhar, H. M. Nepf, Flow-induced reconfiguration of buoyant and flexible aquatic vegetation, Limnology and Oceanography 56 (6) (2011) 2003–2017. 88

[33] E. Svenning, A. Mark, F. Edelvik, Simulation of a highly elastic structure interacting with a two-phase flow, Journal of Mathematics in Industry 4 (1) (2014) 1–11. 88

[34] E. Botia-Vera, A. Souto-Iglesias, G. Bulian, L. Lobovsky, Three sph novel benchmark test cases for free surface flows (06 2010). 88

[35] G. Axtmann, F. Hegner, C. Brücker, U. Rist, Investigation and prediction of the bending of single and tandem pillars in a laminar cross flow, Journal of Fluids and Structures 66 (2016) 110–126. viii, 88, 119, 131, 133

[36] J. Favier, C. Li, L. Kamps, A. Revell, J. O'Connor, C. Brücker, The PELskin project-part I: fluid–structure interaction for a row of flexible flaps: a reference study in oscillating channel flow, Meccanica 52 (8) (2017) 1767 – 1780. doi:
10.1007/s11012-016-0521-0.
URL https://hal.archives-ouvertes.fr/hal-01592866 88

[37] S. Basting, A. Quaini, S. Čanić, R. Glowinski, Extended ale method for fluid–structure interaction problems with large structural displacements, Journal of Computational Physics 331 (2017) 312–336. 89

[38] D. Jodlbauer, U. Langer, T. Wick, Parallel block-preconditioned monolithic solvers for fluid-structure interaction problems, International Journal for Numerical Methods in Engineering 117 (6) (2019) 623–643. 89

[39] P. Ryzhakov, R. Rossi, S. Idelsohn, E. Onate, A monolithic lagrangian approach for fluid–structure interaction problems, Computational mechanics 46 (6) (2010) 883–899. 89

[40] A. J. Gil, A. A. Carreno, J. Bonet, O. Hassan, The immersed structural potential method for haemodynamic applications, Journal of Computational Physics 229 (22) (2010) 8613–8641. 89

[41] T. Wick, Flapping and contact fsi computations with the fluid-solid interface-tracking/interface-capturing technique and mesh adaptivity, Computational Mechanics 53 (10 2013). doi:10.1007/s00466-013-0890-3. 89

141

Bibliography

[42] J. Bruchon, H. Digonnet, T. Coupez, Using a signed distance function for the simulation of metal forming processes : Formulation of the contact condition and mesh adaptation. From a Lagrangian approach to an Eulerian approach, International Journal for Numerical Methods in Engineering 78 (8) (2009) 980–1008. doi:10.1002/nme.2519.
URL https://hal-emse.ccsd.cnrs.fr/emse-00475556 93

[43] R. Codina, O. Soto, A numerical model to track two-fluid interfaces based on a stabilized finite element method and the level set technique, International Journal for Numerical Methods in Fluids 40 (2002) 293 – 301. doi:10.1002/fld.277. 93

[44] L. Formaggia, S. Perotto, Anisotropic error estimates for elliptic problems, Numerische Mathematik 94 (1) (2003) 67–92. 94

[45] J. Hoffman, C. Johnson, Adaptive finite element methods for incompressible fluid flow, Error Estimation and Adaptive Discretization in Computational Fluid Dynamics (Ed. T. J. Barth and H. Deconinck), Lecture Notes in Computational Science and Engineering Vol.25, Springer-Verlag Publishing, Heidelberg, 2003. 94

[46] M. Khalloufi, Y. Mesri, R. Valette, E. Massoni, E. Hachem, High fidelity anisotropic adaptive variational multiscale method for multiphase flows with surface tension, Computer Methods in Applied Mechanics and Engineering 307 (2016) 44 – 67. 94

[47] G. Legrain, N. Moës, Adaptive anisotropic integration scheme for high-order fictitious domain methods: Application to thin structures, International Journal for Numerical Methods in Engineering 114 (8) (2018) 882–904. 94

[48] T. Coupez, Metric construction by length distribution tensor and edge based error for anisotropic adaptive meshing, Journal of Computational Physics 230 (7) (2011) 2391–2405. 94, 95, 96

[49] G. Kunert, R. Verfürth, Edge residuals dominate a posteriori error estimates for linear finite element methods on anisotropic triangular and tetrahedral meshes, Numer. Math. 86 (2) (2000) 283–303. 95

[50] R. Nemer, A. Larcher, T. Coupez, E. Hachem, Stabilized finite element method for incompressible solid dynamics using an updated lagrangian formulation, Computer Methods in Applied Mechanics and Engineering 384 (2021) 113923. doi:https://doi.org/10.1016/j.cma.2021.113923.
URL https://www.sciencedirect.com/science/article/pii/S0045782521002607 99

Bibliography

[51] I. Babuška, Error-bounds for finite element method, Numerische Mathematik 16 (4) (1971) 322–333. 100

[52] T. J. Hughes, L. P. Franca, M. Balestra, A new finite element formulation for computational fluid dynamics: V. circumventing the babuška-brezzi condition: a stable petrov-galerkin formulation of the stokes problem accommodating equal-order interpolations, Computer Methods in Applied Mechanics and Engineering 59 (1) (1986) 85 – 99. 100, 103

[53] E. Hachem, B. Rivaux, T. Kloczko, H. Digonnet, T. Coupez, Stabilized finite element method for incompressible flows with high reynolds number, Journal of Computational Physics 229 (23) (2010) 8643 – 8665. 100, 103

[54] T. J. Hughes, L. P. Franca, A new finite element formulation for computational fluid dynamics: Vii. the stokes problem with various well-posed boundary conditions: Symmetric formulations that converge for all velocity/pressure spaces, Computer Methods in Applied Mechanics and Engineering 65 (1) (1987) 85 – 96. 100

[55] L. P. Franca, T. J. Hughes, A. F. Loula, I. Miranda, A new family of stable elements for nearly incompressible elasticity based on a mixed petrov-galerkin finite element formulation, Numer. Math. 53 (1–2) (1988) 123–141. 100

[56] T. J. Hughes, G. R. Feijóo, L. Mazzei, J.-B. Quincy, The variational multi-scale method—a paradigm for computational mechanics, Computer methods in applied mechanics and engineering 166 (1-2) (1998) 3–24. 100

[57] T. Dubois, Y. Matras, F. Jauberteau, R. Temam, Dynamic multilevel methods and the numerical simulation of turbulence, Cambridge University Press, 1999. 101

[58] R. Codina, J. Principe, Dynamic subscales in the finite element approximation of thermally coupled incompressible flows, International Journal for Numerical Methods in Fluids 54 (6-8) (2007) 707–730. arXiv:https://onlinelibrary.wiley.com/doi/pdf/10.1002/fld.1481, doi:https://doi.org/10.1002/fld.1481.
URL https://onlinelibrary.wiley.com/doi/abs/10.1002/fld.1481 101

[59] E. Hachem, M. Khalloufi, J. Bruchon, R. Valette, Y. Mesri, Unified adaptive variational multiscale method for two phase compressible–incompressible flows, Computer Methods in Applied Mechanics and Engineering 308 (2016) 238–255. doi:https://doi.org/10.1016/j.cma.2016.05.022.
URL https://www.sciencedirect.com/science/article/pii/S0045782516304236 102

[60] R. Codina, Stabilized finite element approximation of transient in-
compressible flows using orthogonal subscales, Computer Methods
in Applied Mechanics and Engineering 191 (39) (2002) 4295–4321.
doi:https://doi.org/10.1016/S0045-7825(02)00337-7.
URL https://www.sciencedirect.com/science/article/pii/
S0045782502003377 102

[61] J. Baiges, R. Codina, The fixed-mesh ale approach applied to solid mechanics
and fluid-structure interaction problems, International Journal for Numerical
Methods in Engineering 81 (2009) 1529 – 1557. doi:10.1002/nme.2740. 104

[62] A. Tello, R. Codina, J. Baiges, Fluid structure interaction by means of vari-
ational multiscale reduced order models, International Journal for Numer-
ical Methods in Engineering 121 (12) (2020) 2601–2625. arXiv:https://
onlinelibrary.wiley.com/doi/pdf/10.1002/nme.6321, doi:https://doi.
org/10.1002/nme.6321.
URL https://onlinelibrary.wiley.com/doi/abs/10.1002/nme.6321 104

[63] D. Han, G. Liu, S. Abdallah, An eulerian-lagrangian-lagrangian method
for 2d fluid-structure interaction problem with a thin flexible struc-
ture immersed in fluids, Computers & Structures 228 (2020) 106179.
doi:https://doi.org/10.1016/j.compstruc.2019.106179.
URL https://www.sciencedirect.com/science/article/pii/
S0045794919303372 104

[64] Z.-Q. Zhang, G. Liu, B. Khoo, Immersed smoothed finite element method for
two dimensional fluid–structure interaction problems, International Journal for
Numerical Methods in Engineering 90 (06 2012). doi:10.1002/nme.4299. 104

[65] G. Xia, C.-L. Lin, An unstructured finite volume approach for structural dy-
namics in response to fluid motions, Computers & structures 86 (7-8) (2008)
684–701. 107

[66] M. Schäfer, S. Turek, F. Durst, E. Krause, R. Rannacher, Benchmark com-
putations of laminar flow around a cylinder, in: Flow simulation with high-
performance computers II, Springer, 1996, pp. 547–566. 113

[67] S. Turek, J. Hron, Proposal for numerical benchmarking of fluid-structure in-
teraction between an elastic object and laminar incompressible flow, in: Fluid-
structure interaction, Springer, 2006, pp. 371–385. 113

[68] C. Brücker, J. Spatz, W. Schröder, Feasability study of wall shear stress imaging
using microstructured surfaces with flexible micropillars, Experiments in fluids
39 (2) (2005) 464–474. 118

[69] T. Bano, F. Hegner, M. Heinrich, R. Schwarze, Investigation of fluid-structure interaction induced bending for elastic flaps in a cross flow, Applied Sciences 10 (2020) 6177. `doi:10.3390/app10186177`. 123

Bibliography

Chapter 5

Industrial Application

Contents

La plongée sous-marine est une action humaine dans laquelle ce dernier descend sous la surface de l'eau pour explorer ou interagir avec l'environnement. Il a un but récréatif, militaire et scientifique. L'être humain n'étant pas apte biologiquement et psychologiquement à cette activité, des équipements sont utilisés pour mieux s'adapter à cet environnement hostile. Beaucoup de recherches vont dans ce domaine pour mieux aider l'être humain dans ses efforts sous-marins. L'objectif de la recherche dans ce domaine est de parvenir à un équipement de pointe permettant à l'utilisateur de respirer sous l'eau avec une résistance minimale comme s'il respirait au-dessus de l'eau à une pression ambiante normale. Les bouteilles de plongée sont des réservoirs hautement pressurisés, contenant le gaz à inhaler. Un être humain a un certain seuil de différence de pression qui peut être respiré sans effets secondaires. Par conséquent, l'un des principaux équipements utilisés en plongée sous-marine est un régulateur de pression, qui permet de réduire la pression présente dans le réservoir vers la pression ambiante. Le régulateur de pression est composé de deux étages ; la diminution de la pression se fait successivement par les étapes un et deux. Tout d'abord, le premier étage réduit la pression à une pression dite intermédiaire, qui est ensuite abaissée par le deuxième étage à une pression ambiante finale. La deuxième étape sera notre objectif principal, et il comprend deux chambres séparées par une membrane et un mécanisme de craquage pour fournir à l'utilisateur du gaz respiratoire. Or pour respirer, il faut fournir une pression d'aspiration suffisamment élevée en valeur absolue, pour déclencher un mécanisme à levier. Cette pression seuil est appelée pression de craquage. Une pression de craquage plus faible entraîne une résistance respiratoire plus faible. La résistance à l'expiration est bien plus importante que la résistance à l'inspiration. Les tests du régulateur de pression sont généralement effectués selon l'Agence nationale pour la science, la technologie et l'innovation (ANSTI). L'objectif fixé par l'US Navy est de 1,3 J/L ou moins à 62,5 L/min RMV (Respiratory Minute Volume) à 132 et 198 fsw (pieds dans l'eau salée) avec un réservoir à 1 500 psi. AquaLung cherche à établir un simulateur pour leur régulateur de pression, afin d'améliorer/optimiser davantage ce dernier. Dans un premier temps, nous sommes partis d'une pure simulation CFD tridimensionnelle d'un des produits de notre partenaire industriel. Cela permet de comprendre leur configuration expérimentale et de pouvoir la représenter sous forme de simulation numérique à des fins de comparaison par la suite. Le but de la simulation est de dupliquer le graphique obtenu à l'aide de tests expérimentaux, créant ainsi une configuration virtuelle qui peut aider à optimiser les performances du régulateur. Après une validation suffisante du cadre FSI AIMM, il a été appliqué à l'application industrielle. Dans cette application particulière, un écoulement multiphasique est nécessaire pour simuler correctement les performances du produit. D'un côté, il y a le gaz de travail pour la plongée, et de l'autre, nous avons l'eau

148

salée. Ces deux fluides sont délimités par une fine membrane composée de parties rigides et flexibles qui actionnent le mécanisme à levier à une certaine pression de claquage. Habituellement, les matériaux, et plus particulièrement les métaux, commencent par avoir une réponse élastique linéaire à une contrainte appliquée jusqu'à atteindre une certaine limite d'élasticité, après quoi une déformation plastique commence à se produire. La striction se produit au point de résistance ultime, après quoi le matériau se déformera jusqu'à la rupture. Cependant, ce n'est pas le comportement typique des polymères. Là où une réponse hyperélastique est attendue. L'application d'intérêt n'induit pas de déformation plastique. Ainsi, nous nous concentrerons sur la réponse hyperélastique du matériau. Le fournisseur du matériau n'avait pas suffisamment de détails sur le comportement de la membrane à portée de main. Par conséquent, une analyse mécanique dynamique (DMA) a été menée sur des échantillons coupés du matériau. Il s'agit d'une méthode pour caractériser et inspecter certains matériaux. Il est principalement utilisé pour les polymères à comportement viscoélastique. Cela signifie un matériau qui subit à la fois un comportement élastique et visqueux sous contrainte. Les matériaux viscoélastiques présentent à la fois un comportement visqueux et élastique, entraînant ainsi une déformation dépendante du temps. La DMA consiste à appliquer une contrainte sinusoïdale, et à mesurer la déformation correspondante du matériau. Cela nous permet de calculer un module complexe. On peut faire varier généralement soit la température, soit la fréquence de la contrainte appliquée. Cela conduira à différentes valeurs du module complexe. Ce qui aide inévitablement à localiser la température de transition vitreuse du matériau en question. Cette température est le seuil pour lequel le matériau passe d'un comportement de type cassant à un comportement de type caoutchouteux. Si le matériau est un solide parfaitement élastique, les courbes de déformation et de contrainte seront parfaitement en phase. Si le matériau est un fluide purement visqueux, on observe un déphasage de 90 degrés de la déformation à la contrainte. Le comportement viscoélastique est caractérisé comme un comportement intermédiaire entre les comportements purs susmentionnés. Un certain décalage de phase est lié à se produire dans un test DMA pour un matériau viscoélastique. Un balayage de température a été effectué à une fréquence de $1Hz$, où une température de transition vitreuse a été déterminée qui est significativement inférieure à la température d'application. Le balayage de température a été effectué deux fois pour tenir compte de la reproductibilité des résultats et de toute hystérésis éventuelle observée dans les données. Un balayage combiné a ensuite été effectué deux fois, pour voir l'effet du changement de fréquence sur les différents intervalles de températures. Maintenant que tous les composants de cette simulation FSI complexe 3D hautefidélité ont été rassemblés, la simulation est exécutée pendant un cycle complet, et les résultats sont présentés ci-après. Ce cadre était capable de gérer une simulation FSI 3D complexe. Cela a été fait en utilisant le cadre AIMM FSI développé dans les chapitres

précédents. La complexité provenait de la nature multi phase de l'écoulement, en ayant l'eau d'un côté et le gaz de travail de l'autre côté. De plus, la membrane séparant les deux domaines est en fait très fine, ajoutant ainsi plus de complexité à la simulation. Sans oublier le nombre de Reynolds très élevé dans le domaine du gaz de travail, notamment pour la phase d'inspiration.

5.1 Introduction

Underwater diving is a human action in which the latter descends below the surface of the water to explore or interact with the environment. It has a recreational, military, and scientific purpose. As the human being is not fit both biologically and psychologically for this activity, equipment is used to better adapt to this harsh environment. A lot of research goes into this field to better help the human being with his underwater endeavors. A homo sapiens has a tidal volume of 0.5 L of air, corresponding to the air breathed in and out, while vital capacity is defined as the maximum quantity of air that can be breathed in or out. In addition to the tidal volume and vital capacity, a human being has a respiratory reserve, which cannot be used unless there is a real-life threatening case, in which the human body response will make use of the reserve. A normal person breathes around 10 to 20 breaths/min, 45 breaths/min while in exercise, and 25 to 31 breaths/min in a relaxing dive. The aim of research in this field is to reach state-of-the-art equipment to enable the user to breathe underwater with minimal resistance as if they are breathing above water in normal ambient pressure. Scuba tanks are highly pressurized tanks, containing the gas to be inhaled. A human being has a certain threshold for the pressure difference which can be breathed with no side effects. Therefore, one of the main equipment used in underwater diving is a pressure regulator shown in Figure 5.1, which helps reduce the pressure present in the tank towards ambient pressure. The pressure regulator is composed of two stages; the pressure decrease is done successively through stages one and two. First, stage one reduces the pressure to a so-called intermediate pressure, which is then lowered by the second stage to a final ambient pressure. Stage one has different configurations, one of which is found in Figure 5.2. The schematic of the second stage, which will be our primary objective is shown in Figure 5.3 below, and it includes two chambers separated by a membrane and a cracking mechanism to supply the user with breathing gas.
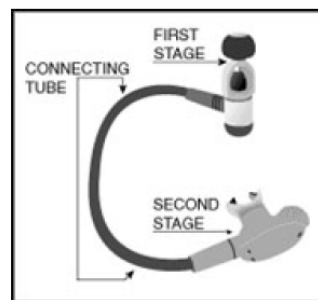

Figure 5.1: Stages one and two of a pressure regulator.

A purge button is readily available on almost all commercial pressure regulators

to remove excess water from the second chamber. Now to breathe, one must provide a suction pressure high enough in absolute value, to trigger a lever mechanism. This threshold pressure is called the cracking pressure. Lower cracking pressure leads to lower breathing resistance. The expiration resistance is far more important than the inspiration resistance. Pressure regulator testing is usually done according to the National Agency for Science, Technology, and Innovation (ANSTI), in which a sample graph that needs to be met or improved is found in Figure 5.4 below. The goal set by the US Navy is 1.3 J/L or less at 62.5 L/min RMV(Respiratory Minute Volume) at both 132 and 198 fsw (feet in saltwater) with a tank at 1500 psi [1] [2]. AquaLung is seeking to establish a simulator for their pressure regulator, to further enhance/optimize the latter.

5.2 Fluid flow simulation

At first, we started with a pure three-dimensional CFD simulation of one of the products of our industrial partner. This helps understand their experimental setup, and how to be able to represent it as a numerical simulation for comparison afterward. First, we must define our computational domain, a description of the problem at hand is given in figure 5.5. The experimental setup forces the air flux through the mouth opening of the second stage of the pressure regulator using the following function

$$V(t) = \frac{V_T}{2}(1 - \cos(\frac{2\pi}{T}t)). \tag{5.1}$$
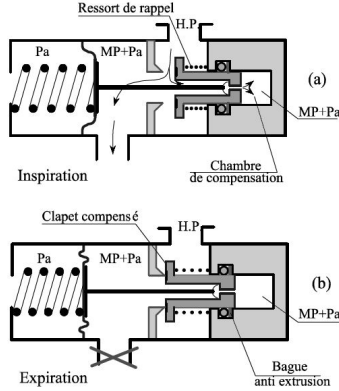

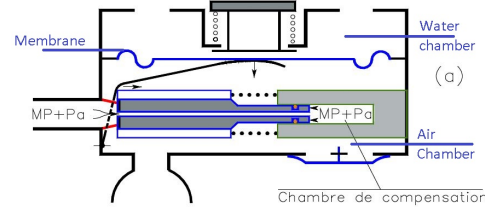Figure 5.2: Schematic of the first stage.

Figure 5.3: Schematic of the second stage.

Where V is the fluid volume through the opening, V_T is the tidal volume, T is the period, and t is time. Taking the derivative with respect to time of the above equation, we obtain the equation of the air flux through the opening

152

```
                        DEMAND REGULATOR PERFORMANCE

──ANSTI─────────────────AQUA-LUNG FRANCE─────────────────────ANSTI──
CERTIFICATE REFERENCE             : ADM050719875
DATE : 21/08/2018                                    TIME : 15:22:47
────────────────────────────────────────────────────────────────────
EQUIPMENT
REGULATOR TYPE                    : LEGEND
SERIAL NUMBER                     : I029602
INTERSTAGE PRESSURE               : 8,72 barg
────────────────────────────────────────────────────────────────────
CONDITIONS OF TEST                  MEAN          MIN           MAX
ROOM TEMPERATURE (C)              : 25,0
WATER TEMPERATURE (C)             : 24,2         24,2          24,2
EXHALE TEMPERATURE (C)            : 25,7         25,6          25,9
FAST RESPONSE TEMP MIN (C)        : 50,2         50,2          50,2
FAST RESPONSE TEMP MAX (C)        : 50,2         50,2          50,2
HP SUPPLY PRESSURE (barg)         : 45,2         44,2          46,7
TIDAL VOLUME (litre)              : 2,50
BREATH RATE (bpm)                 : 24,87        24,77         25,02
VENTILATION RATE (lpm)            : 62,2         61,9          62,6
────────────────────────────────────────────────────────────────────
RESULTS (6 LOOPS)                   MEAN          MIN           MAX
INHALE PRESSURE (mbar)            = 10,46        9,78          11,62
INHALE POS PRESSURE (mbar)        = 2,92         2,43          3,63
EXHALE PRESSURE (mbar)            = 8,92         8,36          9,38
EXT WORK OF BREATHING (J/l)       = 0,66         0,64          0,68
    INHALE WORK (J/l)             = 0,11         0,10          0,12
POS INHALE WORK (J/l)             = 0,07         0,06          0,09
    EXHALE WORK (J/l)             = 0,55         0,53          0,57
────────────────────────────────────────────────────────────────────
```
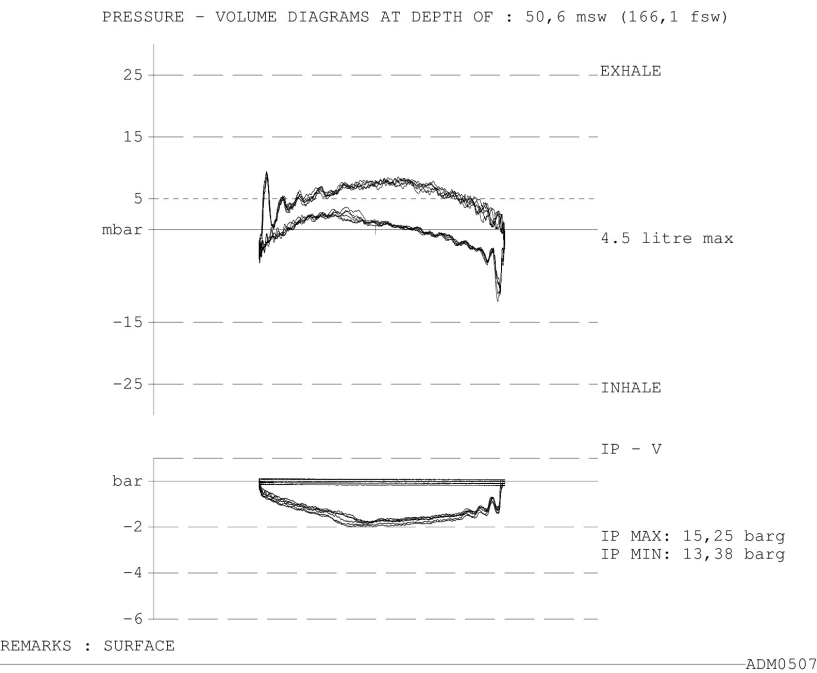

Figure 5.4: ANSTI testing graph example.

153

$$Q(t) = \frac{\pi V_T}{T} \sin(\frac{2\pi}{T}t). \tag{5.2}$$

Where $Q(t)$ is the air flux through the opening. To be able to obtain the velocity at the mouth opening, we divide the flux equation by the area, and we obtain

$$v(t) = \frac{\pi V_T}{AT} \sin(\frac{2\pi}{T}t). \tag{5.3}$$

Where A is the area. A period corresponds to one full breathing cycle (Inspiration/Expiration). For example, let's assume that the experiment is conducted for a breathing rate of $20bpm$, the period will be equivalent to $T = 3s$. Also, a ventilation rate is given for each conducted experiment, which ultimately helps calculate the tidal volume V_T. The first half of the period represents the inspiration phase, while the second half represents the expiration phase. This velocity equation will be used to impose a Dirichlet boundary condition on the velocity for the inlet of the simulation fluid domain. No-slip condition is applied at the walls of the domain. Zero stress condition is applied at the outlets of the truncated domain. Forced membrane valves open and close depending on the half period that we are currently simulating. The fluid properties are given by the temperature and pressure of the experimental setup using thermodynamics principles. For example, assume air is the working fluid, with a temperature of $28C$, and a pressure of $3.5bar$, which is equivalent to a depth of $25m$ in saltwater. Then, the density and dynamic viscosity of the fluid are given by $\rho = 4.0601 Kg/m^3$, and $\mu = 18.6478 \cdot 10^{-6} Pa.s$ respectively.

The goal of the simulation is to duplicate the graph obtained using experimental testing, thus creating a virtual setup that can help optimize the performance of the regulator. In the experimental setup, pressure sensors are strategically positioned at a certain distance from the opening, and data is retrieved and plotted versus the volume as in figure 5.4. Figure 5.4 also shows the truncated computational domain chosen for the simulation. A "Standard Triangle Language" or "Standard Tessellation Language" (STL) file was provided by the industrial partner, which describes the surface with a mesh using triangular elements. It is used to help us create our three-dimensional mesh of unstructured tetrahedral elements like the one shown in figure 5.6. Pressure sensors are placed at the same position in the simulation setup, for us to compare with the experimental results. The fluid domain, along with an idea of the positions of the pressure sensors is given in figure 5.5.

We are using the simulation library CimLib to solve the incompressible Navier-Stokes equations as already described in previous sections. A time step convergence study was first conducted to choose the appropriate time step for the simulator. We chose three different time steps from 1 to 3, with 1 being the biggest, and 3 being the smallest. We also ran the simulations for two whole periods, to ensure reproducibility of the results. The results obtained are shown in figure 5.7. A mesh
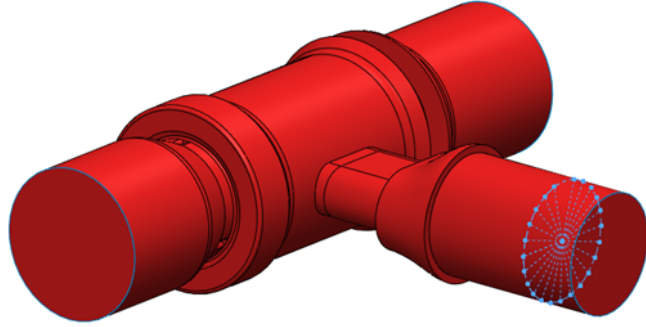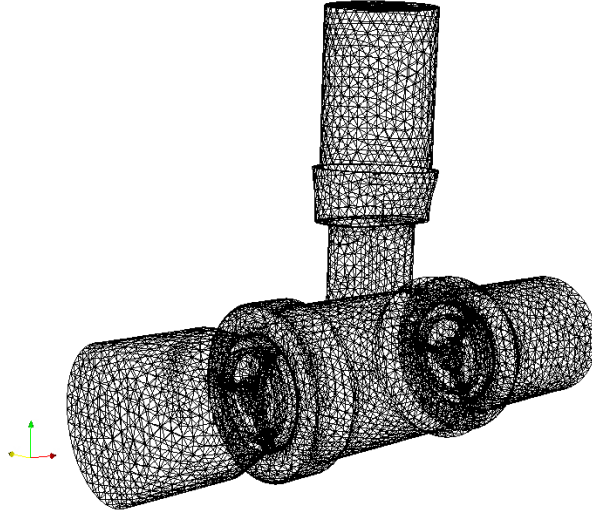
Figure 5.5: Pressure sensors.

Figure 5.6: An example of the domain mesh made up of 3D tetrahedral elements.

convergence study was also conducted. Three different levels of mesh refinement are considered, with 1 being the coarsest, and 3 being the finest. After the third level of refinement, no significant change in the solution was observed. The results obtained are shown in figure 5.8. After establishing a satisfying time step, and mesh refinement level, the simulator was used for three different depths, while varying the ventilation rate at each depth to have enough data to validate the simulator. An example of the obtained numerical simulation results compared to the experimental results are shown in figure 5.9. The streamlines highlighted by the velocity magnitude are shown for both phases of the respiratory cycle (Expiration/Inspiration) in

155

figure 5.10. Velocity magnitudes fields and pressure contours for both the expiration and inspiration phases are shown for a 2D cut of the domain in figures 5.11 and 5.12. While we still are not considering a real FSI problem for now, and are only simulating the fluid flow inside the pressure regulator, we wanted to see the effect of the membrane on the flow. Therefore, for the inspiration phase, we considered a rigid membrane in an assumed opened position to see the effects on the inspiration pressure. A finer mesh was considered to take into account the membrane, which has a very thin cross-section. The finer elements were concentrated in an area of interest which is around the membrane. The membrane was immersed in the fluid domain. No-slip condition is imposed on the membrane in the inspiration phase. In the expiration phase, no boundary conditions are imposed on the flagged elements of mesh, thus the membrane is not taken into account.
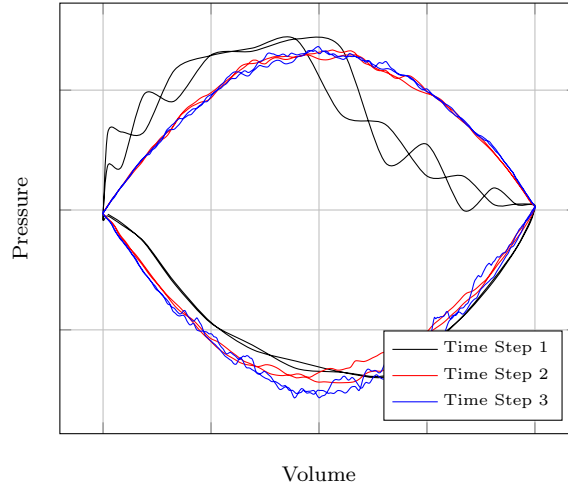
Figure 5.7: Time step convergence study for a CFD simulation of a second stage regulator.

A finer mesh was needed to converge to the same physical solution as before. Figure 5.13, shows the open membrane configuration immersed in the fluid domain and the flow streamline for the inspiration phase. The streamlines are deviated from before, due to the presence of the open membrane in the inspiration phase.

Since the final objective of this fluid flow simulation, was to duplicate the experimental data to create an application for further optimization of the regulator, we suggested a couple of modifications that might be of interest. Two different guiding vanes are positioned inside the regulator that might help guide the flow, thus reducing the overall breathing resistance as shown in figure 5.14. A body-fitted mesh was considered in this case, since the geometry suggested is not to be removed.

Streamlines highlighted by the velocity for both the inspiration and expiration phase respectively are shown in figure 5.15 for the first setup. Figure 5.16 show that of the second setup.
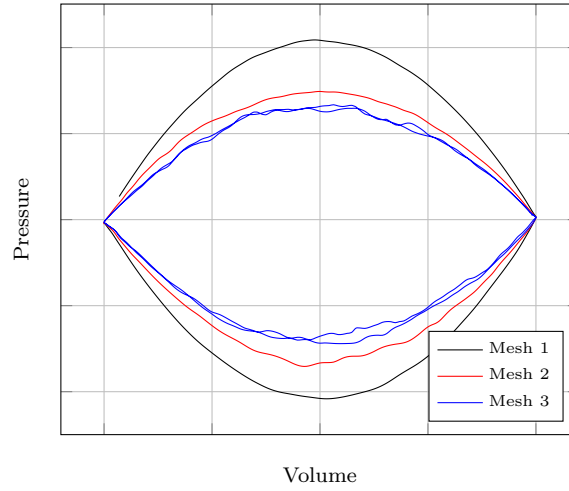
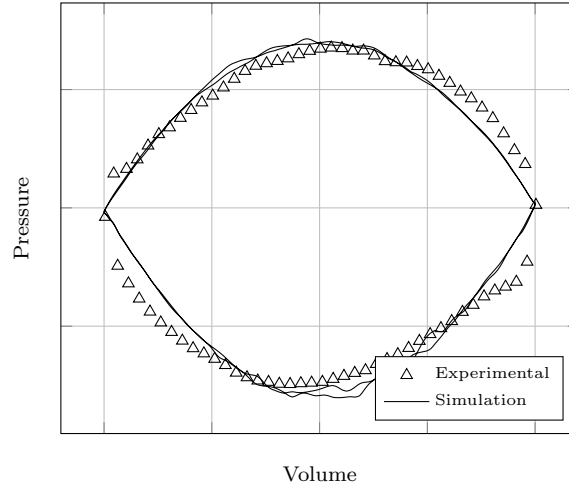*Figure 5.8: Mesh convergence study for a CFD simulation of a second stage regulator.*

Figure 5.9: A comparison between the simulation and experimental data.

5.3 Multi-phase fluid–Membrane interaction simulation

5.3.1 Problem description and fluid flow results

After sufficient validation of the FSI AIMM framework, it was applied to the industrial application. Another second stage commercial regulator is considered for this part of the simulation shown in figure 5.17.

In this particular application, a multi-phase flow is needed to simulate correctly the performance of the product. On one hand, there is the working gas for diving, and on the other, we have the saltwater. These two fluids are delimited by a thin

157
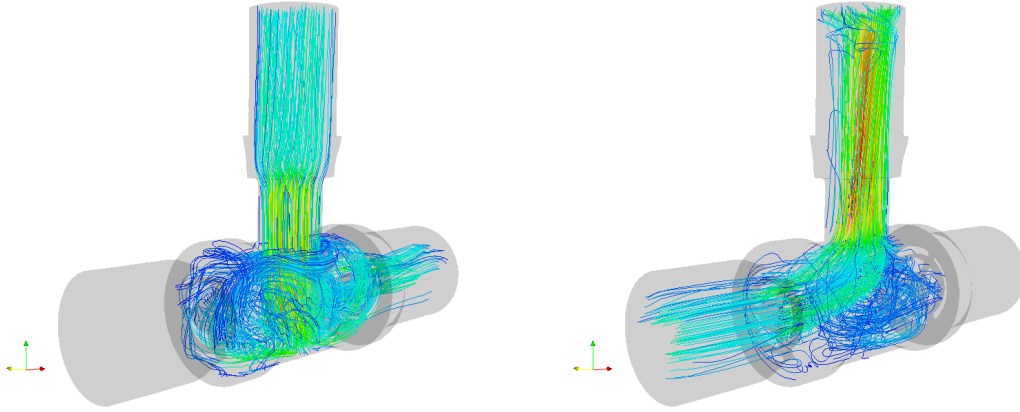
Figure 5.10: *Streamlines highlighted by the velocity field for the expiration and inspiration phase.*
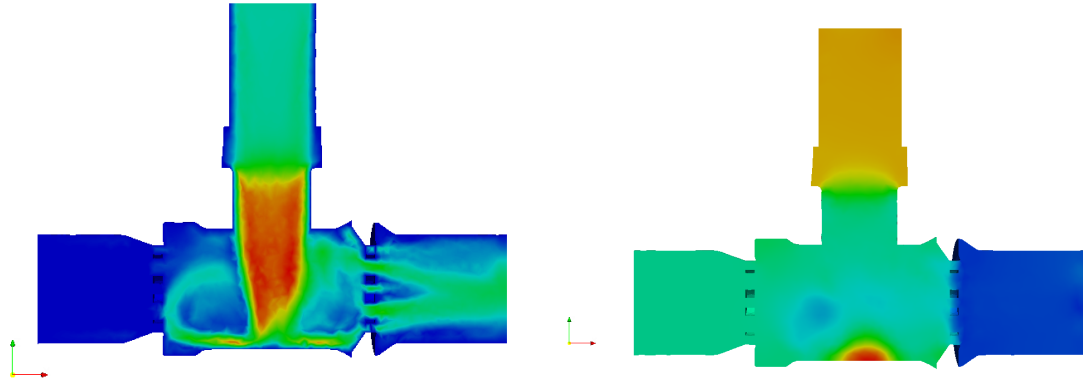
Figure 5.11: *Velocity magnitude and pressure contours for the expiration phase on a plane cut.*

membrane composed of rigid and flexible parts that actuate the lever mechanism at a certain cracking pressure. Figure 5.18, show the inside of the pressure regulator, along with the injection position. Figures 5.19 highlight the areas on which the boundary conditions of the simulator are going to be applied. The first one displays the domain containing the working gas, while highlighting the mouth opening where the sinusoidal velocity function is going to be applied, and the expiration outlet. The second one presents part of the lever mechanism while highlighting the injection surface area. The Computational Fluid Dynamics (CFD) part is like that of the previous application. Figure 5.20 shows a 2D cut schematic of the different components of the simulation. Highlighting specifically:

- The high-pressure gas injection inlet for the inspiration phase.
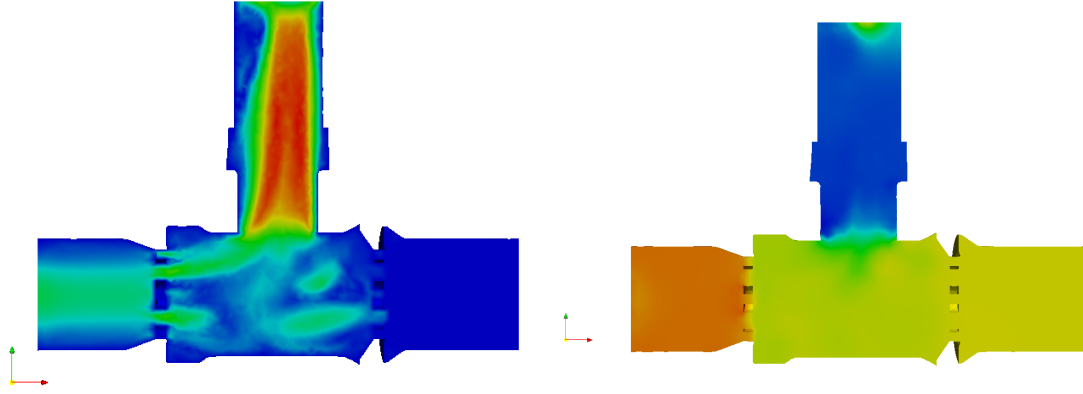
Figure 5.12: Velocity magnitude and pressure contours for the inspiration phase on a plane cut.
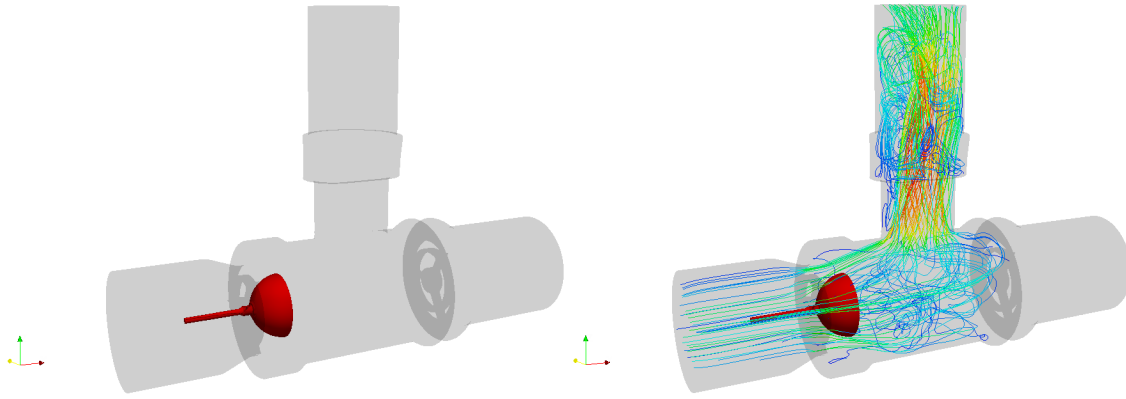
Figure 5.13: Highlighted immersed rigid open membrane configuration, and the streamlines highlighted by the velocity field for the inspiration phase.

- The breathing opening where the sinusoidal function of the velocity is going to be applied.

- The exhaust opening on which the outlet boundary condition is applied during the expiration phase.

- The membrane position, that delimits the water and working gas domain.

The same sinusoidal function is applied at the mouth opening. The domain walls have the no-slip condition applied to them. The highlighted outlet is treated as one for the expiration phase and is considered as a wall for the inspiration phase. The lever mechanism is modeled using a flux function that depends on the maximum displacement of the membrane. Thus, the velocity at the injection surface is zero

159
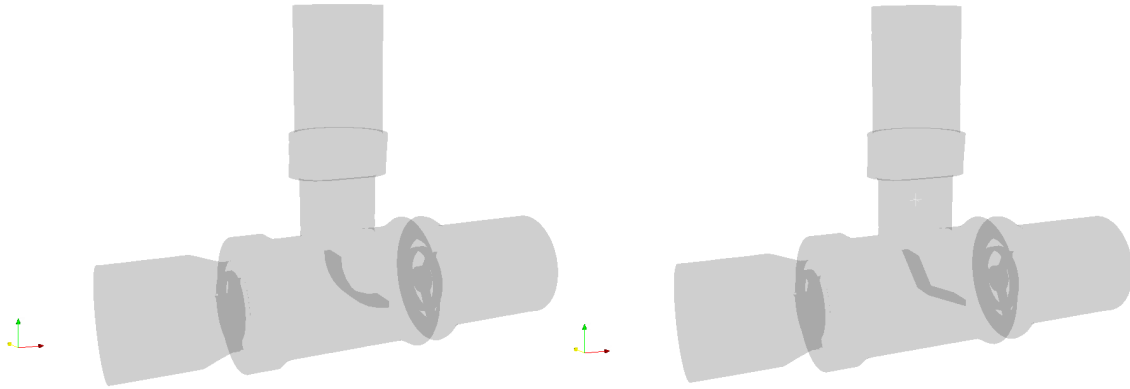
Figure 5.14: First and second guiding vane suggestions respectively.
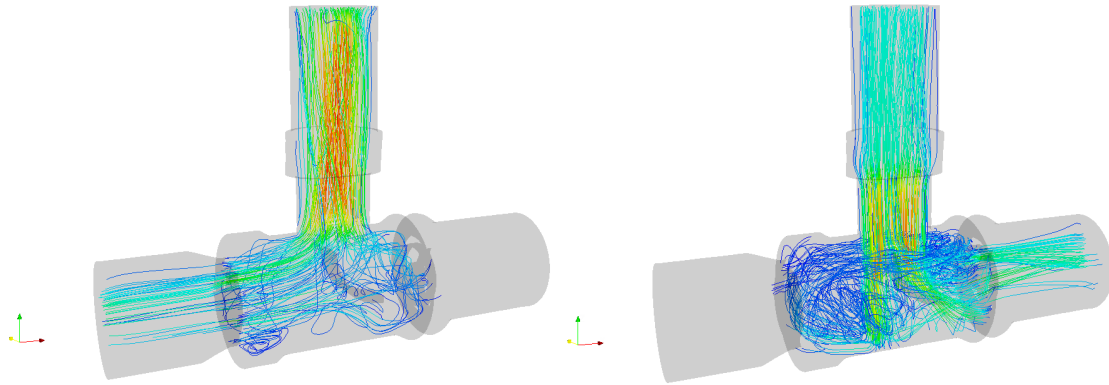
Figure 5.15: Streamlines highlighted by the velocity field for the inspiration and expiration phase of the first configuration.
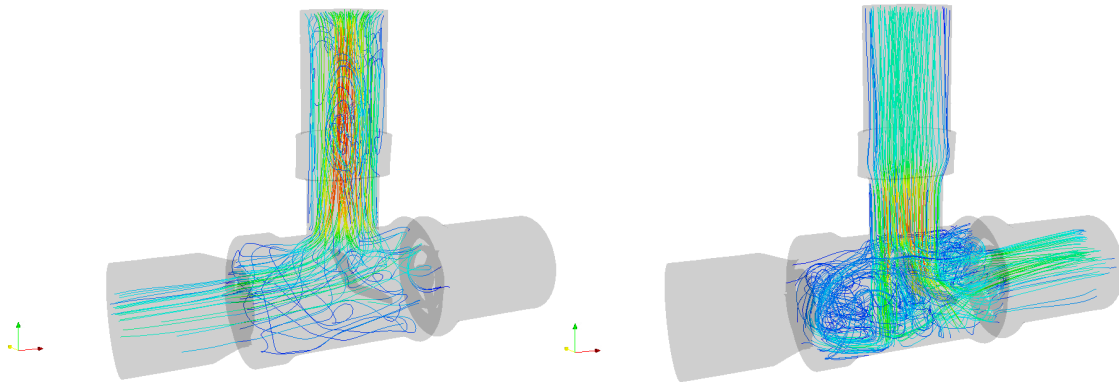

Figure 5.16: Streamlines highlighted by the velocity field for the inspiration and expiration phase of the second configuration.

Figure 5.17: Real life second stage pressure regulator from AquaLung.

during the expiration phase and has an imposed Dirichlet value dependent on the function during inspiration. The mouth opening is enlarged as in the previous application to consider the experimental setup and pressure sensors.
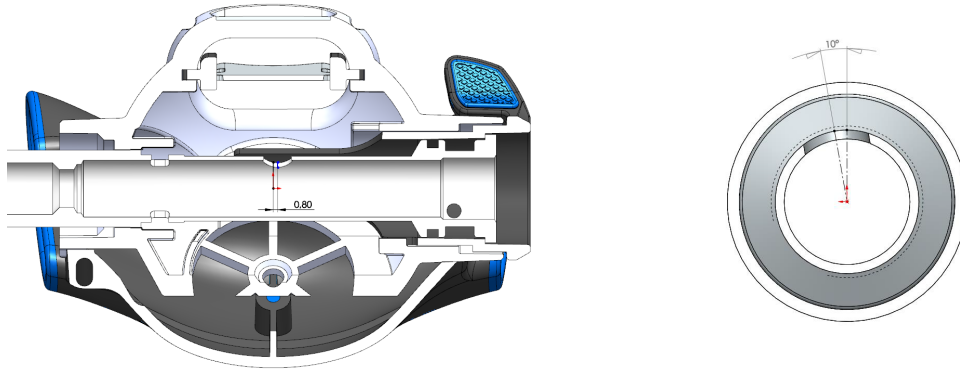
Figure 5.18: Schematic of the inside of a second stage pressure regulator and highlighting the injection position.

A fluid flow simulation was first applied before adding the other components for a full FSI simulation. The considered domain consists of the fluid domain of the working gas delimited by a rigid membrane and the regulator casing. Figure 5.21 shows the computational domain and an example of an unstructured 3D tetrahedral elements mesh for the simulation. Figure 5.22 show the streamlines highlighted by the velocity inside the pressure regulator for the fluid flow simulation. Figure 5.23 gives insight on the flow type inside the regulator for different 2D cuts, which may be
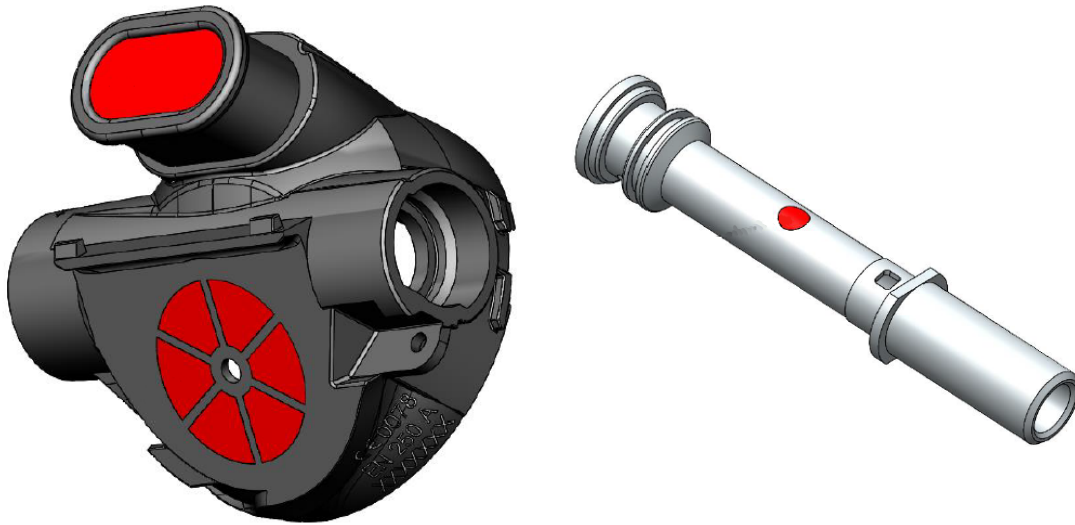
Figure 5.19: *Gas chamber casing highlighting both the mouth opening, and the outlet when air is pushed out and part of the lever mechanism highlighting the injection surface.*
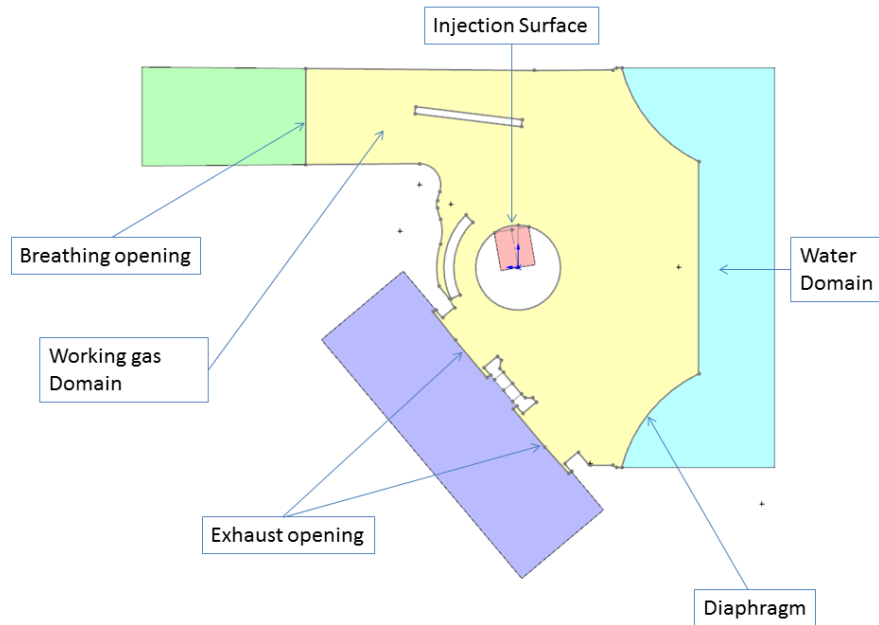

Figure 5.20: *A 2D cut of the computational domain highlighting the different parts of the simulation.*
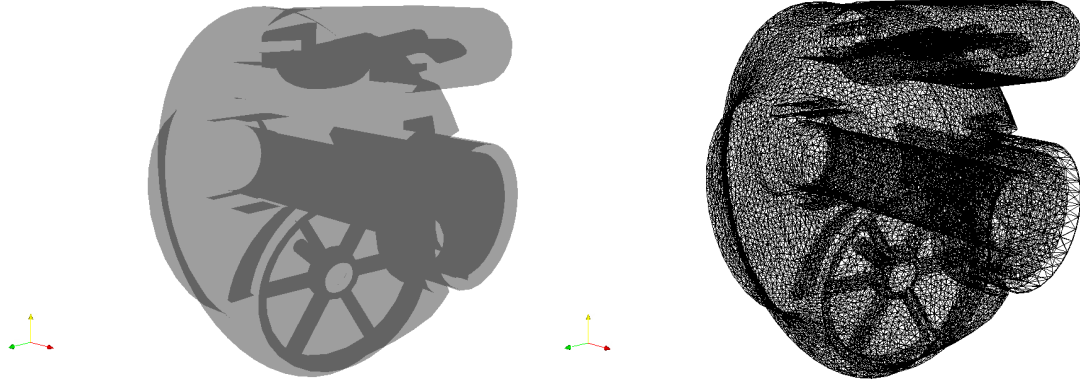
Figure 5.21: 3D depiction of the fluid flow simulation domain and an example of a mesh used for the fluid flow simulation.

compared to insights we get from a Magnetic Resonance Imaging (MRI) scan of the brain. To the best of our knowledge, this is the first time such insight is given for such an application. Now that the fluid flow simulation has been established, the different components are added. Two different views of the FSI computational domain are shown in figure 5.24 for the FSI simulation. An enlarged water domain can be observed to be able to model the multi-phase nature of the flow. A pre-adapted mesh is considered for this simulation, where a high concentration of elements exists in the vicinity of the membrane. Therefore, enabling us to account for the membrane movement, while still being able to immerse it in the fluid-solid mesh.

Figure 5.25 shows the pre-adapted mesh with the immersed solid and a plane cut of the pre-adapted mesh. An enlarged view of the mesh is shown in figure 5.26, along with the immersed solid in the domain for the previously shown mesh. The solid membrane is shown in figure 5.27. The main challenge of such a complex simulation lies in the thickness of the membrane.

As can be seen from the different views of the solid membrane, its thickness is really small compared to the rest of the domain. Therefore, a pre-adapted mesh is of utmost importance. To consider the final component of this simulation, we mix the properties of the two fluids, using the level set function detailed in previous sections. A field showcasing the mixing of the properties of the two fluids with respect to the position of the solid is given in figure 5.28.

5.3.2 Dynamic mechanical analysis (DMA)

Usually, materials, and more specifically metals, have a stress-strain curve like that shown in figure 5.29. They start by having a linear elastic response to a stress applied until reaching a certain yield point, after which plastic deformation starts to
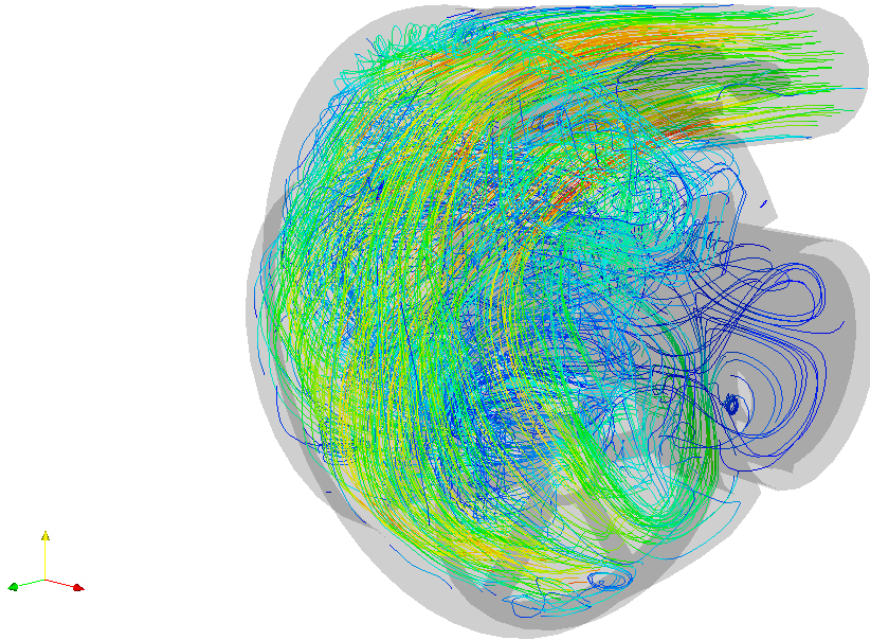
Figure 5.22: Streamlines highlighted with the velocity field for the fluid flow inside the pressure regulator.

occur. Necking occurs at the ultimate strength point, after which the material will deform until failure. However, this is not the typical behavior of polymers. Where more of a hyperelastic response is expected as shown in figure 5.30. The application of interest does not induce plastic deformation. Thus, we will be focusing on the hyperelastic response of the material.

The provider of the material did not have sufficient details on the behavior of the membrane at hand. Therefore, a Dynamic Mechanical Analysis (DMA) has been conducted on cut samples of the material. This is a method to characterize and inspect certain materials. It is mostly used for polymers with a viscoelastic behavior. That means a material that undergoes both elastic and viscous-like behavior under strain. The viscosity of a material, usually a fluid, is the ability to resist shear flow (or shear stress in the case of the solid) and deformation in a linear manner when undergoing stress. Viscosity is the outcome of diffusion of molecules or atoms in a amorphous material. Elasticity however is the ability to strain under stress, and return to the original position when that stress is no longer applied. It is due to bond stretching along crystallographic planes [3]. Viscoelastic materials exhibit both viscous and elastic behavior, thus leading to time dependent strain. The DMA consists of applying a sinusoidal stress, and measuring the corresponding strain of the material. This allows us to calculate a complex modulus. One can vary usually either
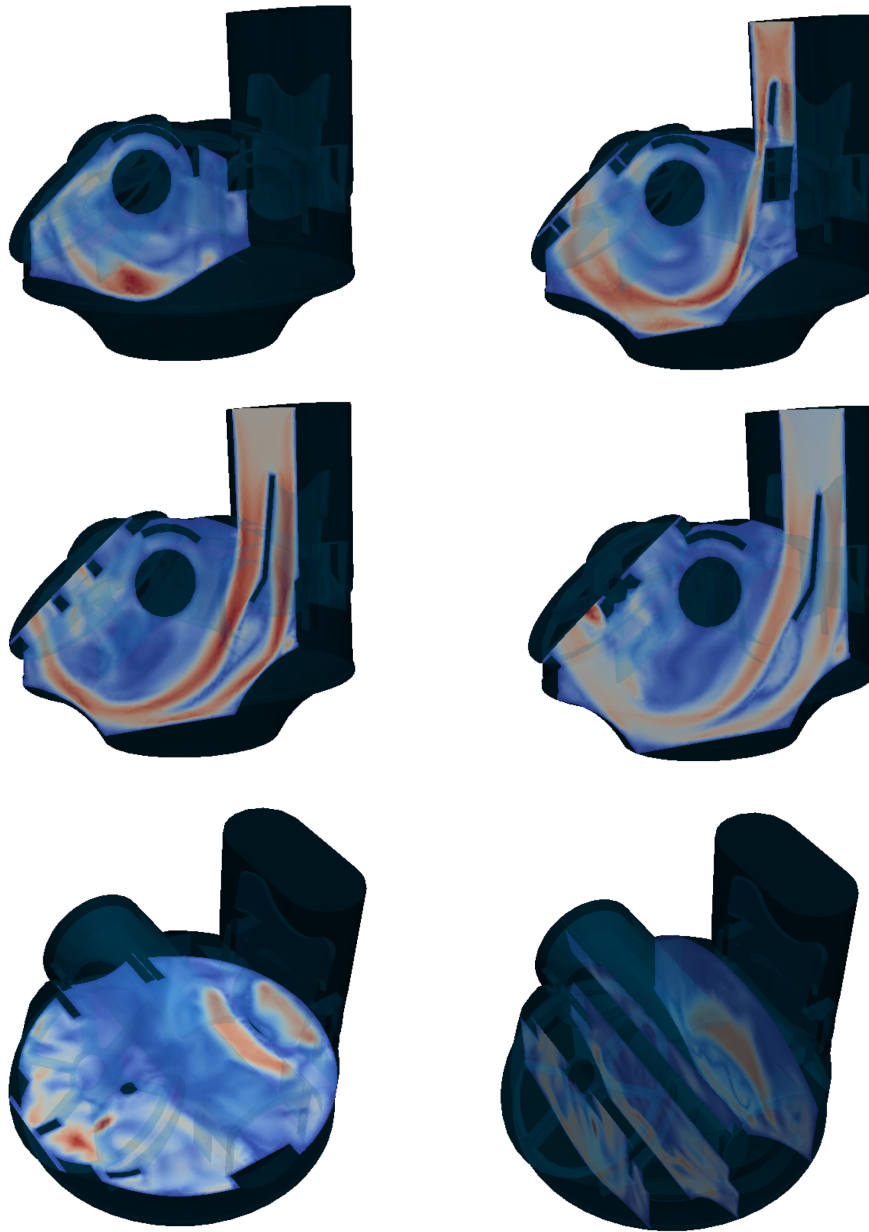
Figure 5.23: Different cuts of the 3D fluid flow simulation giving insights first seen in a pressure regulator.

the temperature or the frequency of the applied stress. This will lead to different values of the complex modulus. Which inevitably helps locate the glass transition temperature of the material at hand [4]. This temperature is the threshold for which
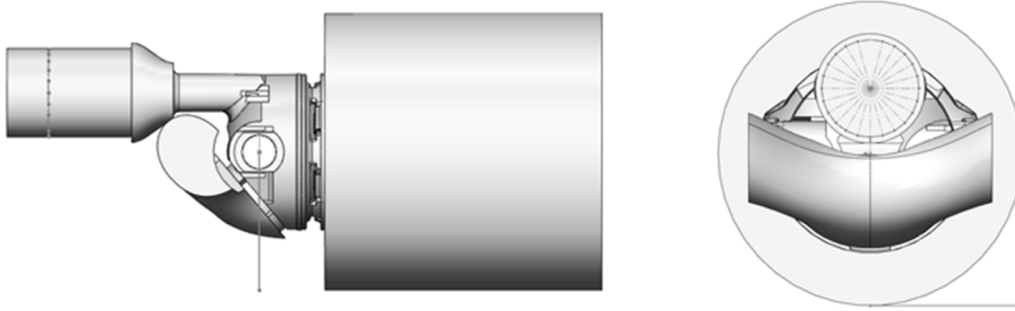
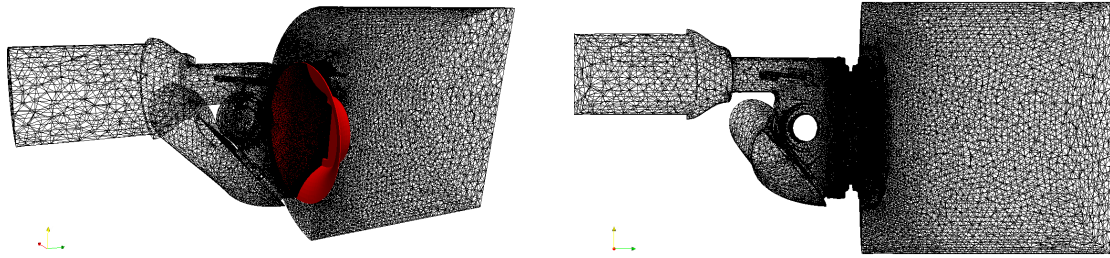*Figure 5.24: FSI simulation computational domain view with the pressure sensors position highlighted.*

Figure 5.25: 3D pre-adapted mesh example made up of 3D tetrahedral elements, while highlighting the solid position and a 2D cut of the pre-adapted mesh.
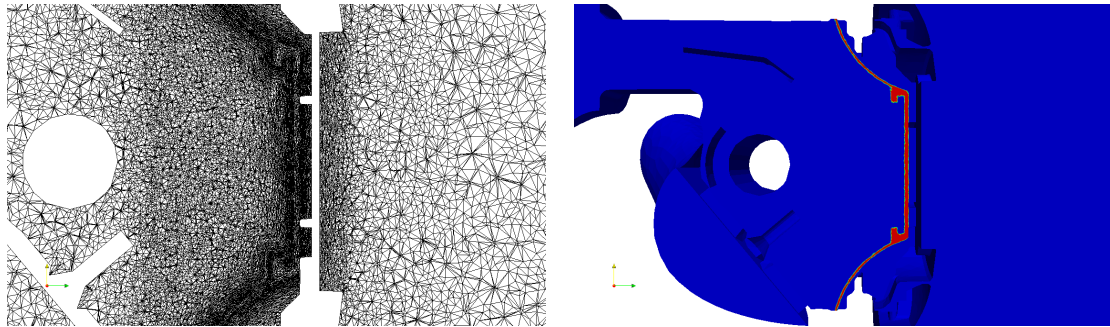

Figure 5.26: An enlarged view of the 2D pre-adapted mesh and the solid membrane immersed in the fluid-solid domain.

the material transforms from a brittle like behavior to a rubbery like behavior. If the material is a perfectly elastic solid, the strain and stress curves will be perfectly in phase. If the material is a purely viscous fluid, a ninety-degree phase lag is observed of the strain to the stress. Viscoelastic behavior is characterized as a behavior in
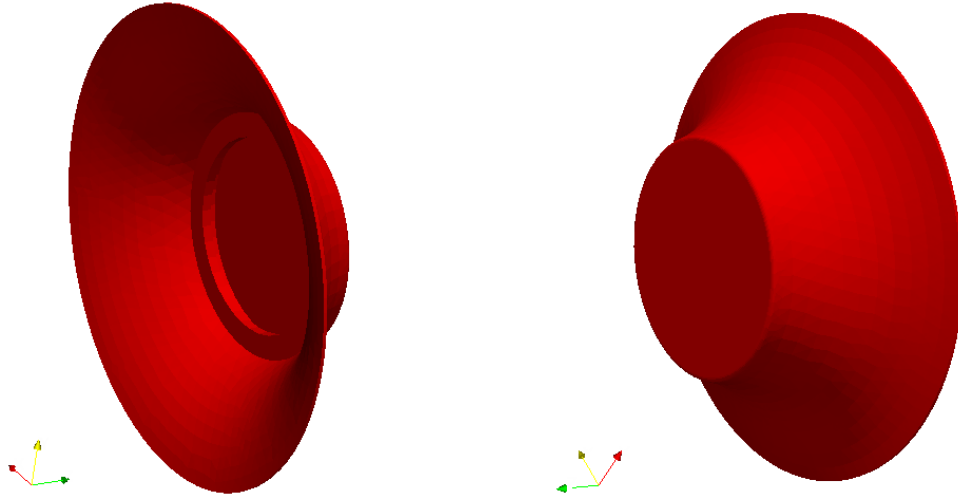
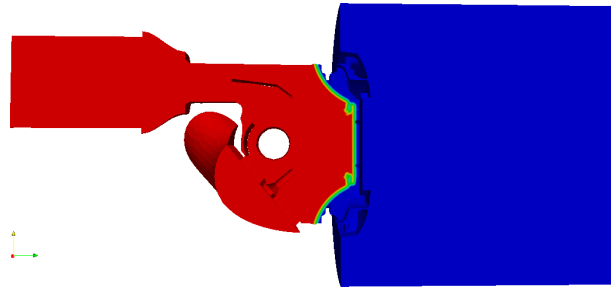*Figure 5.27: Two different view of the membrane.*

Figure 5.28: Second stage pressure regulator from AquaLung.

between the aforementioned pure behaviors. Some phase lag is bound to occur in a DMA test for a viscoelastic material. This behavior is characterized by the following equations

$$\sigma = \sigma_0 \sin(\omega t + \delta), \tag{5.4}$$

$$\varepsilon = \varepsilon_0 \sin(\omega t). \tag{5.5}$$

Where ω is the frequency, t is the time, and δ is the phase lag. If we revert to
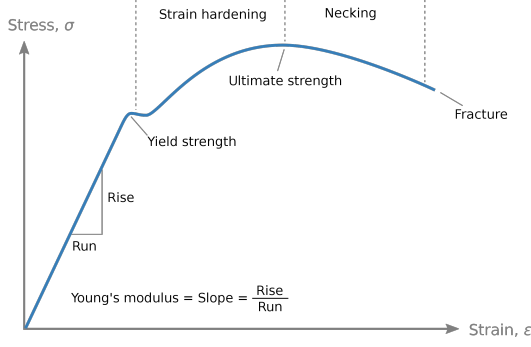
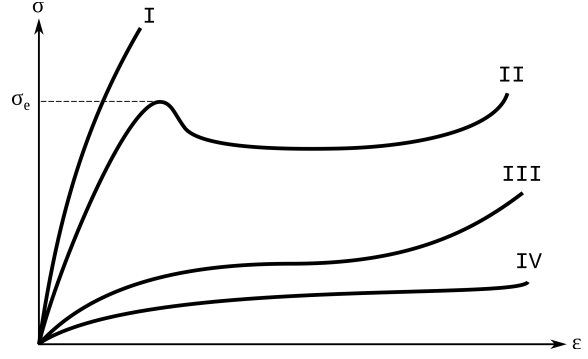Figure 5.29: *Typical material stress strain curve.*

Figure 5.30: *Stress strain curve of polymers.*

the assumption of a pure elastic solid, the following holds

$$\sigma(t) = E\varepsilon(t). \tag{5.6}$$

Which can be rewritten as

$$\sigma_0 \sin(\omega t + \delta) = E\varepsilon_0 \sin(\omega t) \to \delta = 0. \tag{5.7}$$

For the assumption of a purely viscous fluid, we can write

$$\sigma(t) = K\frac{d\varepsilon}{dt}. \tag{5.8}$$

which is reformulated as

$$\sigma_0 \sin(\omega t + \delta) = K\varepsilon_0\omega \cos(\omega t) \to \delta = \frac{\pi}{2}. \tag{5.9}$$

The complex modulus is composed of two components:

1. The storage modulus, which is responsible for the stored energy of the elastic part given by $E' = \frac{\sigma_0}{\varepsilon_0} \cos \delta$.

2. The loss modulus, which represents the energy dissipated of the viscous part written as $E'' = \frac{\sigma_0}{\varepsilon_0} \sin \delta$.

The phase angle δ can be written as $\delta = \arctan \frac{E''}{E'}$. Finally the complex modulus is given by

$$E^* = E' + E'' = \frac{\sigma_0}{\varepsilon_0}e^{i\delta} \tag{5.10}$$

Given the polymeric nature of the membrane, and after consulting with the necessary material experts from the lab, it was deduced that the membrane most likely

has a viscoelastic behavior. We used the apparatus shown in figure 5.31. It consists of a nitrogen tank shown in figure 5.32, that feeds nitrogen gas to cool the sample for a temperature sweep. This is done through careful pressure monitoring system shown in 5.33, that eventually reaches the chamber where the material sample is located presented in figure 5.34. The chamber contains the clamped material sample that undergo cooling, and then is heated for a temperature sweep at a constant frequency of stress. Figures 5.35, and 5.36 show the specimen clamped inside the chamber, and an enlarged view of the specimen respectively. A temperature sweep was conducted at a frequency of $1Hz$, where a glass transition temperature was determined that is significantly lower that the application temperature. The temperature sweep was done twice to account for the reproducibility of the results, and any possible hysteresis observed in the data. The results obtained are shown in figure 5.37. A combined sweep was later conducted twice, to see the effect of frequency change on the different intervals of temperatures.
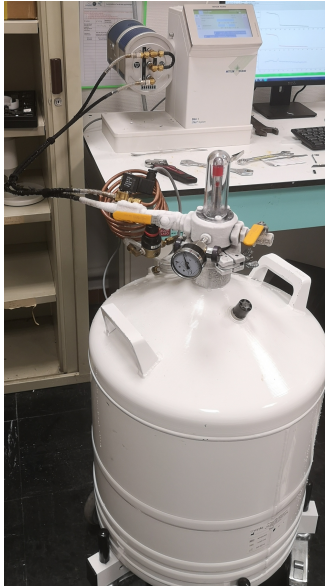

Figure 5.31: Dynamic Mechanical Analysis system.

Figure 5.32: Gas system for cooling.

No significant change of the storage or loss modulus is observed. Therefore we decided to opt for the equation

$$E = \sqrt{E'^2 + E''^2}, \tag{5.11}$$

for the calculations of the Young's modulus of the material, and use a hyperelastic
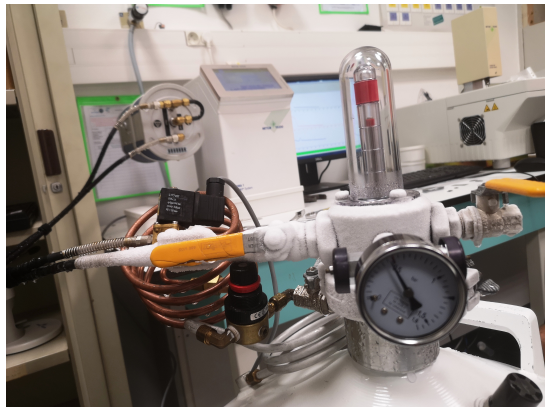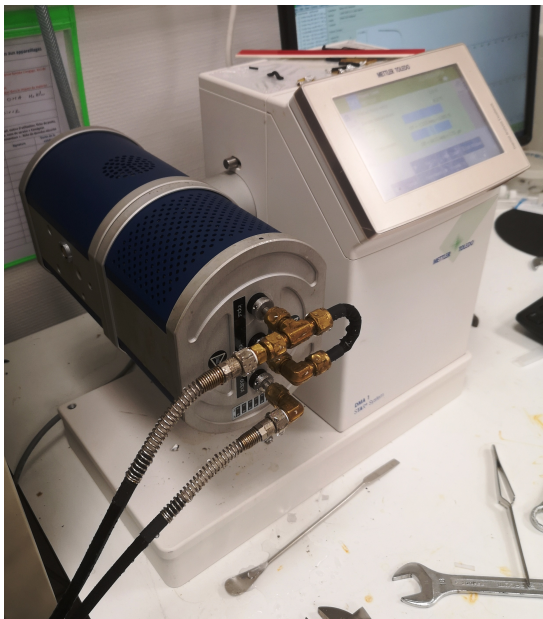
169

Figure 5.33: Pressure gauge system.

Figure 5.34: Chamber containing the specimen of the material undergoing testing.

Figure 5.35: Specimen chamber open.

Figure 5.36: An enlarged view of the specimen inside the chamber.

model as explained in previous sections. Since the experimental setup we are trying to reproduce is at a constant pressure and temperature, the assumption taken is satisfactory.
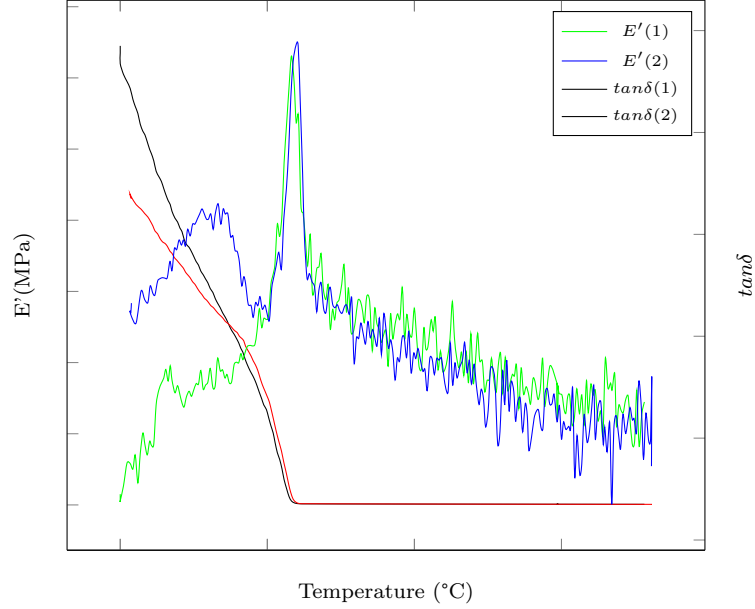

Figure 5.37: Results of the temperature sweep DMA experimental study for two different trials.

5.3.3 Numerical results

Now that all of the components of this high-fidelity 3D complex FSI simulation have been gathered, the simulation is ran for a complete cycle, and the results are presented here after. First, a 2D cut showing the inspiration and expiration phase of the flow inside the fluid-solid domain at different positions in time are shown in figure 5.38. 3D figures showcasing both the inspiration and expiration phase inside domain, and the membrane movement are shown in figures 5.39, 5.40, 5.40, 5.42 and 5.43. Finally, the membrane deformation for the inspiration phase is shown in figure 5.44, and that of the expiration phase is shown in figure 5.45. A close up of an important deformation of the membrane during the inspiration and expiration phase is shown in figure 5.46.

This framework was able to handle a complex 3D FSI simulation. This was done using the AIMM FSI framework developed in the previous chapters. The complexity came from the multi-phase nature of the flow, by having water on one side and the working gas on the other side. Furthermore, the membrane separating

both domains is actually really thin, thus adding more complexity to the simulation. Not to mention, the very high Reynolds number inside the working gas domain, especially for the inspiration phase.

Bibliography

[1] Appareils respiratoires — Appareils de plongée autonomes à air comprimé et à circuit ouvert — Exigences, essai et marquage. 152

[2] H. L. BRIS, PRINCIPES DES DÉTENDEURS DE PLONGÉE, Édition 2018 Edition, 2017. 152

[3] M. A. Meyers, K. K. Chawla, Mechanical behavior of materials, Cambridge university press, 2008. 164

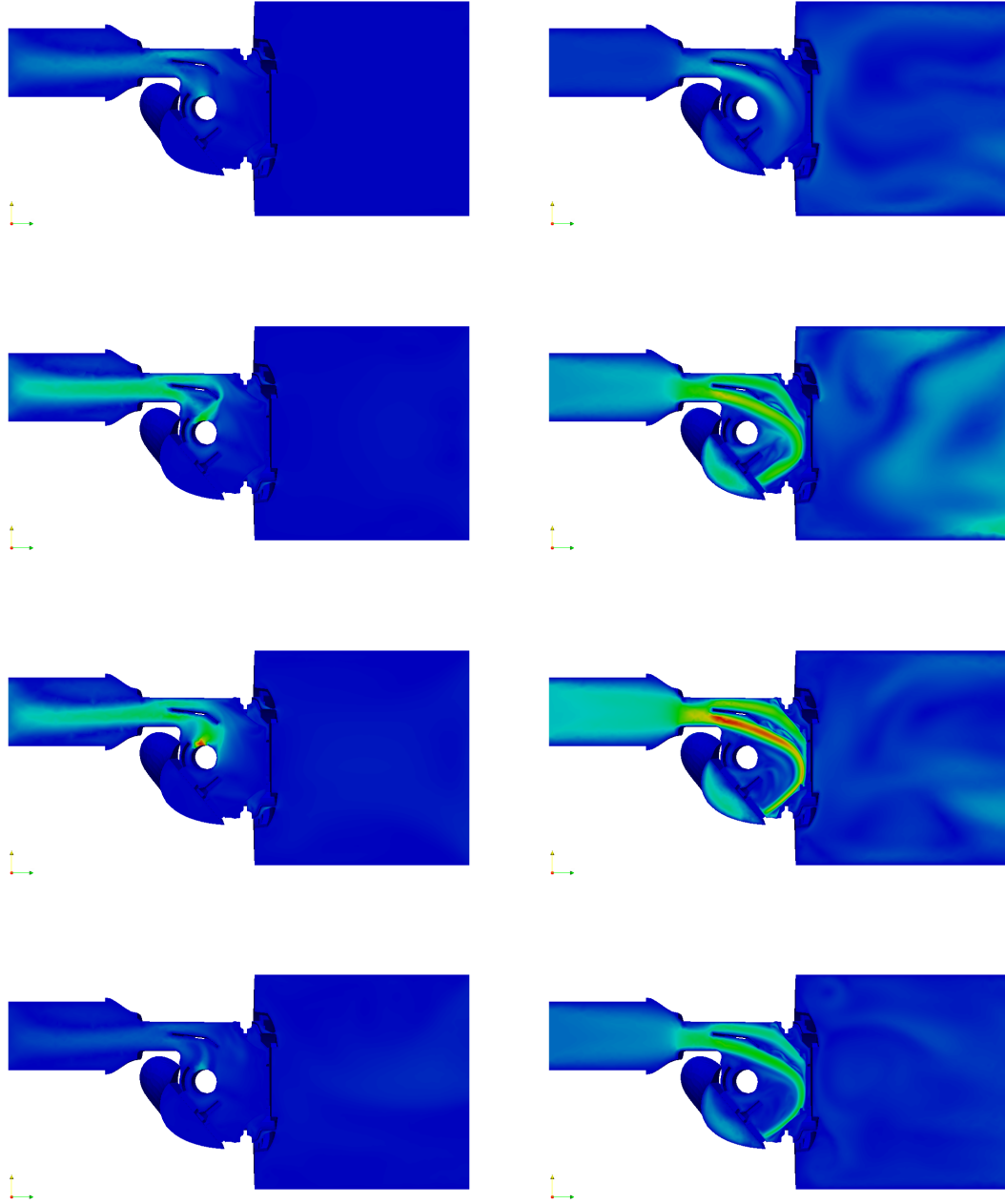[4] E. Turi, Thermal characterization of polymeric materials (2012). 165

Figure 5.38: Velocity contours for the inspiration and expiration phase in a 2D cut of the fluid-solid domain.

Figure 5.39: *Velocity contours for the inspiration phase in a 2D cut of the fluid-solid domain.*

Figure 5.40: Velocity contours for the inspiration phase in a 2D cut of the fluid-solid domain.

Figure 5.41: Velocity contours for the inspiration phase in a 2D cut of the fluid-solid domain.
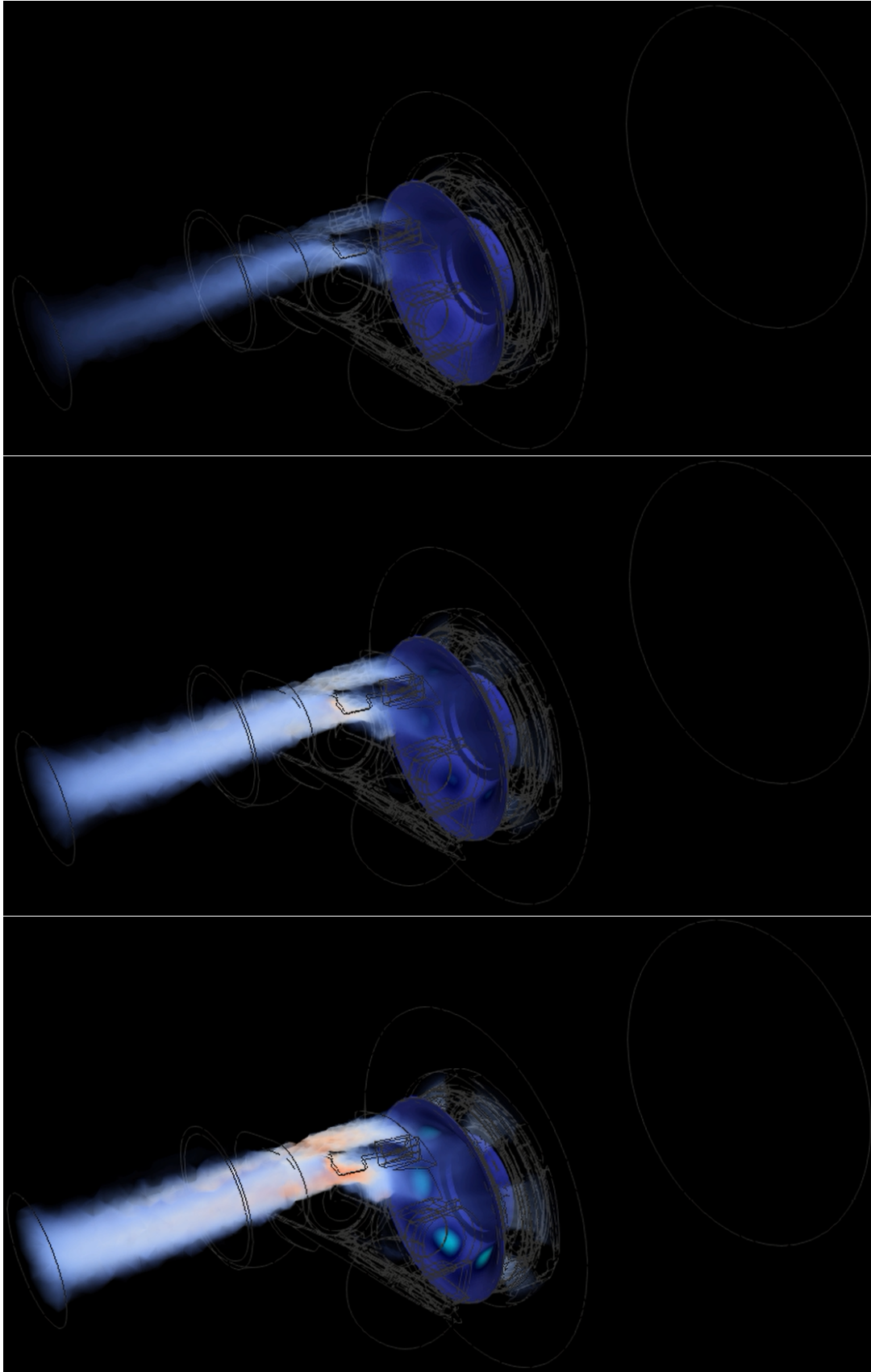
Figure 5.42: Velocity contours for the inspiration phase in a 2D cut of the fluid-solid domain.

Figure 5.43: Velocity contours for the inspiration phase in a 2D cut of the fluid-solid domain.
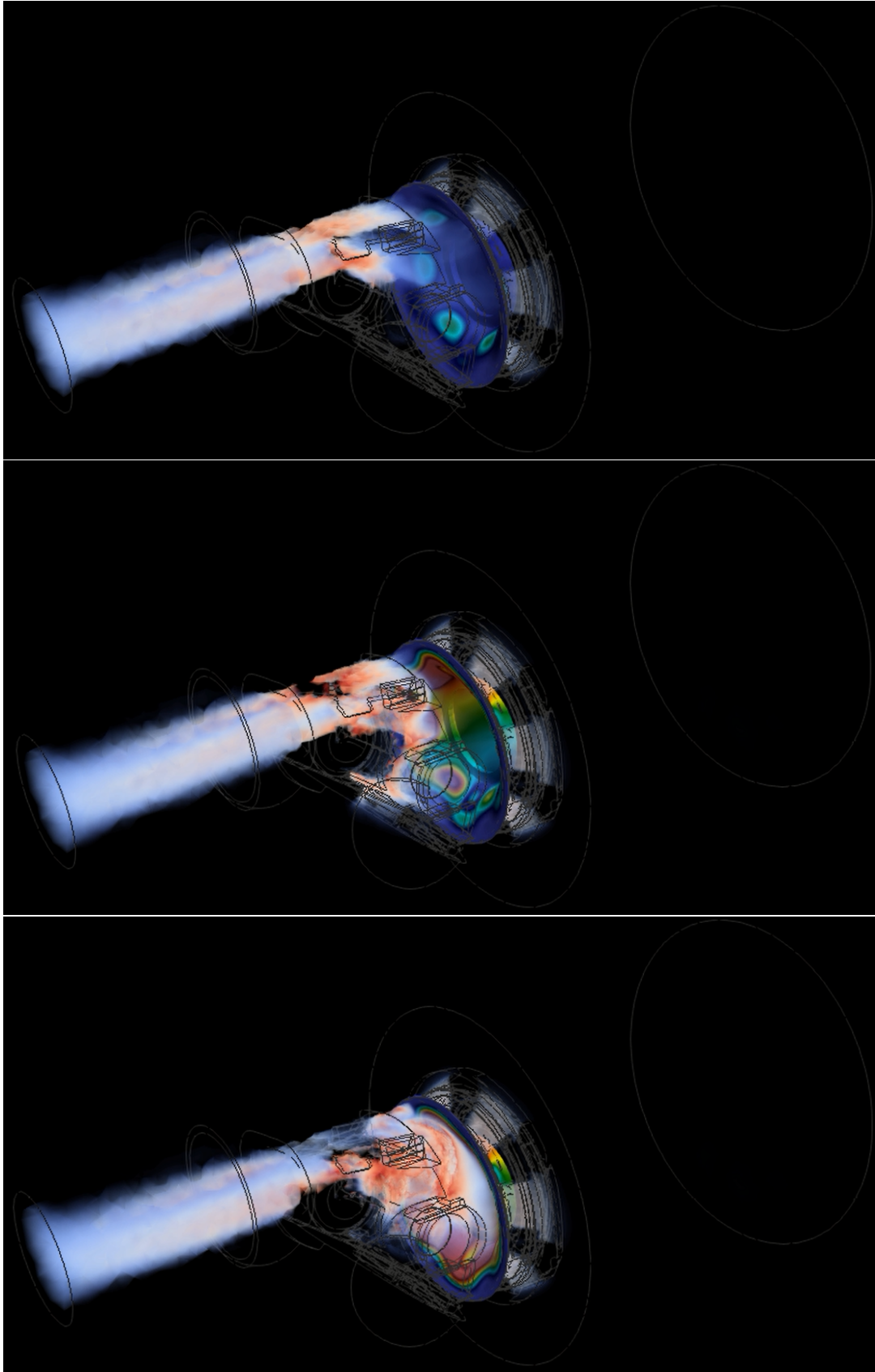
Figure 5.44: Membrane behavior during inspiration cycle.
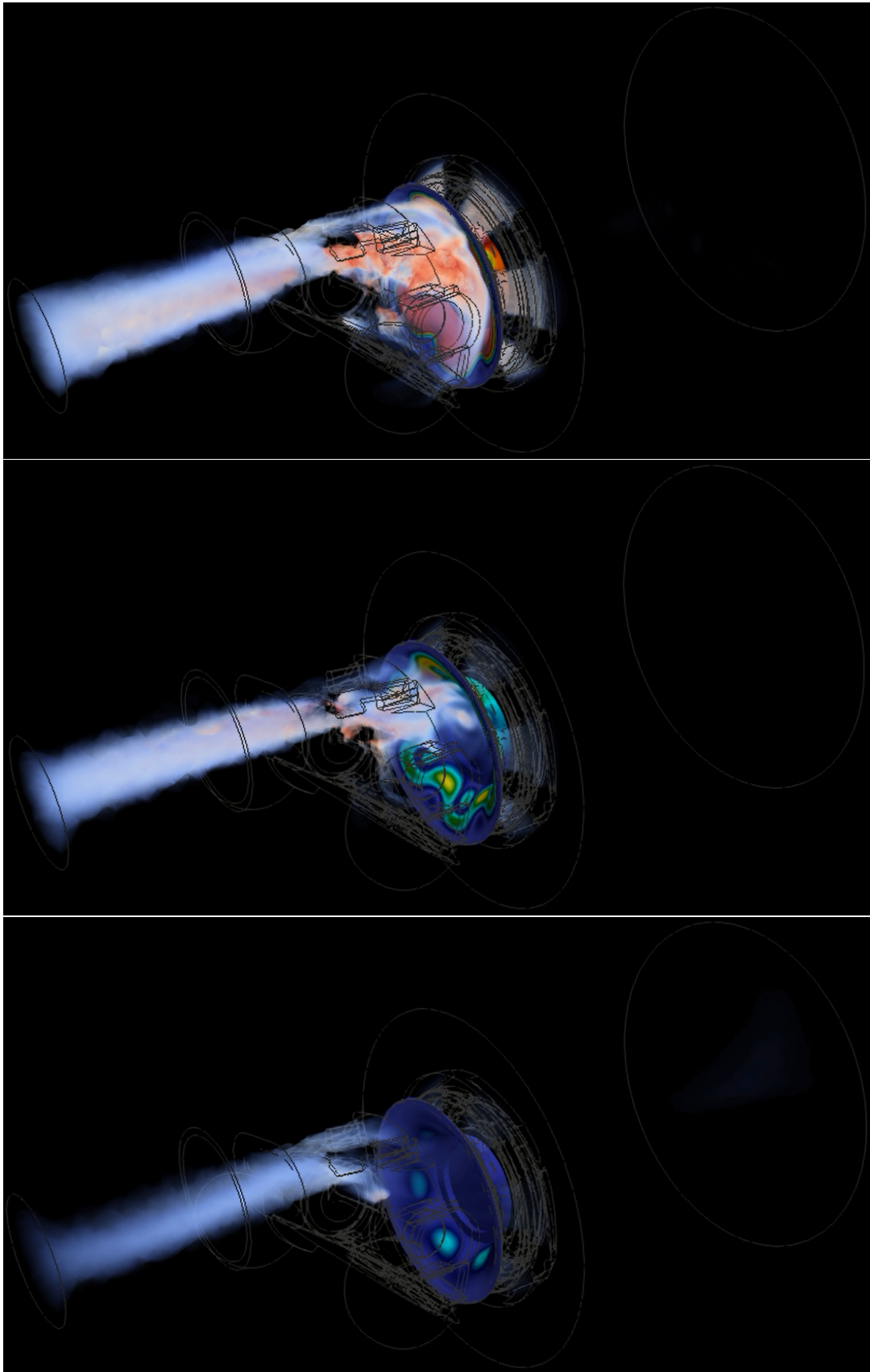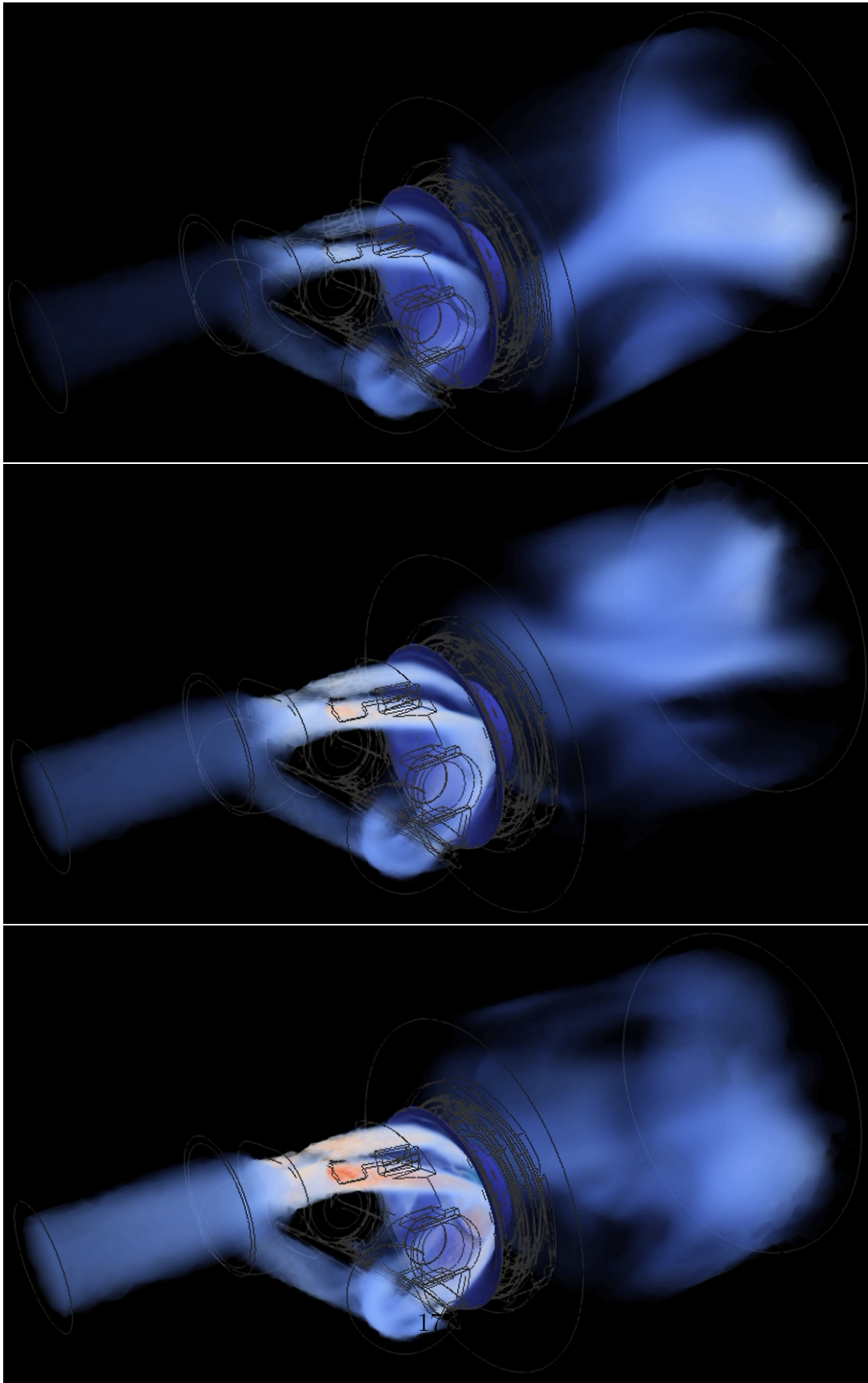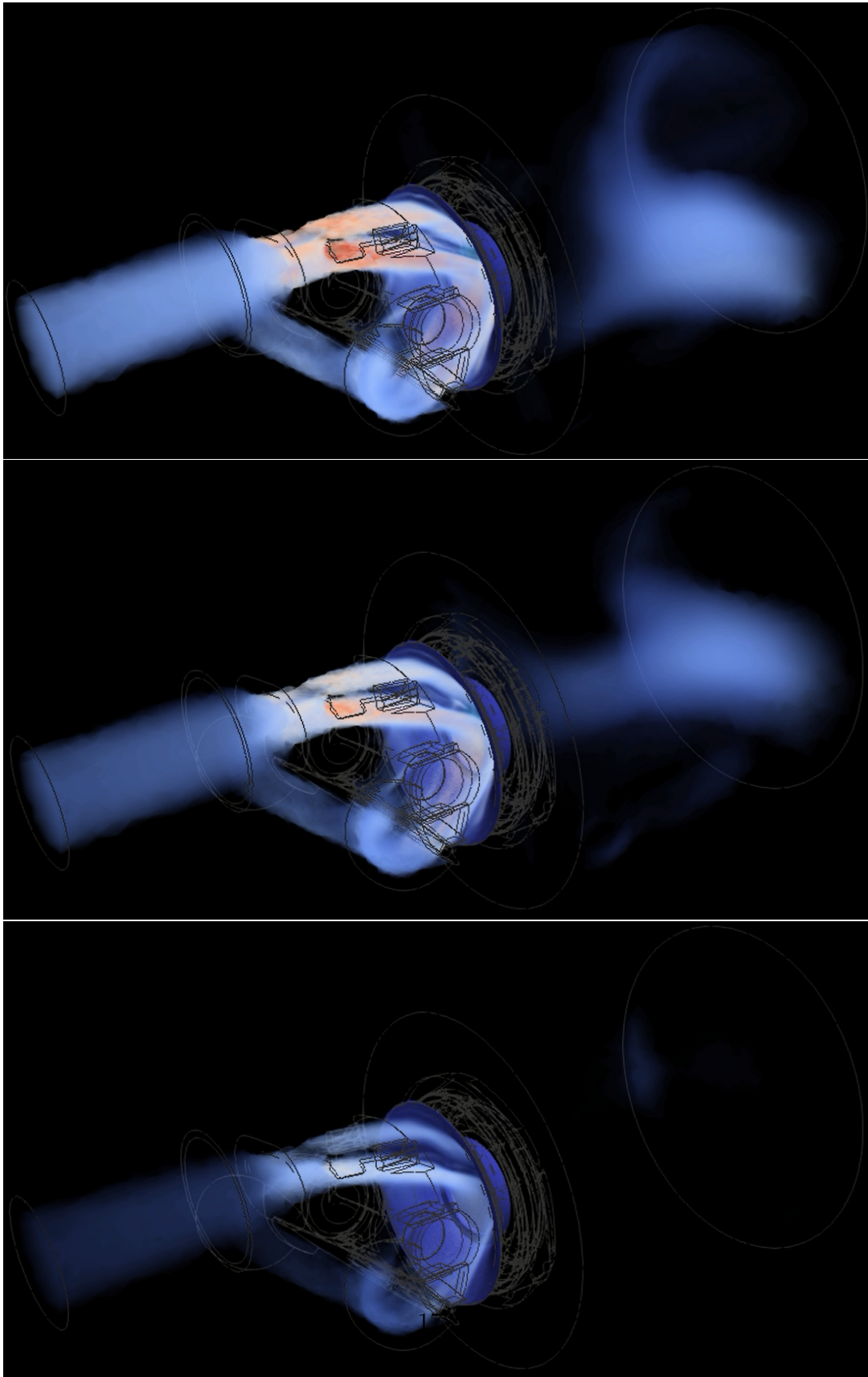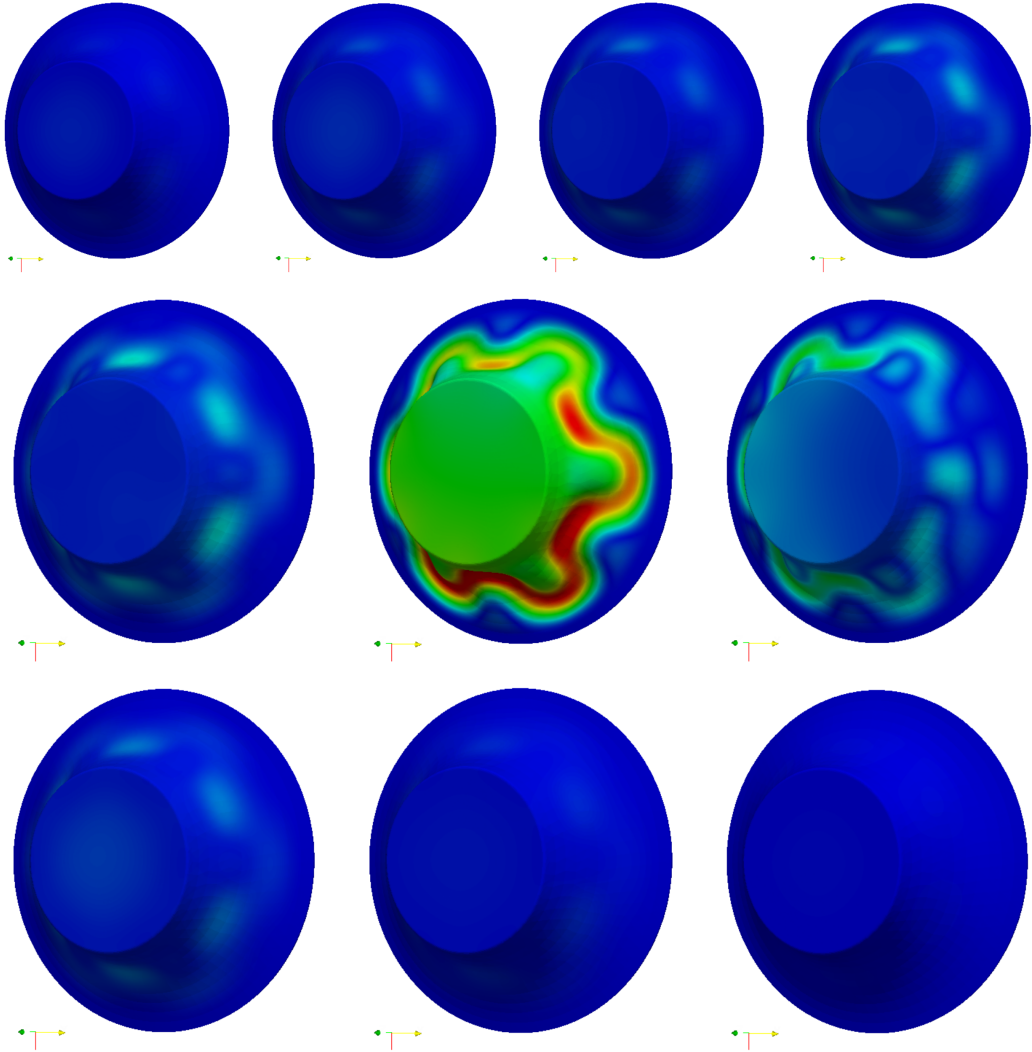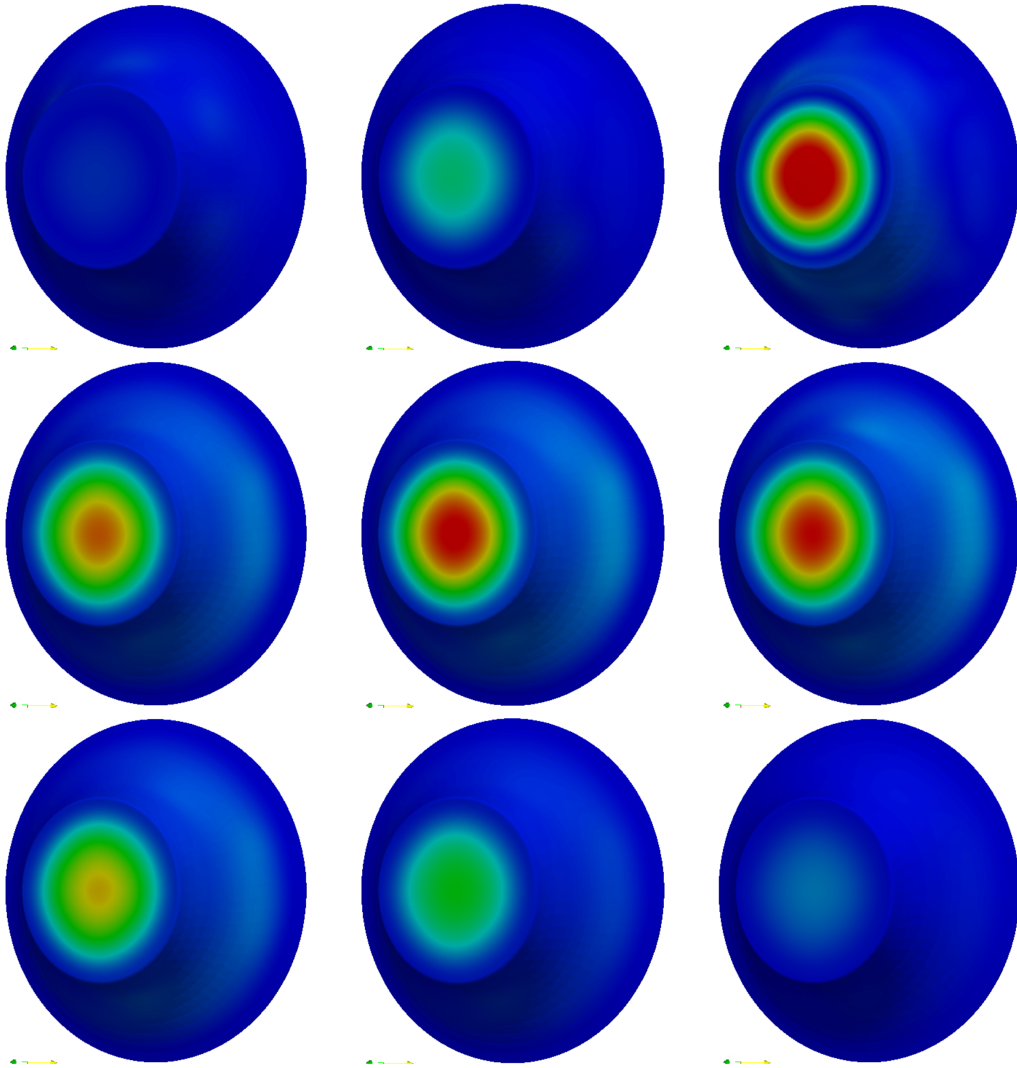
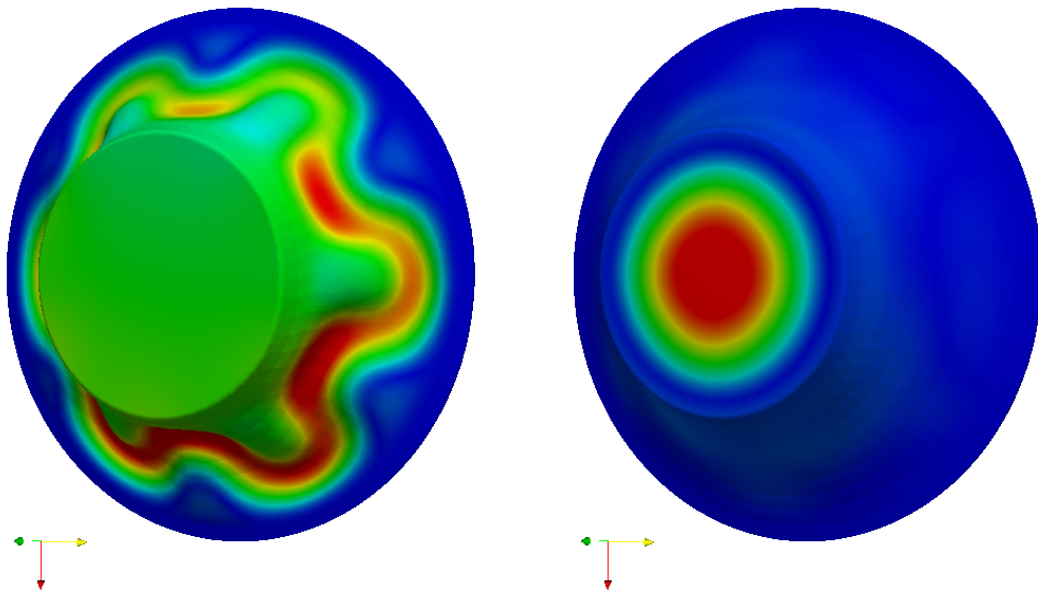*Figure 5.45: Membrane behavior during expiration cycle.*

Figure 5.46: Membrane solid domain during inspiration and expiration - an enlarged view.

Bibliography

Chapter 6

Conclusion and perspectives

Contents

Compte tenu du large éventail d'applications d'ingénierie qui incluent le FSI, de grands efforts sont déployés pour créer des cadres fiables capables de simuler avec précision de tels phénomènes. Les applications FSI incluent l'hydrodynamique, l'aérodynamique et la biomécanique. L'objectif de la thèse est la création d'un cadre FSI, capable de simuler efficacement des phénomènes aussi complexes, et de l'appliquer à un régulateur de pression pour la plongée. Cela se fait dans un contexte hybride, qui inclut à la fois les approches monolithiques et partitionnées. La première partie de la thèse introduit la notion d'Interaction Fluide–Structure (FSI). Ensuite, une brève revue de la littérature des différentes approches existantes dans la littérature est présentée. Il est complété dans les chapitres suivants, en mettant davantage l'accent sur le sujet traité. Les différents composants du framework FSI développé, la méthode hybride de maillage immergé adaptatif (AIMM) utilisant l'expertise multidisciplinaire de CimLib_CFD. Tous les outils numériques déjà développés qui sont utilisés pour le cadre FSI sont détaillés dans le chapitre deux. En particulier, la méthode des volumes immergés (IVM), comprend la méthode des ensembles de niveaux, les lois de mélange pour les écoulements multiphasiques et l'adaptation du maillage anisotrope. Le chapitre trois propose une nouvelle façon de résoudre la dynamique solide transitoire. Il a d'abord été développé pour le cas linéaire et a ensuite été étendu pour inclure le cas hyperélastique. La formulation a été écrite avec l'incompressibilité à l'esprit. Cela signifie que le solveur peut gérer des matériaux compressibles, presque incompressibles et incompressibles. Le cœur de la thèse et le cadre FSI sont présentés dans le chapitre quatre. La méthode de maillage immergé adaptatif (AIMM) est expliquée. Il s'agit d'une nouvelle méthode hybride qui combine les avantages des approches partitionnées et monolithiques traditionnelles pour le FSI. Après une validation suffisante du cadre FSI, il a été appliqué à l'application industrielle. Les premières validations d'écoulement de fluide sont présentées, avant d'appliquer le cadre FSI complet. L'application finale consiste en un écoulement multiphasique à partir duquel, d'une part, nous avons l'eau environnante, et d'autre part, nous avons le gaz de travail à l'intérieur du régulateur de pression. L'objectif de la thèse était de créer un cadre FSI fiable capable de simuler des phénomènes FSI complexes. Les simulations numériques ont été contraintes aux fluides incompressibles newtoniens et aux structures élastiques. Plusieurs autres considérations peuvent être prises en compte pour élargir le nombre d'applications qui peuvent être simulées à l'aide de ce cadre.

6.1 Conclusion and perspectives

Given the wide range of engineering applications that include FSI, great effort is being put to create reliable frameworks that can accurately simulate such phenomena. FSI applications include hydrodynamics, aerodynamics, and biomechanics. The objective of the thesis is the creation of an FSI framework, that can efficiently simulate such complex phenomena, and apply it to a pressure regulator for diving. This is done in a hybrid context, that includes both the monolithic and partitioned approaches.

The first part of the thesis introduces the notion of Fluid–Structure Interaction (FSI). Then a brief literature review of the different approaches existing in the literature is presented. It is complemented in the following chapters, with more emphasis on the subject at hand.

The different components of the developed FSI framework, the hybrid Adaptive Immersed Mesh Method (AIMM) using the multidisciplinary expertise of CimLib_CFD. All the already developed numerical tools that are used for the FSI framework are detailed in chapter two. In particular, the Immersed Volume Method (IVM), includes the level set method, the mixing laws for multi-phase flow, and the anisotropic mesh adaptation. The level set approach is utilized for the interface tracking of the immersed solid mesh at each time step. The mixing laws are particularly useful for the multi-phase flow of the industrial application for example. Finally, the anisotropic mesh adaptation method helps us better depict the FSI interface, allowing us to have a better coupling between the different meshes and higher accuracy at the interface. If we also take into the multiple criteria available, it helps us adapt the mesh for velocity as well, thus reducing the overall computational tile, while still being able to capture important flow structures. Several mesh adaptation techniques are presented: an anisotropic local remeshing method, and a posteriori error estimation method. The first method refines the mesh at the interface by creating a metric field through the gradient of the level set function. The second method is based on a posteriori error estimator. A length distribution tensor approach and its associated edge-based error analysis are used. We can simultaneously adapt the mesh for the level set, and any other physical field like the velocity magnitude or components.

Chapter three proposes a new way to solve the transient solid dynamics. It was first developed for the linear case and was then extended to include the hyperelastic case. The formulation was written with incompressibility in mind. That means the solver can handle compressible, nearly incompressible, and incompressible material. It consists of a mixed formulation in displacement and pressure. The momentum equation is complemented with a pressure equation that handles incompressibility. A split of the stress into its deviatoric and volumetric components enables us to do just that. Given the nonlinear nature of the deviatoric part of the stress, a

linearization technique was employed. All the terms of the equations are written in the updated Lagrangian framework. The interface tracking is done through the R-method for moving meshes. Tetrahedral unstructured elements are used, which enables us to handle complex 3D examples. Finally, the Variational Multi-Scale stabilization method is used to damp out spurious pressure oscillations for piece-wise linear finite elements. Several 2D and 3D examples were presented.

The heart of the thesis and the FSI framework are presented in chapter four. The Adaptive Immersed Mesh Method (AIMM) is explained. It is a novel hybrid method that combines the advantages of the traditional partitioned and monolithic approaches for FSI. The solid mesh is first immersed in a fluid–solid mesh. The Navier–Stokes equations are then solved on the fluid–solid mesh. Full stress is interpolated from the fluid–solid mesh onto the solid mesh. The solid dynamics equations are solved on the solid mesh. The mesh is moved using the Moving Mesh Method (MMM). The velocity of the solid is computed and then interpolated onto the fluid–solid mesh. The new solid mesh position is immersed onto the fluid-solid mesh. We iterate until the final time t is reached. This framework enables us to solve for example the heat equations in the fluid–solid mesh for both fluid and solid. Anisotropic mesh adaptation is used for higher accuracy of the definition of FSI interface, as well as on different criteria. The Variational Multi-Scale method is used for both solvers, to respect the inf-sup condition, and in the case of the fluid flow, to be able to handle highly convective flow regimes. The framework can handle both 2D and 3D numerical simulations, with parallel computing in mind. Extensive 2D and 3D cases have been carried out to validate the overall FSI framework both in 2D and 3D.

After sufficient validation of the FSI framework, it was applied to the industrial application. First fluid flow validations are presented, before applying the full FSI framework. The final application consists of a multi-phase flow wherefrom, on one hand we have the surrounding water, and on the other hand, we have the working gas inside the pressure regulator. These two mediums are separated by a solid elastic membrane. The results of the simulator for the pressure regulator are compared with experimental results from the industrial partner for us to validate the results obtained. It will be used for the optimization of the pressure regulator. Qualitative results are shown in this chapter to respect the confidentiality agreement with the industrial partner.

The focus of the thesis was on the creation of a reliable FSI framework that can simulate complex FSI phenomena. The numerical simulations were constrained to Newtonian incompressible fluid, and elastic structures. Several other considerations can be taken into account to enlarge the number of applications that can be simulated using this framework, including but not limited to

- The development of a compressible flow solver that will enable us to couple it

with the solid solver, thus including more applications.

- Enriching the Lagrangian solid solver to consider different elastic models, as well as different regimes, such as viscoelastoplastic, or more sophisticated biomechanical behavior laws.

- The inclusion of Non-Newtonian models or rheological blood models, thus expanding the range of applications to biomechanical applications such as blood flow, ... etc.

- Conducting FSI experimental studies and replicating the experimental setup numerically for further validation of the framework.

- The ability to include the simulation of composite materials. To that extent, the benchmark simulation of the beam behind a cylinder is revisited. This time, while still considering the same dimensions and boundary conditions of the problem, a sandwich-like composite material was considered. Where the shear modulus of the upper and lower part are equal to that of the second variation of the test, and the middle part is that of the first variation. All boundary conditions correspond to the first iteration of the benchmark. Figures 6.1, 6.2 and 6.3 showcase the stress in the material, and the mixing of properties inside the material for different positions of the solid. If compared to the result of the first iteration of the benchmark, the amplitude of vibration is much less, and the time it took to reach a periodic state of vibration is higher. This test is given to show the capabilities of the framework for future applications.
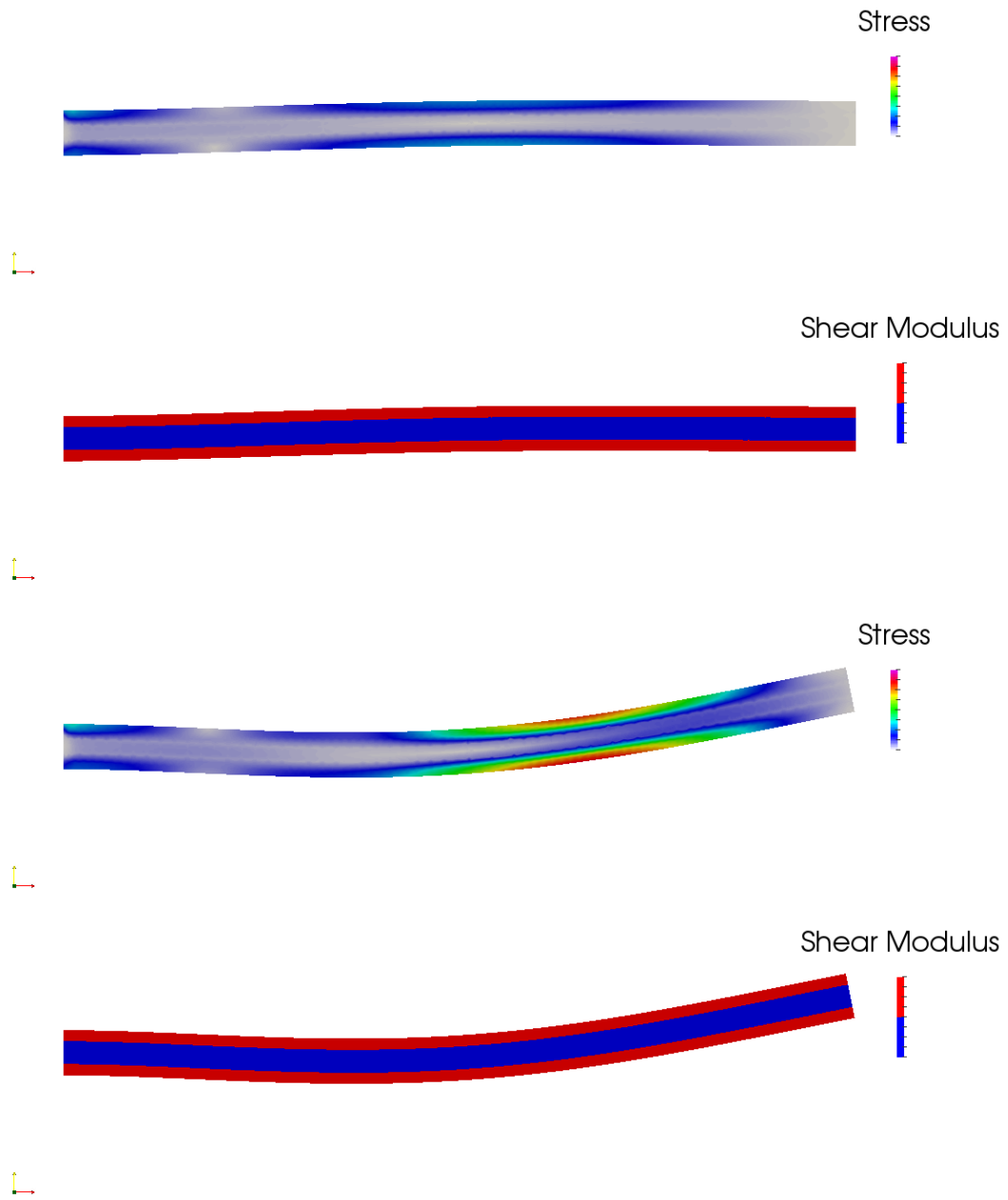
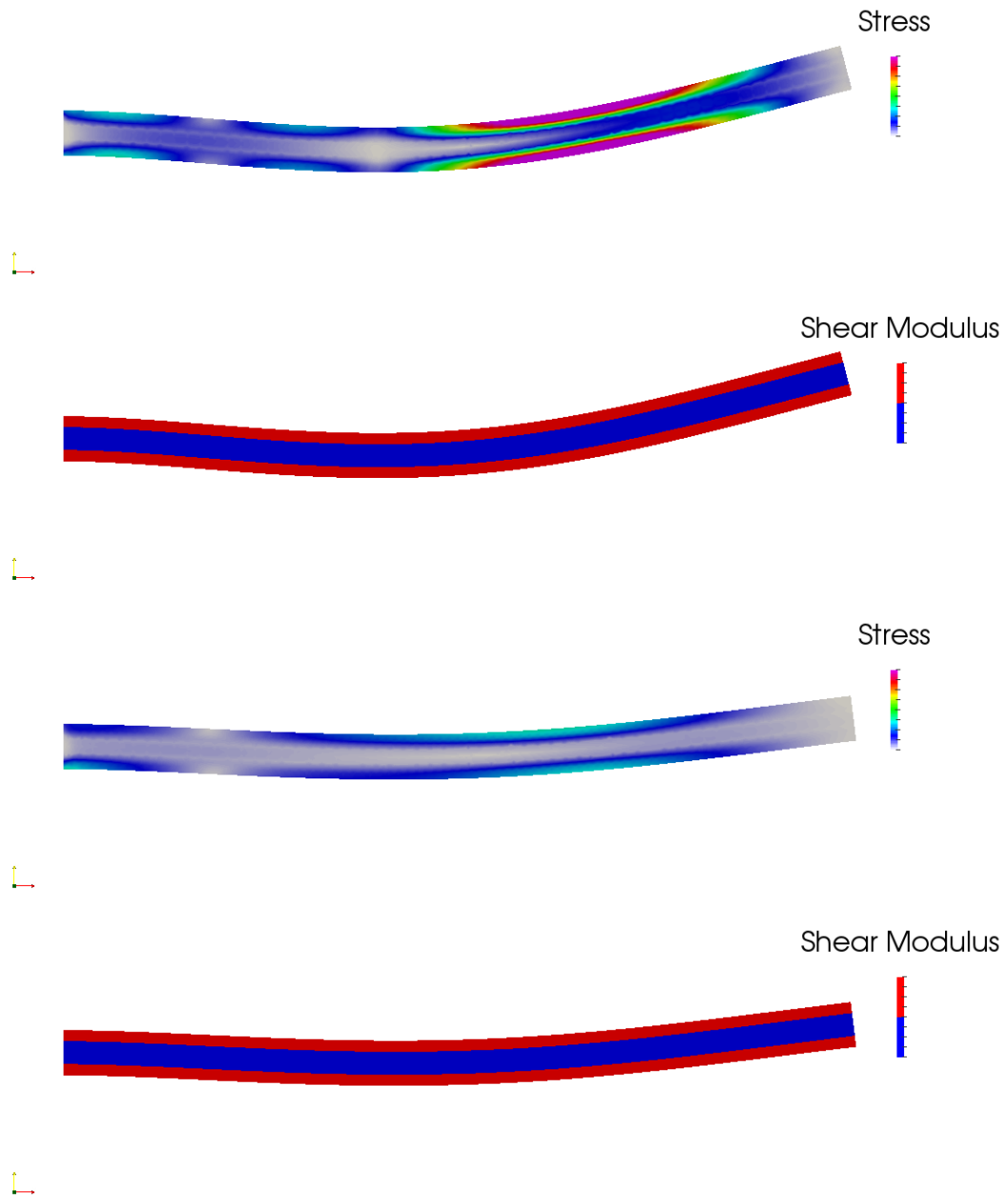Figure 6.1: Stress and the mixing of the shear modulus for different time t.

Stress

Shear Modulus

Stress

Shear Modulus

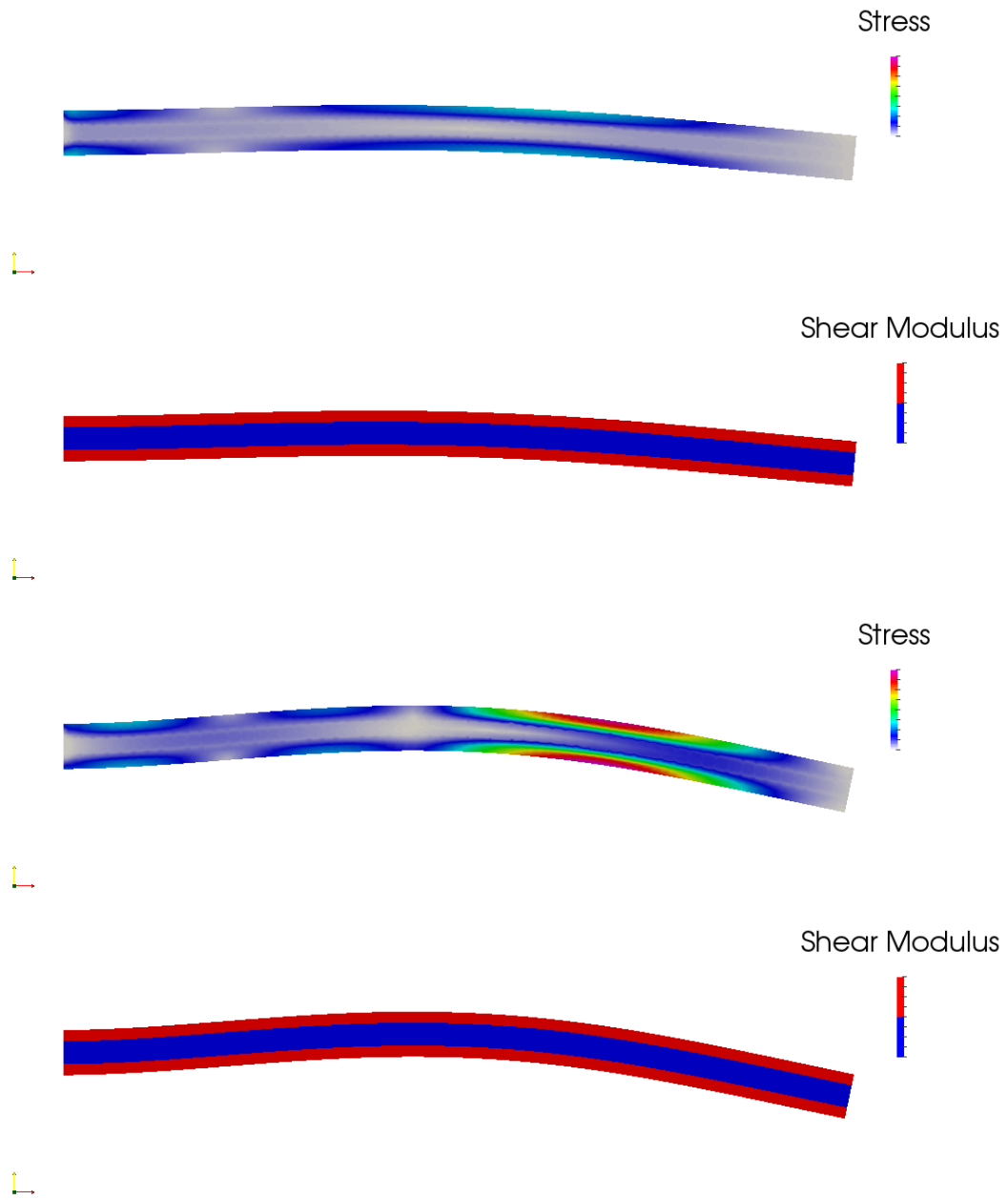Figure 6.2: Stress and the mixing of the shear modulus for different time t.

189

Figure 6.3: Stress and the mixing of the shear modulus for different time t.

RÉSUMÉ

Pour répondre aux besoins d'applications émergeantes impliquant des capteurs cylindriques et des structures membranaires, la simulation de structures de plus en plus fines et flexibles apparait nécessaire. Ces innovations interagissent avec leur environnement pour acquérir des données ou dans une fonction précise. Dans ce contexte, l'interaction fluide-structure (IFS) s'impose pour modéliser les phénomènes mis en jeu. Dans le cadre de cette thèse, une nouvelle méthode de couplage est proposée, combinant les deux méthodes traditionnelles monolithiques et partitionnée en une modélisation hybride. Le maillage solide est immergé dans le maillage fluide-solide à chaque pas de temps, tout en bénéficiant de son propre solveur solide. The solveur hyper-élastique met en place une formulation en déplacement et pression, dans laquelle l'équation de la quantité de mouvement est complétée par une équation de pression qui traduit le caractère incompressible du fluide. Cette formulation est obtenue par séparation du tenseur des contraintes en ses parties volumétriques et déviatoriques, ce qui permet la résolution du problème dans la limite d'incompressibilité. Une linéarisation de la partie déviatorique est également implémentée. Le maillage eulérien contient à la fois les domaines solides et fluides et permet la modélisation de phénomènes physiques complémentaires. Les méthodes d'adaptation de maillage anisotrope et de Level-set sont utilisées pour le couplage à l'interface entre le solide et le fluide afin de capturer plus finement leurs interactions. Tous les éléments précédemment introduits forment la ≪ Adaptive Immersed Mesh Method ≫ (AIMM). La méthode variationnelle multi-échelle est exploitée pour les deux solveurs afin d'amortir les oscillations parasites susceptibles de résulter de la modélisation en éléments tétraédraux linéaires. La méthode a été construite en 3D en gardant en tête les aspects de calcul parallèle. De multiples tests de validations en 2D et 3D sont présentés pour prouver le bon fonctionnement des solveurs mis en place. Pour finir, la méthode a été testée pour une application industrielle.

MOTS CLÉS

Interaction Fluide–Structure(IFS), Eléments Finis, Méthodes multi-échelles variationnelles, Adaptation de maillage anisotrope, Méthode hybride, hyperélastique.

ABSTRACT

The need to simulate flexible, relatively thin structure is of growing interest with applications ranging from thin cylindrical sensors to membrane-like structures. These structures usually interact with their surroundings to accumulate data, or for a specific purpose. The inevitable interaction between the surrounding fluid and the solid is solved using a novel Fluid–Structure Interaction (FSI) coupling scheme. This thesis proposes a novel way to model the interaction between the fluid and solid. It consists of a hybrid method that combines both the traditional monolithic and partitioned approaches for Fluid–Structure Interaction (FSI). The solid mesh is immersed in a fluid-solid mesh at each time step, whilst having its own independent Lagrangian hyperelastic solver. The hyperelastic solver consists of a mixed formulation in both displacement and pressure, where the momentum equation of the continuum is complemented with a pressure equation that handles incompressibility inherently. It is obtained through the deviatoric and volumetric split of the stress that enables us to solve the problem in the incompressible limit. A linearization of the deviatoric part of the stress is implemented as well. The Eulerian mesh contains both the fluid and solid and accommodates additional physical phenomena. Anisotropic mesh adaptation and the Level-Set methods are used for the interface coupling between the solid and fluid to better capture the interaction between them. All the above components form the Adaptive Immersed Mesh Method (AIMM). The Variational Multi-Scale (VMS) method is used for both solvers to damp out any spurious oscillations that may arise for piece wise linear tetrahedral elements. The framework is constructed in 3D with parallel computing in mind. Extensive 2D and 3D test cases are presented that validate the hyperelastic Lagrangian solver, and the FSI AIMM framework. An application of the industrial partners was lastly tackled.

KEYWORDS

Fluid–Structure Interaction(FSI), Finite Elements, Variational Multi-Scale methods, Anisotropic mesh adaptation, Hybrid method, hyperelastic.